ORNL/NRC/LTR-02/02

INSPECTION OF INACCESSIBLE REGIONS OF NUCLEAR POWER PLANT CONTAINMENT METALLIC PRESSURE BOUNDARIES

D. J. Naus
Metals and Ceramics Division
Oak Ridge National Laboratory
Oak Ridge, Tennessee 37831-8056

June 2002

(Milestone C.1.3.E)

Prepared for the
U.S. Nuclear Regulatory Commission
Office of Nuclear Regulatory Research
Under Interagency Agreement No. 1886-N604-3J

NRC JCN No. J6043

Prepared by the
OAK RIDGE NATIONAL LABORATORY
Oak Ridge, Tennessee 37831-8056
managed and operated by
UT-BATTELLE, LLC
for the
U.S. Department of Energy
under Contract No. DE-AC05-00OR2275

Research sponsored by the Office of Nuclear Regulatory Research, U.S. Nuclear Regulatory Commission, under Interagency Agreement 1886-N604-3J with the U.S. Department of Energy under Contract No. DE-AC05-00OR22725.

ABSTRACT

Inspection of inaccessible portions of metallic pressure boundary components of nuclear power plant containments requires special attention. Embedded metallic portions of these components may be subjected to corrosion resulting from ground water permeation through the concrete; a breakdown of the sealant at the concrete-containment shell interface that permits entry of corrosive fluids from spills, leakage, or condensation; or corrosion may occur in areas adjacent to floors where the gap contains a filler material that can retain fluids. Corrosion, should it occur, may challenge the containment structural integrity and, if through-wall, can provide a leak path to the outside environment. At present nondestructive evaluation techniques for use in determining the condition of the containment pressure boundary are time-consuming and costly because they tend to examine only a small area at a time, and generally require at least one accessible surface. A nondestructive technique is required that can be used remotely to examine inaccessible regions of the containment metallic pressure boundary. Such a technique ideally should also be capable of performing global inspections so that determination of the overall condition of the containment metallic pressure boundary can be achieved in a cost- and performance-effective manner. Identification and/or development of such technique(s) becomes increasingly important as the median age of the nuclear power plants now exceeds 20 years, and in the not-too-distant future several of these plants will be nearing the end of their initial operating license.

The overall objective of this study was to provide a status report with respect to potential approaches for inspection of inaccessible portions of containment metallic pressure boundaries. Nuclear power plant containment structures are described, potential degradation factors identified, inspection and testing requirements summarized, and operating experience presented with respect to the containment metallic pressure boundary. A review of nondestructive evaluation methods is provided and prior research related to development of techniques for inspection of inaccessible portions of the containment metallic pressure boundary reviewed. Results obtained under subcontracted activities with Cambridge Acoustical Associates/Engineering Technology Center (high frequency acoustic imaging), Southwest Research Institute (magnetostrictive sensors), and the Pennsylvania State University (multimode guided waves and electromagnetic acoustic transducers) are reiterated. Study conclusions and recommendations for further research are provided.

TABLE OF CONTENTS

Page

ABSTRACT iii

LIST OF FIGURES vii

LIST OF TABLES xi

ACKNOWLEDGEMENTS xiii

1.0 INTRODUCTION 1

1.1 Background 1
1.2 Statement of Problem 2
1.3 Objective and Scope 2
1.4 Organization of Report 2
1.5 References 2

2.0 CONTAINMENT STRUCTURES 5

2.1 General Description 5
2.2 Potential Degradation Factors 6
2.3 Testing and Inspection requirements 7

2.3.1 Testing 8
2.3.2 Inspection 9

2.4 Operating Experience 9

2.4.1 Metal Containments 10
2.4.2 Liner Plate Corrosion in Concrete Containments 13

2.5 References 17

3.0 REVIEW OF IN-SERVICE INSPECTION TECHNIQUES AND PRIOR RESEARCH 31

3.1 In-Service Inspection Techniques and Methodologies 31

3.1.1 Visual Inspection 31
3.1.2 Liquid Penetrant Testing 32
3.1.3 Eddy Current Inspection 32
3.1.4 Magnetic Particle Testing 32
3.1.5 Ultrasonic Testing 32
3.1.6 Radiographic Techniques 34
3.1.7 Acoustic Emission 35
3.1.8 Thermographic Inspection 35
3.1.9 Electrochemical Corrosion 36

3.2 Inaccessible Pressure Boundary Regions 36

3.2.1 Ultrasonic Testing 36
3.2.2 Electromagnetic Acoustic Transducers 38

3.3 References 39

4.0 HIGH-FREQUENCY ACOUSTIC IMAGING 49

4.1 Numerical Simulations 49

4.1.1 Range-Independent Results 49
4.1.2 Range-Dependent Results 49
4.1.3 Three-Dimensional Issues 50
4.1.4 Conclusions from Numerical Simulations 52

Page

4.2 Experimental Simulations ... 52
4.2.1 Testing Equipment ... 53
4.2.2 System Performance and Operability ... 53
4.2.3 Source and Waveguide Characterization ... 54
4.2.4 Assessment of Signal Loss Components ... 55
4.2.5 Concrete Effects ... 55
4.2.6 Implications of Masking Signals ... 56
4.2.7 Conclusions from Experimental Simulations ... 57
4.3 Recommendations ... 58
4.4 References ... 59
5.0 MAGNETOSTRICTIVE SENSORS ... 81
5.1 Numerical Modeling Studies ... 82
5.1.1 Analytical Results ... 82
5.1.2 Conclusions from Numerical Studies ... 83
5.2 Experimental Studies ... 83
5.2.1 Experimental Setup and Procedures ... 83
5.2.2 Experimental Results ... 83
5.3 MsS System and Time Requirements for Containment Inspection ... 87
5.4 Conclusions and Recommendations ... 89
5.5 References ... 90
6.0 MULTIMODE GUIDED WAVE TECHNIQUES ... 105
6.1 Introduction ... 105
6.2 Multimode Guided Waves ... 105
6.2.1 Theoretical Background ... 106
6.2.2 Experiment ... 106
6.3 Elements of Defect Sizing in a Wave Guide Using SH Guided Waves ... 108
6.3.1 Problem Statement and Solution ... 108
6.3.2 Experiment ... 110
6.4 Concluding Remarks ... 110
6.5 References ... 110
7.0 SUMMARY, CONCLUSIONS AND RECOMMENDATIONS ... 131
7.1 Summary ... 131
7.2 Conclusions ... 134
7.3 Recommendations ... 135

LIST OF FIGURES

Figure		Page
2.1	Example of a cross section for a BWR MK III freestanding steel containment housed in a reinforced concrete shield building	21
2.2	Example of a cross section for PWR large-dry prestressed concrete containment	22
2.3	Example of BWR MK I metal containment	23
2.4	Example of cross section for a German PWR spherical steel containment housed in a reinforced concrete containment building	24
2.5	Example of a cross section for a French PWR single-barrier prestressed concrete containment	25
3.1	Guided wave generation and detection in a plate using piezoelectric transducers	41
3.2	Common EMAT setup for guided waves	41
3.3	General plate, defect, and EMAT layout	42
3.4	Schematic of experimental setup	42
3.5	Typical amplitude-time waveform	43
4.1	Range-independent OASES simulation scenario – approximate model of containment scenario	59
4.2	Range-dependent numerical simulation scenario for containment scenario	60
4.3	Results of simulation scenario for a steel layer surrounded by air only	61
4.4	Results of simulation scenario for embedded steel containment	62
4.5	Signal level from a degradation located 5 cm below air/concrete interface as a function of degradation depth and frequency	63
4.6	Signal level from a 4-mm-deep degradation as a function of degradation distance from interface and frequency	63
4.7	Simulation scenario for steel-lined concrete containment with a 6-mm-thick steel layer backed by a concrete halfspace below	64
4.8	Results of simulation scenario for steel-lined concrete containment	64
4.9	Illustration of localization by means of beam steering for bearing determination and range gating for distance determination	65
4.10	Illustration of beam-forming parameters and their effect on beam shape	65
4.11	Sensor array cut from a single piezoelectric block, with left side showing initial bonding of piezoelectric material to wires and substrate, and right side the array cut into individual elements prior to potting	65
4.12	Array spacing and beam overlap for a scannable array system with maximum penetration dictated by propagation physics	66
4.13	Proposed approach for detection of degradation below air/concrete interface	66
4.14	Procedure used for angle-beam inspections	67
4.15	Test setup and measured return for thickness measurement	67
4.16	Power spectral densities of maximum and minimum signals	68
4.17	Received signal ratios for different source/receiver separation distances	68

Figure **Page**

4.18 Test setup for monitoring forward-travelling waves in free plate. ... 69
4.19 Combined envelopes of received signals at several locations relative to a fixed source (forward-travelling waves) ... 69
4.20 Combined envelopes of received signals at several locations relative to a fixed source (backward-travelling waves reflected waves) ... 70
4.21 Schematic of test setup for degradation shape study ... 70
4.22 Simple reflected return signal from a rectangular notch ... 71
4.23 Results of degradation shape study ... 71
4.24 Time-windowed returns from different notch geometries ... 72
4.25 Test setup for degradation depth study ... 72
4.26 Results of degradation depth study. ... 73
4.27 Molds for embedding portions of steel plates in concrete ... 73
4.28 Test setup for concrete effects tests ... 74
4.29 Transmitted signal level: (a) free-standing steel plates and (b) steel plates embedded in concrete over part of their length ... 74
4.30 Effect of coupling wedge angle on transmitted signal levels for a bonded steel plate embedded in concrete over part of its length ... 75
4.31 Test setup for simulated field conditions to investigate role of competing signals ... 75
4.32 Mechanisms o source "self noise" ... 76
4.33 Test setup for bistatic measurements to eliminate "self noise" ... 76
4.34 Time histories of reflected signals from rectangular notch for three different conditions ... 77
4.35 Bistatic measured return from rectangular notch in a bonded steel plate embedded in concrete over part of its length ... 77
4.36 Time histories of signals transmitted through free-standing steel plate, unbonded steel plate with concrete, and bonded steel plate with concrete ... 78
5.1 Schematic of magnetostrictive sensor setup for generation and detection of guided waves in pipes ... 91
5.2 Calculated dispersion curves for longitudinal guided waves in a plate for three conditions: (a) free plate, (b) plate is backed by concrete on one side, (c) plate is backed by concrete on both sides ... 92
5.3 Displacements of antisymmetric (A) and symmetric (S) wave modes across plate thickness ... 93
5.4 Calculated wave attenuation for: (a) plate backed by concrete on one side and (b) plate backed by concrete on both sides ... 94
5.5 Schematic of coil wound around a stack of U-shaped magnets ... 95
5.6 Schematic of plate test article with wetup for MsS probes ... 95
5.7 Photograph of the overall experimental arrangement ... 96
5.8 Photograph of the 30-cm-long notch in plate specimen ... 66

Figure		Page
5.9	MsS data from plate specimen using pitch-catch technique	97
5.10	Time-frequency representation of data in Fig. 5.9 obtained by using short-time Fourier transform (STFT)	97
5.11	Illustration of mode conversion at the lateral boundaries of a finite-sized plate	98
5.12	Divergence of the beam from a guide-wave probe of length D	98
5.13	MsS data using pulse-echo mode for steel plate prior to introducing a defect	99
5.14	Pulse-echo data for 40-kHz S0 mode obtained from plate containing different length notches	100
5.15	Pulse-echo data for 20-kHz A0 mode obtained from plate containing different length notches	101
5.16	Plots of signal amplitude versus notch length	102
5.17	Conceptual drawing of MsS system deployed for liner inspction	103
6.1	SH wave propagation mode where propagation is along x_1 and Particle displacements are along x_3	112
6.2	Sample dispersion curves for steel plate (c_T = 3.1 μm/msec)	113
6.3	Wave structures for the pseudo-surface mode and A3 mode at frequency of 565 kHz	114
6.4	Schematics of plate specimens	115
6.5	Typical EMAT system and application	116
6.6	SH guided wave experimental results with EMAT SH system	117
6.7	Transducer mounted on wedge for Lamb wave excitation	118
6.8	Pseudo-surface Lamb wave mode for plate inspections	119
6.9	Pulse-echo signals for the A3 Lamb wave mode	120
6.10	Boundary element Method (BEM) wave scattering model	121
6.11	SH phase and group velocity dispersion curves for 10-mm-thick steel plate	122
6.12	Reflection and transmission coefficients	123
6.13	Reflection and transmission coefficients showing linear increase in amplitude with percent through-wall depth	124
6.14	Reflection and transmission coefficients for 6.35-mm elliptical defect width and either 10, 30 or 50 percent through-plate thickness depth	125
6.15	Reflection and transmission coefficients for 12.7-mm elliptical defect width and either 10, 30 or 50 percent through-plate thickness depth	125
6.16	Experimental setup	126
6.17	Through-transmission signal from a 0.3-mm-wide notch 10 percent through depth of 10-mm-thick plate	127
6.18	Pulse-echo signal from a 0.3-mm-wide notch 10 percent through depth of 10-mm-thick plate	127
6.19	Theoretical and experimental relative amplitude results for 12.7-mm, 6.35-mm, and 0.3-mm-wide notches of different depth in a 10-mm-thick plate	128

Figure **Page**

6.20 Theoretical and experimental pulse-echo signal amplitude versus through-plate flaw depth for a 0.3-mm-wide notch 129

6.21 Theoretical and experimental pulse-echo signal amplitude versus through-plate flaw depth for a 0.3-mm-wide notch 129

LIST OF TABLES

Table		Page
2.1	Instances of containment pressure boundary component degradation at commercial nuclear power plants in the United States	26
3.1	Applicability and important material characteristics of selected metallic materials NDE methods	44
3.2	Dominant sources of variance of selected metallic materials NDE methods	45
3.3	Interior and exterior containment surface areas that could experience accelerated degradation and aging	46
3.4	Factors associated with pressure-retaining steel component degradation	47
3.5	Equipment used to aid visual inspection	48
4.1	Material properties used in OASES models	79
4.2	Piezoelectric sensor characteristics	79
4.3	Measured spreading loss values	79
5.1	Material property values	104
5.2	Calculated beam divergence angles	104
6.1	Benefits of guided waves	130
7.1	Summary of Techniques Evaluated for Inspection of Inaccessible Regions of NPP Metallic Pressure Boundaries	136

ACKNOWLEDGEMENTS

As part of the activities conducted to meet the overall objective of providing a status report with respect to potential approaches for inspection of inaccessible portions of containment metallic pressure boundaries, three candidate approaches were addressed through subcontracted activities. High-frequency acoustic imaging was evaluated by Cambridge Acoustical Associates/Engineering Technology Center (Cambridge, MA), magnetostrictive sensor technology was investigated by Southwest Research Institute (San Antonio, TX), and multimode guided wave technology was explored by the Pennsylvania State University (University Park). The valuable contributions of J. Bondaryk, M. Conti, C.N. Corrado, V. Godino, and J. Rudzinsky at Cambridge Acoustical Associates/Engineering Technology Center; H. Kwun at Southwest Research Institute; and J. Li, S.P. Pelts, and J.L. Rose at the Pennsylvania State University are greatly appreciated.

1. INTRODUCTION

The Inspection of Aged/Degraded Containments Program has primary objectives of (1) understanding the significant factors relating corrosion occurrence, efficacy of inspection, and structural capacity reduction of steel containments and liners of reinforced concrete containments; (2) providing the United States Nuclear Regulatory Commission (USNRC) reviewers a means of establishing current structural capacity margins or estimating future residual structural capacity margins for steel containments, and concrete containments as limited by liner integrity; (3) providing recommendations, as appropriate, on information to be requested of licensees for guidance that could be utilized by USNRC reviewers in assessing the seriousness of reported incidences of containment degradation; and (4) providing technical assistance to the USNRC (as requested) related to concrete technology. The program is organized into three tasks: Program Management, Pressure Boundary Condition Assessment and Root-Cause Resolution Practices, and Reliability-Based Condition Assessment of Containments. Information contained in this document was conducted under the second of these tasks and addresses the second objective noted above.

1.1 Background

As of August 1999, 104 nuclear power reactors were licensed for commercial operation in the United States that provide approximately one-fifth of the nation's electricity [1.1]. The Atomic Energy Act (AEA) of 1954 limits the duration of operating licenses for most of these reactors to a maximum of 40 years. The median age of these reactors is over 20 years, with 61 having been in commercial operation for 20 or more years. Expiration of the operating licenses for these reactors will start to occur early in this century, with licenses for these plants starting to expire in large numbers in 2010; licenses for 13 plants representing almost 12,000 MW(e) expire in 2014 alone. In many regions of the nation, the loss of NPPs would not only have negative environmental impacts, but also could threaten the overall reliability of the electricity systems. Under current economic, social, and political conditions in the U.S., the prospects for early resumption of building of new nuclear power plants (NPPs) to replace lost generating capacity are very limited [1.2]. The continued operation of the nation's NPPs can provide a reliable, economical source of energy during the current period as electric utilities transition to a fully deregulated industry. Therefore, continuing the service of existing NPPs through a renewal of their initial operating licenses provides a timely and cost-effective solution to the problem of meeting future electricity demand. In fact, 10 NPPs have already gone through the license renewal process, 13 NPPs have submitted applications to the USNRC, and 27 additional NPPs plan on submitting applications within the next 6 years. However, a concern as plants approach the end of their initial operating license is that the capacity of the safety-related systems to mitigate extreme events has not deteriorated unacceptably due to either aging or environmental stressor effects. As all but one of the construction permits for existing NPPs in the U.S. were issued prior to 1978, the focus of technical development and support has shifted from design to condition assessment. Here, the aim is demonstrating that structural margins of existing plants have not or will not erode during the desired service life due to aging or environmental effects.

Safety-related NPP structures are designed to withstand loadings from a number of low-probability external and interval events, such as earthquakes, tornadoes, and loss-of-coolant accidents. Loadings incurred during normal plant operation therefore generally are not significant enough to cause appreciable degradation. However, these structures are susceptible to aging by various processes depending on the operating environment and service conditions. The effects of these processes may accumulate within these structures over time to cause failure under design conditions, or lead to repair. For example, any corrosion (metal thinning) of the containment metallic pressure boundary could change the failure threshold of the pressure boundary under a challenging environment or accident condition. Section thinning changes the geometry of the pressure boundary creating different transitions and strain concentration conditions. This may reduce the design margins of safety against postulated accident and environmental loads [1.3].

To ensure that adequate margins are maintained with respect to structural capacity and leak-tight integrity, accurate information on the overall condition of the containment metallic pressure boundary is essential. Containment in-service inspection regulations are provided in Section XI Subsections IWE [1.4] and IWL [1.5] of the American Society of Mechanical Engineers (ASME) Boiler and Pressure Vessel Code. Portions of the pressure boundary that are backed by concrete or otherwise inaccessible during construction or as a result of a repair/replacement activity are exempted from examination provided that they meet certain conditions [1.4]. Surface areas likely to experience accelerated degradation and aging require augmented examination (e.g., visual examination when both sides are accessible or ultrasonic thickness measurements when only one side is accessible).

In addition, evaluation of the acceptability of inaccessible regions is required when conditions exist in accessible regions that could indicate the presence of or result in degradation of inaccessible regions (e.g., damaged waterstop or presence of moisture accumulation). This can result in a requirement to remove a component or material to provide accessibility for inspection.

1.2 Statement of Problem

Inspection of inaccessible portions of metallic pressure boundary components of NPP containments (e.g., fully embedded or inaccessible containment shell or liner portions, the sand pocket region in Mark I and II drywells, and portions of the shell obscured by obstacles such as platforms or floors) requires special attention. Embedded metallic portions of the containment pressure boundary may be subjected to corrosion resulting from ground water permeation through the concrete; a breakdown of the sealant at the concrete-containment shell interface that permits entry of corrosive fluids from spills, leakage, or condensation; or corrosion may occur in areas adjacent to floors where the gap contains a filler material that can retain fluids. Corrosion, should it occur, may challenge the containment structural integrity and, if through-wall, can provide a leak path to the outside environment. At present nondestructive evaluation techniques for use in determining the condition of the containment pressure boundary are time-consuming and costly because they tend to examine only a small area at a time. A nondestructive technique is required that can be used remotely to examine inaccessible regions of the containment metallic pressure boundary. Such a technique ideally should also be capable of performing global inspections so that determination of the overall condition of the containment metallic pressure boundary can be achieved in a cost- and performance-effective manner. Identification and/or development of such technique(s) becomes increasingly important as the median age of the NPPs now exceeds 20 years, and in the not-too-distant future several of these plants will be nearing the end of their initial operating license.

1.3 Objective and Scope

The overall objective of this study is to provide a status report with respect to potential approaches for inspection of inaccessible portions of containment pressure boundaries. In meeting the objective of this study, containment structures are described, current inspection and testing requirements are summarized, in-service inspection techniques and methodologies are presented, prior research addressing inspection of inaccessible pressure boundary regions is reviewed, and results obtained from three activities conducted under the Inspection of Aged/Degraded Containments Program are presented.

1.4 Organization of Report

Chapter 2 presents a general description of NPP containment structures, identifies potential degradation factors, summarizes inspection and testing requirements, and presents operating experience with respect to the containment metallic pressure boundary. A review of prior research related to development of techniques for inspection of inaccessible portions of the containment metallic pressure boundary is summarized in Chapter 3. Chapters 4, 5, and 6 presents results obtained under subcontracted activities with Cambridge Acoustical Associates/Engineering Technology Center (high frequency acoustic imaging), Southwest Research Institute (magnetostrictive sensors), and the Pennsylvania State University (multimode guided waves and electromagnetic acoustic transducers), respectively. Finally Chapter 7 presents a summary, conclusions and recommendations.

1.5 References

1.1 U.S. Nuclear Regulatory Commission, *Information Digest*, NUREG-1350, Vol. 11, Division of Budget and Analysis, Office of the Chief Financial Officer,, Washington, D.C., November 2000.

1.2 H.J.C. Kouts, "Aging Nuclear Plants," *Nuclear Plant Journal*, 13(1), pp. 39–41, 1995.

1.3 *Liner Plate Corrosion in Concrete Containments*, IE Information Notice No. 97-10, Office of Inspection and Enforcement, U.S. Nuclear Regulatory Commission, Washington, DC, pp. 1-3, March 13, 1997.

1.4 American Society of Mechanical Engineers, "Rules for Inservice Inspection of Nuclear Power Plant Components," *ASME Boiler and Pressure Vessel Code*, Section XI, Subsection IWE, *Requirements for Class MC and Metallic Liners of Class CC Components of Light-Water Cooled Plants*, New York, New York, 2001.

1.5 American Society of Mechanical Engineers, "Rules for Inservice Inspection of Nuclear Power Plant Components," *ASME Boiler and Pressure Vessel Code*, Section XI, Subsection IWL, *Requirements for Class CC Concrete Components of Light-Water Cooled Plants*, New York, New York, 2001.

2. CONTAINMENT STRUCTURES

A nuclear power plant (NPP) design incorporates multiple barriers between the prime radioactivity and the public to provide protection from unacceptable radiation exposure. These barriers include the fuel element cladding that encapsulates the fuel material and fission products, the reactor coolant system boundary that contains any leakage from the fuel elements, and a containment structure that encloses a major portion, if not all, of the reactor coolant system. Of these, the containment is of primary importance because it serves as the final engineered barrier to the release of fission products to the outside environment under postulated accident conditions.

Nuclear power plant containments are of two function types: dry or vapor suppression. Dry containments rely on volume and physical strength to contain energy released by a loss-of-coolant accident (LOCA). Vapor suppression containments use ice or other means to condense or suppress the effects of energy contained in the steam or vapor released by an accident. Intended functions of a containment can include ensuring: the integrity of the reactor coolant pressure boundary, the capability to contain a shut down of the reactor and maintain it in a safe shutdown condition (i.e., provide structural support), the capability to prevent or mitigate the consequences of accidents that could result in potential offsite exposure comparable to the 10CFR100 ("Reactor Site Criteria") guidelines [2.1], and compliance with the USNRC's regulations for environmental qualification in 10CFR50.49 ("Environmental Qualification of Electric Equipment Important to the Safety of Nuclear Power Plants") [2.1]. Containment design and construction details have a significant affect on the safety of a NPP, thus ensuring that the structural capacity and leak-tight integrity of the containment has not deteriorated unacceptably due either to aging or environmental stressor effects is essential to reliable continued service evaluations and informed aging management decisions.

2.1 General Description

Each boiling-water reactor (BWR) or pressurized-water reactor (PWR) unit in the U.S. is located within a much larger metal or concrete containment that also houses or supports the primary coolant system components. Although the shapes and configurations of the containment can vary significantly from plant-to-plant, leak-tightness is assured by a continuous pressure boundary consisting of nonmetallic seals and gaskets, and metallic components that are either welded or bolted together. There are several *Code of Federal Regulations* (CFR) [2.1] General Design Criteria (GDC) and ASME Code sections that establish minimum requirements for the design, fabrication, construction, testing, and performance of containment structures. The GDC serve as fundamental underpinnings for many of the most important safety commitments in licensee design and licensing bases. General Design Criterion 16, "Containment Design," requires the provision of reactor containment and associated systems to establish an essentially leak-tight barrier against the uncontrolled release of radioactivity into the environment and to ensure that the containment design conditions important to safety are not exceeded for as long as required for postulated accident conditions. Criterion 53, "Provisions for Containment Testing and Inspection," requires that the reactor containment be designed to permit: (1) appropriate periodic inspection of all important areas, such as penetrations; (2) an appropriate surveillance program; and (3) periodic testing at containment design pressure of leak-tightness of penetrations that have resilient seals and expansion bellows.

Prior to 1963, metal containments for NPPs were designed according to rules for unfired pressure vessels that were provided by the ASME in Section VIII of the ASME Code [2.2]. Subsequent metal containments were designed either as Class B vessels or as Class MC components according to rules provided in Section III of the ASME Code [2.3]. Almost every aspect of metal containment design is addressed by the Code. The Code also recognizes that service-related degradation to pressure-retaining components is possible, but rules for material selection and in-service degradation are outside its scope. It is the Owner's responsibility to select materials suitable for the service conditions and to increase minimum required thickness of the base metal to offset material thinning due to corrosion, erosion, mechanical abrasion, or other environmental effects. Current rules for construction of metal containments are provided in Section III, Division 1, Subsection NE of the ASME Code. Currently operating metal containments are freestanding, welded steel structures that are enclosed in a reinforced concrete reactor or shield building. The reactor or shield buildings are not part of the pressure boundary and their primary function is to provide protection for the containment from external missiles and natural phenomena (e.g., tornadoes or site-specific environmental events). Thirty-two of the NPPs licensed for commercial operation in the U.S. employ a metal containment. Figure 2.1 presents an example of a cross section for a BWR MK III freestanding metal containment housed in a reinforced concrete shield building.

Concrete containments are metal lined, reinforced concrete pressure-retaining structures that in some cases may be post-tensioned. The concrete vessel includes the concrete shell and shell components, shell metallic liners, and penetration liners that extend the containment liner through the surrounding shell concrete. The reinforced concrete shell, which generally consists of a cylindrical wall with a hemispherical or ellipsoidal dome and flat base slab, provides the necessary structural support and resistance to pressure-induced forces. Leak-tightness under conditions encountered throughout the operating life of the plant is provided by a steel liner fabricated from relatively thin plate material, generally 6 to 10-mm thick, that is joined by continuous welding and anchored to the concrete shell by means of stud anchors, rolled structural shapes, or both. Anchorage is such that the overall deformation of the liner is the same as the concrete structure under all loading conditions. Initially, existing building codes, such as American Concrete Institute (ACI) Standard 318, *Building Code Requirements for Reinforced Concrete* [2.4], were used in the nuclear industry as the basis for design and construction of concrete structural members. However, because the existing building codes did not cover the entire spectrum of design requirements and because they were not always considered adequate, additional criteria were developed for design of seismic Category 1 (i.e., safety related) structures (e.g., definitions of load combinations for both operating and accident conditions). Plants that used early ACI codes for design were reviewed by the USNRC through the Systematic Evaluation Program to determine if there were any unresolved safety concerns [2.5]. Current rules for construction of concrete containments are provided in Section III, Division 2 of the ASME Code. The USNRC has developed supplemental load combination criteria and provides information related to concrete and steel internal structures of steel and concrete containments [2.6,2.7]. Rules for design and construction of the metal liner that forms the pressure boundary for the reinforced concrete containments are found in ASME Section III, Division 1, Subsection NE of the ASME Code. Seventy-two of the NPPs licensed for commercial operation in the U.S. employ either a reinforced concrete (37 plants) or post-tensioned concrete (35 plants) containment. Figure 2.2 presents an example of a cross section for a PWR large-dry prestressed concrete containment.

2.2 Potential Degradation Factors

Service-related degradation can affect the ability of a NPP containment to perform satisfactorily in the unlikely event of a severe accident. Degradation is considered to be any phenomenon that decreases the load-carrying capacity of a containment, limits its ability to contain a fluid medium, or reduces the service life. The root cause for containment degradation can generally be linked to a design or construction problem, inappropriate material application, a base-metal or weld-metal flaw, maintenance or inspection activities, or excessively severe service conditions.

Containment metallic pressure boundary (i.e., steel containments and liners of reinforced concrete containmetns) degradation can be classified as either material or physical damage. Material damage occurs when the microstructure of the metal is modified causing changes in its mechanical properties. Degradation mechanisms that can potentially cause material damage to containment steels include (1) low-temperature exposure, (2) high-temperature exposure, (3) intergranular corrosion, (4) dealloying corrosion, (5) hydrogen embrittlement, and (6) neutron irradiation. Material damage to the containment pressure boundary from any of these sources is not considered likely, however. Physical damage occurs when the geometry of a component is altered by the formation of cracks, fissures, or voids, or its dimensions change due to overload, buckling, corrosion, erosion, or formation of other types of surface flaws. Changes in component geometry, such as wall thinning or pitting caused by corrosion, can affect structural capacity by reducing the net section available to resist applied loads. In addition, pits that completely penetrate the component can compromise the leak-tight integrity of the component. Primary degradation mechanisms that potentially can cause physical damage to containment pressure boundary components include (1) general corrosion (atmospheric, aqueous, galvanic, stray-electrical current, and general biological); (2) localized corrosion (filiform, crevice, pitting, and localized biological); (3) mechanically-assisted degradation (erosion, fretting, cavitation, corrosion fatigue, surface flaws, arc strikes, and overload conditions); (4) environmentally-induced cracking (stress-corrosion and hydrogen-induced); and (5) fatigue. Material degradation due to either general or pitting corrosion represents the greatest potential threat to the containment pressure boundary.

Primary mechanisms that can produce premature deterioration of reinforced concrete structures include those that impact either the concrete or steel reinforcing materials (i.e., mild steel reinforcement or post-tensioning system). Degradation of concrete can be caused by adverse performance of either its cement-paste matrix or aggregate materials under chemical or physical attack. Chemical attack may occur in several forms: efflorescence or leaching; attack by sulfate, acids, or bases; salt crystallization; and alkali-aggregate reactions. Physical attack

mechanisms for concrete include freeze/thaw cycling, thermal expansion/thermal cycling, abrasion/erosion/cavitation, irradiation, and fatigue or vibration. Degradation of mild steel reinforcing materials can occur as a result of corrosion, irradiation, elevated temperature, or fatigue effects. Post-tensioning systems are susceptible to the same degradation mechanisms as mild steel reinforcement plus loss of prestressing force, primarily due to tendon relaxation and concrete creep and shrinkage. Degradation of the concrete materials and structures was addressed in detail under the Structural Aging Program [2.8].

2.3 Testing and Inspection Requirements

Proper maintenance is essential to the safety of NPP containments, and a clear link exists between effective maintenance and safety. To reduce the likelihood of failures due to degradation, the "Maintenance Rule" was issued by the USNRC as 10 CFR 50.65 ("Requirements for Monitoring the Effectiveness of Maintenance at Nuclear Power Plants") on July 10, 1991. As discussed in the rule summary, in order to maintain safety, it is necessary to monitor the effectiveness of maintenance, and to take timely and appropriate corrective action, when necessary, to ensure that the maintenance process continues to be effective for the lifetime of NPPs, particularly as plants age. The rule requires that plant owners monitor the performance or condition of structures, systems, and components (SSCs) against owner-established goals, in a manner sufficient to give reasonable assurance that such SSCs are capable of fulfilling their intended functions. It is further required that the licensee take appropriate corrective action when the performance or condition of a SSC does not conform to established goals. In order to verify the implementation of 10 CFR 50.65, the USNRC issued Inspection Procedure 62002, "Inspection of Structures, Passive Components, and Civil Engineering Features at Nuclear Power Plants."

Subsequently, on May 8, 1995, the USNRC published a final rule amending 10 CFR Part 54, "Requirements for Renewal of Operating Licenses for Nuclear Power Plants," that contained the requirements an applicant must meet to renew an operating license. The final rule is intended to ensure that important SSCs will continue to perform their intended function in the period of extended operation. Only passive, long-lived structures and components are subject to an aging management review for license renewal, and the USNRC license renewal review will focus on the adverse effects of aging. The USNRC concluded that passive, long-lived components should be subject to an aging management review because, in general, functional degradation of these components may not be apparent so that the regulatory process and existing licensee programs may not adequately manage detrimental effects of aging in the period of extended operation.

In June 1995, the USNRC published NUREG-1522, "Assessment of Inservice Conditions of Safety-Related Nuclear Plant Structures." The report contains information from various sources on the condition of structures and civil engineering features at operating nuclear plants. The most significant information came from inspections performed by the USNRC Staff of six plants licensed before 1977. Most of the information on degraded conditions of the containment structures was submitted by the licensees under the Licensee Event Reporting System (10 CFR 50.73), or in fulfilling the requirement under limiting conditions of operation of technical specifications for their plants. Most of the information on the degradation of other structures and civil engineering features come from an industry survey, reported incidences, and plant visits. Types of containment-related potential problem areas found included coating degradation and base metal pitting, leakage of tendon corrosion inhibitor, lower than anticipated tendon prestressing forces, bulging and spot corrosion of liner plate, concrete surface cracking, deteriorating concrete repair patches, and torus corrosion. The main conclusion of the report was that a properly established and periodically applied inspection and maintenance program would be beneficial to the plant owners in ensuring the integrity of the plant structures. The importance of periodic inspections of structures, as part of the systematic maintenance program, cannot be over emphasized. Substantial safety and economic benefit can be derived if the scope of the investigations is comprehensive and includes degradation sites having difficult access that may not otherwise be inspected. Timely remedial actions to arrest continuing or address benign degradations will ensure continued safety of the structures, particularly in areas of difficult access.

Most of the degradation occurrences noted above were first identified by the USNRC through its inspections or audits of plant structures, or by licensees while performing an unrelated activity or after they were alerted to a degraded condition at another site. Since none of the existing requirements for containment inspection provided specific guidance on how to perform the necessary containment examinations, there was a large variation with regard to the performance and effectiveness of licensee containment examination programs. Furthermore, based on results of the inspections and audits, the USNRC was concerned because many licensee containment

examination programs did not appear to be adequate to detect degradation that could potentially compromise the containment leak-tight integrity. The number of occurrences and extent of degradation experienced by a few of the structures at some plants resulted in the USNRC publishing new rules regarding testing and in-service inspection.

2.3.1 Testing

One of the conditions of all operating licenses for water-cooled power reactors is that the primary reactor containments shall meet the containment leakage test requirements set forth in Appendix J, "Primary Reactor Containment Leakage Testing for Water-Cooled Power Reactors," to 10 CFR 50 [2.9]. These test requirements provide for preoperational and periodic verification by tests of the leak-tight integrity of the primary reactor containment, and systems and components that penetrate containment of water-cooled power reactors, and establish the acceptance criteria for such tests. The purposes of the tests are to assure that (a) leakage through the primary reactor containment and the systems and components penetrating primary reactor containment shall not exceed allowable leakage-rate values as specified in the technical specifications or associated bases, and (b) periodic surveillance of reactor containment penetrations and isolation valves is performed so that proper maintenance and repairs are made during the service life of the containment, and systems and components penetrating primary containment.

Contained in this regulation are requirements pertaining to Type A, B, and C leakage-rate tests that must be performed by each licensee as a condition of their operating license. Type A tests are intended to measure the primary reactor containment overall integrated leakage rate (a) after the containment has been completed and is ready for operation, and (b) at periodic intervals thereafter. Type B tests are intended to detect local leaks and to measure leakage across each pressure-containing or leakage-limiting boundary for primary reactor containment penetrations (e.g., penetrations that incorporate resilient seals, gaskets, or sealant compounds; and air lock door seals). Type C tests are intended to measure containment isolation valve leakage rates. Requirements for system pressure testing and criteria for establishing inspection programs and pressure-test schedules are contained in Appendix J.

On September 26, 1995, the USNRC amended Appendix J (60 FR 49495 - 49505) to provide a performance-based option for leakage-rate testing as an alternative to the existing prescriptive requirements. The amendment is aimed at improving the focus of the body of regulations by eliminating prescriptive requirements that are marginal to safety and by providing licensees greater flexibility for cost-effective implementation methods for regulatory safety objectives. Now that Appendix J has been amended, either Option A—*Prescriptive Requirements* or Option B — *Performance-Based Requirements* can be chosen by a licensee to meet the requirements of Appendix J. Licensees may voluntarily comply with Option B requirements rather than continue using established leakage-rate test schedules. Option B allows licensees with good integrated leakage-rate test performance histories to reduce the Type A testing frequency from three tests in ten years to one test in 10 years. For Type B and C tests, Option B allows licensees to reduce testing frequency on a plant-specific basis based on the operating experience for each component and establishes controls to ensure continued performance during the extended testing interval. However, a general inspection of accessible interior and exterior surfaces of the containment structure and components must be performed prior to each Type A test and during two other refueling outages before the next Type A test if the interval for the Type A test has been extended to ten years. The USNRC position on performance-based containment leakage-rate testing is discussed in Regulatory Guide 1.163 [2.10]. Methods considered acceptable to the USNRC Staff for complying with the provisions of Option B are provided in guidance documentation [2.11].

The Nuclear Energy Institute document [2.11] presents an industry guideline for implementing the performance-based option and contains an approach that includes continued assurance of the leak-tight integrity of the containment without adversely affecting public health and safety, licensee flexibility to implement cost-effective testing methods, a framework to acknowledge good performance, and utilization of risk and performance-based methods. The guideline delineates the basis for a performance-based approach for determining Type A, B, and C containment leakage-rate surveillance testing frequencies using industry performance data, plant-specific performance data, and risk insights. It does not address how to perform the tests because these details can be found in existing documents [2.12]. Licensees may elect to use other suitable methods or approaches to comply with Option B, but they must obtain USNRC approval prior to implementation.

2.3.2 Inspection

Appendix J to 10 CFR Part 50, requires a general inspection of the accessible interior and exterior surfaces of the containment structures and components to uncover any evidence of structural deterioration that may affect either the containment structural integrity or leak-tightness. The large number of reported occurrences (over 60) and the extent of the degradation led the USNRC to conclude that this general inspection was not sufficient. Thus, on August 8, 1996, the USNRC published an amendment (61 FR 41303) to 10 CFR 50.55a of its regulations to require that licensees use portions of the American Society of Mechanical Engineers Boiler and Pressure Vessel Code (ASME Code) for containment in-service inspection. The regulations were amended to assure that critical areas of the containments are routinely inspected to detect and to take corrective action for defects that could compromise a containment's structural integrity. The amended rule became effective September 9, 1996. Specifically, the rule requires that licensees incorporate the 1992 Edition with the 1992 Addenda of Subsection IWE, "Requirements for Class MC and Metallic Liners of Class CC Components of Light-Water Cooled Power Plants," and Subsection IWL, "Requirements for Class CC Concrete Components of Light-Water Cooled Power Plants," of Section XI, of the ASME Code into their in-service inspection plans. In addition, several supplemental requirements with respect to the concrete and metal containments were included in the rule (e.g., expansion of evaluation of inaccessible areas of concrete containments to include metal containments and liners of reinforced concrete containments, permission to use alternative lighting and resolution requirements for remote visual inspection of containment, examination of pressure-retaining welds and pressure-retaining dissimilar welds is optional, and prevention of duplicate examinations required by both the periodic routine and expedited examination program). A five-year implementation period was permitted for licensees to develop and implement the provisions of Subsections IWE and IWL (i.e., no later than September 9, 2001). Also, any repair and replacement activity to be performed on a containment after the effective date of the amended rule has to be carried out in accordance with respective requirements of Subsections IWE and IWL of the ASME Code. However, the Director of the Office of Nuclear Reactor Regulation at his discretion can grant relief from the requirements of 10 CFR 50.55a relative to repair and replacement activities to licensees who submit a justifiable need to use an alternative that provides an acceptable level of safety or who encounter extreme hardship or unusual difficulty without a compensating increase in the level of quality or safety.•

2.4 Operating Experience

As NPP containments age, degradation incidences are starting to occur at an increasing rate, primarily due to environmental-related factors. There have been at least 66 separate occurrences of degradation in operating containments (some plants may have more than one occurrence of degradation). One-fourth of all containments have experienced corrosion, and nearly half of the concrete containments have reported degradation related to either the reinforced concrete or post-tensioning system [2.13].

Since 1986, there have been over 36 reported occurrences of corrosion of steel containments or liners of reinforced concrete containments. In two cases, thickness measurements of the walls of steel containments revealed areas that were below the minimum design thickness. Two instances have been reported where corrosion has completely penetrated the liner of reinforced concrete containments. There have been four additional cases where extensive corrosion of the liner has reduced the thickness locally by nearly one-half [2.13]. Only four of the reported degradation occurrences were detected through containment inspection programs prior to Type A leakage-rate testing conducted according to requirements in effect at the time {i.e., preadoption by reference of basic requirements in Subsection IWE [2.14]}. Nine of these occurrences were first identified by the USNRC through its inspections or audits of plant structures. Eleven occurrences were detected by licensees while performing an unrelated activity, or after they were alerted to a degraded condition at another site. Examples of problems identified include corrosion of the steel containment shell in the drywell sand cushion region (Oyster Creek), shell

---

• On September 22, 1999 the USNRC again amended 10 CFR Part 50.55a to endorse use of the 1995 Edition up to and including the 1996 Addenda of Section XI, Subsections IWE and IWL, of the ASME Code for inspection of containment structures. Subsequently on August 3, 2001 the USNRC announced that it intends to amend 10 CFR Part 50.55a to incorporate by reference the 1997 Addenda, the 1998 Edition, the 1999 Addenda, and the 2000 Addenda of Section XI of the ASME Code ("Proposed Rules," Vol. 66, No. 150, pp. 40626-40640, Office of Federal Register). Comments on the proposed amendment are presently being addressed.

corrosion in ice condenser plants (Catawba and McGuire), corrosion of the torus of the steel containment shell (Fitzpatrick, Cooper, and Nine Mile Point Unit 1), coating degradation (Dresden 3, Fitzpatrick, Millstone 1, Oyster Creek, Pilgrim, and H. B. Robinson), and concrete containment liner corrosion (Brunswick, Beaver Valley, North Anna 2, Brunswick 2, and Salem). Also there have been incidences of transgranular stress corrosion cracking in bellows (Quad Cities 1 and 2, and Dresden 3). Table 2.1 presents a listing of reported instances of containment pressure boundary degradation at commercial NPPs in the U.S. More detailed information on several incidences of metallic pressure boundary corrosion is provided below.

2.4.1 Metal Containments

Free-standing metal containments are constructed of carbon steel plate joined by welding. Shell plate thicknesses are generally in the range of 13 (vent system) to 38 mm. In some cases, plates as thick as 38 to 102 mm may be present in local regions such as the transition section of the spherical portion of the drywell (Mark I), or insert plates have been used as reinforcements at locations of vessel penetrations or supports. The thickened plates are used to compensate for any discontinuity effects and potential stress concentrations. When exposed to oxygen and moisture, general and pitting corrosion of the metal containment can occur. Examples of incidences where this has occurred are described below.

2.4.1.1 Drywell Corrosion at Oyster Creek

The Oyster Creek NPP is located near Forked River, New Jersey. This plant includes a BWR nuclear steam supply system with a Mark I pressure suppression containment. The containment pressure boundary consists of a steel drywell that surrounds the reactor pressure vessel and much of the primary coolant piping and a torus that is connected to the bottom of the drywell by ten vent pipes. In the unlikely event of an accident, the drywell and torus are designed to safely contain the heat, steam, and radioactive materials preventing their release into the surrounding environment. The containment is a code stamped pressure vessel that was constructed in the 1960s in accordance with requirements provided in Section VIII of the Code [2.2]. Figure 2.3 presents an example of a BWR MK I metal containment cross section.

The drywell is essentially a free-standing pressure vessel that is surrounded by a concrete biological shield wall. Support for the drywell, reactor pressure vessel, and other steam supply system components is provided by a concrete pedestal that extends upward from the bottom of the drywell shell. The bottom of the drywell shell rests on concrete that is part of the basemat foundation for the plant. There is a nominal 2.54 to 7.62 mm air gap between the drywell shell and the concrete biological shield wall. This gap, which is filled with compressible insulation, allows the drywell to expand and contract in response to thermal and pressure loads during normal plant operations. A sandbed is provided at the base of the air gap where the outside of the drywell shell intersects with the concrete biological shield wall. This feature was required in the original design to provide transitional radial support for the drywell thereby reducing local stresses in the drywell shell.

In the early 1980s, water was discovered leaking out the top of the sandbed through an annulus around the torus vent line. Inspection of this area during a refueling outage revealed that water from the reactor cavity was leaking down and around the outside of the drywell, through the insulation in the air gap, and into the sandbed [2.15]. During subsequent investigations, it was discovered that the five 102-mm diameter drains that had been installed in the sandbed during the original construction of the plant to remove water from the sandbed were clogged allowing water to saturate the sand and corrode the outside surface of the exposed carbon steel drywell shell. After compacted sand was removed from the drain lines during the twelfth refueling outage in 1988, hundreds of liters (several hundred gallons) of water drained from the sandbed.

Because corrosion of the outside surface of the drywell shell was suspected, extensive ultrasonic testing (UT) was performed from inside the containment to determine the extent and severity of the degradation. These measurements revealed that thinning was most severe in the sandbed region where the original plate thickness was 29.3 mm and that shell thicknesses in some local areas were as low as 20.3 mm. These findings were particularly alarming because the minimum acceptable drywell shell thickness in the sandbed region was 18.8 mm. Verification of the UT measurements was achieved by removing 51-mm diameter cores from the drywell shell and physically measuring their thicknesses. Holes produced by the core drilling operation were replaced with machined plugs that were seal welded to the drywell shell from inside the containment. Welding was performed in accordance with the

rules and requirements of the original construction code and approved by an Authorized Nuclear Inspector. Once completed, inspected, tested, and accepted, the leak-tight integrity of the Oyster Creek containment was restored to its original condition.

Initial efforts to stop the corrosion process involved fixing leaks in the drywell-to-refueling-cavity seal and installing a cathodic protection system in 1988. Anodes were inserted into the sandbed using small-diameter holes through the concrete biological shield wall. This scheme for arresting the corrosion process by controlling the flow of current between anodic and cathodic surfaces was only effective for a short period of time. As the sand around the anodes dried out, the electrical circuit between the cathode (drywell shell) and the anodes was broken thereby rendering the system ineffective. The ineffectiveness of the cathodic protection system was verified by UT measurements. Analysis of time-dependent UT data revealed that the rate of corrosion before and after installation of the cathodic protection system was the same.

After attempts to stop the corrosion process by application of cathodic protection failed, aggressive efforts were undertaken to remove the sand and apply a protective coating of epoxy paint to accessible areas of the drywell shell in the sandbed region. Access to the sandbed was provided by drilling 508-mm diameter holes through the concrete biological shield wall about 305 mm away from the ten vent lines. These holes, which were completed in November 1992, were large enough to allow workers to crawl from the torus region into the sandbed. About one week into the fourteenth refueling outage that started on November 28, 1992, workers entered the sandbed and began vacuuming out the sand and cleaning the drywell shell surface in preparation for painting. The workers discovered that the corrosion was relatively uniform and that it could be easily removed with scrapers and hand-held equipment. By the end of January 1993, the drywell shell had been cleaned and painted with a two-part, self-curing epoxy coating allowing the plant to return to service at the end of the refueling outage in early February. Application of the protective coating on the outside of the drywell shell was not required by the NRC because coatings provide no specific safety-related function to mitigate the consequences of postulated accidents. Quality assurance requirements provided in 10 CFR 50, Appendix B [2.1] also were not applicable in this situation because failure and disbonding of the protective coating during operating and emergency conditions would not interfere with engineered safety system required for safe shutdown and cooling of the reactor vessel.

As the sand was being removed, workers discovered other problems.

- The floor of the sandbed was rough and irregular (large voids were found in some parts of the sandbed floor).
- Segments of reinforcing bars were not embedded in concrete.
- The drain pipes were protruding about 76 to 102 mm above the rough concrete floor surface.

According to the original design documents, a smooth concrete floor with troughs leading to the five drains was to have been constructed to serve as the floor for the sandbed. Because this work was never performed, some standing water always remained at the bottom of the sandbed to sustain the corrosion process even when the drains were functioning properly. In order to solve this problem, a new sandbed floor was installed using an epoxy-based system to fill the voids, cover the exposed reinforcing bars, and pour a new floor up to the level of the top of the five drain pipes.

Even though the original design called for sand to be installed in the sandbed to provide transitional radial support for the drywell shell, sand was not reinstalled after the floor was repaired and the walls were painted. This consensus decision between the utility, General Electric, and NRC personnel was based on results of detailed analytical studies performed to resolve this issue. Results of the entire Oyster Creek investigation also provided the basis for reducing the containment peak pressure from 427 kPa to 303 kPa and for establishing a new minimum drywell shell thickness in the sandbed region of 13.7 mm.

The utility continues to monitor the long-term performance of the drywell shell as part of its overall aging management strategy. Monitoring activities include:

- periodic visual examinations of the epoxy paint,

- UT measurements of the drywell shell above the sandbed, and
- inspections for leakage from the reactor cavity.

So far, no additional thinning of the drywell shell has been detected, the epoxy paint appears to be in excellent condition, and efforts to eliminate water from the sandbed region have been effective.

2.4.1.2 Torus Corrosion at Nine Mile Point, Unit 1

Nine Mile Point, Unit 1 NPP is located near Lycoming, New York, on the southeastern shore of Lake Ontario. This plant includes a BWR nuclear steam supply system that produces 1,850 MW(t) and a Mark I pressure suppression containment. The torus is a free-standing carbon steel pressure vessel fabricated in 1965 by Chicago Bridge and Iron, Co. consisting of 20 pipe-shaped segments or bays that are mitered and welded together [2.16]. The diameter of the pipe-shaped segments is 8.23 m, and the total length of the torus is 112 m. Structural support is provided by a series of steel columns that are welded to the torus shell and rest on a concrete floor slab. Four columns are provided in every other bay; two on the outer side and two on the inner side of the torus. The bottom surface of the torus is about 450 mm above the concrete floor. A concrete biological shield wall surrounds the torus creating an enclosure called the torus room. Carbon steel plates that conformed to ASTM A 201, Grade B requirements were used to fabricate the torus shell [2.17]. The nominal thickness of these plates was 11.7 mm which included a 1.6 mm corrosion allowance. Most areas on the outside surface of the torus are accessible for visual inspection, but the surface is coated to prevent corrosion. The inside of the torus is partially filled with water, and all surfaces above and below the water line are not coated. Consequently, thinning of the torus shell due to corrosion has slowly occurred.

The utility has monitored the thickness of the torus shell since 1975 because of its degradation potential and significance to containment integrity. Periodic UT was performed to quantify the amount of wall thinning that had occurred and to estimate the rate of corrosion. Based on visual inspections performed inside the torus, nondestructive examination results, and laboratory analyses of water samples, the utility concluded that the observed wall thinning was being caused by general corrosion and that local attack (pitting, crevice, and biological corrosion) was not occurring. In about 1980, the torus was reanalyzed to address new load combinations and ASME Code allowable stresses. These analyses were based on the minimum nominal wall thickness of 11.7 mm and took full credit for the 1.6 mm corrosion allowance provided in the original design calculations. After NRC inspections in March 1988 revealing that the torus wall was very near its minimum allowable thickness, additional calculations were performed establishing a worst case minimum wall thickness of 11.4 mm. These calculations reflected a reduction in condensation oscillation loads and indicated that the most critical location was at the bottom of the torus shell.

Following the engineering evaluation, a new corrosion monitoring program was initiated in August 1989 to measure the thickness of all 40 mid-bay plates on the bottom surface of the torus. Part of the program included suspending metal samples in the torus water so that the thickness of these samples could also be periodically measured. The samples were fabricated from carbon steel that conformed to ASTM A 516, Gr. 70 requirements [2.18]. This particular steel was used because steel conforming to ASTM A 201, Gr. B requirements was no longer manufactured, and its chemistry was similar to that used in construction of the torus shell. Prior to installation, the samples were preconditioned in the same way that laboratory corrosion test specimens are preconditioned prior to exposure testing [2.19]. Since the monitoring program began, UT measurements have been performed at six-month intervals. Every effort is made by the utility to use the same personnel and equipment to examine the same locations during each inspection. Results of these UT measurements are used to update the thickness of the plates and to estimate remaining service life of the torus. At the current rate of corrosion, it is estimated that the torus shell will be at its minimum acceptable thickness in about the year 2007, which is very near the end of the plant's 40-year initial operating license. Additional background information about the corrosion at Nine Mile Point Unit 1 and analyses performed by Brookhaven National Laboratory to address this type of Mark I torus problem are presented in a reported issued by the NRC [2.20].

2.4.1.3 German NPPs

There are 20 operating NPPs in Germany. The majority of these plants are of the PWR type with spherical-steel containments that range in diameter from 44 to 56 m. Older containments have a 30-mm thick metal shell with a 1-mm corrosion allowance. Newer designs use a 38-mm thick metal shell with a 2-mm corrosion allowance. Except for the lower portion of the metal containment shell embedded in concrete, all areas of the shell are coated. A reinforced concrete shield building about 1.5 to 1.8 m in thickness surrounds each metal containment primarily to provide protection from aircraft impact. The metal containment shell and the shield building are isolated from each other except for a common foundation. Figure 2.4 presents an example of a cross section for a German pressurized-water steel containment.

Instances of metal containment corrosion have occurred at the Obrigheim (KWO) and Neckar I (GKN-1) NPPs [2.21]. These plants are PWRs that started commercial operation in March 1969 and December 1976, respectively. Corrosion was detected during an inspection of the KWO plant on the inside surface of the containment in the transition area where the metal shell becomes embedded in the concrete floor slab. Thermal insulation was installed at this location during construction to protect the metal shell from high-temperature exposure during a loss-of-coolant accident. Corrosion of the metal shell occurred when high humidity levels inside the containment penetrated the thermal insulation and reached the inside surface of the metal shell. The average depth of corrosion adjacent to the moist insulation was about 1 mm with local areas to 6 mm. In addition to corrosion of the metal shell, galvanized sheet metal covers installed over the insulation were also heavily corroded. During inspection of the KWO plant, a portion of the concrete adjacent to the outside surface of the metal shell was removed to a depth of about 100 mm to provide access for visual examination of this suspect area. This examination revealed no corrosion.

Using information obtained from the condition assessments, an evaluation of the degradation was performed indicating that the corrosion was limited, it was not significant enough to present a safety problem, and the metal shell did not need to be restored to its original thickness. Based on these conclusions, a repair program designed to halt the corrosion process and thereby stop further degradation was developed and implemented. Inside the containment, corroded areas of the metal shell were cleaned and reconditioned, a coating was applied to affected areas, and a new seal design (silicone plus metal covers) was installed at the interface between the metal shell and the concrete floor slab. The thermal insulation was not reinstalled because the evaluation revealed that it was not needed. Outside the containment, areas of concern were coated and the thermal insulation was reinstalled at the interface between the metal shell and concrete.

Inspection of the GKN-1 containment revealed corrosion on the inside surface of the metal shell in a transition region similar to that in the KWO plant. Based on this finding, the same repair procedure used at the KWO plant was implemented. Damage observed at the GKN-1 plant provided the basis for recommending that all plants having a transition region of similar design be inspected to determine if the thermal insulation is moist and the metal shell has corroded.

A similar investigation at BWR plants was also performed. Suspect areas such as the transition region where the metal shell penetrates the concrete and locations where platforms are in close proximity to the metal shell were inspected, but no corrosion was detected.

2.4.2 Liner Plate Corrosion in Concrete Containments

Liners of reinforced and post-tensioned concrete containments are typically constructed using relatively thin (about 6.4-mm thick) carbon steel plates that are welded together to create a leak-tight barrier against the uncontrolled release of radioactivity to the surrounding environment. Although liner plates are not designed to carry loads, corrosion could have a detrimental affect on containment reliability and availability under design basis accidents and beyond design basis events. Any liner plate thinning can create geometrical transitions that influence strain concentration. This influence could change the failure threshold under challenging environmental or accident conditions and may reduce the design margin of safety. Corrosion that results in thinning, pitting, or cracking is of particular concern when the entire thickness of the liner plate is affected. Holes, pits, and cracks that penetrate completely through the liner plate disrupt the pressure boundary and may create pathways to the surrounding environment. Instances of liner plate corrosion have been reported at NPPs in the United States and France.

2.4.2.1 U.S. Experience

Potential locations for containment liner plate corrosion in NPPs in the U.S. include:

- the junction of the containment cylinder and intermediate floors and basemat concrete for PWR and BWR Mark III containments,
- the junction of the drywell and the base or intermediate concrete floors for BWR Mark I and II containments,
- surfaces adjacent to crane rail girders and supports attached to the liner plate,
- water-soaked areas where carbon steel liner plate is used in BWR Mark I and II containments, and
- surfaces behind insulation and ice condenser baskets.

Inspections of containment liners have shown various degrees of corrosion at several NPPs [2.22]. The types of corrosion that were detected are listed below.

- Corrosion of the drywell liner was detected at Brunswick Units 1 and 2 at various locations near the junction of the concrete floor and the drywell liner.
- Through-wall defects in drywell liner due to corrosion at Brunswick Unit 2 and North Anna Unit 2 discovered while performing visual inspections.
- Peeled coatings and spots of liner corrosion were identified at Trojan and Beaver Valley Unit 1.
- Minor corrosion of the containment liner at Salem Unit 2 was detected prior to an integrated leakage-rate test.
- Discoloration of the vertical portion of the containment liner was observed at an insulation joint at Robinson Unit 2.

Additional information on corrosion that occurred at Brunswick and North Anna NPPs is provided below.

Brunswick NPPs. In 1993 corrosion of the drywell liner (ASTM A 516, Grade 60 carbon steel plate) at Brunswick Unit 2 (BWR MK I concrete containment) was identified (a subsequent examination of Unit 1 showed similar corrosion). General and pitting corrosion affecting as much as 50 percent of the nominal 8-mm thick liner was detected at several locations along a narrow band around the inside circumference of both drywells at their junction with the base floor [2.23-2.28]. The corrosion was caused by an accumulation of water at the junction of the drywell liner and the concrete floor surface at the bottom of the containment. Degradation of sealing materials applied around the inside circumference of the containments at this junction allowed the water to enter and accumulate in this region. Procedures used by the licensee to quantify the extent and depth of the corrosion damage involved:

- removing concrete adjacent to the liner to provide access for inspection (Unit 1 only),
- cleaning (sandblasting and wire brushing) the liner plates,
- selecting designated inspection zones,
- measuring the base metal plate thickness using ultrasonic testing methods, and
- determining the depth of pitting and general corrosion using dental molding compound.

Metal loss and pitting depth measurements revealed that there were locations of the liners that were below the minimum acceptable thickness of 5 mm. Five such sections were identified in Unit 2, but the damage in Unit 1 was more severe. Corrosion was observed around virtually the entire circumference of the Unit 1 drywell. The damage even extended below the level of the concrete floor surface making removal of concrete adjacent to the liner necessary. Although corrosion of the drywell liner for Unit 1 was more severe than the corrosion for Unit 2, the leak-tight integrity of both Brunswick containments was never jeopardized because the thinning and pitting did not penetrate completely through the liner plates.

In order to restore damaged liner plates to the required minimum thickness and thereby allow the units to be returned to service, the licensee performed a series of construction activities. Details of these activities are described below.

- Areas with significant metal loss or pitting were repaired by overlay welding in which weld metal was deposited on the damaged liner plates to supplement the existing thickness. During welding, efforts were taken to limit the interpass temperature of the liner plates to 79°C.

- Following welding, each area was examined using the liquid penetrant test method. Results of this test were used to determine the acceptability of the welding repairs. All damaged and repaired areas were recoated.

- Mortar was placed in Unit 1 to return the concrete floor to its original elevation and configuration.

- Intersections of the concrete floors and drywell liners were sealed with an elastomeric sealant.

During a more recent refueling outage while performing a visual inspection of the Brunswick Unit 2 drywell steel liner several defects were identified. At the 5.5 m elevation a defect was initially identified as a broken blister in the epoxy coating with corrosion products visible through the break in the coating. After removal of the blister and corrosion products, an 8–mm-diameter cylindrical through-wall indication exhibiting surface corrosion was identified with an adjoining area of approximately 25-mm diameter under the coating. A small wire inserted into the hole indicated the presence of a 14-mm deep void in the concrete. Subsequent UT measurements showed nominal metal thickness readings except for one subsurface indication connected to the through-wall defect that was about 6-mm wide and showed a reduced thickness of approximately 3 mm on the back of the plate. A metal burr was used to enlarge the opening to about 19 mm by 50 mm to reach sound metal and prepare the cavity for a weld repair. The subsurface defect had a rust stain, but with no significant corrosion products and the concrete surrounding the void was sound. Corrosion was thought to initiate due to a break in the protective coating that resulted from either a localized coating break or mechanical damage. A second cluster of defects was found at the 17 m elevation and was identified by the presence of fresh rust stains streaming down the drywell liner from a cluster of blisters in the coating. Removal of the blisters and corrosion products revealed eight small pits as well as a pronounced bulge in the liner at the location of the defects. Visual examination revealed subsurface corrosion in the liner plate at shallow depth. UT indicated that the depth of sound metal adjacent to the pits averaged about 0.3 mm indicating a significant metal loss on the backside of the liner. Two small sections of liner plate were removed to permit visual examination. A large corrosion product deposit was visible through each of the openings so a section of liner about 180 mm by 250 mm was removed. A large bright red corrosion product was found intact behind the plate indicating corrosion activity. Approximately 50 mm of a 200 mm long by 12-mm diameter Nelson stud had also been consumed by corrosion. Removal of the corrosion product from the surface of the concrete revealed a void in the concrete that contained an irregularly-shaped foreign material. The foreign material was identified as being from a work glove that had apparently fallen into the concrete adjacent to the liner during construction. Further excavation was performed until sound concrete was located resulting in a maximum concrete cavity depth of about 90 mm depth. The liner plate, anchor stud, and protective coating were reestablished. At the 21 m elevation a blister with a corrosion product about 6-mm diameter at the surface and tapering to about 3-mm diameter in the bottom of the pit was identified. Upon grinding, a small through-wall defect about 3-mm diameter by about 9-mm deep was revealed, but no cavity was present in the concrete. UT measurements indicated full-metal thickness in all directions except for one area extending downward approximately 25 mm by 3 mm wide by 2 mm deep on the backside of the plate. The exposed concrete exhibited rust stain, but was dry and sound with no indication of moisture being present. The cause of corrosion was believed to be the same as for that which occurred at the 5.5 m elevation. All defects were repaired by welding and each area was given a local leakage-rate pressure test. Finally,

coating and base metal degradation were observed in all the eight drywell-to-torus vent lines at the upper and/or lower test channels. The slope of the vent lines and location of the test channels provided a ridge that acted like a dam. The degradation was attributed to failure of the epoxy coating. Th epoxy coating applied to the vent lines during construction was not designed for immersion service so it had limited service life in this environment.

North Anna. In 1999, as a result of Surry's discover of corrosion of the liner at its juncture with the concrete foundation mat, the licensee at North Anna Unit 2 performed a visual inspection of the lower portions of the containment liner [2.29]. At a location about 6 m above the mat a blister in the liner coating was identified. Upon scraping the blister evidence of rust and a 6-mm-diameter hole through the 10–mm-thick liner were revealed. Behind the liner a horizontal102 by 102 mm oak post was found embedded along the inner surface of the concrete shield. A series of seven portholes, ranging in size from 76 by 140 mm to 76 by 510 mm, were cut in the liner. The porthole locations were spaced such that about a 152-mm ligament of the liner remained between the holes to retain the integrity of the Nelson studs attached to the backside of the liner. The portholes spaned a liner length of about 2.5 m. The oak post was found to extend about 1.1 m to the right of the initial 6-mm-diameter hole and about 1.2 m to the left. The oak post was removed from the concrete through the portholes and the remaining void filled with grout. The liner repair scheme involved full-penetration welds with magnetic particle inspection at the root pass, after the next two passes, and after the final three passes. Inspection of the remainder of the liner revealed some minor blisters that upon scraping revealed clean base metal with no evidence of corrosion. A ten-year integrated leakage-rate test followed completion of the weld repair.

2.4.2.2 French Experience

In France liner plate corrosion was discovered near the bottom of several of the thirty-four 900-MW PWR post-tensioned concrete containments [2.21]. Corrosion of the 6-mm thick carbon steel liner plates occurred in two separate areas. Both areas were inside the containments and involved liner plates located between the basemat and the 1-m-thick concrete floor slab. Figure 2.5 presents an example of a cross section for a French PWR post-tensioned concrete containment.

Liner plate corrosion was first detected at a plant that had been in service for about 10-15 years. Corrosion occurred in the conical-shaped portion of the liner in an inaccessible area located beneath the concrete floor slab. The corrosion started near the joint sealant at the intersection of the concrete floor and the steel liner and extended downward about 200 mm. At some locations the corrosion produced holes through the liner plates that were up to 10 mm in diameter. Even though holes through the liner plates were present at some plants, air that escaped from the containments through the holes during periodic integrated leakage-rate tests did not adversely affect the test results. The measured leakage from the containment was less than the allowable leakage limit.

The cause for the corrosion was attributed to a breakdown in the joint sealant in conjunction with the presence of high humidity during construction and operation. Examination of construction details in this area also revealed that water containing corrosive substances was stagnating in some of the pressurization channels that were welded to the outer surface of the liner. These channels were installed during construction and used to inspect the welds that joined the liner plate sections. After the concrete was placed and construction completed, access to the space between the channels and the liner plates was restricted making inspection impossible.

Thinning of liner plates was also observed in some plants at the bottom of the joint in the concrete floor slab. The corrosion reduced the thickness of the liner plates to 3 mm in some locations. This damage was attributed to decomposition of the joint sealant and the presence of acidic water (pH = 5) at the liner-concrete interface.

In order to halt the corrosion process and stop further damage, a repair technique was developed. Steps taken to repair pits and holes through the liner plates involved removing portions of the concrete floor slab at selected locations, sandblasting the corroded liner plates, inspecting the damaged areas, welding cover plates over the pits and holes, coating (painting) the repaired areas, and replacing the concrete to restore the floor to its original configuration. In addition, the pressurization channels were filled with cement grout, the cavity between the liner and the floor slab was filled with a corrosion inhibitor (wax), and a new joint sealant was installed. The new joint sealant consisted of a composite elastomeric material that was shielded by a series of metallic sheets attached by bolts. This method of attachment was selected so that the sheets could be periodically removed to provide access for inspection of the elastomeric material.

2.5 References

2.1 *Code of Federal Regulations*, Title 10 – Energy, Office of the Federal Register, National Archives and Records Administration, Washington, DC, January 1, 1995.

2.2 American Society of Mechanical Engineers, "Rules for Construction of Unfired Pressure Vessels," *ASME Boiler and Pressure Vessel Code*, Sect. VIII, New York, New York, 1965.

2.3 American Society of Mechanical Engineers, "Rules for Construction of Nuclear Power Plant Components," *ASME Boiler and Pressure Vessel Code*, Sect. III, New York, New York, 1998.

2.4 American Concrete Institute, *Building Code Requirements for Reinforced Concrete*, ACI Standard 318-71, ACI Committee 318, Detroit, Michigan, 1971.

2.5 "Containment Integrity of SEP Plants Under Combined Loads," in *Proceedings of the ASCE Conference on Structural Engineering in Nuclear Facilities*, J. Ucciferro (ed.), American Society of Civil Engineers, New York, New York, 1984.

2.6 U.S. Nuclear Regulatory Commission, "Concrete Containment," Sect. 3.8.1 in *Regulatory Standard Review Plan*, NUREG-0800, Directorate of Licensing, Washington, D.C., 1981.

2.7 U.S. Nuclear Regulatory Commission, "Concrete and Steel Internal Structures of Steel and Concrete Containments," Sect. 3.8.3 in *Regulatory Standard Review Plan*, NUREG-0800, Directorate of Licensing, Washington, DC, 1981.

2.8 D.J. Naus, C.B. Oland and B.R. Ellingwood, *Report on Aging of Nuclear Power Plant Concrete Structures*, NUREG/CR-6424 (ORNL/TM-13148), Lockheed Martin Energy Research Corporation, Oak Ridge National Laboratory, Oak Ridge, Tennessee, 1996.

2.9 Office of Federal Register, " Appendix J - Primary Reactor Containment Leakage Testing for Water-Cooled Power Reactors," pp. 748-753 in *Code of Federal Regulations*, 10 CFR Part 50, Washington, D.C., 1995.

2.10 U.S. Nuclear Regulatory Commission, *Performance-Based Containment Leak-Test Program*, Regulatory Guide 1.163, Washington, D.C., 1995.

2.11 Nuclear Energy Institute, *Industry Guideline for Implementing Performance-Based Option of 10 CFR Part 50, Appendix J*, NEI 94-01, Revision 0, Washington, D.C., 1995.

2.12 American Nuclear Society, *Containment System Leakage Testing Requirements*, ANSI/ANS - 56.8, La Grange Park, Illinois, 1994.

2.13 U.S. Nuclear Regulatory Commission, *Issuance of Final Amendment to 10 CFR § 50.55a to Incorporate by Reference the ASME Boiler and Pressure Vessel Code (ASME Code), Section XI, Subsection IWL*, SECY 96-080, Washington, D.C., 1996.

2.14 American Society of Mechanical Engineers, "Rules for Inservice Inspection of Nuclear Power Plant Components," *ASME Boiler and Pressure Vessel Code*, Section XI, Subsection IWE, Requirements for Class MC and Metallic Liners of Class CC Components of Light-Water Cooled Plants, American Society of Mechanical Engineers, New York, New York, 2000.

2.15 B.L. Lipford and J.C. Flynn, "Drywell Corrosion Stopped at Oyster Creek," *Power Engineering* 97(11), pp. 47-50, November 1993.

2.16 *Manufacturers Data Report for Nuclear Vessels*, Form N-1, Vessel No. G-1293, Chicago Bridge and Iron Company, Greenville, Pennsylvania, 1965.

2.17 *Tentative Specification for Carbon-Silicon Steel Plates of Intermediate Tensile Ranges for Fusion-Welded Boilers and Other Pressure Vessels*, ASTM Designation: A 201-61T, American Society for Testing and Materials, West Conshohocken, Pennsylvania, 1961.

2.18 "Standard Specification for Pressure Vessel Plates, Carbon Steel, for Moderate- and Lower-Temperature Service," ASTM Designation: A 516-90, *1990 Annual Book of ASTM Standards*, West Conshohocken, Pennsylvania, 1990.

2.19 "Standard Practice for Preparing, Cleaning, and Evaluating Corrosion Test Specimens," ASTM Designation: G 1-90 (Reapproved 1994), *1994 Annual Book of ASTM Standards*, West Conshohocken, Pennsylvania, 1990.

2.20 C.P. Tan and G. Bagchi, *BWR Steel Containment Corrosion*, NUREG-1540, U.S. Nuclear Regulatory Commission, Washington, DC, April 1996.

2.21 *Report of the Task Group Reviewing National and International Acticvities in the Area of Ageing of Nuclear Power Plant Containment Structures*, ODCE/GD(96)31, Committee on the Safety of Nuclear Installations, OECD Nuclear Energy Agency, Issy-les-Moulineaux, France, 1996.

2.22 *Liner Plate Corrosion in Concrete Containments*, IE Information Notice No. 97-10, Office of Inspection and Enforcement, U.S. Nuclear Regulatory Commission, Washington, DC, March 13, 1997, pp. 1-3.

2.23 *Inspection Report Nos.: 50-325/93-02 and 50-324/93-02, Brunswick 1 and 2*, U.S. Nuclear Regulatory Commission, Region II, Atlanta, Georgia, March 4, 1993, NRC Public Document Room, Docket Nos.: 50-324 and 50-325, Fiche 74228: 193-225.

2.24 *Inspection Report Nos.: 50-325/93-15 and 50-324/93-15, Brunswick 1 and 2*, U.S. Nuclear Regulatory Commission, Region II, Atlanta, Georgia, April 23, 1993, NRC Public Document Room, Washington, DC, Docket Nos.: 50-324 and 50-325, Fiche 74770:006-039.

2.25 *Inspection Report Nos.: 50-325/93-25 and 50-324/93-25, Brunswick 1 and 2*, U.S. Nuclear Regulatory Commission, Region II, Atlanta, Georgia, June 18, 1993, NRC Public Document Room, Washington, DC, Docket Nos.: 50-324 and 50-325, Fiche 75542:283-302.

2.26 *Inspection Report Nos.: 50-325/93-31 and 50-324/93-31, Brunswick 1 and 2*, U.S. Nuclear Regulatory Commission, Region II, Atlanta, Georgia, October 1, 1993, NRC Public Document Room, Washington, DC, Docket Nos.: 50-324 and 50-325, Fiche 76732:086-110.

2.27 *Errata Letter for Inspection Report Nos.: 50-325/93-31 and 50-324/93-31, Brunswick 1 and 2*, U.S. Nuclear Regulatory Commission, Region II, Atlanta, Georgia, November 10, 1993, NRC Public Document Room, Washington, DC, Docket Nos.: 50-324 and 50-325, Fiche 77189: 126-130.

2.28 *Inspection Report Nos.: 50-325/93-45 and 50-324/93-45, Brunswick 1 and 2*, U.S. Nuclear Regulatory Commission, Region II, Atlanta, Georgia, October 1, 1993, NRC Public Document Room, Washington, DC, Docket Nos.: 50-324 and 50-325, Fiche 77004:222-239.

2.29 *Docket No. 50-330*, North Anna-2, Virginia Power, Richmond, Virginia, 1999.

2.30 *Examination of Mark-1 Containment Torus Welds*, U.S. Nuclear Regulatory Commission, Office of Inspection and Enforcement, IE Bulletin 78-11, pp. 1-3, July 24, 1978.

2.31 *Cracks in Boiling Water Reactor Mark I Containment Vent Headers*, U.S. Nuclear Regulatory Commission, Office of Inspection and Enforcement, IE Bulletin No. 84-01, pp. 1-2, February 3, 1984.

2.32 *Problems with Liquid Nitrogen Cooling Components Below the Nil Ductility Temperature*, U.S. Nuclear Regulatory Commission, Office of Inspection and Enforcement, IE Information Notice No. 84-17, pp. 1-2, March 5, 1984.

2.33 *Cracking in Boiling-Water-Reactor Mark I and Mark II Containments Caused by Failure of the Inerting System*, U.S. Nuclear Regulatory Commission, Office of Inspection and Enforcement, IE Information Notice No. 85-99 including Attachment 1, pp. 1-3, December 31, 1985.

2.34 V.N. Shah and P.E. MacDonald, Eds., *Residual Life Assessment of Major Light Water Reactor Components — Overview*, NUREG/CR-4731 (EGG-2469), Vol. 2, Idaho National Engineering Laboratory, Idaho Fall, Idaho, November 1989.

2.35 *Fire in Compressible Material at Dresden Unit 3*, U.S. Nuclear Regulatory Commission, Office of Inspection and Enforcement, IE Information Notice No. 86-35, pp. 1-2, May 15, 1986.

2.36 *Degradation of Steel Containments*, U.S. Nuclear Regulatory Commission, Office of Inspection and Enforcement, IE Information Notice No. 86-99 including Attachment 1, pp. 1-3,December 8, 1986.

2.37 Generic Letter 87-05, U.S. Nuclear Regulatory Commission To All Licensees of Operating Reactors, Applicants for Operating Licenses, and Holders of Construction Permits for Boiling Water Reactors (BWRs) with Mark I Containments, Subject: *Request for Additional Information-Assessment of Licensee Measures to Mitigate and/or Identify Potential Degradation of Mark I Drywells*, March 12, 1987, pp. 1-8.

2.38 U.S. Nuclear Regulatory Commission, Docket No. 50-219, August 2, 1991, *Summary of July 24, 1991 Meeting with GPU Nuclear Corporation (GPUN) to Discuss Matters Related to Oyster Creek Drywell Corrosion and Containment Reliability*, (Fishe 58722, Frame 320 to Fishe 58723, Frame 039).

2.39 *Survey of Licensees for Torus Coating and Surveillance*, letter dated May 19, 1988, from J. P. Durr, Chief, Engineering Branch, Region I, U.S. Nuclear Regulatory Commission, to G. Bagchi, Chief, Structural and Geosciences Branch, Office of Nuclear Reactor Regulation, U.S. Nuclear Regulatory Commission, Washington, DC.

2.40 *NRC Inspection Report Nos. 50-325/93-02 and 50-324/93-02*, Brunswick Units 1 and 2, U.S. Nuclear Regulatory Commission, Region II, Atlanta, Georgia March 4, 1993.

2.41 *Torus Shells with Corrosion and Degraded Coatings in BWR Containments*, U.S. Nuclear Regulatory Commission, Office of Inspection and Enforcement, IE Information Notice No. 88-82, pp. 1-2, October 14, 1988.

2.42 *Heat Damage to Upper Elevation Drywell Components Due to Closed Ventilation Hatches*, Dresden Nuclear Station, Unit 2, Licensee Event Report (LER) 88-022-02, Docket No. 50-237, pp. 1-28, December 13, 1988.

2.43 *Bent Anchor Bolts in Boiling Water Reactor Torus Supports*, U.S. Nuclear Regulatory Commission, Office of Inspection and Enforcement, IE Information Notice No. 89-06, pp. 1-2, January 24, 1989.

2.44 *Degraded Coatings and Corrosion of Steel Containment Vessels*, U.S. Nuclear Regulatory Commission, Office of Nuclear Reactor Regulation, IE Information Notice No. 89-79, pp. 1-3, December 1, 1989.

2.45 *Abnormal Degradation of Steel Containment Vessels Due to Corrosion Caused by Standing Water in the Annulus Area*, Catawba Nuclear Station, Unit 1, Licensee Event Report (LER) 89-020-00, Docket No. 50-413, pp. 1-5, January 9, 1990.

2.46 *Abnormal Degradation of Steel Containment Vessels Due to Corrosion Caused by Standing Water in the Annulus Area Because of Unknown Causes*, McGuire Nuclear Station, Unit 1, Licensee Event Report (LER) 89-020-00, Docket No. 50-369, pp. 1-9, September 25, 198,.

2.47 *Degraded Coatings and Corrosion of Steel Containment Vessels*, U.S. Nuclear Regulatory Commission, Office of Nuclear Reactor Regulation, NRC Information Notice No. 89-79, Supplement 1, pp. 1-2, June 29, 1990.

2.48 *Corrosion Occurred on the Steel Containment Vessel because of Design Deficiency Caused by Unanticipated Environmental Interactions*, McGuire Nuclear Station, Unit 1, Licensee Event Report (LER) 90-006-00, Docket No. 50-369, pp. 1-9, May 30, 1990.

2.49 *Quad Cities Nuclear Power Station Unit 1 and 2, 10 CFR Part 21 Notification*, letter dated March 27, 1991, from T. J. Kovach, Nuclear Licensing Manager, Commonwealth Edison, to A. B. Davis, Regional Administrator, U.S. Nuclear Regulatory Commission, Lisle, Illinois.

2.50 *Quad Cities Nuclear Power Station Unit 1, Primary Containment Penetration Bellows Assembly*, letter dated April 19, 1991, from R. Stols, Nuclear Licensing Administrator, Commonwealth Edison, to T. E. Murley, Director, Office of Nuclear Reactor Regulation, U.S. Nuclear Regulatory Commission, Washington, DC.

2.51 H. Ashar and G. Bagchi, *Assessment of Inservice Conditions of Safety-Related Nuclear Plant Structures*, NUREG-1522, U.S. Nuclear Regulatory Commission, Washington, DC, July 1995.

2.52 Beaver Valley Power Station Trip Report; Assessment of Structures and Civil Engineering Features at Operating Plants; FIN L-1521, Task Assignment No. 6, letter dated July 24, 1992, from J. Braverman, Engineering Research and Applications Division, Brookhaven National Laboratory Associated Universities, Inc., to H. Polk, U.S. Nuclear Regulatory Commission, Washington, DC.

2.53 *Ninety-Day Containment Integrated Leak Rate Report, Ninth Refueling Outage, Salem Generating Station, Unit No. 1, Docket No. 50-272*, letter dated July 3, 1991, from S. LaBruna, Vice President Nuclear Operations, Public Service Electric and Gas Company, to Document Control Desk, U.S. Nuclear Regulatory Commission, Washington, DC.

2.54 *NRC Inspection Report Nos. 50-327/93-52 and 50-328/93-52*, Sequoyah Units 1 and 2, December 23, 1993, U.S. Nuclear Regulatory Commission, Region II, Atlanta, Georgia.

2.55 *NRC Inspection Report Nos. 50-325/93-31 and 50-324/93-31*, Brunswick Units 1 and 2, September 28, 1993, U.S. Nuclear Regulatory Commission, Region II, Atlanta, Georgia.

2.56 *McGuire Nuclear Station, Units 1 and 2, Proposed Technical Specification Change*, letter dated June 23, 1993, from T. C. McMeekin, Duke Power Company, to Document Control Desk, U.S. Nuclear Regulatory Commission, Washington, DC.

2.57 *Integrated Leak Rate Test Report for Braidwood 1, March 4 to April 22, 1994*, Commonwealth Edison provided ILRT report to the U.S. Nuclear Regulatory Commission, Washington, DC.

2.58 *Docket No. 50-324*, Brunswick-2, Carolina Power & Light Co., Raleigh, North Carolina, April 27, 1999.

2.59 *NRC Inspection Report Nos. 50-280/99-03 and 50-281/99-03*, Surry Units 1 and 2, April 11- May 22, 1999, U. S. Nuclear Regulatory Commission, Region II, Atlanta, Georgia, pp. 19-20.

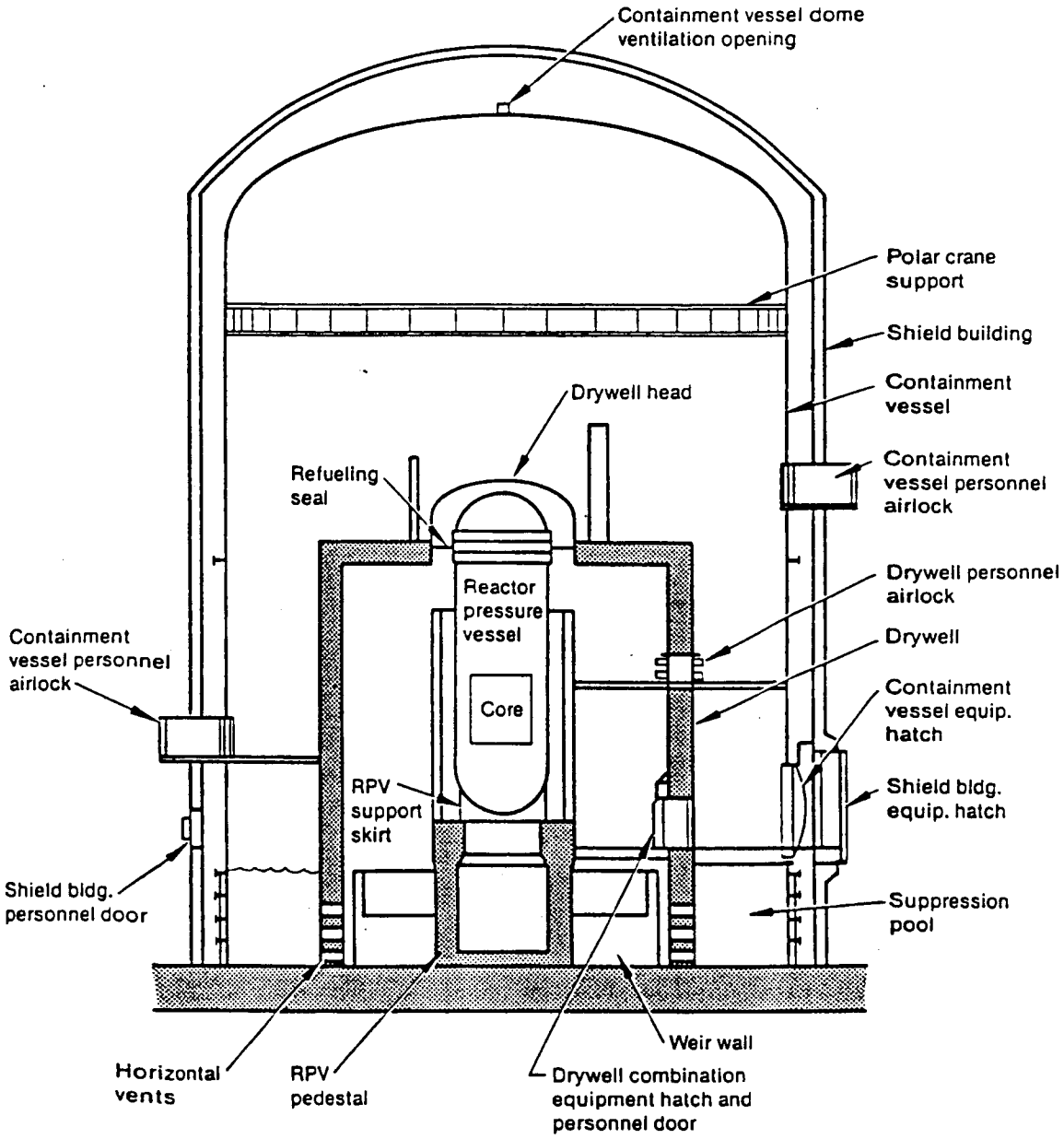

Figure 2.1 Example of a cross section for a BWR MK III freestanding steel containment housed in a reinforcced concrete shield building.

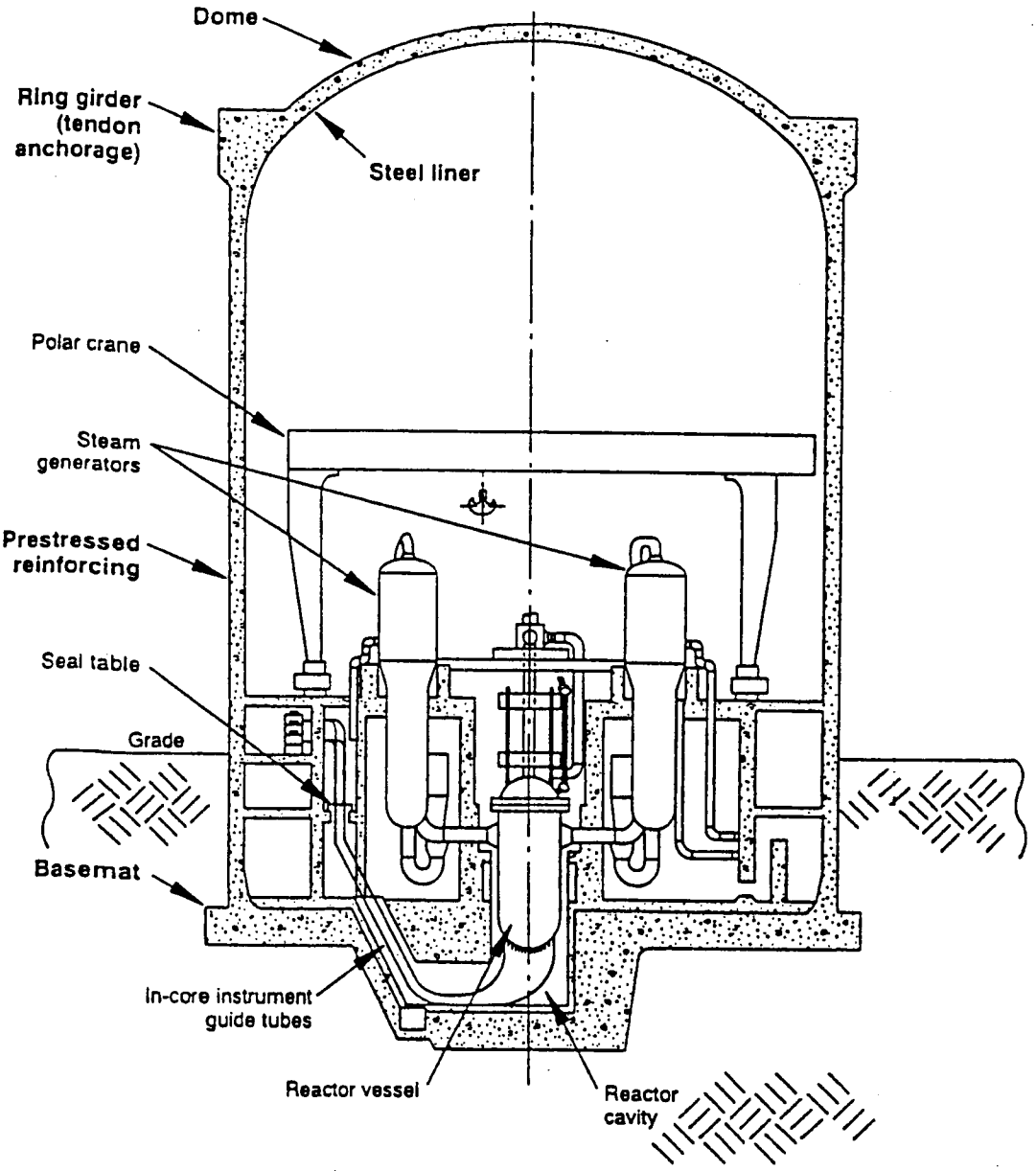

Figure 2.2 Example of cross section for PWR large-dry prestressed concrete containment.

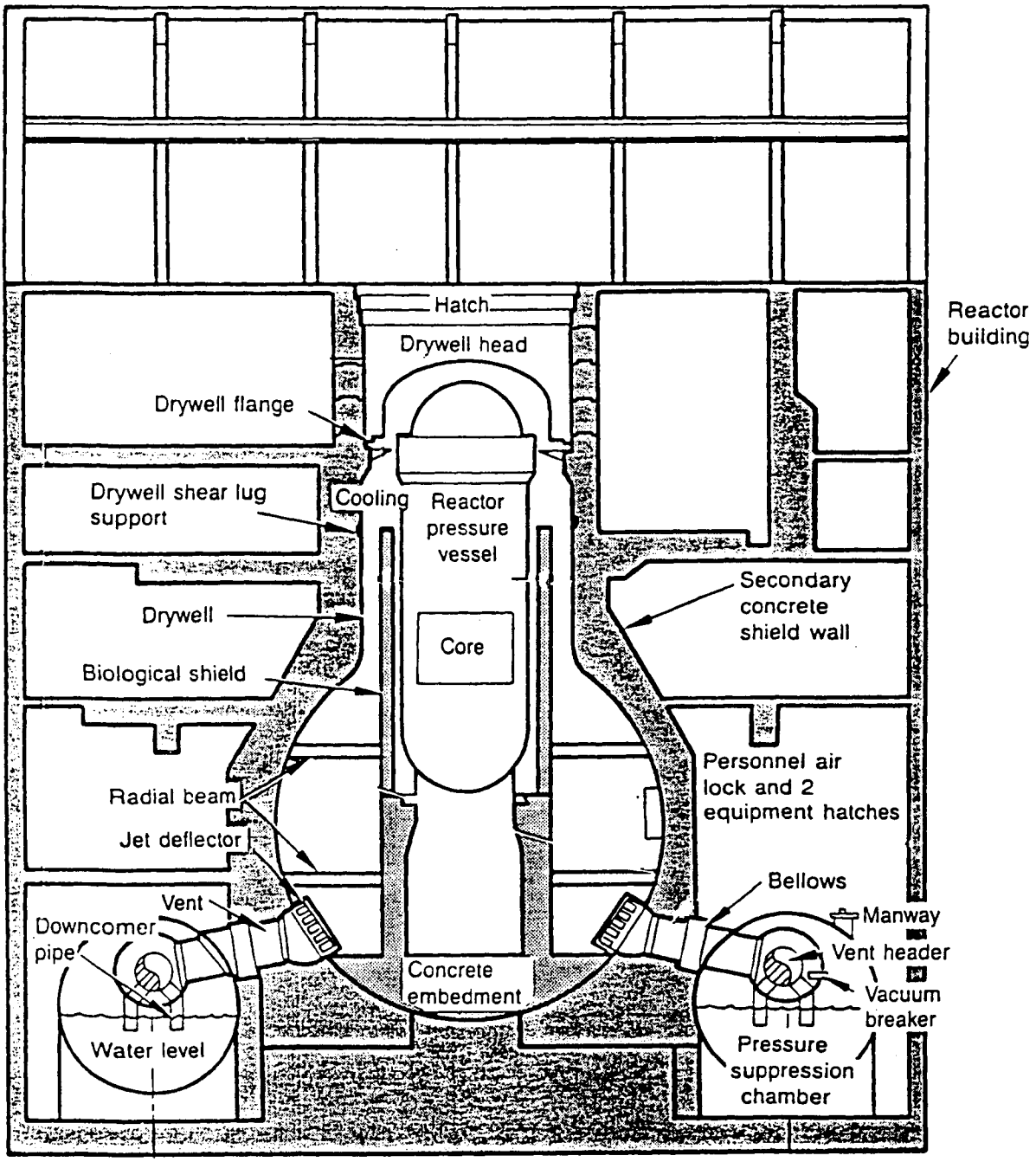

Figure 2.3 Example of BWR MK I metal containment.

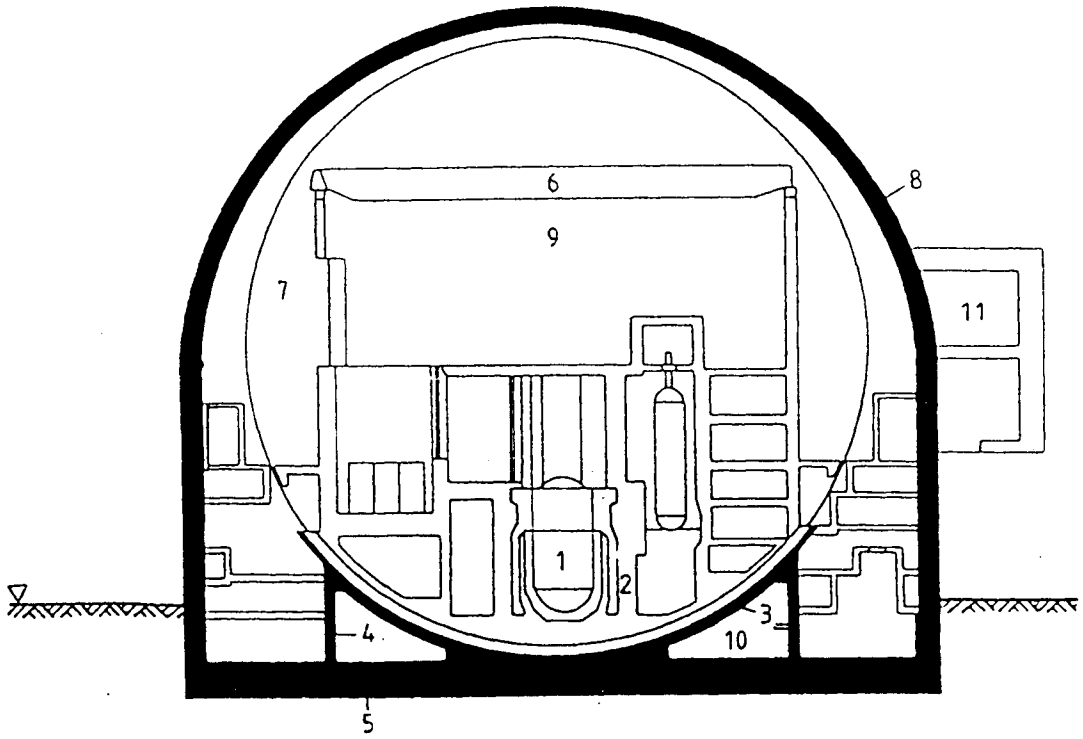

1 steel reactor pressure vessel
2 biological shield
3 spherical section
4 circle wall
5 foundation plate
6 reactor building crane
7 primary steel containment
8 secondary reinforced concrete containment
9 inner rooms
10 annular rooms
11 steam and feed water valve compartment

Figure 2.4 Example of a cross section for a German PWR spherical steel containment housed in a reinforced concrete containment building.

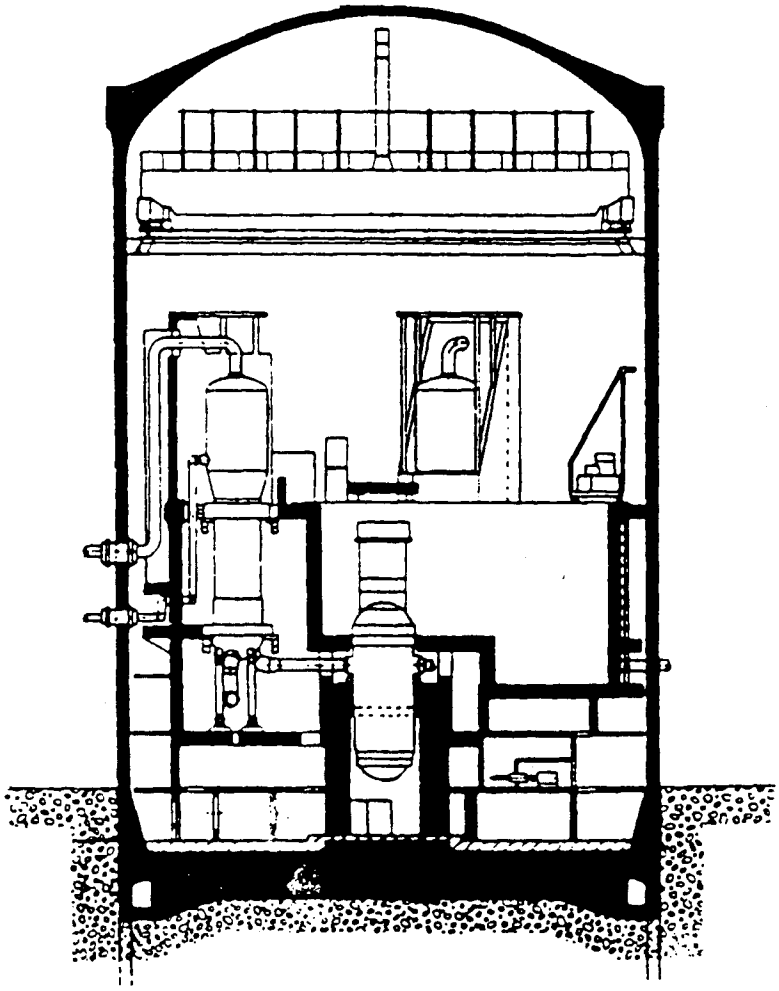

Figure 2.5 Example of a cross section for a French PWR single-barrier prestressed concrete containment.

Table 2.1 Instances of containment pressure boundary component degradation at commercial nuclear power plants in the United States.

Plant Designation (Occurrence Date) Plant Type (Source)	Containment Description (No. of Similar Plants)	Degradation Description	Detection Method
Vermont Yankee (1978) BWR/4 (Ref. 2.30)	Mark I Steel drywell and wetwell (22)	Surface cracks in the overlay weld-to-torus base metal heat-affected zone	Visual examination (As part of modifications to restore the originally intended design safety margins)
Hatch 2 (1984) BWR/4 (Refs. 2.31, 2.32, and 2.33)	Mark I Steel drywell and wetwell (22)	Through-wall cracks around containment vent headers within the containment torus (Brittle fracture caused by injection of cold nitrogen into torus during inerting)	Visual examination of torus interior
Hatch 1 (1985) BWR/4 (Ref. 2.33)	Mark I Steel drywell and wetwell (22)	Through-wall crack in nitrogen inerting and purge line (Brittle fracture caused by injection of cold nitrogen during inerting)	In-service inspection testing using magnetic particle method
Monticello (1986) BWR/3 (Ref. 2.34)	Mark I Steel drywell and wetwell (22)	Polysulfide seal at the concrete-to-shell interface became brittle allowing moisture to reach the steel shell	Visual examination (A small portion of the drywell shell was excavated as a part of a life extension study)
Dresden 3 (1986) BWR/3 (Ref. 2.35)	Mark I Steel drywell and wetwell (22)	Coating degradation due to exposure to fire with peak metal temperatures of 260°C (500°F) and general corrosion of metal shell by water used to extinguish fire	Visual examination (Polyurethane between the drywell shell and concrete shield wall was ignited by arc-air cutting activities producing smoke and heat)
Oyster Creek (1986) BWR/2 (Refs. 2.36, 2.37, and 2.38)	Mark I Steel drywell and wetwell (22)	Defective gasket at the refueling pool allowed water to eventually reach the sand cushion region causing drywell shell corrosion	Visual examination of uncoated areas and ultrasonic inspection
Fitzpatrick (1987) BWR/4 (Refs. 2.34 and 2.39)	Mark I Steel drywell and wetwell (22)	Degradation of torus coating with associated pitting	Visual examination of uncoated areas and ultrasonic inspection (Technical specification surveillance performed during outage)
Millstone 1 (1987) BWR/3 (Ref. 2.39)	Mark I Steel drywell and wetwell (22)	Degradation of torus coating	Visual examination of uncoated areas and ultrasonic inspection (The torus had been drained for modifications)
Oyster Creek (1987) BWR/2 (Ref. 2.39)	Mark I Steel drywell and wetwell (22)	Degradation of torus coating with associated pitting	Visual examination of uncoated areas and ultrasonic inspection

Table 2.1 Instances of containment pressure boundary component degradation at commercial nuclear power plants in the United States (cont.).

Plant Designation (Occurrence Date) Plant Type (Source)	Containment Description (No. of Similar Plants)	Degradation Description	Detection Method
Brunswick 1 (1987) BWR/4 (Ref. 2.40)	Reinforced concrete with steel liner (9)	Corrosion of steel liner	General visual examination of coated areas
Nine Mile Point 1 (1988) BWR/5 (Ref. 2.41)	Steel drywell and wetwell (22)	Corrosion of uncoated torus surfaces	Visual examination of uncoated areas and ultrasonic inspection
Pilgrim (1988) BWR/3 (Ref. 2.39)	Steel drywell and wetwell (22)	Degradation of torus coating	Visual examination of uncoated areas and ultrasonic inspection (Licensee inspection as a result of occurrences at similar plants)
Brunswick 2 (1988) BWR/4 (Ref. 2.40)	Reinforced concrete with steel liner (9)	Corrosion of steel liner	General visual examination of coated areas
Dresden 2 (1988) BWR/3 (Ref. 2.42)	Steel drywell and wetwell (22)	Coating, electrical cable, and valve operator component degradation due to excessive operating temperatures	Visual examination of uncoated areas and ultrasonic inspection (Ventilation hatches in the drywell refueling bulkhead inadvertently left closed)
Hatch 1 and 2 (1989) BWR/4 (Ref. 2.43)	Steel drywell and wetwell (22)	Bent anchor bolts in torus supports (due to weld induced radial shrinkage)	Visual examination
McGuire 2 (1989) PWR (Ref. 2.44)	Ice Condenser Reinforced concrete with steel liner (4)	Corrosion on outside of steel cylinder in the annular region at the intersection with the concrete floor	General visual examination prior to Type A leakage-rate test
McGuire 1 (1989) PWR (Ref. 2.44)	Ice Condenser Reinforced concrete with steel liner (4)	Corrosion on outside of steel cylinder in the annular region at the intersection with the concrete floor	General visual examination (Inspection initiated as a result of corrosion detected at McGuire 2)
Catawba 1 (1989) PWR (Refs. 2.44 and 2.45)	Ice Condenser Steel cylinder (5)	Corrosion on outside of steel cylinder in the annular region	General visual examination (Inspection initiated as a result of corrosion detected at McGuire 2)
Catawba 2 (1989) PWR (Ref. 2.44)	Ice Condenser Steel cylinder (5)	Corrosion on outside of steel cylinder in the annular region	General visual examination (Inspection initiated as a result of corrosion detected at McGuire 2)

Table 2.1 Instances of containment pressure boundary component degradation at commercial nuclear power plants in the United States (cont.).

Plant Designation (Occurrence Date) Plant Type (Source)	Containment Description (No. of Similar Plants)	Degradation Description	Detection Method
McGuire 1 (1990) PWR (Ref. 2.46)	Ice Condenser Reinforced concrete with steel liner (4)	Corrosion on outside of steel cylinder in the annular region	General visual examination (Follow-up inspection by licensee)
McGuire 1 (1990) PWR (Ref. 2.46, 2.47, and 2.48)	Ice Condenser Reinforced concrete with steel liner (4)	Corrosion on inside surface of coated containment shell under the ice condenser and between the floors near the cork filler material	Visual examination and ultrasonic inspection (Degradation possibly caused by moisture from the ice condenser or condensation)
Quad Cities 1 (1991) BWR/3 (Refs. 2.49, 2.50, and 2.51)	Steel drywell and wetwell (22)	Two-ply containment penetration bellows leaked due to transgranular stress-corrosion cracking	General visual examination (Excessive leakage detected)
Quad Cities 2 (1991) BWR/3 (Refs. 2.49 and 2.50)	Steel drywell and wetwell (22)	Two-ply containment penetration bellows leaked due to transgranular stress-corrosion cracking	General visual examination (Excessive leakage detected)
Dresden 3 (1991) BWR/3 (Ref. 2.50)	Steel drywell and wetwell (22)	Two-ply containment penetration bellows leaked due to transgranular stress-corrosion cracking	General visual examination (Excessive leakage detected)
Point Beach 2 (1992) PWR (Ref. 2.51)	Post-tensioned concrete cylinder with steel liner (35)	Liner plate separated from concrete	General visual examination
H. B. Robinson (1992) PWR (Ref. 2.51)	Post-tensioned concrete cylinder (vertical only) with steel liner (35)	Degradation of liner coating	General visual examination
Cooper (1992) BWR/4 (Ref. 2.51)	Steel drywell and wetwell (22)	Corrosion of interior torus surfaces and corrosion stains on exterior torus surface in one area	General visual examination
Beaver Valley 1 (1992) PWR (Refs. 2.51 and 2.52)	Subatmospheric Reinforced concrete cylinder with steel liner (7)	Corrosion of steel liner, degradation of liner coating, and instances of liner bulging	General visual examination prior to Type A leakage rate test
Salem 2 (1993) PWR (Ref. 2.53)	Reinforced concrete cylinder with steel liner (13)	Corrosion of steel liner	General visual examination prior to Type A leakage rate test

Table 2.1 Instances of containment pressure boundary component degradation at commercial nuclear power plants in the United States (cont.).

Plant Designation (Occurrence Date) Plant Type (Source)	Containment Description (No. of Similar Plants)	Degradation Description	Detection Method
Sequoyah 1 (1993) PWR (Ref. 2.54)	Ice Condenser Steel cylinder with concrete shield building (5)	Degradation of moisture barriers resulting in corrosion of the steel shell	General visual examination and visual examination of coated areas
Sequoyah 2 (1993) PWR (Ref. 2.54)	Ice Condenser Steel cylinder with concrete shield building (5)	Degradation of moisture barriers resulting in corrosion of the steel shell	General visual examination and visual examination of coated areas
Brunswick 2 (1993) BWR (Refs. 2.40 and 2.55)	Reinforced concrete drywell and wetwell with steel liner (9)	Corrosion of steel liner	General visual examination and visual examination of coated areas (Follow-up inspection based on conditions noted in 1988)
Brunswick 1 (1993) BWR/4 (Ref. 2.55)	Reinforced concrete drywell and wetwell with steel liner (9)	Corrosion of steel liner	General visual examination and visual examination of coated areas (Inspection initiated as a result of corrosion detected at Brunswick 2
McGuire 1 (1993) PWR (Ref. 2.56)	Ice Condenser Reinforced concrete with steel liner (4)	Main steam isolation line bellows leakage	Leakage testing conducted on bellows following successful Type A leakage rate test
Braidwood 1 (1994) PWR (Ref. 2.57)	Post-tensioned concrete cylinder with steel liner (35)	Liner leakage detected but not located	Type A leakage rate test
North Anna 2 (1999) PWR (Ref. 2.29)	Subatmospheric Reinforced concrete with steel liner (7)	6-mm-diameter hole in liner due to corrosion	General visual examination and visual examination of coated areas
Brunswick 2 (1999) Ref. 2.58)	Reinforced concrete drywell and wetwell with steel liner (9)	Corrosion of liner ranging from clusters of surface pitting corrosion to a 2-mm-diameter hole	General visual examination and visual examination of coated areas
Surry 1 and 2 (1999) (Ref. 2.59)	Subatmospheric Reinforced concrete cylinder with steel liner (7)	Coating failure and corrosion of steel liner at interface of liner and concrete slab	General visual examination and visual examination of coated areas

3. REVIEW OF IN-SERVICE INSPECTION TECHNIQUES AND PRIOR RESEARCH

3.1 In-Service Inspection Techniques and Methodologies

The primary goal of inspection is to identify the location, type, and magnitude of structural imperfections or flaws. The ASME Code [3.1] requires that when defect flaws or evidence of degradation exist that require evaluation in accordance with ASME Code acceptance criteria, either surface or volumetric examinations are to be conducted. Nondestructive examination is the primary method used to evaluate the presence and significance of indications of degradation of the containment pressure boundary. Selection of the appropriate method depends on the type and nature of the degradation, the component geometry, and the type and circumstances of inspection. Cost and availability are also factors.

Nondestructive examination methods for metallic materials principally involve surface and volumetric inspections to detect the presence of degradation (i.e., loss of section due to corrosion or presence of cracking). The surface examination techniques primarily involve visual, liquid penetrant, and magnetic particle methods. Volumetric methods include ultrasonic, eddy current, and radiographic. Rules for surface and volumetric examinations of containment pressure boundary components are provided in Subsection IWA of the ASME Code [3.2]. Alternative techniques, combinations of techniques, and newly developed techniques are permitted provided the results are considered to be equivalent or superior to those of the specified technique. Acceptance standards are defined in Article IWE-3000 of the ASME Code [3.3]. In order to obtain repeatable and reproducible nondestructive examination results using any of the methods described below, several factors must be understood and controlled: material evaluated, evaluation procedure utilized, environment, calibration/baseline reference, acceptance criteria, and human factors. Table 3.1 presents a summary of the application by flaw type and important material characteristics for the techniques discussed below. Table 3.2 presents the dominant sources of variance for these techniques.

3.1.1 Visual Inspection

Visual inspection is one of the most common and least expensive methods for evaluating the condition of a weld or component (e.g., presence of surface flaws, discontinuities, or corrosion). It is generally the first inspection that is performed as part of an evaluation process and is beneficial for performing gross defect detection and in identifying areas for more detailed examination. Interior and exterior containent surface areas that could experience accelerated degradation and aging are identified in Table 3.3. Table 3.4 provides factors associated with damage to pressure-retaining steel components. Visual inspections can identify where a failure is most likely to occur, and when failure has commenced (e.g., rust staining or coating cracks). Once a suspect area is identified, all surface debris and protective coatings are removed so that the area can be inspected in more detail.

Visual examinations can be performed either with the unaided eye or optical magnifiers. Three classifications of visual examinations are specified in the ASME Code: (1) VT-1 (detect discontinuities and imperfections on the surfaces of components such as cracks and corrosion), (2) VT-2 (detect evidence of leakage from pressure-retaining components), and (3) VT-3 (determine general mechanical and structural condition of components and their supports). Without material or component removal, visual inspections are limited to accessible areas. In situations where access is limited or normal visual acuity is not sufficient, examination may require the use of visual aids such as the equipment listed in Table 3.5. Subsection IWA of the ASME Code [3.2] provides rules for remote visual examination and examinations using surface replication methods. To examine underwater portions of the suppression chamber, either the chamber must be drained or underwater examination techniques must be used. Drainage of the chamber relieves the hydrostatic pressure on the coating surfaces and may cause additional blistering or bursting of existing coating blisters. Underwater techniques have been developed that include desludging, ultrasonic mapping of critical areas, coating adhesion tests, dry-film thickness determinations, and repair of localized areas [3.4]. Since crevice corrosion is possible at hatch locations, and under bolts, nuts, and gaskets, proper maintenance, use of grease and lubricants, and routine visual inspections are used to address and inspect for corrosion. The effectiveness of a visual inspection is dependent on the experience and competence of the person performing the inspections.

3.1.2 Liquid Penetrant Testing

Liquid penetrant testing can be used to detect, define and verify surface flaws in solid or essentially nonporus components (e.g., cracks, porosity, laminations or other types of discontinuities that have a capillary opening to the surface) of virtually any size and shape. Indications of a wide spectrum of flaw sizes can be found with little capital expenditure regardless of the configuration of the test article or the flaw orientation. The procedure consists of thoroughly cleaning and drying the surface to be examined followed by application of a liquid penetrant. Surface defects or cracks absorb the penetrant through capillary action. After a dwell period, excess penetrant is removed from the surface and a developer is applied that acts as a blotter to draw penetrant from the defects to reveal their presence. Colored or fluorescent penetrants may be utilized, with white light or black light, respectively, used for viewing. Effectiveness of the method is dependent on the properties of the penetrant and the developer. Limitations of the technique are that operator skill requirements are fairly high, only surface flaw defects can be detected, area inspected must be clean since scale or paint film may hide flaws, results are affected by surface roughness and porosity, and no permanent record of inspection is provided.

3.1.3 Eddy Current Inspection

Eddy current inspection methods are based on electromagnetic induction and can be applied to electrically-conductive materials for detection of cracks, porosity, and inclusions, and to measure the thickness of nonconductive coatings on a conductive metal. In the flaw-detection mode eddy current can detect surface-connected or near-surface anomalies. It is based on the principle that alternating current flow in a coil proximate to an electrical conductor will induce current flow in the conductor. The current flow (i.e., eddy current) creates a magnetic field that opposes the primary field created by the alternating current flow in the coil. The presence of a surface or near-surface discontinuity in the conductor will alter the magnetic field (i.e., magnitude and phase) which can be sensed as a change in the flow of current in a secondary coil in the probe or change of inductance of the probe. The output signal from the detection circuit is fed to an output device, typically a meter, oscilloscope, or chart recorder. Flaw size is indicated by extent of response change as the probe is scanned along the test object. Eddy current techniques do not require direct contact with the test piece, and paint or coatings do not have to be removed prior to its application. For discontinuities of a given size, the sensitivity of eddy current decreases with distance below the surface. Best results are obtained when the magnetic field is in a direction that will intercept the principal plane of the discontinuity. Also, the technique requires calibration, is sensitive to geometry of the test piece, results may be affected by material variations, no permanent record is provided, and demagnification may be necessary following inspection.

3.1.4 Magnetic Particle Testing

Magnetic particle testing is used to detect surface and shallow subsurface discontinuities in ferromagnetic materials. A magnetic field is induced into the ferromagnetic material by using permanent magnets, electromagnets, or by passing high currents through or around the component. The surface is dusted with iron particles that may be dry, suspended in a liquid, colored, or fluorescent. The magnetic lines of force (flux) will be disrupted locally by the presence of the flaw with its presence indicated by the iron particles that are attracted by leakage of the magnetic field at the discontinuity. The resulting magnetically-held collection of particles forms a pattern that indicates the size, shape, and location of the flaw. Effectiveness of the method quickly diminishes depending on flaw depth and type, and scratches and surface irregularities can give misleading results. Special equipment, procedures, and process controls are required to induce the required magnetic fields (e.g., use of proper voltage, amperage, and mode of induction). Factors that can affect sensitivity include orientation of the discontinuity with respect to the induced magnetic field; strength of the magnetic field; shape of component; and size, shape, and general characteristics of the magnetic particles as well as the fluid carrying the particles. Also, linear discontinuities that are oriented parallel to the direction of the magnetic flux will not be detected. Under ideal conditions, it is possible to detect cracks with a width as little as 10^{-3} mm, and when magnetization by DC current is used subsurface defects may be detected at depths on the order of 3 to 7 mm [3.5].

3.1.5 Ultrasonic Testing

Ultrasonic testing uses sound waves of short wavelength and high frequency (e.g., 0.5 to 20 MHz) to detect surface and subsurface flaws, and measure material thickness. Piezoelectric materials, which dilate or strain when a

voltage is applied across the crystal faces, form the basis for electromechanical transducers.* The expansion and contraction produced by alternating voltage generates a compression wave in the surrounding medium. The compression wave can be transmitted at right angles to the component surface, or a coupling wedge can be used to transmit shear or Rayleigh waves into the object. The ultrasound is transmitted as a series of pulses of extremely short duration and during the time interval between transmissions the transducer can detect reflected signals. A sound wave propagating through a material continually loses a part of its energy because of scattering and internal friction effects within the material. Attenuation losses, together with beam divergence, account for the major limitation on the depth of penetration that can be achieved for component inspection. The extent of attenuation increases with an increase in frequency.

Either one transducer, which acts as both transmitter and receiver, or two transducers, where one transducer transmits the signal and a second receives the signal, have been used. The most commonly used technique is pulse-echo in which sound is introduced into the test object and travels through the material examined with some attendant loss of energy. Reflections (echoes) are returned to the receiver from internal imperfections or the component's surfaces. The returning pulse is displayed on a screen that gives the amplitude of the pulse and the time taken to return to the transducer. Inclusions or other imperfections are detected by partial reflection or scattering of the ultrasonic waves, time of transit of the wave through the test object, and features of the spectral response for either a transmitted or reflected signal. Operator interpretation is made by pattern recognition, signal magnitude, timing, and probe positioning.

Flaw size, distance, and reflectivity can be interpreted. The technique has good penetration capability, high sensitivity to permit detection of very small flaws, good accuracy relative to other nondestructive examination methods, only one surface has to be accessible, and rapid results are provided. For thickness measurements digital meters are commonly used. In the pulse-echo mode an ultrasonic transducer transmits waves normal to the component surfaces, signals are reflected from the front and back surfaces, and the difference in arrival times of the two signals is used to indicate the thickness. Cross-section loss is then calculated by taking the difference between the as-built thickness and the thickness measured. Components can also be scanned to detect subsurface abnormalities such as cracks or voids. Information obtained during a test can be displayed as either an "A" scan (displays initial pulse, any defect echoes, and backwall echo), "B" scan (initial signal, defect echoes, and backwall echoes recorded as a function of probe position), or "C" scan (provides plan view of specimen). "A" scans are most commonly used. Ultrasonic testing is commonly used in nuclear plants to monitor wall thinning of the containment vessel caused by corrosion. Rough surface conditions such as could be present on metallic components of containment pressure boundary systems present problems relative to signal scattering. Focused transducers provide the best results where rough surfaces are present. Because of its complexity, ultrasonic testing requires considerable technician training and skill. One major disadvantage of this approach is the requirement of a coupling medium. The contact wedge-type transducers are sensitive to the plate surface condition and the coupling state and, therefore, inspection results may not be satisfactory. A coupling medium consisting of a column of water appears to be the most suitable for this approach [3.6,3.7]. Since conventional piezoelectric transducers operate at frequencies higher than 500 kHz, the corresponding inspection range is relatively short (a few meters) because of a relatively high wave attenuation in that frequency range. Also, defects just below the surface may not be detected, and reference standards are required.

Instead of using the typical approach described above, dry-coupled piezoelectric transducers employed for guided-wave inspection of piping [3.8] may also be used for plates. Compared to the thickness vibration of a conventional transducer, the piezoelectric transducer in this case expands or contracts lengthwise. When pressed against the surface of a material under inspection, the lengthwise motion of the transducer imparts the force to the material through friction and generates the guided wave. Detection of the guided wave is achieved by the reverse process. The operating frequency of the dry-coupled transducer is low (100 kHz or less) and, therefore, it is well suited for long-range inspection (tens of meters) because of a correspondingly low wave attenuation. The requirement of direct physical contact to the plate surface may be a disadvantage of this approach.

---

* Conversely, if the crystal is subjected to a mechanical strain, an electrical field will be created in which the voltage produced is proportional to the amount of strain [3.5].

Noncontact ultrasonic pulses can be generated through focusing a series of light impulses from a laser onto the surface of the object inspected [3.5]. The remotely positioned laser sends out a series of very short high-energy light impulses that are converted by thermomechanical effects into sound impulses. The laser pulse at the point of incidence on the object surface produces rapid heating (without damage) resulting in a localized temperature rise that generates ultrasonic waves. The emission from a second laser illuminates the surface of the test object and ultrasonic echoes returning to the test object surface cause deflections that produce modulation of the reflected light from the illuminating laser. An interferometer analyzes the modulated reflected light signal and converts it into a signal that can be presented on a cathode-ray tube. The main advantages of laser-induced ultrasonics is that no mechanical coupling is required and the acquisition of results is rapid, however, sensitivity is not as good as more conventional ultrasonic systems.

Another ultrasonic testing technique is the time of flight diffraction (TOFD) method that relies on the diffraction of ultrasonic waves from cracks or defect tips, rather than reflection such as in pulse-echo methods. Usually two probes (transmitter and receiver) are used, with the probes aligned geometrically on either side of the object being inspected (e.g., crack or weld). The transmitter produces a relatively wide beam spread in order to maximize the extent of a scan. A scan ("A" scan) is taken in sequential positions along the length of interest. The wave propagation times are used to indicate and locate the diffraction source. If both tips of a defect can be resolved, then the actual depth and "through-wall" thickness of the flaw can be accurately calculated. Interpretation of results can be difficult, however, because it is hard to achieve clear signals in the "A" scans due to the nature of the weak diffracted signals coupled with noise, and interference derived from very small pores or material nonuniformity (particularly for welds). Data enhancing algorithms such as the synthetic aperture focusing technique can be used to improve defect characterization by eliminating beam spread effects. One of the best applications of this method has been to on-line weld inspection since it can inspect the full weld with rejection of unwanted signals, and scans are continuous and contain all data from individual "A" scans.

3.1.6 Radiographic Techniques

Radiographic techniques involve the use of penetrating γ- (decay process of radioactive substances) or X-radiation (bombarding a metal target with a beam of high-velocity electrons) and are based on differential absorption of the radiation. X-radiographic inspection is applied to the detection of surface connected and internal anomalies as well as the internal configuration of a test object. Radiation is capable of detecting any feature in a component or structure provided that there are sufficient differences in thickness or density within the test article. The source is placed close to the material to be inspected and the radiation passes through the material and is captured on film placed on the opposite side of the test article from the source. Sensitized paper (paper radiography), fluorescent screen viewing (fluoroscopy), and detection and monitoring by electronic sensing equipment (xeroradiography) can also be used to monitor the intensity of radiation passing through a material. A two-dimensional projection of the area being inspected is displayed on the film (permanent record). The thickness, density, and absorption characteristics of the material affect the intensity of radiation passing through an object. Possible imperfections are indicated on the film as density changes (i.e., series of gray shades between black and white). The choice of type of source is dependent on the thickness of material to be tested. Gamma rays have the advantage of portability. Gamma radiometry systems consist of a source that emits gamma rays through the specimen and a radiation detector and counter. Direct transmission or backscattering modes can be used to make measurements. The count or count rate is used to measure the specimen dimensions or physical characteristics (e.g., density and composition). Primary limitations of radiography are that radiation protection has to be observed while applying the method, personnel must be licensed or certified, results are not immediately available, the structure must be accessible from both sides, detection of crack-like anomalies is highly dependent on the exposure geometry and orientation of the crack with respect to incident irradiation, and it tends to be expensive relative to many other nondestructive examination methods. Best results are generally obtained when the defect has an appreciable thickness in the direction parallel to the radiation beam.

Neutron radiography involves the transmission of neutrons through a component with the associated production of a radiograph on film. Sources of neutron beams include a radioactive isotope, a particle accelerator, or a nuclear reactor. Neutron emissions are classified according to their kinetic energies as cold (slow neutrons), thermal (medium speed), or fast [3.5]. Generally the thermal neutrons are used in neutron radiography. As a neutron beam passes through a medium it will be attenuated due to neutron scatter (collisions with atom nuclei) and capture (absorption of neutron into nucleus creating an isotope of the atom). With neutron beam radiography there

is a greater tendency for the thermal neutron beam attenuation to increase as the atomic mass number of the element increases. The general principles of beam attenuation with increasing thickness, shadow formation, and other geometrical effects are similar to those of γ- or X-radiography, however, recording of results differs. Either direct-exposure or transfer screens are used. In the direct-exposure method the screen is placed in direct contact with the film and neutrons falling on the screen are absorbed and a secondary emission, to which the film emulsion is sensitive, is released. Transfer screens are positioned behind the object to be radiographed, a neutron exposure made, and the transfer screen used to expose the film. Neutron radiation is a highly specialized and costly process, but has been used for a number of applications including inspection of nuclear fuel elements.

A special form of radiograpy, neutron tomography, merges standard neutron radiography with the computed tomography techniques common to most of today's medical scanners to enable two- and three-dimensional external and internal visualizations of objects. The object to be scanned is located in front of the neutron beam port and activation film used to record the results. The activation film is then used to expose photographic film. The object is then rotated a precise amount and the procedure repeated until images have been taken over 180°. After processing the film, the images are digitized on a scanning microdensitometer and stored for computer processing. Data from each of the stored images is aligned and normalizd to the same exposure and used to reconstruct images of cross sections of a scanned object. Density variations can be indicated using colors. As neutron tomography is particularly effective in detecting hydrogen-based substances, it is useful in identifying corrosion products since they absorb the neutrons, however, since results are averaged, pitting corrosion may not be detectable. Computed tomography also can be used in conjunction with γ- and X-radiography beam measurements.

3.1.7 Acoustic Emission Inspection

Acoustic emission inspection is based on monitoring and interpretation of stress waves generated by a structure under load. Acoustic emissions are small amplitude stress waves (50 kHz to 10 MHz frequency) resulting from release of kinetic energy as a material is strained beyond its elastic limit (e.g., crack growth and plastic deformation). Material stress can come from mechanical or thermal loading, as well as from a variety of other means. There are basically two types of acoustic emissions from materials – a continuous type of low amplitude associated with plastic deformation and movement of dislocations within a material, and a burst type of high amplitude and short duration resulting from development and growth of cracks. The stress waves propagate throughout the specimen and may be detected as small displacements by piezoelectric transducers positioned on the surface of the material. A typical acoustic emission system consists of a number of sensors, preamplifiers, signal filters, amplifier, and a recording system. Signal measurement parameters most commonly used to interpret results include ringdown counts (threshold-crossing pulses), energy counts (area under rectified signal envelope), duration (elapsed time for ringdown counts), amplitude (highest peak voltage), and rise time (time from first threshold crossing to signal peak). Primary applications of acoustic emission inspection include continuous monitoring or proof testing of critical structures, monitoring of production processes, and experimental research related to material behavior. Advantages of acoustic emission are that it is extremely sensitive, the entire structure can be monitored, it is relatively unobtrusive, onset of failure can be identified, and triangulation can be used to identify source location. Acoustic emission can detect growing cracks of a much smaller size than is detectable by conventional techniques, and since there is a marked increase in activity when a crack or discontinuity approaches critical size, it can warn of impendent instability and catastrophic conditions. Certain aspects of the corrosion process are detectable by acoustic emission (e.g., stress-corrosion cracking, hydrogen cracking, corrosion fatigue, and gas evolution) [3.5, 3.9]. Disadvantages are that it requires considerable technical experience to conduct the test and interpret results, background noise can interfere with signals, and a material may not emit until the stress level exceeds a prior applied level (i.e., Kaiser effect).

3.1.8 Thermographic Inspection

Thermographic inspection methods are applied to measure a variety of material characteristics and conditions. In the flaw detection mode they are used for detection of interfaces and/or variation of properties of interfaces within layered systems. The test object must be thermally conductive and reasonably uniform in color and texture. The procedure involves inputting a pulse of thermal energy that is diffused within the test object according to thermal conductivity, thermal mass, inherent temperature differentials, and time of observation. The thermal state of the test object is monitored by a thermographic scanner camera that has infrared energy spectrum

detection capability. Interpretation of results is done through visual monitoring of the relative surface temperature as a function of time and relating the time-dependent temperature differences to the internal condition of the test object. Irregularities in temperature contours can be related to defects as flaws or irregularities that affect the amount of heat conduction in their vicinity. Results are recorded as a function of time and the process is relatively rapid. Specialized equipment is required and since the method is a volume inspection process, resolution is lost near the edges and at locations of nonuniform geometry change. Thermal inspection becomes less effective in the detection of subsurface flaws as the thickness of the object increases. Pulsed infrared techniques have been developed that can perform inspections through the thickness of test objects. The process basically entails providing heat through a high-intensity thermal pulse or step heating, and dynamically collecting infrared images of the material surface using an infrared thermal imager tied to a video recording system. Digitized image processing can be used to enhance the images received. To be successful, the heat applied at the top surface must penetrate to the bottom surface with a temperature differential of several degrees for good infrared contrast.

3.1.9 Electrochemical Corrosion Monitoring

Electrochemical corrosion monitoring techniques are available to make measurements directly related to corrosion rate rather than indirectly in terms of the flaws produced by corrosion. Potential surveys, linear polarization, and AC impedance are techniques that have been utilized. Electrochemical potential measurements using a standard half-cell (e.g., copper-copper sulfate) can be used to locate anodic portions of a structure (i.e., potential gradients indicate possibility of corrosion). The more negative the value of the standard half-cell potential, the greater the tendency of the metal to lose its electrons (i.e., corrode). The linear polarization resistance method impresses DC current from a counter electrode onto the working electrode (e.g., steel structure). Current is passed through the counter electrode to change the measured potential difference by a known amount with the working electrode being polarized. An electronic meter measures the potential difference between the reference electrode and the working electrode. Measurements as a function of DC voltage applied across the cell provide an indirect measure of the corrosion current. The AC impedance-polarizing technique utilizes an alternating applied voltage with the data analyzed as a function of frequency. The AC technique provides polarization resistance as well as information on polarization mechanisms at the anode and cathode which are important for interpretation of the AC impedance data. The technique requires rather sophisticated equipment (e.g., AC frequency generator and analyzer system) and the Tafel slopes must be known to convert AC impedance data into corrosion rate information [3.10]. Each of these methods requires contact with the part of the structure monitored and, where corrosion rates are provided, the rates are only since equipment installation and monitoring.

3.2 Inaccessible Pressure Boundary Regions

Inspection of NPP structures can be difficult because there are a number of functionally different components in a variety of environments. In the previous section it was noted that there are many techniques that may be either nondestructive, destructive, or semi-destructive, that are available for indicating the condition of the basic components that comprise a NPP containment metallic pressure boundary. Application of these techniques, however, generally requires that at least one surface of the component inspected be accessible and the techniques are most effective when an approach is utilized in which the structures have been prioritized with respect to such things as aging significance, environmental factors, and risk. Guidance on component selection is available [3.11, 3.12]. Once the components have been selected for inspection, however, there are several conditions in NPPs where performing the inspections may not be straight forward. One example of this relates to inspection of inaccessible portions of metallic pressure boundary components of NPP containments. Although no completely suitable technique for inspection of inaccessible portions of containment metallic pressure boundaries has been demonstrated to date, preliminary investigations have been conducted using conventional ultrasonics and electromagnetic acoustic transducers.

3.2.1 Ultrasonic Testing

Guided (or Lamb) wave generation and detection using a conventional piezoelectric transducer, Fig. 3.1, is based on Snell's law [3.7, 3.8]. The transmitting transducer generates plane acoustic waves in the coupling medium between the transducer and the plate. The medium may be either a fluid such as water or a wedge material such as plexiglass (for the latter case, an additional thin layer of couplant is required to couple the generated wave into and out of the plate). When the longitudinal (or compressional) wave in the coupling medium arrives at the plate surface

a mode conversion takes place according to Snell's law, and the guided wave is subsequently produced and propagated in the plate. The guided-wave mode produced in the plate satisfies the following equation for Snell's law:

$$\text{Sin}\,\theta = V / Vp \tag{3.1}$$

where θ is the incident angle, V is the longitudinal wave velocity in the coupling medium, and Vp is the phase velocity of the guided-wave mode in the plate. Detection of the guided waves in the plate is achieved when the guided wave is mode-converted back to the longitudinal wave in the coupling medium. One major disadvantage of this approach is the requirement of a coupling medium. The contact wedge-type transducers are sensitive to the plate surface condition and the coupling state and, therefore, inspection results may not be satisfactory. A coupling medium consisting of a column of water appears to be the most suitable for this approach [3.7, 3.8]. Since conventional piezoelectric transducers operate at frequencies higher than 500 kHz, the corresponding inspection range is relatively short (a few meters) because of a relatively high wave attenuation in that frequency range

In Germany, an extensive evaluation was conducted by Technical Inspection Service (Munich) to evaluate the feasibility of using ultrasonic methods to detect corrosion damage of the containments of PWRs or liners of BWRs in areas that are inaccessible (i.e., embedded bottom portion of containments of PWRs, areas of containments of PWRs adjoining platforms, penetrations through the containments of PWRs, and steel liners of BWRs inside pressure-suppression chamber) [3.13]. In order to establish suitable search units (favorable signal-to-noise ratio) for detection of metal containment corrosion, a calibration block with simulated corrosion was prepared. A sharp-edged and a cambered shallow pit were machined to a depth of 2.5 mm into a 39-mm-thick calibration block. The sharp-edged pit was used to qualify the search units considered. Corrosion-inhibiting paint was applied to one surface of the block.

Several angle beam search units were used to examine the calibration block (45°, 60°, 70°, and 90°). In setting up the qualification tests, experience has shown that locations of corrosion in containments can occur at distances to approximately 100 mm below the interface where the containment shell becomes embedded in concrete. This results in long beam paths with correspondingly large projection distances for the ultrasonic examinations. A pulse-echo unit was used in the tests with sensitivity adjusted based on signal-to-noise ratio (average method). Results obtained showed that the sharp-edged pit was detectable (signal-to-noise ratio >12, input angles from 45° to 90°), but the rounded pit (input angles from 35° to 80°) could not be detected. Supplemental testing was then performed on a PWR containment and corroded calibration blocks.

During repairs to the containment of a PWR at a German NPP it was possible to perform ultrasonic examinations and to establish the extent to which such examinations were suitable for detecting corrosion damage. To facilitate detection of surface corrosion on the inside of the containment, which later became visible when the concrete was removed, angle beam search units were used to scan zones with different coupling conditions. When selecting search units for examination of containment corrosion several aspects were taken into account: (1) surface conditions of the calibration block and the containment differed, (2) the containment was coated internally and externally while the corrosion block was coated only with a corrosion-inhibiting paint, and (3) reflection characteristics of corrosion points in the containment differ from those of the sharp-edged or cambered shallow pits in the corrosion block. Supplemental examinations were carried out to characterize the corrosion and to qualify the testing technique. The tests involved coated surfaces and surfaces machined until they were bright metal. With the 45° search unit it was found that the influence of the coating could be disregarded and locations of corrosion could be separated from the interference level of the detection zone (~ 6 dB) in single to triple skips. For the 60° and 70° search units, because of the long paths and surface roughness of the component, the indications of corrosion were masked by interference. With coating present, signals from the 90° search units were highly damped so wave propagation distance was inadequate. When the coating was removed by grinding, the noise level from surface roughness was too high to use the 90° search units. With this as background, ultrasonic tests were performed from the inside and outside of the containment with varying beam paths (single to triple skip distances).

Measurements on the inside containment surface were performed at four locations. The locations included those with and without corrosion. Coupling conditions were such that the surface was either coated or bright metal (e.g., ground). Indications of corrosion pits were obtained from each of the locations where corrosion pits were present. For measurements from the outside of the containment, the coupling area was coated and slightly

smoothed. Echo heights indicative of corrosion were obtained from the outside surface of the containment for only one of the four corrosion locations. Removal of the concrete adjacent to this area revealed corrosion that was about 100 mm below the interface. Wall thickness measurements were then performed on the containment at this same location. The initial wall thickness at coated locations ranged from 31.2 to 31.4 mm. The smallest measured wall thickness at this location was 29.3 mm indicating an approximate wall thinning of 2 mm, or a loss in thickness of 6.4%. General corrosion was found to be difficult to detect.

Further examinations were carried out on calibration blocks with artificial corrosion induced. These examinations were performed to verify whether and under which test conditions corrosion could be safely detected with 45° angle beam search units. The previous calibration block and another calibration block containing a 2-mm-deep pit, sharp-edged on one side and flattened on the other, were artificially corroded for a period of seven months using a 1% NaCℓ solution at 20°C to produce corrosion pits up to 2.4-mm deep. The corrosion pits were detectable in both calibration blocks with adequate signal-to-noise ratio.

The study concluded that corrosion pits could be adequately detected by ultrasonic testing with 45° angle beam search units if the corroded surfaces were sufficiently pitted (e.g., $\geq$2.4-mm deep). In this case sufficient sound intensity is transmitted back to the search unit as a result of adequate reflectivity. The ultrasonic wave length is a measure of reflectivity and it must be on the order of magnitude of the extent of the corrosion pits. Signal-to-noise ratio should be on the order of 12 dB for detectability. Results of this study indicate that it was possible to detect well-developed corrosion pits (pit depth of same order of magnitude as ultrasonic wave length) with 45° angle beam 2 MHz search units within a distance of up to 130 mm below the interface between the concrete and metal containment.

3.2.2 Electromagnetic Acoustic Transducers

An electromagnetic acoustic transducer (EMAT) is a device that generates and detects ultrasonic waves in metal based on the Lorentz force [3.14] which is a force that acts on a moving charge in a static magnetic field EMATs are highly reproducible and quantifiable ultrasonic transducers. The EMAT consists of a transmitter and receiver, both of which contain a permanent magnet or electromagnet and a coil (Fig. 3.2). The transmitter coil is excited by high radio-frequency current to induce an eddy current into the surface of the metal examined. The eddy current interacts with the magnetic field generated by the transmitter coil to produce a Lorentz force that interacts with alternating current (supplied by the EMAT coil) and an externally supplied magnetic flux to generate guided plate waves in the metal (i.e., pulse-echo and through-transmission modes generate low frequency horizontal shear (SH) plate or Lamb waves). Detection of elastic waves is accomplished by the reverse process in which the wave in the presence of a static magnetic field gives rise to eddy currents in the metal that induces a voltage to the EMAT coil. EMATs have been applied to long-range inspections of tubes [3.15] and steel sheets [3.16]. EMATs have advantages for detection of corrosion because: a couplant is not needed, the ultrasound is generated directly in the metal rather than in the transducer, the high-energy waves can travel relatively long distances parallel to the plate surface, the wave velocity is independent of plate thickness, and the ultrasound can be generated through a surface coating up to about 1.5-mm-thick. Disadvantages of EMATs are that its efficiency is low and thus the signal-to-noise ratio may be poor, and they lose sensitivity when the gap to the surface of the component inspected is increased.

The capability of adapting EMATs to detect corrosion in Mark I containment vessels and correlating EMAT signals with corrosion damage to make quantitative evaluations were evaluated in the laboratory by Innovative Sciences, Inc. (San Leandro, California) for the Electric Power Research Institute [3.17]. Pulse-echo and through transmission-modes were evaluated. In the pulse-echo mode the transmitter generates a wave in the plate parallel to its surface. The signal, which is scattered by a defect such as a crack or corrosion, is detected by a receiver located near the transmitter. In the through-transmission mode, the transmitter also generates a wave that travels parallel to the plate surface, however, the signal is detected by a receiver that is located at the opposite end of the plate.

Since it had been shown that the SH_0 mode had less attenuation than the SH_1 mode, the SH_0 mode was primarily used for the experiments. Simulated corrosion-like defects (13-mm wide by 102-mm long by 11-mm deep) were milled into a 2.1-m-wide by 4.9-m-long by 25.4-mm-thick plate at a distance of 0.6 m from one end.

Figure 3.3 presents the general plate, defect, and EMAT layout that was used for most of the results obtained in the study. The EMAT launches a plate wave (primarily an SH_0 mode) in both directions. The receiver EMAT detects the plate wave as it passes beneath the receiver (the "direct" signal). A portion of this signal is scattered back toward the receiver by the defect. The remaining signal is reflected from the end, scattered slightly by the defect and is detected by the receiver as an END 1 reflection. The plate wave launched in the opposite direction is reflected from END 2 and then detected by the receiver. Depending on the location of the receiver and transmitter, the END 1 reflection may be either before or after the END 2 reflection. Figure 3.4 presents a schematic of the arrangement used for the measurements. Figure 3.5 presents the digitized wave form taken with the receiver 0.9 m from the transmitter and 2.1 m from END 2 using a tuned amplifier and averaging the signal 16 times. The signal labeled "A" is the direct propagation from the transmitter to the receiver located about 0.9 m from the transmitter. Signal "B" is the same waveform after traveling to END 1 and back to the receiver, an additional distance of 3.7 m, while signal "C" is the corresponding reflection from END 2. Signal "D" is the scattering from a 1.27-cm wide by 1.14-cm deep by 10.16-cm long slot located on the plate centerline at a distance of 61 cm from END 1. Signals "E" are coherent noise background after the first arrival signal, much of which could be removed by spatial averaging or other synthetic aperture types of signal processing. Signal "F" is due to scattering of the transmitter side lobe and/or peripheral portions of the main lobe from the plate edge and end. If plate-to-plate welds were present, signals similar to "F" would be generated, but much smaller magnitude. Signal processing techniques can be used to separate geometric scatterings such as "F" from those due to corrosion.

Experimental results show that SH waves scattered from planar slots (also for planar cracks and similar boundaries) produce signals that are measurable at substantial distances (3 m or more) from a small (two wavelength) scatterer that extends halfway through the plate. In the pulse-echo geometry, a flaw at least half-way through the plate thickness and two wave lengths long (~127 mm) provided strong scattering signals that could be detected at distances to 4.6 m. Rounding of the flaw causes the signal to become weaker and spreads it more over a larger angle (i.e., scattered energy from planar slot is primarily SH_0 mode while semi-circular slot scatters a great deal of energy into other modes). Although the through-transmission mode was not as sensitive (lower relative detectability), it was felt that deep corrosion damage (i.e., >75% of the plate thickness) could be detected at a distance to 15 m or more, but defect sizing would be difficult. The significant amount of coherent elastic wave energy present in the plate indicates that discrimination of any type of scattering anomaly will be improved dramatically using synthetic aperture signal processing.

3.3 References

3.1 *ASME Boiler and Pressure Vessel Code,* American Society of Mechanical Engineers, New York, New York, 1988.

3.2 "Rules for Inservice Inspection of Nuclear Power Plant Components," *ASME Boiler and Pressure Vessel Code*, Section XI, Division 1, Subsection IWA, General Requirements American Society of Mechanical Engineers, New York, New York, July 1, 1995.

3.3 "Rules for Inservice Inspection of Nuclear Power Plant Components," *ASME Boiler and Pressure Vessel Code*, Section XI, Division 1, Subsection IWE, Requirements for Class MC and Metallic Liners of Class CC Components of Light-Water Cooled Power Plants, American Society of Mechanical Engineers, New York, New York, July 1, 1995.

3.4 C.O. Stuart, "Underwater Coating Repair Cuts Nuclear Maintenance Costs," *Power Engineering*, Vol. 97, No. 7, pp. 31-34, July 1993.

3.5 B. Hull, and V. John, *Non-Destructive Testing*, MacMillan Press Ltd., London, England, 1994.

3.6 D. N. Alleyne, and P. Cawley, "Optimizations of Lamb Wave Inspection Techniques, *NDT&E Intenational* 25, pp. 11-22, 1992.

3.7 T. Ghosh, T. Kundu, and P. Karpur, "Efficient Use of Lamb Modes for Detecting Defects in Large Plates," *Ultrasonics* 36, pp. 791-801, 1998.

3.8 D. N. Alleyne and P. Cawley, "The Excitation of Lamb Waves in Pipes Using Dry-Coupled Piezoelectric Transducers," *J. NDE* 15, pp. 11-20, 1996.

3.9 R. E. Beissner, and A. S. Birring, *Nondestructive Evaluation Methods for Characterization of Corrosion*, NTIAC-88-1, Nondestructive Testing Information Analysis Center, San Antonio, Texas, December 1988.

3.10 ASM International, "Corrosion," *ASM Handbook*, Vol. 13, Materials Park, Ohio, 1992.

3.11 D.J Naus, C.B. Oland, and B.R. Ellingwood, *Report on Aging of Nuclear Power Plant Reinforced Concrete Structures*, NUREG/CR-6424 (ORNL/TM-13148), Oak Ridge National Laboratory, Oak Ridge, Tennessee, March 1996.

3.12 C. B. Oland, and D. J. Naus, *Degradation Assessment Methodology for Application to Steel Containments and Liners of Reinforced Concrete Structures in Nuclear Power Plants*, ORNL/NRC/LTR-95/29, Oak Ridge National Laboratory, Oak Ridge, Tennessee, February 1996.

3.13 D.C. Pocock, J.C. Worthington, R. Oberpichler,, H. Van Exel, D. Beukelmann., R. Huth, and B. Rose, *Long-Term Performance of Structures Comprising Nuclear Power Plants*, Report EUR 12758 EN, Directorate-General Science, Research and Development, Commission of European Communities, Luxembourg, 1990.

3.14 J. Krautkramer, and H. Krautkramer, *Ultrasonic Testing of Materials*, Chapter 8, 4th Ed., Springer Verlag, New York, New York, 1990.

3.15 W. Mohr, and P. Holler, "On Inspection of Thin-Walled Tubes for Transverse and Longitudinal Flaws by Guided Ultrasonic Waves," *IEEE Transactions on Sonics and Ultrasonics*, SU-23, pp. 369-374, New York, New York, 1976.

3.16 W.M. Latham, P..J. Latimer, and E. T. MacLauchlan, "EMAT-Generated Lamb Waves for Volumetric Inspection of Strip Steel," *Process Control and Sensors for Manufacturing*, Editors Boss, R. H. and Pepper, D. M., SPIE 3399, pp. 139-150, Bellingham, WA., 1998.

3.17 Electric Power Research Institute, *The Feasibility of Using Electromagnetic Acoustic Transducers to Detect Corrosion in Mark I Containment Vessels*, EPRI NP-6090, Palo Alto, California, November 1988.

3.18 V.N. Shah, and P.E. MacDonald, Eds., *Residual Life Assessment of Major Light Water Reactor Components — Overview,* NUREG/CR-4731, (EGG-2469) Vol. 2, Idaho National Engineering Laboratory, Idaho Fall, Idaho, November 1989.

3.19 V.N. Shah, and P.E. MacDonald, Eds., *Residual Life Assessment of Major Light Water Reactor Components — Overview,* NUREG/CR-4731, (EGG-2469) Vol. 1, Idaho National Engineering Laboratory, Idaho Fall, Idaho, June 1987.

3.20 S. Smith, and F. Gregor, *BWR Containments License Renewal Industry Report; Revision 1*, EPRI TR-103840, prepared by MDC-Ogden Environmental and Energy Services Co., Inc., for the Electric Power Research Institute, Palo Alto, California, July 1994.

3.21 D. Deng, J. Renfro, and J. Statton, *PWR Containments License Renewal Industry Report; Revision 1*, EPRI TR-103835, prepared by Bechtel Power Corporation for the Electric Power Research Institute, Palo Alto, California, July 1994.

3.22 R.F. Sammataro, "Updated ASME Code Rules for Inservice Inspection of Steel and Concrete Containments," *Proceeding of the Fifth Workshop on Containment Integrity,* NUREG/CP-0120, (SAND92-0173) U.S. Nuclear Regulatory Commission, Washington, DC, July 1992.

3.23 "Volume 17 — Nondestructive Evaluation and Quality Control," *ASM Handbook*, formerly ninth edition, *Metals Handbook*, ASM INTERNATIONAL, Materials Park, Ohio, 1989.

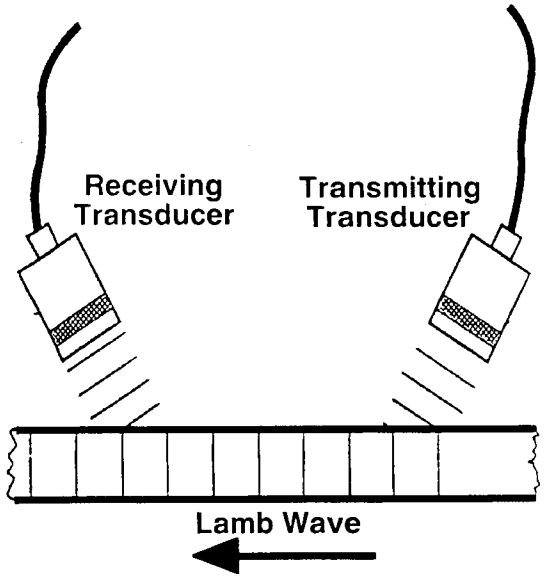

Fig. 3.1 Guided wave generation and detection in a plate using piezoelectric transducers.

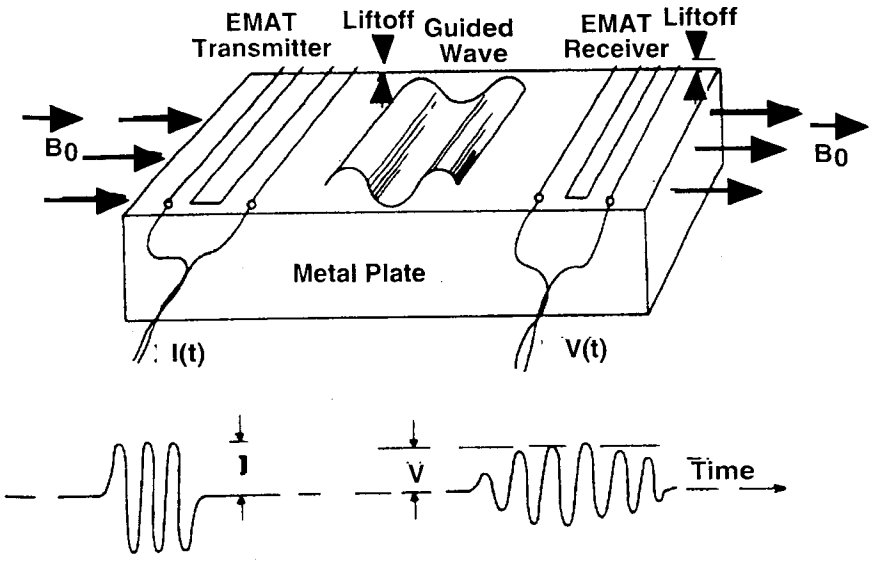

Fig. 3.2 Common EMAT setup for guided waves.

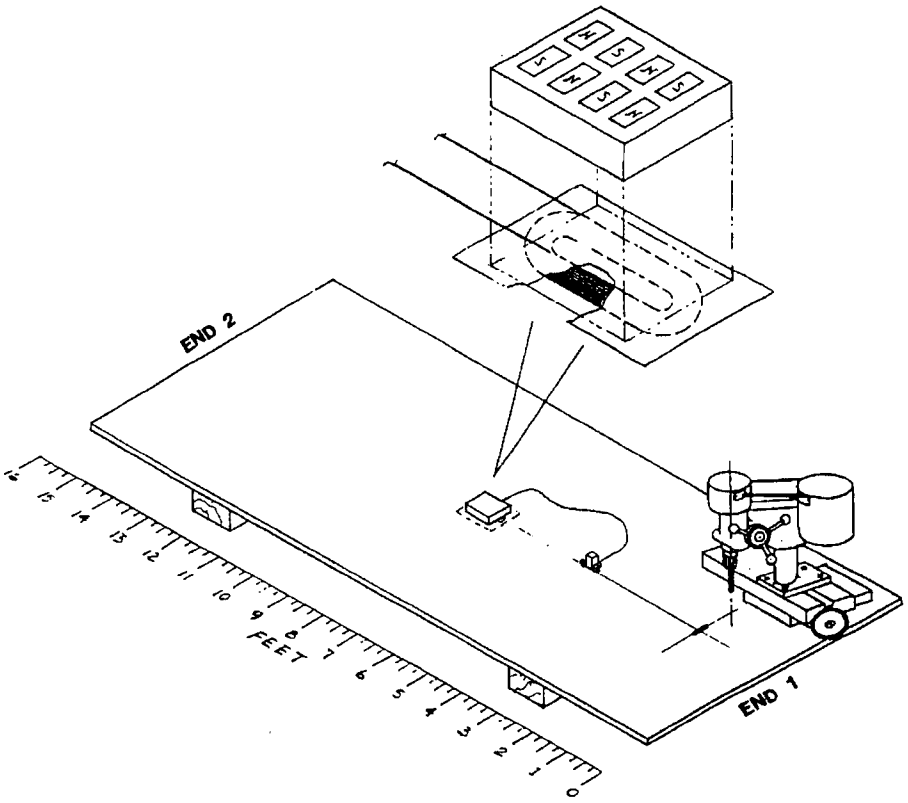

Figure 3.3 General plate, defect, and EMAT layout.

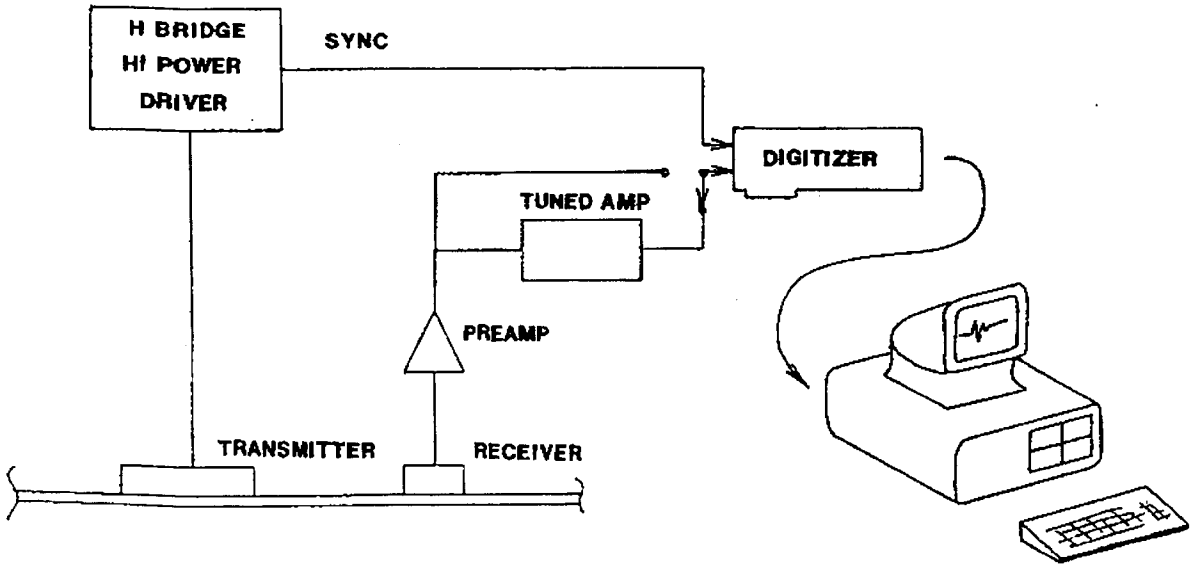

Figure 3.4 Schematic of experimental setup.

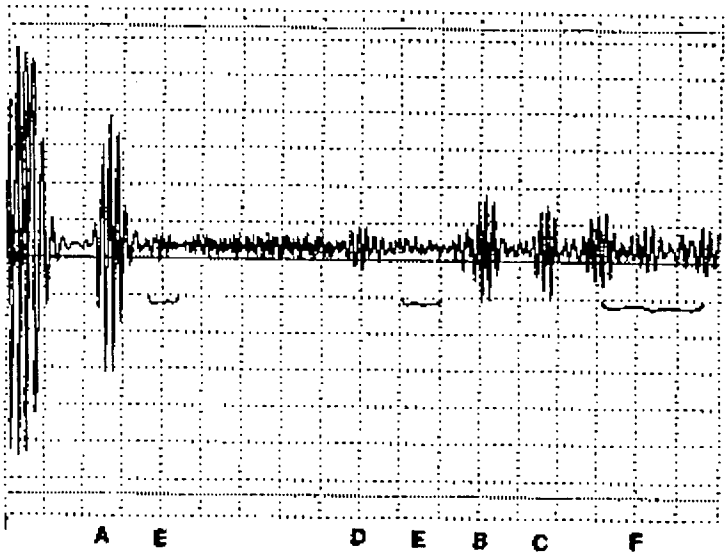

Figure 3.5 Typical amplitude-time waveform.

A = direct propagation from the transmitter to the receiver located about 0.9 m from the transmitter
B = same waveform as A after traveling to END 1 and back to the receiver
C = corresponding reflection from END 2
D = scattering from slot located on the plate centerline at a distance of 61 cm from END 1
E = coherent noise background after the first arrival signal
F = scattering of transmitter side lobe and/or peripheral portions of the main lobe from the plate edge and end

Table 3.1 Applicability and Important Material Characteristics of Selected Metallic Materials NDE Methods

Technique	Applicability by Flaw Type				Important Material Characteric
	Surface	Planar**	Interior	Volumetric	
Visual	X	X		X[3]	None, accessibility
Liquid Penetrant	X			X[3]	Flaw must intercept surface
Magnetic Particle	X	X	X[1]	X[3,4]	Material must be magnetic
Ultrasonic	X	X	X	X	Acoustic properties
Eddy Current	X	X	X	X	Material must be electrically/magnetically conductive
Radiography			X	X	Changes in thickness and density
Acoustic Emission	X	X	X		Material sensitive since is AE source
Thermography	X	X	X[2]	X	Material heat transfer characteristics

*Adaptation of: J. D. Wood, "Guide to Nondestructive Evaluation Techniques," ASM Handbook, Vol. 17, pp. 49-51. ASM International, Materials Park, Ohio, 1992.
**Thin in one direction.
1 = limited application, 2 = possible, 3 = surface, and 4 = subsurface.

Table 3.2 Dominant Sources of Variance of Selected Metallic Materials NDE Methods*

Technique	Variance Sources					
	Materials	Equipment	Procedure	Calibration	Criteria	Human Factors
Visual			X		X	X
Liquid Penetrant	X		X			X
Magnetic Particle	X	X	X			X
Ultrasonic		X	X	X	X	X
Eddy Current		X	X	X	X	X
Radiography	X	X	X			X
Acoustic Emission	X	X	X	X	X	X
Thermography		X	X	X		X

*Adaptation of Table 7-1 in "Nondestructive Evaluation (NDE) Capabilities Data Book," prepared by W. D. Rummel et al., Nondestructive Testing Information Analysis Center, Texas Research Institute Austin, Inc., Austin, Texas, May 1996.

Table 3.3 Interior and exterior containment surface areas that could experience accelerated degradation and aging.

Environmental or Operating Conditions	Typical Areas	Likely Locations
Areas subject to accelerated corrosion with no or minimal corrosion allowance or Areas where the absence or repeated loss of protective coating has resulted in substantial corrosion or pitting	Areas exposed to standing water Areas exposed to repeated wetting and drying Areas where persistent leakage has occurred Areas subject to microbiological attack Areas with geometries that permit water accumulation	Penetration sleeves and bellows Surfaces wetted during refueling Concrete-to-steel shell or liner interface Shell regions embedded in concrete including areas shielded by diaphragm floors Leak-chase channels Drain areas including sand pocket regions Sump liners Interior surfaces of BWR MK I and II suppression pools Exterior surfaces of BWR MK I and II drywells Emergency core cooling system suction intake at bottom of BWR suppression pool Dissimilar metal welds
Areas subject to excessive wear from abrasion or erosion	Areas where mechanical wear, abrasion, or erosion cause loss of protective coatings, deformations, or material loss Areas that experience frequent vibration	Surfaces subject to substantial traffic Sliding pads or supports (baseplates of BWR MK I suppression chamber support columns) Pins or clevices Shear lugs Seismic restraints Surfaces exposed to water jets from testing operations Safety relief valve discharge areas BWR drywell head, vent system supports, and downcomers and bracing Personnel airlocks, equipment hatches, and control rod drive hatches

Source: Refs. [3.3], [3.18-3.21]

Table 3.4 Factors associated with pressure-retaining steel component degradation.

Factor	Description
Pressure-Retaining Steel Components	Degradation can adversely affect the structural capacity or leak-tight integrity of metal containment shells, concrete containment liners, penetration liners, heads, nozzles, structural and non-structural attachments, embedment anchors, pipes, tubes, fittings, fasteners, and bolting items that are used to join other pressure-retaining components.
Damage Characteristics	Damage could involve loss of net section or wall thinning, cracks, pits, crevices, erosion, cavitation, surface flaws, arc strikes, plastic deformation, buckling, fracture, or bulging.
Damage Indicators	Rust, discoloration, staining, blistering and peeling of coatings, spalling of concrete, buckling or separation of liners, leakage from drains, and clogged drains.
Potential Problem Areas	Locations where degradation could be suspect include areas of water accumulation; surfaces exposed to chemical or borated water spills; flashed, caulked, or sealed joints; dissimilar metal connections; penetrations; condensation and leakage paths; sand pockets or cushions; heat trace areas; and locations with stray electrical currents.
Damage Detection	Damage detection techniques include leakage rate testing, visual inspection, destructive testing, and nondestructive examination.
Mitigation Procedures	Effects of degradation can potentially be mitigated by eliminating leaks; repairing or replacing defective components; removing and replacing cracked or torn seals, gaskets, and caulked joints; opening clogged drains; providing additional drains; repairing or replacing damaged coatings; proving improved spill response; and installing cathodic protection systems.
Potential Failure Modes	Degradation can cause cracking, fracture, instability, distortion, or excessive displacement that could result in loss of leak-tight integrity, decreased load-carrying capacity, or reduced service life.

Source: Ref. [3.22]

Table 3.5 Equipment used to aid visual inspection.

• Flexible or rigid borescopes for illuminating and observing internal closed or inaccessible areas
• Image sensors for remote sensing or for the development of permanent visual records in the form of photographs, video tapes, or computer-enhanced images
• Magnifying systems for evaluating surface finish, surface shape, and surface microstructure
• Dye and fluorescent penetrants and magnetic particles for enhancing the observation of cracks

Source: Ref. [3.23].

4. HIGH-FREQUENCY ACOUSTIC IMAGING•

Limited analytical and experimental simulations have been conducted by Cambridge Acoustical Associates/Engineering Technology Center (Cambridge, MA) to investigate the feasibility of applying high-frequency acoustic imaging techniques to the detection and localization of thickness reductions in the metallic pressure boundaries of NPP containments [4.1,4.2].

4.1 Numerical Simulations

The analytical study used an elastic layered-media code (OASES Code, Massachusetts Institute of Technology) to perform a series of numerical simulations to determine the fundamental two-dimensional propagation physics [4.3,4.4]. Results from the two-dimensional studies were used to address three-dimensional issues related to defect classification.

4.1.1 Range-Independent Results

Initial evaluations utilized the range-independent version of the OASES Code. The code was developed and validated for the evaluation of an acoustic field in a system of stratified fluid and/or elastic layers. The propagation scenario must be horizontally layered with the material parameters of each layer fully specified in terms of sound speed, density, and absorption. An arbitrary number of fluid or solid elastic layers can be interleaved, though the outer layers are modeled as halfspaces. The received field due to an arbitrary source array can be calculated at arbitrary depth and range positions. The response is determined for a single frequency by means of an exact fully-elastic calculation by wavenumber integration. Table 4.1 presents the material properties used in the numerical models. Figure 4.1 presents the approximate model of the containment scenario that was created. The model represents a portion of the problem addressed either above or below the interface, but does not represent the interface. A nominal 25-mm-long source array represents the ultrasonic sensor and the array is steered down at an angle to couple to a particular shear wave angle in the steel. The model was run for angles (35 to 70°) and frequencies (0.5 to 5 MHz) of currently available commercial sensors. Normal stress was calculated over a grid at a spacing of 1 cm in range and depth with the field calculated to a depth extending from 25 mm above to 25 mm below the steel layer. Degradation of the steel layer was represented by spatially uncorrelated surface roughness on the bottom of the steel layer. Although it was demonstrated that the code could model the basic scenario, clear modal structural dependence on frequency was seen. After several runs of the model utilizing a wide range of parameters, it became clear that the range-independent version of the code was inadequate to capture the important processes of propagation. The levels of roughness on the interface used to represent degradation were essentially meaningless. Roughness was modeled simply as an attenuation of a forward-propagating wave with no backscatter wave generated by the roughness. As a result, the approach was changed to use of the range-dependent version of OASES in which the full interface scenario could be modeled.

4.1.2 Range-Dependent Results

The range-dependent version of OASES also applies to evaluation of the acoustic field in a system of stratified fluid and/or elastic layers. This version of the code permitted modeling of the full scenario, which includes the air/concrete interface, a finite-length source, and discrete degradation regions. The field in one sector is propagated to the next sector by a virtual array of sources located on the sector boundary. A single scatter model is used (i.e., the field is calculated once forward through the sectors and then once backward).

The two-dimensional numerical model for the embedded steel containment scenario is presented in Fig. 4.2. Degradation of the steel is represented by a 10-cm-long notch cut from both surfaces. The degradation thickness, T, and its distance from the interface, dx, are parameters used in the simulation. A nominal 25-mm-long source array in a "wedge" material represents the ultrasonic sensor with the wedge material modeled as a fluid and thus only supports compressional waves. The array is steered down at an angle to couple to a particular shear wave

---

• Material presented in this chapter was developed from information provided in two reports [4.1,4.2] prepared under a subcontract with Cambridge Acoustical Associates/Engineering Technology Center, Cambridge, Massachusetts.

angle in the steel. Results for simulation of a 0.5 MHz source which excites a 45° shear wave in the steel surrounded only by air are presented in Fig. 4.3. Degradation is present on both sides of the steel, T = 4 mm, located at a distance of 55 cm from the source. The top plot shows the normal stress in dB as a function of range and depth for the forward-propagating field. Attenuation due to absorption by the steel is fairly low. The middle plot shows the same information for the backward-propagating field and indicates significant reflection of energy by the presence of degradation. The bottom plot shows line plots of the forward- and backward-propagating fields at the top of the steel layer. For this scenario, the degradation gives a signal level of –17 dB, which includes the scattering strength of the degradation and the attenuation of the steel. This return is significant and easily measurable. Results when concrete is added to the model are presented in Fig. 4.4. For the same degradation parameters as before, significant loss of energy occurs to the concrete as noted by high field levels above and below the steel layer to the right of the interface in both the forward and backscatter plots. The mechanism is phase-speed matching, shear waves in the steel leak off via Snell's Law into compressional waves in the concrete. Also, an additional 20 dB (37 –17 dB) of energy, normally seen by the sensor, has been lost due to leakage into the concrete. This will limit penetration ability.

In order to determine the dependence of the field on frequency and depth of degradation, the model in Fig. 4.2 was run for frequencies from 0.1 to 1 MHz and two-sided degradation depth from 0.5 to 10 mm. Figure 4.5 presents plots of signal level in dB versus degradation depth in mm. Results indicate that the system will be able to distinguish between relatively small surface imperfections (e.g., $\leq$1 mm) and more serious degradation (e.g., >2 mm). However, as the change in signal level (<10 dB) for defects in the range of 4 to 10 mm is relatively small, quantification of defect size in this range will require careful calibration. In order to evaluate the signal penetration capabilities, the model in Fig. 4.2 was rerun for frequencies from 0.1 to 1 MHz and a two-sided, 4-mm-deep degradation located at interface distances from 5 to 20 cm. Results in Fig. 4.6 show a high attenuation of received signal with distance. The concrete adds 3-4 dB of two-way signal loss per cm of concrete penetrated. The range of depths that can be penetrated will depend on the capabilities of the transducer used.

The two-dimensional numerical model for the steel-lined concrete containment scenario is presented in Fig. 4.7. Since the purpose is to detect degradation in the liner, which is thin compared to the concrete section, the field was limited to the steel liner (i.e., the containment was modeled as a pure halfspace). Normal stress in dB as a function of depth and range for the forward-and backward-propagating fields resulting from a 0.5 MHz, 25-mm-long source array coupled with a wedge to excite a 45° shear wave in the steel are presented in Fig. 4.8. In this scenario a 2-mm-deep, two-sided degradation, located 5 cm from the air/concrete interface was used. The figure shows that most of the forward energy from the source is injected through the plate directly into the concrete and lost so that the returned signal levels are very low. This will limit the ability of a practical system to excite waves in the liner. Signal levels are 40 dB (factor of 100) lower than the comparable values for the steel containment scenario. Also, if there are scatterers in the concrete, such as reinforcement, studs, or voids, they will tend to reflect energy back to the plate that may interfere with the desired measurements. Degradation depth (degradation depths from 0.5 to 3 mm located 5 cm from the interface, and frequencies from 0.1 to 1 MHz), and penetration (2-mm-deep degradation, located from 5 to 20 cm from interface, and frequencies from 0.1 to 1 MHz) studies indicate that for this scenario unacceptably high loss to the concrete (e.g., on order of 100 dB) occurs for a small degradation close to the interface. Due to this magnitude of loss, it appears unlikely that acoustic imaging technology can be applied to this scenario.

4.1.3 Three-Dimensional Issues

Having established the basic restrictions imposed by important parameters of the two-dimensional scenario as well as by the sensors themselves, the feasibility of designing an array of sensors that can scan the surface of the containment to localize and map thickness reductions was investigated.

Localization and mapping are similar operations from the point of view of a sensor system. Generally, a sensor system searches an area or volume by scanning in two or three dimensions. The search can be active, where the sensor sends out pulses of energy and listens for returns, or passive, where the sensor just listens for energy from an active source. The system under consideration here is an active system, since there are no active sources in our scenario. For an active system, sufficient energy must be input into the medium so that a signal reflected back from the target is of sufficient magnitude that it is measurable at the receiver. The search area or volume is divided up into bins in some coordinate system (e.g., rectangular, cylindrical or spherical). The results of a sensor sweep in

which the transmitter is sequentially moved from bin to bin are recorded for each bin. If the record is a "target/no target" decision, this is known as localization and locates the target. If the record is a received level, either in the form of raw data or interpreted via some transform, this is known as mapping. The problem at hand is a mapping problem, as the desired output is a spatial map of the degree of degradation over the entire surface of the containment.

Array processing is used to do either localization or mapping. Localization is a bit easier to describe. From there, mapping is a simple generalization. In order to localize a point scatterer, several directional views of it must be obtained and correlated. A classical [4.5] way to do this in two dimensions is with an array of sensors using a "range-bearing" type of algorithm (Fig. 4.9). Typically, a line array of N individual, omni-directional sensors is used in a coherent fashion. In a narrow-band frequency sense, the sensors are electronically phased to transmit and receive a tight angular beam of propagating energy. As shown on the left of the figure, this beam can be steered in a particular direction, θ. By sweeping the beam over this angle and identifying which angle gives the strongest return, the bearing of the target relative to the array can be found. Once bearing is known, the range is determined by using time-of-flight information. The range of the target is given by multiplying the two-way travel time, 2τ, by half the medium sound speed, c/2. Range and bearing information then uniquely locate the target in cylindrical coordinate space (although a line array does have an up-down ambiguity). The localization accuracy is dictated by the resolution of the array in the angular direction, and the bandwidth of the pulse in the range direction. These constraints give the minimum bin size in the two directions.

Figure 4.10 provides a simple illustration of the important parameters that govern the resolution of line arrays. In order to avoid spatial aliasing of the array, the elements must have a spacing, dx, smaller than $\lambda/2$, where λ is the wavelength of the signal (λ=c/f), c is the sound speed of the material and f is the frequency of the signal. This is similar to the Nyquist condition of signal processing and must be met to prevent bearing ambiguity. In the far-field, the beam pattern of the array is a sine function whose main lobe width is dictated by the length of the array, L. The angular resolution, θ_{3dB}, of the array in radians is simply the wavelength, λ, divided by the length of the array, L. The resolution, D, at a particular range, R, is this angular resolution multiplied by that range. This is only true in the far-field of the array which starts at a range equal to $2r_T = 2L^2/\lambda$. The strength of the array side lobes is a function of the amplitude taper applied across the array. For a Hamming taper, a target in the side lobe will have a level more than 40 dB below the level of a target in the main lobe. Since the range bin size is proportional to the duration of the pulse sent out by the source, a good estimate of this pulse duration is τ = 1/BW, where BW is the bandwidth of the signal.

Using the characteristics of typical ultrasonic sensors noted in Table 4.2, bin sizes can be calculated. The range bin width is computed from the bandwidth of the sensor. With a $Q = \Delta f/f_c = 0.6$, a 1 MHz sensor has a τ = 1.7μs, or ΔR = 5 mm. Thus, the range bin size is 0.5 cm. The total range of primary interest for the containment inspection scenario is on the order of 30 cm, which is equal to about 60 bins. This is not a very taxing burden for a system to measure and calculate. If one would like to localize down to about 3 cm, a 0.5 cm range bin size more than meets the criterion and is a good practical range resolution.

Angular resolution presents more of a problem with available sensors. A typical sensor is in the form of a piston that is large compared to a wavelength. Also, the typical sensor is not an omni-directional source, as is required for the formation of an array. To understand the high directionality of this sensor, one can model it as a dense array of finite length L, phased coherently in one direction. At 1 MHz, a 25-mm shear sensor has a main lobe width of only $\theta_{3dB} = 7°$. To understand the severity of this limitation, note that at 25 cm from the sensor location the diameter of the spot the sensor interrogates is D, where D is 3 cm wide. These ultrasonic sensors cannot be used together in a scanning array, as each sensor beam pattern would make looking in any direction other than the intrinsic sensor direction impossible. Thus, the current sensor technology can only be used in spot detection and mapping scenarios. If there were suspected degradation in an area of the containment, the sensor could be physically moved along at 3 to 5 cm intervals to sweep out a small area. As this is a labor-intensive process that would be warranted if degradation was suspected, but would not be practical to interrogate a large area.

Scannable sensor technology, such as used for medical ultrasound, should be capable of being developed. The medical ultrasound sensors are manufactured by bonding many signal wires to a solid piezoelectric block on a substrate, and then cutting the block into individual sensors, leaving a line array of N sensors in the substrate

(Fig. 4.11). For example, at 1 MHz, the spacing on this array would have to be on the order of 1.5 mm to avoid aliasing and 2.54 cm in total length for an angular resolution of $\theta_{3dB} = 7°$. This would require a 17-element array, that would be very reasonable in terms of cost and complexity to drive electronically. The finite size of the individual sensors would allow a total scan sector width of 120°, or about 18 angular bins. Experiments with the wedge material would have to be made to demonstrate that the directionality of the sensor would not interfere with the coupling characteristics of the wedge, and vice versa. Given the fixed scan sector size of 120°, the maximum penetration ability of the sensor and the required depth of coverage will limit the array offset, as shown in Fig. 4.12. Array offset is the separation between scanning stations so that the scan cones overlap, as shown in the figure, to provide complete coverage. Using parameters provided, it is estimated that the array offset will be on the order of 1.5 m, or 75 stations (scan locations) would be required to interrogate a 36-m diameter containment.

4.1.4 Conclusions from Numerical Simulations

The range-dependent version of the OASES Code successfully modeled the steel containment and steel-lined concrete containment scenarios using the discrete notch approach. For the steel containment scenario, significant degradations (> 2 mm) located below the concrete/air interface give reasonable intrinsic backscatter levels (-15 dB) that are 10 – 15 dB above the expected noise level due to surface imperfections. Dependence of degradation depth is small, but measurable. The embedding concrete introduces large losses that will limit penetration ability. Backscatter strength was not very sensitive to frequency or angle of the transducer (< 5 dB) for the sharp-edge degradations examined. Results indicate that acoustic imaging technology can be applied to this scenario. For the steel-lined reinforced concrete containment scenario, the thin steel liner in conjunction with the concrete produce unacceptably high signal losses to concrete (~100 dB). Application of acoustic imaging technology to this scenario seems unlikely. Currently available sensors cannot be used in array configurations to interrogate a large area (global inspection) due to their intrinsic narrow beam pattern, which does not allow steering. This limits these sensors to spot detection and mapping scenarios, where degradation is already suspected; however, scannable sensor technology, such as used for medical ultrasound, should be capable of being developed.

4.2 Experimental Simulations

Based on the prior numerical simulations, the proposed solution is to propagate ultrasonic waves (either shear or compressional), whose wavelengths are a fraction of the plate thickness, from accessible regions of a free-standing steel containment vessel (or liner of reinforced concrete containments) laterally to detect degradations located below the air-concrete interface (Fig. 4.13). Ideally, the reflected returns from material defects can be processed to generate an image of the degradation. The proposed technique is known as an angle-beam inspection, where instead of placing an ultrasonic transducer in direct contact with a test specimen, a plastic wedge is used to couple the transducer to a test structure (Fig. 4.14). The transducer generates compressional waves in the wedge that are refracted in the test structure, usually as shear waves. Shear waves are used because for a given inspection frequency they have shorter wavelengths than compressional waves and therefore can resolve smaller defects. These refracted waves "skip" laterally away from the source through the structure. When the waves encounter discontinuities, acoustic reflections occur. This technique is often used to inspect welded joints and to determine the presence of cracks or other structural flaws. The incident waves for this type of inspection are not typically required to propagate over considerable distances or to propagate in constrained or embedded regions of the test structure, as required to do in order to demonstrate success in the proposed test scenarios. Moreover, the significance of the embedding concrete on propagation of ultrasonic waves in the steel and how well corrosive type degradations act as acoustic reflectors are unknown.

The feasibility of employing the technique under the proposed scenario therefore centers on determining if a measurable and decipherable signal is returned from an area exhibiting degradation (e.g., wall thinning due to corrosion). In an effort to not only provide a basis for improving the numerical models, but also to continue the feasibility study in a more practical forum, a series of controlled laboratory experiments was designed. The experiments attempt to limit conditions to two-dimensional scenarios where only degradation variations in the direction of the incident wave are considered, and flat plates can be used as propagating media. The physics side of the problem was addressed by investigating the energy lost from the interrogating signals into the surrounding concrete, as well as characterizing acoustic scatter arising from different defect geometries. Also of primary importance was the practical issue of determining the performance limits exhibited by a commercially available angle-beam inspection system. The ability to discern and extract the degradation characteristics using acoustic

signals that include information about both the corrosive damage and the propagation path are important, but at this early stage of development, a secondary concern.

4.2.1 Testing Equipment

A completely integrated laboratory ultrasonic testing package was provided by a commercial vendor. The testing equipment consisted of a pulser/receiver card, a high frequency analog-to-digital acquisition board, software, piezoelement contact transducers, coupling wedges, and industrial grade ultrasonic gel couplant. The transducers had a 25-mm-diameter circular radiating face that produced an estimated half-angle beam width of just over six degrees. The transducers were tuned to 0.5 MHz, which is a relatively low frequency for ultrasonic testing (shear wave length in steel at 0.5 MHz is about 6 mm), but allows for additional penetration. The equipment can be utilized in either the through-transmission mode, where separate transducers act as source and receiver (bistatic), or the pulse-echo mode, in which a single transducer injects a wave and then passively listens for a return (monostatic). When operated in the through-transmission mode, the source and receiver transducers are attached to coupling wedges having the same angle. The coupling wedges are specified by the refracted shear-wave angle (measured from the surface normal) introduced into the test structure. All the wedge angles used (i.e., 45°, 60°, and 70°) were past the compressional wave critical angle for steel (i.e., compressional waves will not be excited in the steel plate). As the transducer does not generate a planar incident field, the energy is injected in all directions. Therefore, the main lobe of the incident sound field does not excite compressional waves in a steel test structure, but the side lobes below the main lobe may excite compressional waves.

The input-voltage waveform was a tone burst, with the signal length, level (in percent of maximum), and center frequency specified by the user. The signal length used in the experiments was 4 microseconds, and the frequency was 0.5 MHz. The maximum input voltage that the pulser can generate was 300 V. Because the transducers were uncalibrated, the relationship between input voltage and mechanical force was unknown.* The acquisition board range was $\pm$0.5 volts with a precision of 8 bits. The receiver gain ranges from 0-70 dB.

4.2.2 System Performance and Operability

The initial experimental activity consisted of verifying operability of the equipment through conduct of a conventional ultrasonic thickness test. Figure 4.15 shows a sketch of the experiment and the measured return. The transducer was placed in direct contact (i.e., no coupling wedge) with the longest edge of a 25-mm thick by 203-mm wide by 914-mm long mild steel plate, for the purpose of injecting compressional waves across the plate's width. The plate thickness was chosen to approximate that used for fabrication of steel containment vessels. Plate width was selected so that no side interactions would take place when waves were directed down the length of the test platform and the width-centered source and receiver were not more than 178 mm apart (124 mm for a 45° propagation angle, 168 mm for a 70° propagation angle). Thus, where propagation distances were less than 89 mm, the plate width was rendered effectively infinite.

When operating in a monostatic configuration as shown in Fig. 4.15, the transducer also acted as the receiver (i.e., input and free-vibration ringdown of the piezoelectric element were both measured). This is shown as the clipped portion of the signal before 40 microseconds (receiver gain was set to record the reflected signal from the plate's opposite edge, which displayed significantly lower levels than signals listed above). The first returns after the source had died down were from the direct path to the opposite edge of the plate, and they occurred at 75 microseconds. When half of this delay (time of flight for one-way travel) was multiplied by the assumed compressional wave speed in steel (0.55 cm/μs), the 203-mm width was estimated to be 206 mm. Although the transducer used was not specifically designed for this type of test, the results demonstrate a properly operating system.

The system's input/output dynamic range was experimentally determined by measuring the maximum signal that the system could inject and the minimum signal that the system could read. Two transducers (both attached to 45° coupling wedges) were placed adjacent to one another on the 25-mm-thick steel plate. With the receiver gain set to the allowed minimum (0 dB) and the input level set to the allowed maximum (100%), the signal

* More expensive pulser/receiver cards that can generate inputs of 1000 V are commercially available.

transmitted from one transducer to the other was monitored. The receiver position was slowly moved away from the source until the received signal obtained its first maximum (i.e., the receiver fell on the first "hot spot"). This was assumed to be the maximum signal level that could be injected. The maximum measurable signal, with no receiver gain, coincidentally, just filled the acquisition board range. The maximum measurable signal was –6 dB re. 1 volt. The source was then removed from the plate, receiver gain maximized (70 dB), signal levels determined for one hundred background signal measurements on the plate, and results averaged to obtain a minimum measurable signal level (to suppress uncorrelated sensor noise). Figure 4.16 presents the power spectral densities for the maximum and minimum signals. At 0.5 MHz, where the source signal is concentrated, a 125 dB difference can be seen. This difference represents the system's input/output dynamic range.

In order to attribute differences in measured signals to physical effects, measurement repeatability was quantified. The tests were performed on vertically oriented plates to incorporate any problems associated with fixing the transducers in this orientation. The tests involved measuring the transmitted signal from one transducer to another for several different relative separation distances. Transmitted signals were recorded over a three-day period on three plates, with a total of nine measured signals obtained at each separation distance. Of the nine measured signals at each separation distance, the ratios of the maximum to minimum received signal levels were determined and the results are presented in Fig. 4.17 for five different source/receiver separation distances. The plot indicates a maximum variability of 2 dB, thus indicating that measured differences greater than 2 dB could be attributed to effects outside of pure chance.

4.2.3 Source and Waveguide Characterization

In order to accurately image the location and shape of a degradation, the distortion caused by wave guide propagation of unfocused incident waves must be considered. For this purpose, numerical modeling can be an invaluable tool, however, the modeling assumptions are critical. Therefore, as a basis for refining the numerical modeling assumptions, wave guide effects on signal propagation were addressed by a series of tests.

Using one transducer as a source and a second as a roving receiver (both transducers fixed to a 45° coupling wedge), a bistatic array was simulated. By doing so, the incident wave interactions with the plate's edges could be effectively monitored as the wave propagated down the plate. The experimental setup for monitoring forward-travelling waves in a plate is shown in Fig. 4.18. Combined envelopes of received signals at several locations relative to a fixed source are presented in Fig. 4.19. Image brightness is proportional to the envelope of the received signal level. Several results that can be derived from this experiment are:

- "Hot spots," seen as bright features, correspond to structural wave interactions with the measured surface. These features appear with regular spatial periodicity corresponding to the "skip length" of a 45° incident signal.

- The magnitudes of the hot spots diminish as the receiver is moved further from the source. Table 4.3 summarizes spreading loss values. Spreading losses at 254 mm are about 8 dB (this accounts for incident coupling losses as well) and for every additional 254 mm of propagation distance, 6 dB of additional spreading loss occurs (note that these propagation distances are measured along the plate and are based on injection through a 45° coupling wedge, for the 70 degree wedge the spreading losses must be scaled by sin 70°/sin 45°=1.33). Because there is no strong evidence of scattering to non-specular waves due to surface interactions, the edge reflections must be "specular" (i.e., similar to a pool ball bouncing off the edge of a pool table). Consequently, the measurement noise floor due to spurious reflections from surface imperfections should be low.

Figure 4.20 shows the results of a similar series of tests measuring the backward-travelling wave signal reflected from the plate's opposite edge. The "packets" of signal comprising the reflected returns have now been spread over time due to geometric spreading and multi-bounce interference. Although even in the ideal case of an edge reflector it is difficult to determine the exact position of the reflector in any given time signal, the signal "packets" plotted together "point" to the reflector.

4.2.4 Assessment of Signal Loss Components

Figure 4.21 presents a schematic of the test setup used to study the signal level returned from "artificial" degradations of various shapes. The "artificial" degradations are uniform cross-section slots, either rectangular, rounded, or "V" shaped, cut across the plate's 203-mm width. Because side interactions are intentionally avoided, the degradations are rendered effectively two-dimensional. All of the degradations were 4–mm deep by 10-mm wide. Monostatic returns were measured at several distances from each slot's leading edge. Figure 4.22 shows a sample return signal from a rectangular slot. The reflected signal "level" is defined as the maximum value in the signal packet that is assumed by simple time gating procedures to have emanated from the slot.

Figure 4.23 presents reflected signal levels at several source locations relative to the slot geometry. For the 45° coupling wedge, the returns from the rectangular slot were, averaged over source location, around 1 dB higher than those from the rounded slot and 4 dB higher than those from the "V" shaped slot. For the 70° coupling wedge, the differences were 5 and 9 dB, respectively. When an increase in received signal level was obtained at a position located a greater distance from the notch leading edge, this was due to the location's proximity to a hot spot. These results include the effects of geometric spreading, which are greater for the 45° coupling wedge than for the 70° wedge because the path to and from the slot is longer for the deeper angle. A more thorough analysis of the measured differences would incorporate advanced acoustic scattering theories, which was beyond the scope of this study.

It is useful to develop an average "reflection coefficient" for the rectangular notch, where the reflection coefficient is the ratio of incident to reflected signal level minus geometric spreading. For sources located in a continuous three-dimensional medium, the spreading loss is inversely proportional to the distance from the source and is termed spherical spreading. For sources located in a continuous two-dimensional medium, the spreading loss is inversely proportional to the square root of the distance from the source and is termed cylindrical spreading. Because the geometric spreading estimates account for incident coupling losses, removal of the spreading loss from the measured signal level generates a useful result based on the maximum measurable signal. The average reflection coefficient for the rectangular notch using the 45° coupling wedge is about –23 dB and for the 70° coupling wedge about -23.5 dB. By comparing the reflected returns from notches of various cross-sections to those from the rectangular notch, this result can be used as a basis for estimating reflection coefficients for other notch shapes. Figure 4.24 presents examples of the time-windowed returns reflected from the three different notch geometries. A comparison of these returns reveals that the arrival times of the reflected signals are very nearly equal despite the fact that the reflected fields from each notch geometry theoretically are markedly different. The implication here is that the component of the reflected signal propagating at 45° is biasly received, while other propagation angles are filtered out to varying degrees. Consequently, the scattered field is measured at very nearly a single angle. Without measuring the entire field it will be difficult to make statements on the character of the reflector. Phased array receivers can be used to effectively sample the scattered field over a much wider band of angles [4.1].

Reflected signal level was also used to investigate the effect of degradation depth. Figure 4.25 shows a sketch of the notches used in this test. All notches were rectangular in shape, 10-mm wide, and had notch depths of either 4, 8, or 12 mm. Differences in reflected signal at several source locations relative to the notch for both a 45° and 70° coupling wedge pair are presented in Fig. 4.26. For the 45° coupling pair, the returns from the 4-mm-deep notch are, averaged over source location, around 3 dB lower than those from the 8-mm-deep notch, and about 6 dB lower than those from the 12-mm-deep notch. This trend is as expected, as deeper notches project a greater area of acoustic impedance. Figure 4.26 shows the reflected signal levels from the three different notches using a 70° coupling wedge pair. The resulting trend for this case is not as expected. For some source-receiver separation distances, the reflected returns from the shallowest notch are actually greater than those received from the deepest notch. The odd trend was qualitatively observed over a broad range of separation distances, eliminating skipping effects as a possible explanation. The explanation for these results may, again, only be realized after incorporating advanced scattering theories, which was beyond the scope of this study.

4.2.5 Concrete Effects

The final series of tests to assess the individual components of signal loss involved measuring the effect that concrete has on waves travelling in an embedded plate. Figure 4.27 shows the wooden molds that were built to allow the midsection of steel plates to be embedded in concrete. To determine the effect that bond quality had on

induced losses, one of the plates was wrapped with a single layer of 4-mil-thick plastic sheet prior to casting to prevent bonding between the concrete and plate ("unbonded"). Two other plates were cast without the plastic sheet to permit bond development between the concrete and plates ("bonded").

Figure 4.28 presents a simplified schematic of the test setup for the concrete effects tests. The source transducer location, s, was varied from 6.3 cm to 11.4 cm in 1.27-cm steps in order to sufficiently sample one half of a skip length for a 45° coupling wedge. A receiving transducer maintained at a fixed position was used to monitor the signal that propagated through the plate. The received signal level was defined as the maximum value in the incident signal packet that arrived at the receiver. Figure 4.29a presents the maximum value in received signal level for the three free-standing plates prior to their embedment in concrete using an input source positioned at several locations. As expected, there was only minimal variation from plate to plate and the plastic wrap had no noticeable effect. Figure 4.29b presents results after embedding the midsections of the three plates in concrete. The two "bonded" plates display a significant loss in signal level (30 dB, or 1.6 dB per centimeter of two-way travel), while the "unbonded" plate signal level remained relatively high, incurring virtually no losses. Note that the results for the "bonded" plates are very similar, with the differences being attributable to a combination of measurement and concrete bond variations. These results show that the interface, or bond, between the concrete and steel plays a critical role in determining the proportion of energy lost from waves travelling in the steel.

Figure 4.30 presents the effect of wedge coupling angle on received signal level for a plate after it was embedded in concrete (bonded). The 70° coupling wedge shows transmitted signal levels that are roughly 4 - 5 dB higher than those received using the 45° coupling wedge. Assuming that both wedges couple equally to the test structure, this result is to be expected because the incident wave injected by the 70° coupling wedge experiences fewer interactions with the concrete-steel interface due to the longer skip distances.

Results of the concrete-effects tests show that characterizing degradation based on reflected returns may be difficult, even if the degradation location can be determined. The propagation path plays a prominent role in determining the level of the returned signal. Path conditions cannot be well known without destructive testing. Also, the overall level of the reflected returns cannot be used (for the system and procedure employed here) to confidently characterize degradation located below the air/concrete interface.

4.2.6 Implications of Masking Signals

To determine the role that competing signals may play in dictating the technique's feasibility, a simulated field condition was tested, Figure 4.31. Signals reflected from a 4-mm-deep rectangular notch located 127 mm from the air-concrete interface were measured and compared to those obtained with no concrete present.

Previous tests indicated that the source "self-noise" tended to mask low-level returns. Mechanisms of source "self-noise" are illustrated schematically in Fig. 4.32. As noted in the figure, the incident signal:

- couples to an injected shear wave,
- reverberates inside the wedge due to the surface reflection from the wedge-test structure interface and the side lobes "spraying" the sides of the wedge,
- bounces repeatedly across the thickness of the test structure directly under the wedge, and
- couples to other wave types, such as surface and compressional waves.

By altering the test setup to that shown in Fig. 4.33, where a second transducer is used to receive the reflected returns (bistatic condition), the inner wedge reverberant field and the through-thickness standing echoes are eliminated. This is illustrated in Fig. 4.34 which shows the reflected signal received for the 70° coupling wedge located 203 mm from the notch's leading edge for three cases: monostatic measurements with no concrete; monostatic measurements with concrete; bistatic measurements with concrete. As shown by the middle plot, the additional receiver gain needed to monostatically measure the return reflected from the notch embedded in concrete causes the previously low-level source self-noise to now completely mask the return. When the returns are measured bistatically (bottom plot), the source self-noise is suppressed and the returns from the notch are apparent.

Without this simple procedural alteration, the inspection technique would not be able to clearly detect returns from the notch. Based on results from the signal loss component experiments, the reflected signal for the embedded case should be about -51 dB (9.4 dB of spreading loss, 23.5 dB reflection coefficient, 18 dB of loss to concrete) down from the maximum measurable signal (-6 dB). It was measured at 50.5 dB, thus supporting the signal loss estimation technique.

Figure 4.35 shows in greater detail the bistatically-measured return from the rectangular notch in the plate embedded in concrete. Although the return from the notch is evident, there are still competing return signals occurring between 50 and 130 microseconds that have not been eliminated by using a bistatic approach. These returns would normally be considered secondary, but because the peak in the reflected signal packet from the notch is suppressed by the effect of the concrete, they are now down only 6-10 dB (linear factor of about 2-3). It is interesting to note that the reflected signal builds somewhat sharply at around 60 microseconds. This time delay corresponds very nearly to the time it would theoretically take a compressional wave propagating directly down the plate's axis to traverse to and from the notch's leading edge. Thus, it appears as though an incident side lobe has coupled to a compressional wave in the steel plate. These signals could be considered a localizing aid as opposed to competing signals, as the compressional signal returns are down by a linear factor of 3 (or 9.5 dB) relative to the reflected shear wave field. An important point is that if a competing signal can be identified, then it can in all likelihood be removed from the return signal during post-processing.

In light of the above, the through-transmission tests to determine the effect of the embedding concrete were re-scrutinized. Figure 4.36 shows (from top to bottom): the transmitted signal through a free plate without concrete, an unbonded plate embedded in cured concrete, and a bonded plate embedded in cured concrete. As shown by the top and middle plots, the effect of the plastic wrap was to virtually eliminate additional losses imposed by the embedding concrete. Also, the character of the transmitted signal for these two conditions was not altered significantly. However, as noted in the bottom plot in this figure, the character and overall level of the transmitted signal through the bonded embedded plate does change. Thus it appears as though the transmitted shear wave, which skips down the plate and therefore interacts repeatedly with the concrete interface, is affected by the concrete to a much greater degree than waves propagating directly down the axis of the plate. As the degradation distance below the air/concrete interface increases, effects of the concrete will act to suppress the returned shear wave field, which propagates at an angle to the plate surface, to levels below the returned compressional wave field, which propagates parallel to the plate surface. By using signals that are directed down the axis of the plate at angles deeper than 70°, the return signal level's strong dependence on path conditions may be suppressed.

4.2.7 Conclusions from Experimental Simulations

The series of experiments performed were designed to assess the performance of a commercially available fully integrated angle-beam inspection system, and to investigate the propagation physics that govern the use of angle-beam inspections. The measurement system displayed an input/output dynamic range of 125 dB. Therefore, in the absence of competing signals, 105 dB of losses can be incurred while still maintaining a 20 dB signal-to-noise ratio. The mild steel plates used in the experiments propagated signals as if they were effectively free of surface imperfections, which would otherwise act as random scatterers. Under similar conditions, the surface-generated noise baseline due to surface flaws should be minimal. Results obtained from rectangular, rounded, and "V" shaped notches provide a preliminary basis for estimating reflected signal levels from a vast array of two-dimensional degradations. Results for the steel plates embedded in concrete indicate that an additional 1.6 dB and 1.4 dB of signal loss is incurred for each centimeter of two-way signal travel when using 45° and 70° coupling wedges, respectively. Thus, waves directed at shallow angles are least affected by the concrete, regardless of coupling condition, and may be of more value for the inspection scenario of interest. Steel plates that are not bonded to concrete show virtually no additional losses compared to free plate signal losses; however, if fluids are present at the interface between the concrete and steel plate, increased signal losses will occur. Results from the signal-loss component experiments provide a basis for estimating the total loss induced on an incident signal for many scenarios (e.g., in the absence of competing signals, a 4-mm-deep rounded degradation located 30 cm below the air/concrete interface for the steel containment scenario should be detectable using a 70° coupling wedge because 50 dB of signal-to-noise ratio remains after estimated losses of 73 dB). Competing signal environments (e.g., compressional wave field) may mask the signal return to make defect detection difficult; however, use of bistatic measurements and discrimination techniques can minimize or eliminate competing signals.

4.3 Recommendations

Several procedural recommendations can be made based on the practical knowledge gained in this study:

- The system used in these experiments can only be applied to more challenging scenarios with the aid of algorithms that can discriminate the compressional and shear wave fields. This can be done by measuring the reflected signal at several locations and employing a Radon Transform, which discriminates waves travelling at different velocities [4.6].

- The transducers used in these experiments act as relatively narrow-band mechanical filters (in relation to conventional, highly damped transducers) and are tuned to 0.5 MHz nominally. Frequency concentrated tone burst waveforms were used to minimize the energy lost outside of the effective transducer filter and therefore to maximize the injected power. In retrospect, added problems of a relatively lightly damped piezo crystal (which had a significant ring down period) and a relatively long (in time) input signal (required for frequency focusing) do not justify their selection over a highly damped crystal excited with short pulses, which would return more temporally focused reflections.

- Because the source "self-noise" is sufficiently high to mask returns from moderately sized degradations near the source, or small, distant degradations, a bistatic arrangement is recommended. Dual element transducers, that incorporate this idea into a single device, are presently used for through-thickness testing and would be advantageous for the present application as well.

- Waves that are directed down the axis of the plate are much less affected by the presence, and more importantly the condition of the surrounding concrete. For this reason, it would be advantageous to inject waves at extremely deep angles to maximize penetration and to utilize overall return level as a degradation characterizing tool.

- It is imperative that the gel couplant completely fills the space between the transducer-wedge interface and the wedge-test structure interface. This becomes increasingly difficult when wedges are coupled to vertical structures. If proper measures are not taken, the measurement repeatability suffers greatly.

The following is a list of practical issues that should be addressed before attempting to employ the technique:

- Three-dimensional effects, such as plate curvature, degradation curvature, and mixing of return signals from several closely spaced degradations.

- Effects of structural discontinuities in the metallic pressure boundary, such as presence of welds, anchors, studs or other structural members.

- Effect of form that corrosion takes on results (e.g., pitting or general).

- Effect of quality of bond between concrete and steel on results, particularly the significance of corrosion occurrence.

The spatial filtering inherent to the transducers used in this study effectively limits the measured reflected field to a narrow propagation angle band. Reflector characterization schemes would ideally be based on the full field. This can be accomplished using a phased array of sensors. Unfortunately, waves returning at different angles are affected to various degrees by the condition of the surrounding concrete. This is considered to be the single biggest obstacle to applying the technique, because return levels are not solely dependent on the overall size of the defect from which they emanate. It may be necessary to develop nondestructive techniques to determine the condition of the steel/concrete bond.

4.4 References

4.1 J.E. Bondaryk, C.N. Corrado and V. Godino, *Feasibility of High Frequency Acoustic Imaging for Inspection of Containments*, NUREG/CR-6614, U. S. Nuclear Regulatory Commission, Washington, DC, August 1998.

4.2 J. Rudzinsky, J. Bondaryk, and M. Conti, *Feasibility of High Frequency Acoustic Imaging for Inspection of Containments: Phase II*, ORNL/NRC/LTR-99/1, Lockheed Martin Energy Systems, Inc., Oak Ridge National Laboratory, Oak Ridge, Tennessee, July 1999.

4.3 H. Schmidt, *SAFARI: Seismo-Acoustic Fast-Field Algorithm for Range Independent Environments, User's Guide*, SACLANT ASW Research Centre I-19100 La Spezia, Italy, May 1987.

4.4 H. Schmidt, *OASES User Guide and Reference Manual*, Version 2.1, Massachusetts Institute of Technology, Cambridge, Massachusetts, 1997.

4.5 D.H. Johnson, and D.E. Dudgeon, *Array Signal Processing*, Prentice-Hall, Inc., Englewood Cliffs, New Jersey, 1993.

4.6 M.C. Junger, and D. Feit, *Sound, Structures and Their Interactions*, 2nd Edition, 1986.

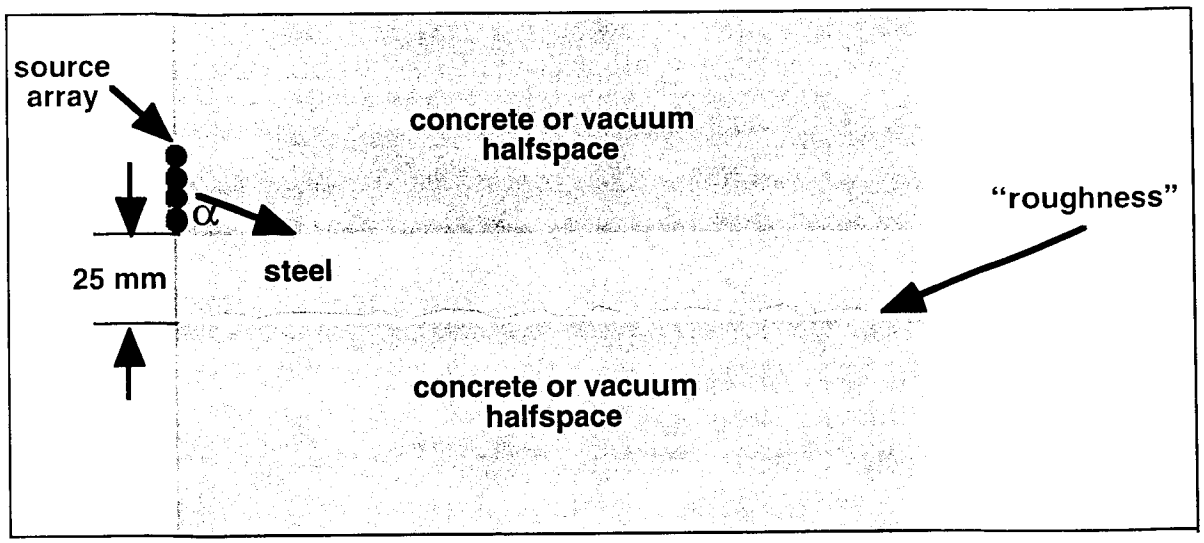

Fig. 4.1 Range independent OASES simulation scenario – approximate model of containment scenario.

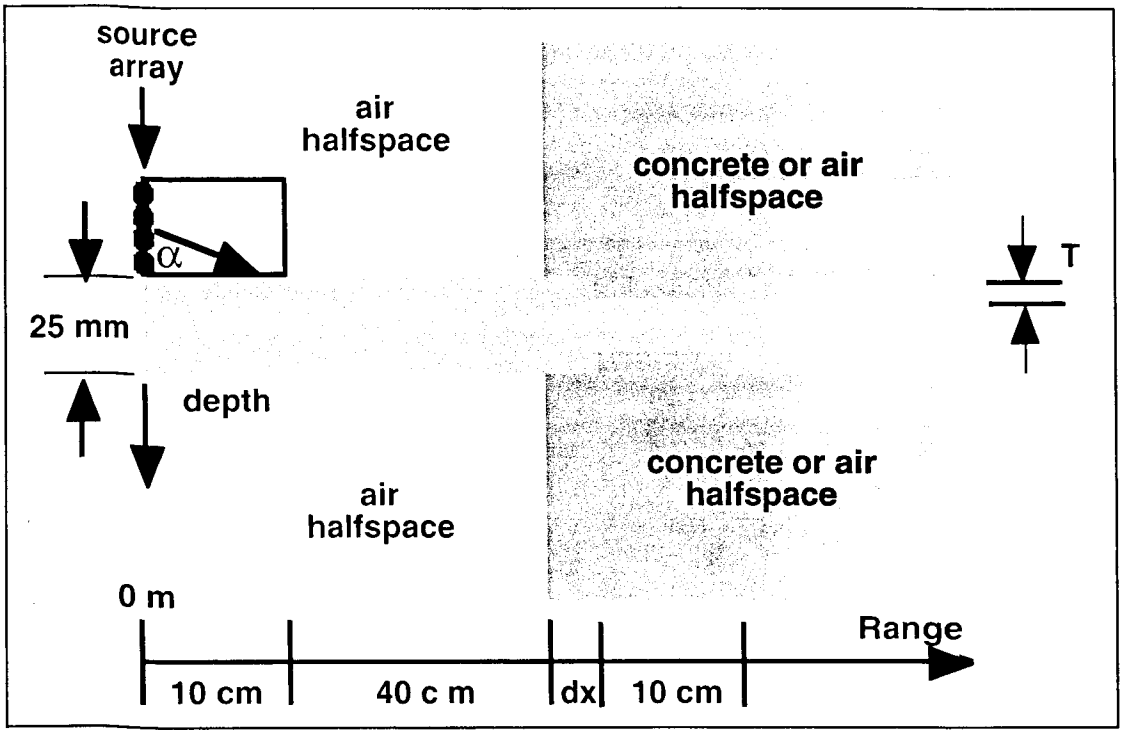

Fig. 4.2 Range-dependent numerical simulation scenario for steel containment scenario.

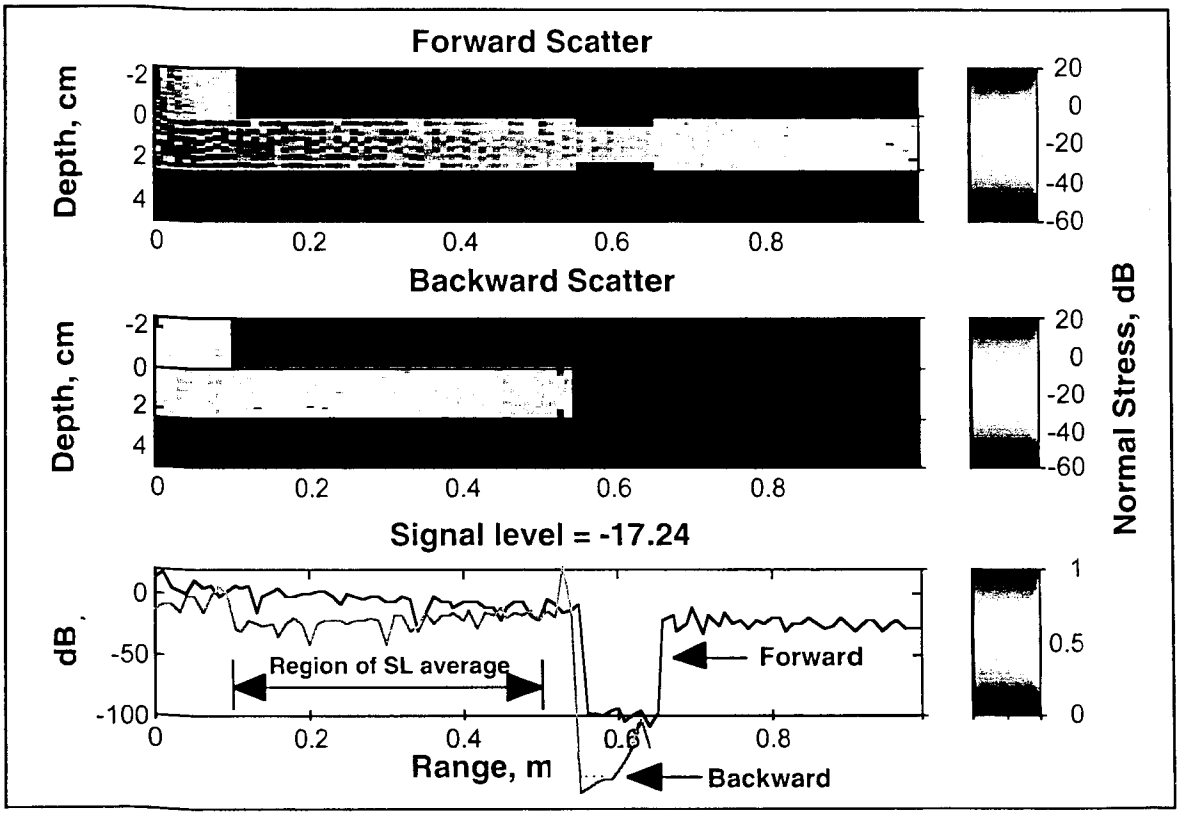

Fig. 4.3 Results of simulation scenario for a steel layer surrounded by air only

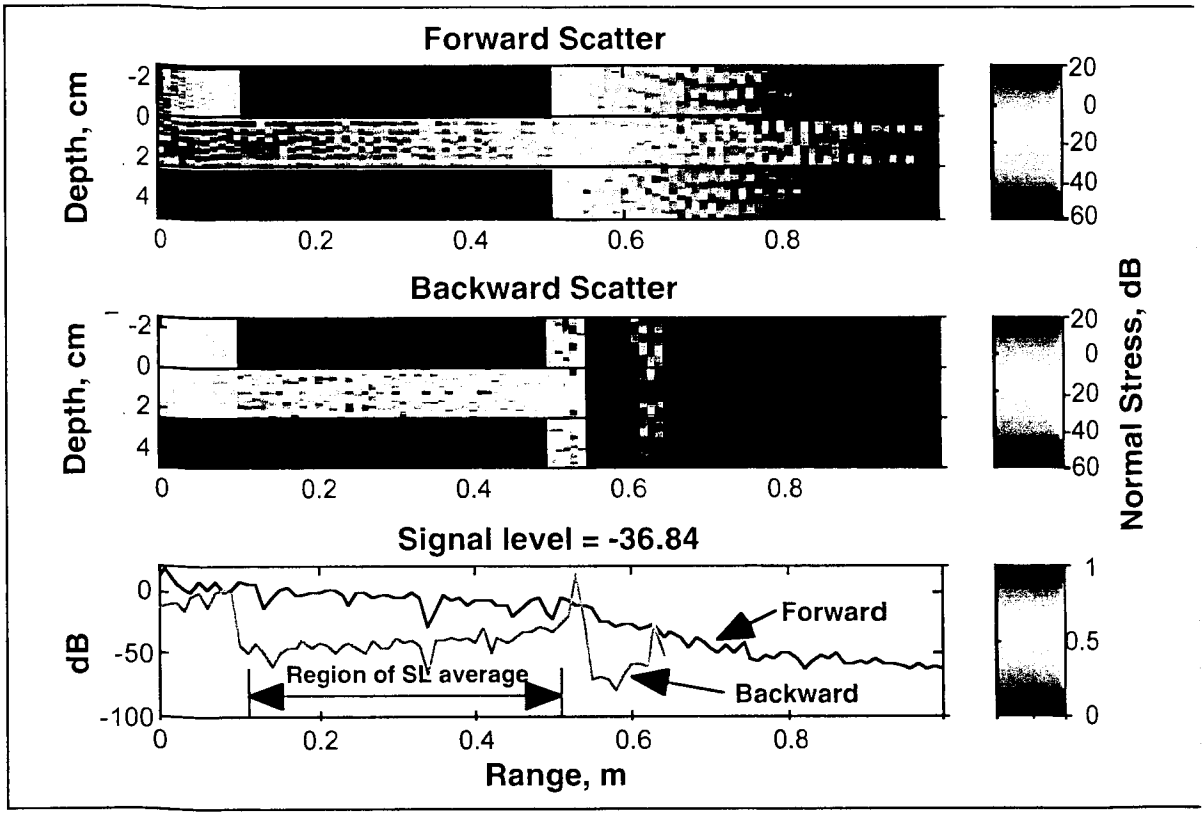

Fig. 4.4 Results of simulation scenario for embedded steel containment.

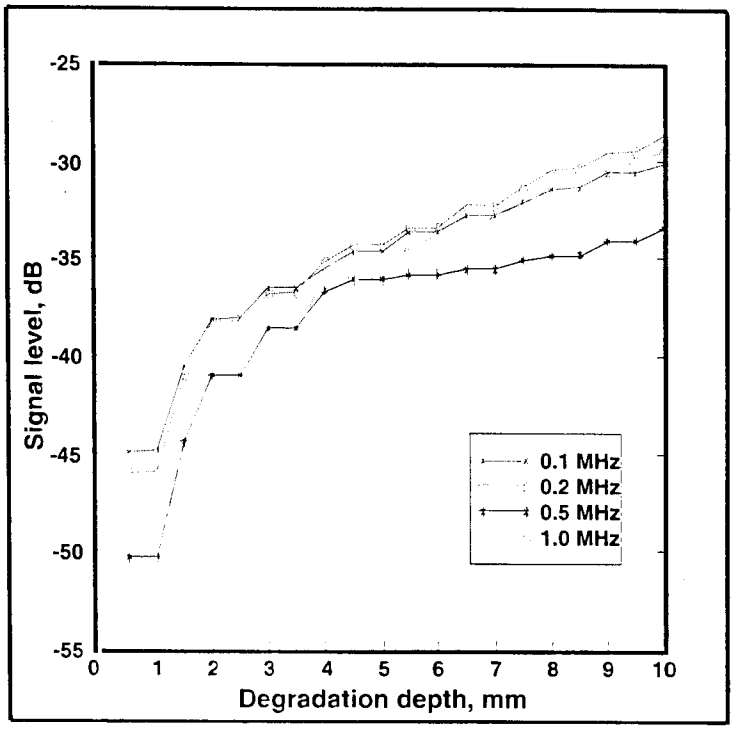

Fig. 4.5 Signal level from a degradation located 5 cm below air/concrete interface as a function of degradation depth and frequency.

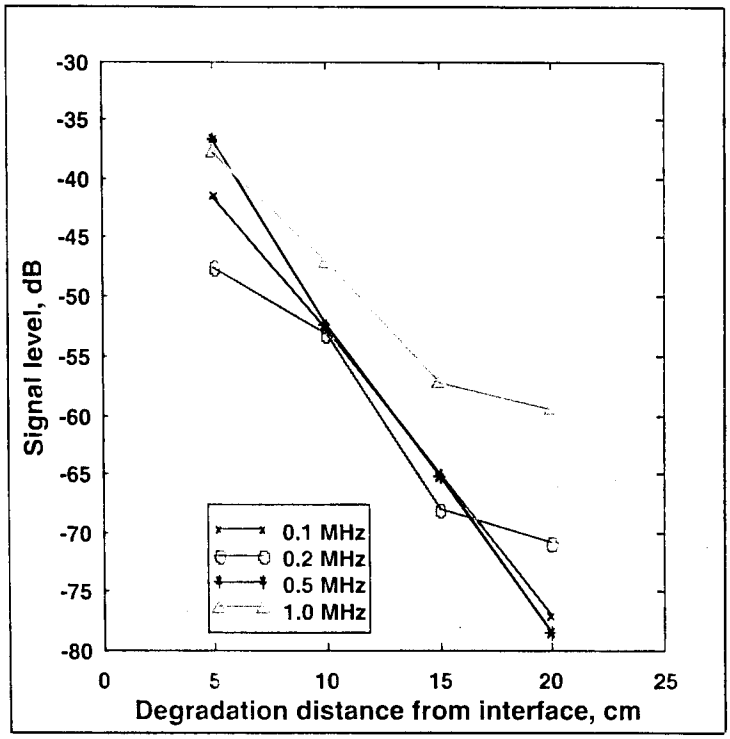

Fig. 4.6 Signal level from a 4-mm-deep degradation as a function of degradation distance from interface and frequency.

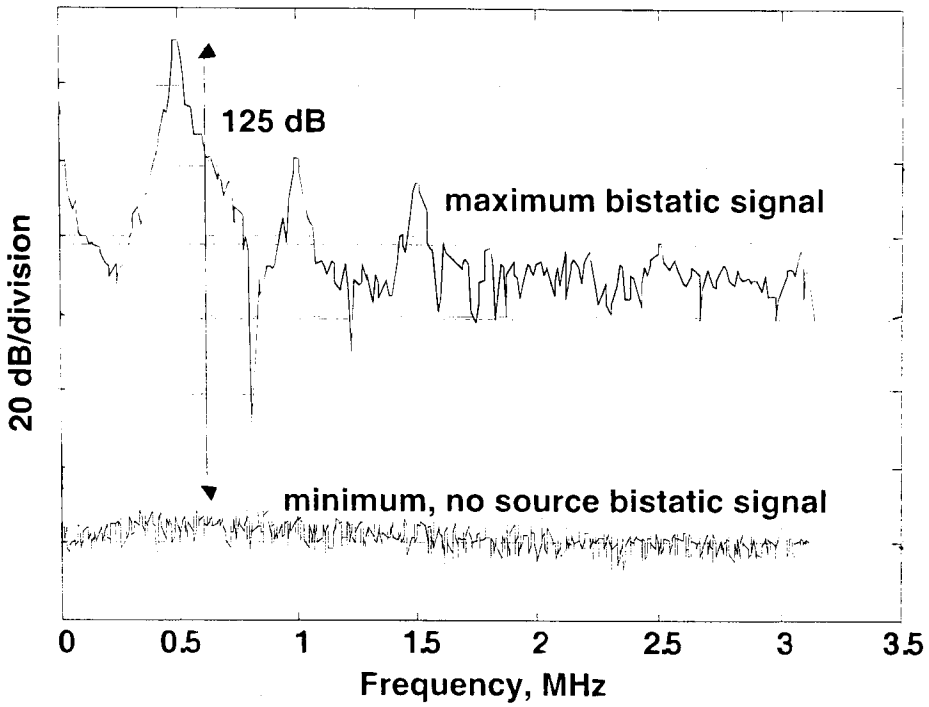

Fig. 4.16 Power spectral densities of maximum and minimum signals.

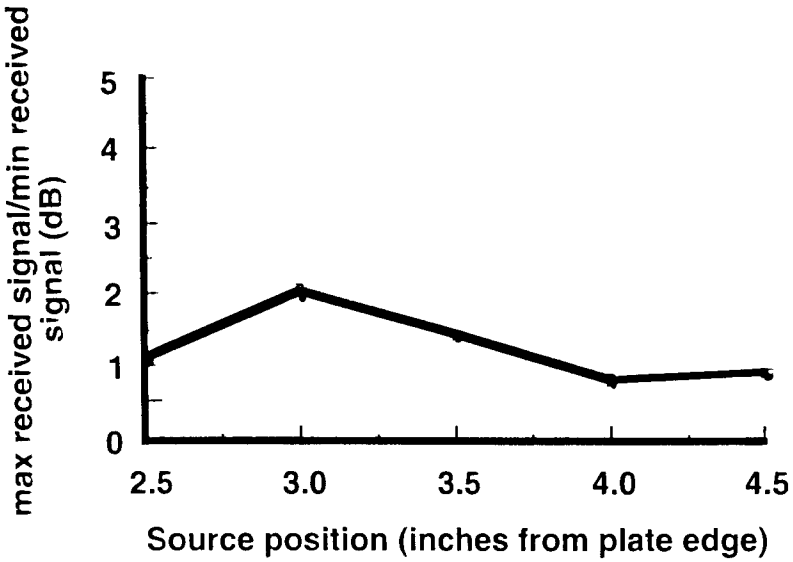

Fig. 4.17 Received signal ratios for different source/receiver separation distances.

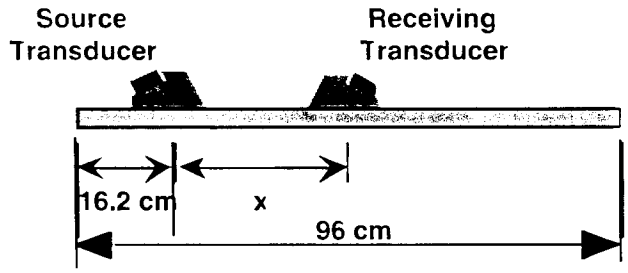

Fig. 4.18 Test setup for monitoring forward-travelling waves in free plate.

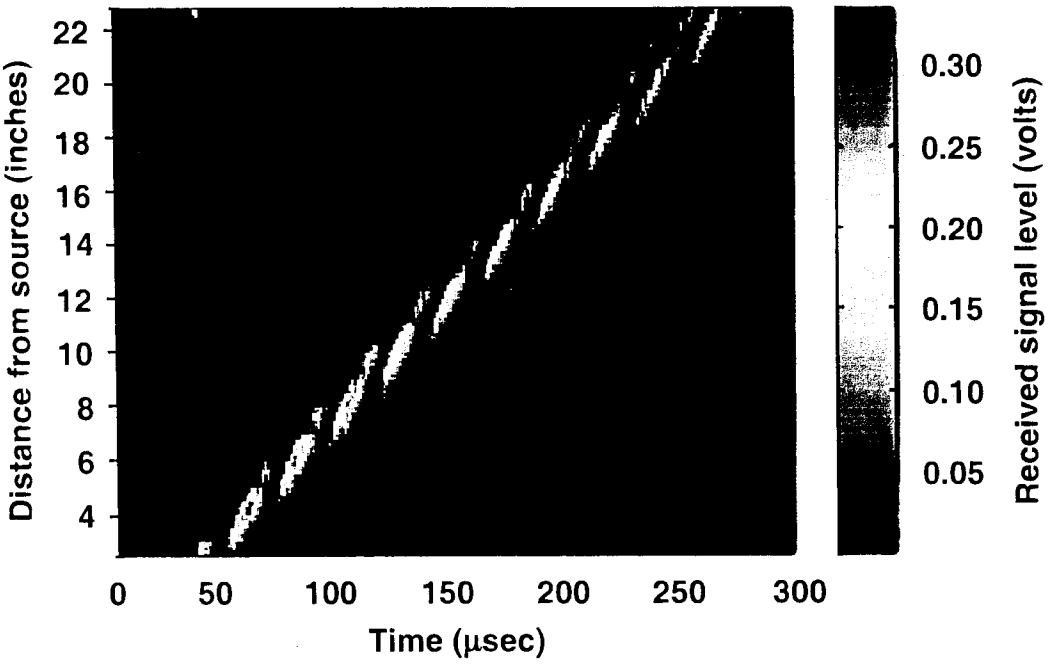

Fig. 4.19 Combined envelopes of received signals at several locations relative to a fixed source (forward-travelling waves).

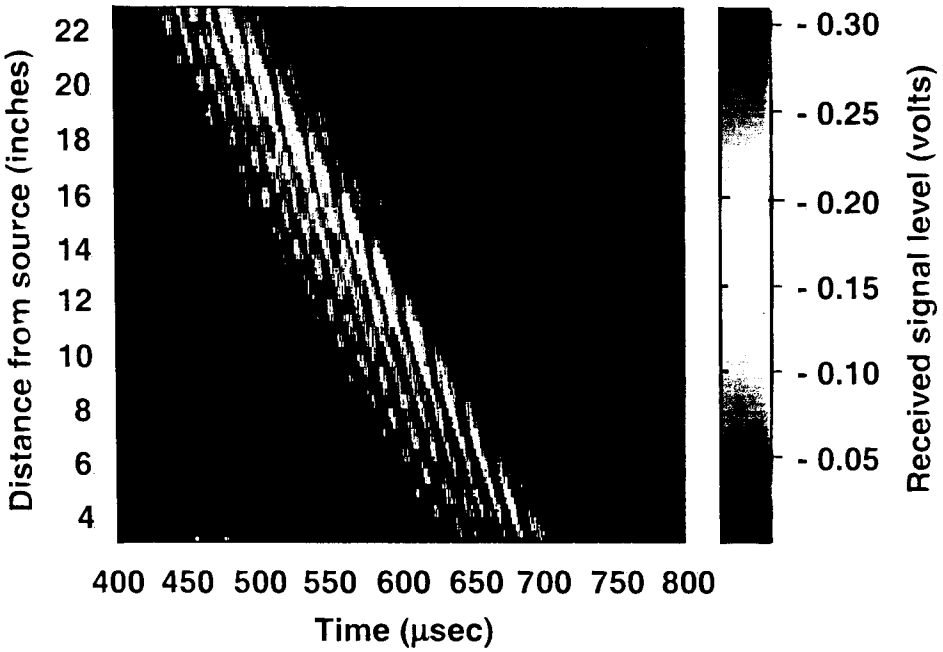

Fig. 4.20 Combined envelopes of received signals at several locations relative to a fixed source (backward-travelling reflected waves).

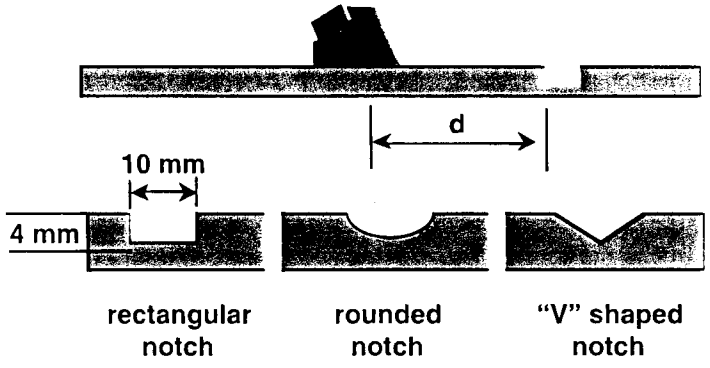

Fig. 4.21 Schematic of test setup for degradation shape study.

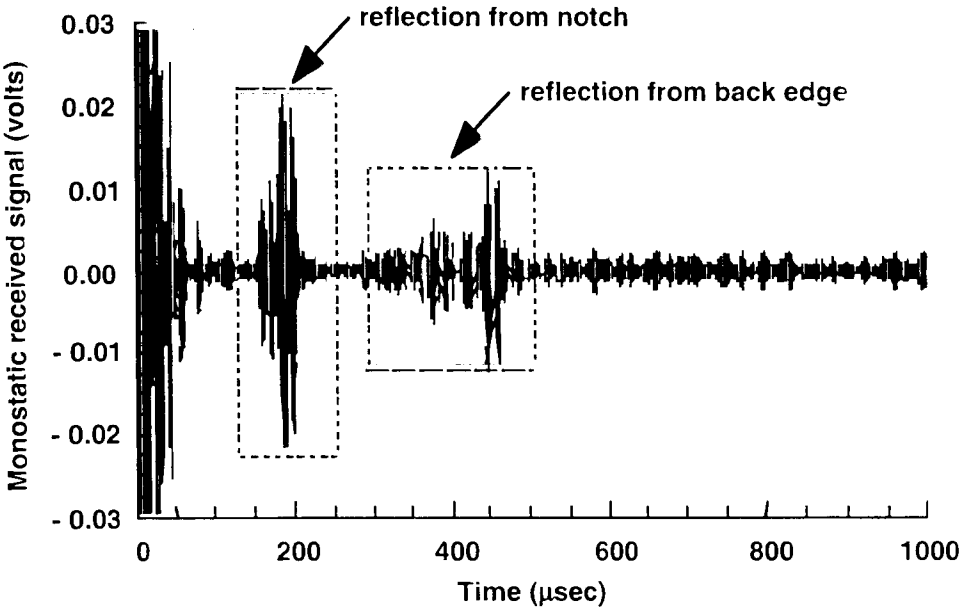

Fig. 4.22 Sample reflected return signal from rectangular notch.

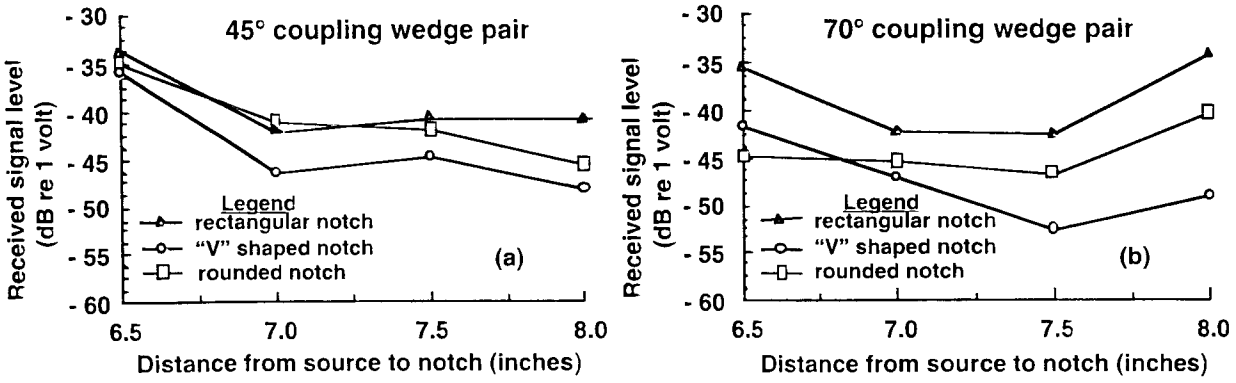

Fig. 4.23 Results of degradation shape study.

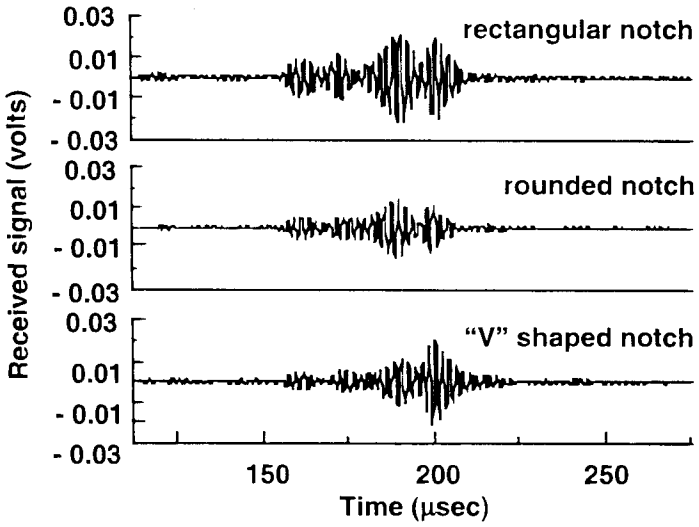

Fig. 4.24 Time-windowed returns from different notch geometries.

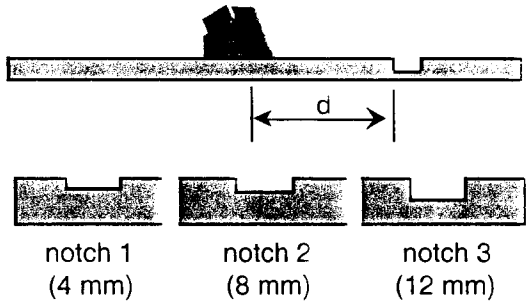

Fig. 4.25 Test setup for degradation depth study

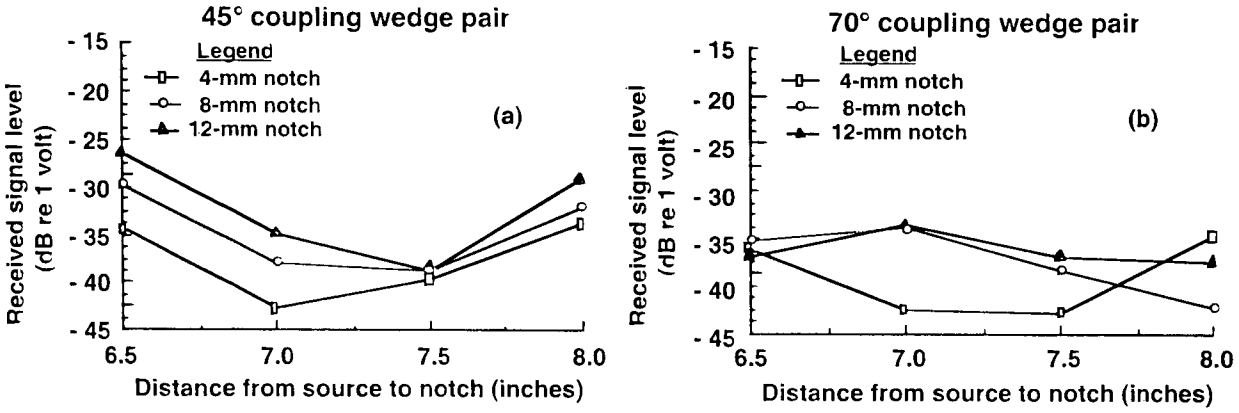

Fig. 4.26 Results of degradation depth study.

Fig. 4.27 Molds for embedding portions of steel plates in concrete.

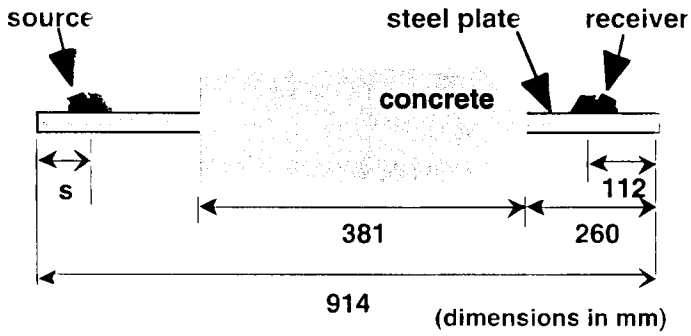

Fig. 4.28 Test setup for concrete effects tests.

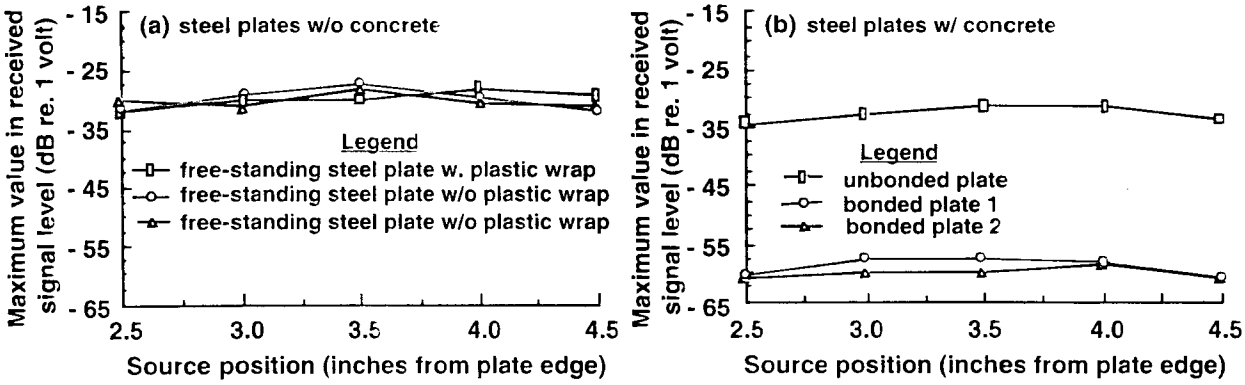

Fig. 4.29 Transmitted signal level: (a) free-standing steel plates and (b) steel plates embedded in concrete over part of their length.

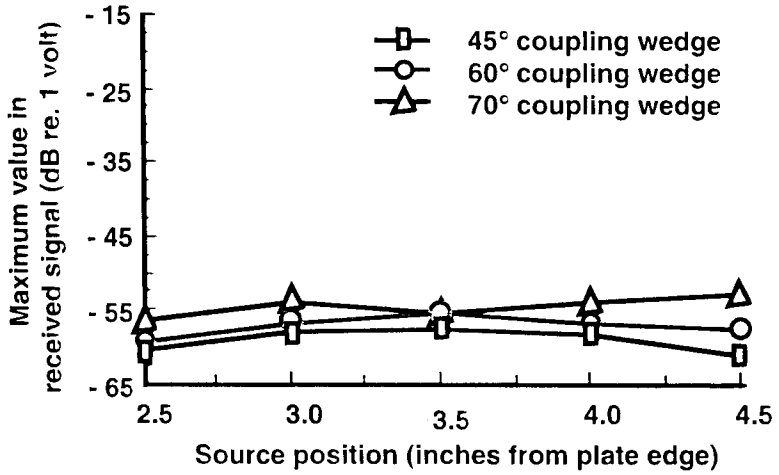

Fig. 4.30 Effect of coupling wedge angle on transmitted signal levels for a bonded steel plate embedded in concrete over part of its length.

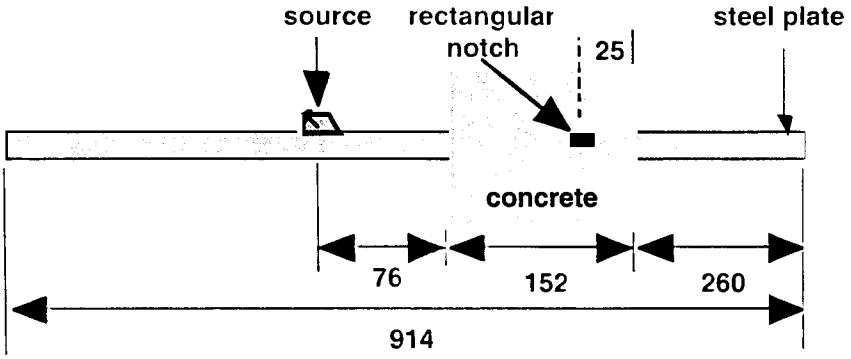

Fig. 4.31 Test setup for simulated field conditions to investigate role of competing signals.

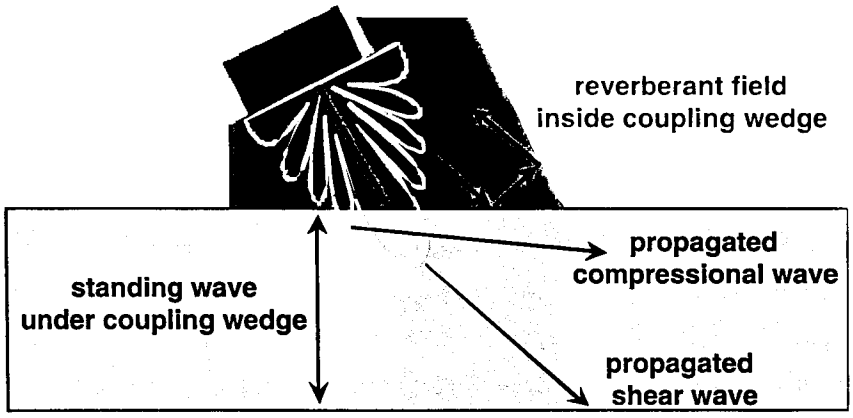

Fig. 4.32 Mechanisms of source "self noise."

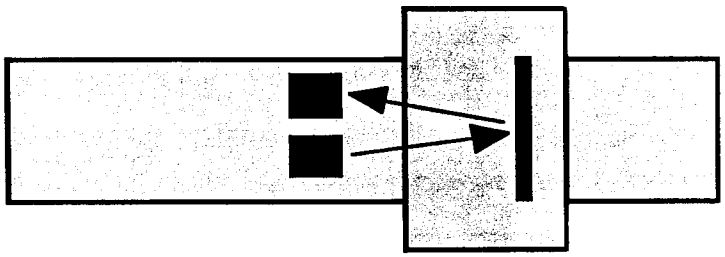

Fig. 4.33 Test setup for bistatic measurements to eliminate "self noise."

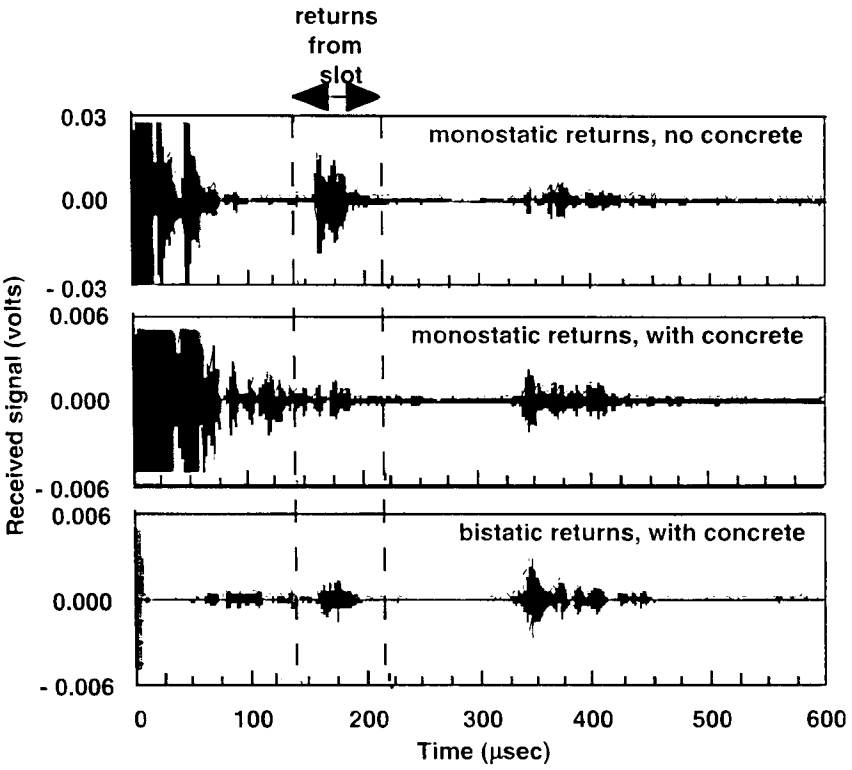

Fig. 4.34 Time histories of reflected signals from rectangular notch for three different conditions.

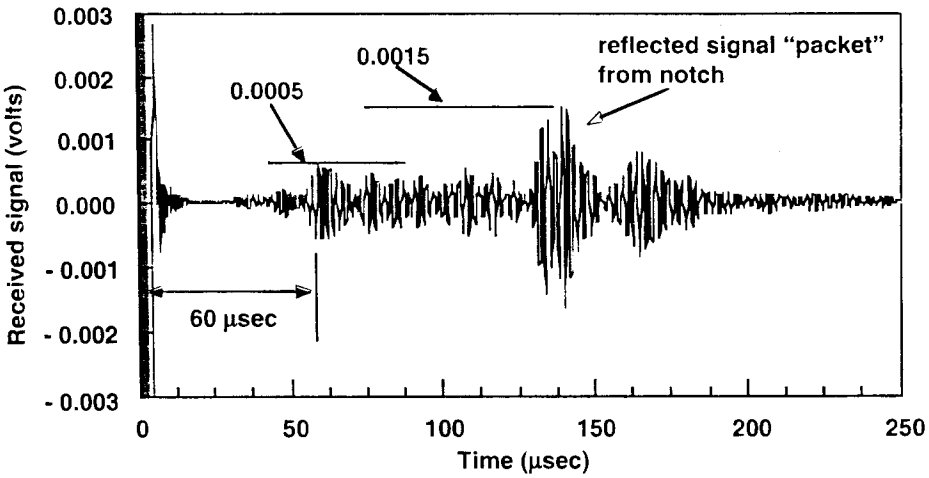

Fig. 4.35 Bistatic measured return from rectangular notch in a bonded steel plate embedded in concrete over part of its length.

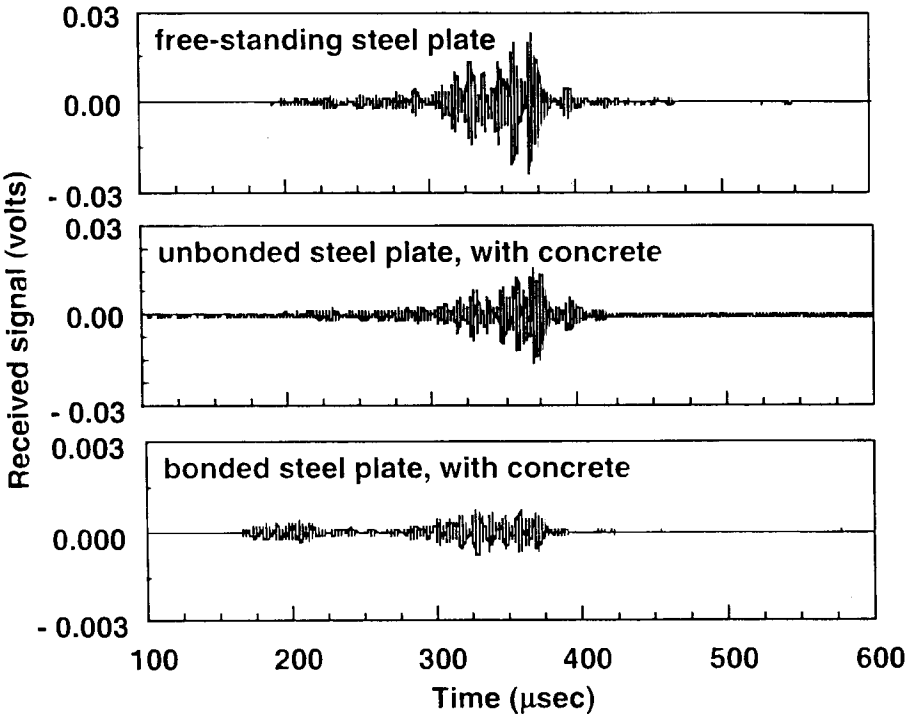

Fig. 4.36 Time histories of signals transmitted through free-standing steel plate, unbonded steel plate with concrete, and bonded steel plate with concrete.

Table 4.1. Material properties used in OASES models.

Material	Modulus E (GPa)	Shear Modulus G (GPa)	Density ρ (kg/m^3)	Comp. speed c_p (m/s)	Shear speed c_s (m/s)	Lamb speed c_r (m/s)	Loss Factor η	Poisson ratio ν
Steel	200	77	7850	5048	3132	2896	1xE-4	0.28
Concrete	24	9	2569	3056	1872	1747	2xE-2	0.34
Air			1.2	345			3.5xE-3	

Table 4.2 Piezoelectric sensor characteristics.

Frequencies	0.5, 1.0, 2.25, 3.5, 5.0 MHz
$Q = \Delta f/f_c$	0.6
Size	0.25", 0.5", 1.0" in diameter
Shear Angles in Steel	30, 45, 60, 70 degrees
Typical Cost	pulser/receiver - $7K, sensors - $400

Table 4.3 Measured spreading loss values.

Distance along plate, 45° coupling wedge (cm)	Distance along plate, 70° coupling wedge (cm)	Loss (dB)
10.5	13.9	11.4
20.6	27.4	13.0
30.8	40.9	15.4
41.0	54.4	17.8
51.1	67.9	19.5

5. MAGNETOSTRICTIVE SENSORS•

Magnetostrictive sensors (MsS) are devices that launch guided waves and detect elastic waves in ferromagnetic materials electromagnetically to determine the location and severity of a defect based on timing and signal amplitude. The magnetostrictive force refers to the force that acts in ferromagnetic materials due to strains associated with magnetic domain motion [5.1]. With MsS, the magnetostrictive force is produced directly in the part under inspection by setting the magnetic domains in the material into a vibrational motion by applying alternating magnetic fields to the material. For piping, the magnetic fields are applied by supplying an alternating electric current to the MsS coil that encircles the pipe. This magnetostrictive force generates the guided waves. Detection of the guided waves is achieved by the reverse process where the guided waves cause domains to vibrate and, consequently, cause the magnetic induction of the material to change with time. The changing magnetic induction induces an electric voltage in the MsS coil. The magnetostrictive force is independent of the sign of the applied magnetic field and is in the direction of the applied field. Therefore, in the absence of a static bias magnetic field, the alternating magnetic field results in generation of guided waves of twice the frequency of the applied magnetic field [5.2]. To produce the wave of the same frequency and to enhance the efficiency of the sensor (which is proportional to the magnetostriction coefficient), a static magnetic field is also applied to the material [5.3,5.4].

With MsS technology, elastic guided waves at sonic or ultrasonic frequencies are generated and propagated in the structure under inspection. The operating frequency of the MsS ranges from a few Hz to several hundred kHz. The sensor has a broad frequency response and it can be used over the entire operating range. It is applicable up to the Curie temperature of a material at which the material will lose its ferromagnetism. Waves reflected from defects (e.g., crack or section loss due to corrosion) are detected, typically by using the pulse-echo method. Occurrence time of a defect signal (from time of initial pulse) and the signal amplitude are then used to determine the severity and location (relative to the sensor position) of the defect. The technique is noncontact, couplant free, and requires minimum surface preparation. The sensor can be operated with a lift-off space of more that a few centimeters. In addition, the technique has a sensing or inspection range from a single sensor location that can exceed one hundred feet on bare metals, the sensor can detect defects on the inside and outside diameters of pipe surfaces, and by being an electromagnetic sensor, it can inspect structures whose surfaces are not directly accessible due to the presence of paint materials, it can also be made to work on nonferromagnetic metals, such as aluminum, and nonmetals such as composites or plastics, by providing a ferromagnetic material in areas where sensors are to be placed (e.g., by plating with a thin coat of ferromagnetic material such as nickel or bonding a ferromagnetic medium such as a wire or ribbon on the component surface). Its primary application has been to piping systems. Figure 5.1 presents a schematic diagram of a MsS used for generation and detection of guided waves in a pipe [5.3].

A preliminary study has been conducted by Southwest Research Institute (San Antonio, TX) to investigate the feasibility of applying magnetostrictive sensor technology to inspection of plate-type materials and to evaluate its potential for detecting and locating thickness reductions in a NPP containment metallic pressure boundary resulting from corrosion [5.5]. This study has involved both modeling and experimental studies. Also, preliminary MsS system requirements for NPP containment inspection have been developed.

• Material in this chapter was developed from information provided in a report [5.5] prepared under a subcontract with Southwest Research Institute, SanAntonio, Texas. Since completion of this study, a follow-on study was funded by the Electric Power Research Institute at Southwest Research Institute. Possible limitations of the MsS inspection technique caused by the presence of concrete were investigated in the laboratory by testing samples of a 1.22 m by 6.1 m by 6.4-mm-thick steel plate embedded in concrete. It was found that the concrete significantly increased the guided wave attenuation. In the A0 wave mode at relatively low frequency (e.g., below 25 KHz) relatively large defects could be detected at distances to a few feet. If the concrete was not bonded to the plate there were no measurable effects of the concrete on wave attenuation. More detailed results of this investigation are available in EPRI Report 1000105, "Experimental Validation of Concrete Effects on Guided Waves in Plates," published 19 December 2000. Since completion of the EPRI-funded study, the MsS technology has advanced significantly. For long-range plate inspection the technology now primarily uses shear horizontal (SH) waves because they provide better inspection results than Lamb waves (due to dispersion and extraneous wave mode generation). Also, a thin-strip-shaped MsS probe has been developed that can be permanently bonded to a structure's surface for active structural health monitoring of large structures (e.g., containment).

5.1 Numerical Modeling Studies

Dispersion properties of Lamb waves, which refer to longitudinal guided waves in plates, were investigated theoretically using a general-purpose software package called DISPERSE [5.6,5.7] (Imperial College, University of London). Using this software package, dispersion curves of Lamb waves in a plate were calculated for three different boundary conditions—free boundary, one side in contact with concrete, and both sides in contact with concrete. Table 5.1 presents the material property values used in the calculations [5.7]. In the modeling studies the plate was assumed to be 12.7 mm thick, and the concrete was assumed to be infinitely thick and perfectly bonded to the plate.

5.1.1 Analytical Results

Figure 5.2 presents calculated dispersion curves of longitudinal guided waves for a plate that is free, backed by concrete on one side, and backed by concrete on both sides. The vertical axis represents the group velocity of the wave expressed in units of mm/μsec, where 1 mm/μsec is equivalent to 10^5 cm/sec. The horizontal axis represents the product of the wave frequency and the plate thickness expressed in units of MHz-mm. The use of the frequency-thickness product in the horizontal axis normalizes the effects of plate thickness on the dispersion curves and makes the plots valid for plates of arbitrary thickness (e.g., the 1 MHz-mm point in the horizontal axis corresponds to 1 MHz of frequency in a 1-mm-thick plate, or 100 kHz of frequency in a 10-mm-thick plate). Curves indicated by S0, S1, and S2 are those for the first three symmetric (S) wave modes. Curves indicated by A0, A1, and A2 are those for the first three antisymmetric (A) wave modes. With respect to the median line of the plate thickness, the displacement of S wave modes has a symmetric distribution, whereas that of A wave modes has an antisymmetric distribution, as illustrated in Fig. 5.3.

For cases where the plate is backed on one or both sides by concrete, the DISPERSE program became somewhat unstable, so the calculation was performed for only S0, A0, and A1 modes. Comparing the plots in Fig. 5.2 for the three plate conditions, the minimum velocity of the S0 mode increased from approximately 1.8 mm/μsec in (a) to 2.05 mm/μsec in (b), and then to 2.4 mm/μsec in (c). Also, comparing the A0 mode velocities for the free plate and plates backed by concrete, there was only a slight decrease (i.e., no more than 0.3 mm/μsec) in the low-frequency range (i.e., below 1 MHz-mm). Overall, the effect of concrete on the group velocity appears to be relatively small.

In addition to dispersion curves, the DISPERSE program calculates wave attenuation. Results for a plate backed by concrete on one side and on both sides are shown in Figs. 5.4(a) and 5.4(b), respectively. It was assumed that the attenuation in the plate material was negligible and, thus, the free plate had zero wave attenuation. The attenuation plots in Fig. 5.4 therefore represent the energy loss into the surrounding concrete. In these plots, only A0 and S0 modes are shown. Attenuation of other modes was much higher and out of range of the plot. The plots show a large increase in attenuation when the concrete was placed on one side of a plate. As might be expected, the effect of concrete on attenuation increased by a factor of two or more when the concrete was placed on both sides of the plate. The plots also show that attenuation was significantly less for the A0 mode than for the S0 mode. Interestingly, the plots show negligible attenuation for the A0 mode when the frequency-thickness was less than about 0.55 MHz-mm. According to these results, the A0 mode would be better than the S0 mode for long-range inspection of plates backed by concrete on one or both sides. Particularly, if the frequency of the A0 mode is less than 0.55 MHz-mm no reduction in the inspection range due to concrete-induced attenuation is expected to occur (e.g., in a 12.7-mm-thick plate, this frequency corresponds to less than about 43 kHz).

The guided wave loses its energy into the surrounding concrete by generating both shear and compressional waves at the plate and concrete interface that propagate away in the concrete medium. The propagation angle, θ, of these waves is governed by Snell's law

$$\theta = \sin^{-1} (V_c / V_p) \qquad (5.1)$$

where V_c is the velocity of a bulk (shear or compressional) wave in the concrete, and V_p is the phase velocity of the guided wave in the plate. If V_p is less than V_c, then θ would be imaginary. This means that the bulk wave in the concrete cannot be generated, and consequently the energy of the guided wave would not be leaked away and there

would be no increase in guided-wave attenuation. Below 0.55 MHz-mm, the phase velocity of the A0 mode is smaller than the velocity of the shear (and compressional) wave in concrete. This explains why the attenuation of the A0 mode is negligible in that frequency region, even if the plate is backed by concrete on both sides.

5.1.2 Conclusions from Numerical Studies

The validity of the DISPERSE program calculations for simple geometries such as pipes and plates has been well confirmed experimentally. Although its validity for complicated geometries such as a plate backed by concrete on both sides has yet to be confirmed, it appears possible to achieve long-range inspection under this scenario using a low-frequency A0 wave mode.

5.2 Experimental Studies

For generation and detection of guided waves in plates, the MsS design shown schematically in Fig. 5.5 was used [5.8]. The probe consisted of a stack of U-shaped cores (e.g., made of ferrite) and a coil wound on the core. When an alternating electric current was supplied to the probe, an alternating magnetic field was applied to the plate underneath in the widthwise direction. The applied magnetic field generated guided waves in the plate that propagated in the same direction. Guided wave detection was achieved by the reverse process in which the alternating magnetic induction of the plate caused by the guided waves was electromagnetically coupled to the core material and a voltage signal induced in the coil. In addition to the MsS probe, a device was added (i.e., permanent magnets) to apply the required static bias magnetic field to the plate.

5.2.1 Experimental Setup and Procedures

The overall experimental setup is shown in Fig. 5.6 and Fig. 5.7 presents a photograph of the overall experimental arrangement. A carbon steel plate (ASTM A-36), approximately 6.35-mm-thick by 1.23-m-wide by 6.11-m long placed on two wooden supports, was used as the test article. Due to its weight, the plate arched somewhat toward the floor. The transmitting and receiving MsS probes were approximately 30 cm long and 2.5 cm wide. The length of the probe was aligned parallel to the width of the plate so that the wave was launched in the lengthwise direction of the plate. Static magnetic fields were applied in the lengthwise direction of the plate using permanent magnetic circuits. Excitation and detection of guided waves were accomplished using an instrument called the "magnetostrictive sensor reflectometer (MsSR)," that had been developed by SwRI for piping inspections.

Initial activities addressed the capability of the MsS to generate and detect guided waves. Both the pitch-catch and pulse-echo techniques were employed for data acquisition. For the pitch-catch technique, the transmitting MsS probe was placed near one end of the plate and the receiving probe near the mid-length location of the plate. For the pulse-echo technique, both probes were placed near one end of the plates (Fig. 5.6). After investigating guided-wave generation and detection capability using the pitch-catch technique, the feasibility of detecting defects in the plate was investigated using the pulse-echo technique. For this purpose, a notch was machined into the plate at a position corresponding to approximately 2/3 the plate length (Fig. 5.6). The notch was approximately 3-mm deep by 6-mm wide, and had a length that was changed from 10 to 30 cm in 10–cm increments to evaluate the relationship between notch length and signal amplitude. A photograph of the 30-cm-long notch is shown in Fig. 5.8.

5.2.2 Experimental Results

As noted, the experimental studies addressed the generation and detection of guided-waves in plates, and the capability to detect defects in a plate.

5.2.2.1 Guided Wave Generation and Detection

An example of data obtained from the plate sample using the pitch-catch technique is shown in Fig. 5.9. The data were taken with the transmitting and receiving probes placed at approximately 5 cm and 2.73 meters from one end of the plate, respectively. The transmitting probe was excited with a 3-cycle-long, 60 kHz sinusoidal pulse. The detected signals after the initial pulse were relatively complex. To identify each of the detected signals by observing their dispersion characteristics [5.9], the short-time Fourier transform (STFT) was performed on the time-amplitude data in Fig. 5.9, and the results are presented in Fig. 5.10. In this figure. the logarithms of the absolute

values of the STFT are shown as gray-scale images (the brighter the image the larger the amplitude of the spectral component). The time evolution of each frequency component comprising the detected signals can be observed and used to study wave dispersion [5.9].

From the data in Fig. 5.10, the highest frequency component contained in the signals in Fig. 5.9 was no more than about 120 kHz. Referring to the dispersion curves for a free plate given in Fig. 5.2(a), the above frequency corresponds to about the 0.76 MHz-mm point in the frequency-thickness axis. Over that frequency range, there are only two possible longitudinal guided waves—the lowest order symmetric wave mode (S0) and the lowest order antisymmetric wave mode (A0). According to the dispersion curves in Fig. 5.2(a), the group velocity of the S0 mode over that frequency range is approximately constant (e.g., 5.44 x 10^5 cm/sec at 20 kHz, 5.42 x 10^5 cm/sec at 60 kHz, and 5.38 x 10^5 cm/sec at 100 kHz), whereas that of the A0 mode increases rapidly with frequency (e.g., 1.98 x 10^5 cm/sec at 20 kHz, 2.81 x 10^5 cm/sec at 60 kHz, and 3.10 x 10^5 cm/sec at 100 kHz).

Based on the expected behavior of the S0 and A0 modes, the curved lines in Fig. 5.10 are easily identified as the A0 mode. They are curved to the right because the lower frequency components have a slower group velocity and thus arrive at the receiving MsS probe later in time than the higher frequency components. The second signal after the initial pulse in Fig. 5.9 is then identified as the A0 mode that was detected when the wave reached the receiving probe while traveling toward the far end of the plate. The subsequent A0 mode signals are those that were detected after the wave was reflected from the far end of the plate sample and was traveling back and forth between the two ends. The pulse length of the A0 mode signals gets longer with time because of the dispersion. Using the first and third A0 mode signals in Fig. 5.10, the round-trip time of the wave was measured at 6.150 msec at 20 kHz and 4.305 msec at 60 kHz. The corresponding group velocities are then 1.99 x 10^5 cm/sec at 20 kHz and 2.84 x 10^5 cm/sec at 60 kHz, respectively, which agree well with the calculated values given earlier. The straight lines in Fig. 5.10 are identified as those produced by the S0 mode. The lines are straight because the S0 mode has an approximately constant velocity and thus is nearly dispersionless over the frequency range investigated. The signal after the initial pulse in Fig. 5.9 was identified as the S0 mode, detected when the wave reached the receiving probe while traveling toward the far end of the plate. Excluding those identified as A0 signals, all subsequent signals in Fig. 5.9 should therefore be S0 mode signals.

Unlike the A0 mode signals, however, there were more S0 mode signals than the number that would be normally expected when the wave travels back and forth between the two ends of the plate sample. Based on the calculated group velocity of the S0 mode and the position of the receiving MsS probe, the signals that occur at normally expected arrival times are identified and indicated as S0 in both Figs. 5.9 and 5.10. The other signals that occur at abnormal arrival times were unexpected. These signals first appeared after approximately 0.31 msec from the second normal S0 signal (that was detected while the wave was traveling back after reflection from the far end of the plate sample). With increasing traveling time, the occurrence of the abnormal signals became more frequent. They also occurred at a regular interval of approximately 0.31 msec.

An investigation of the possible cause of the abnormal S0 signals led to the following conclusions: (1) the phenomenon is exactly analogous to the generation of multiple secondary echoes that trail the backwall echo with a regular interval when an ultrasonic beam is propagated along the length of a narrow test piece [5.10], and (2) it is a result of mode conversion at the lateral boundaries of the plate sample. Figure 5.11 illustrates the mechanism that produced the abnormal S0 signals. Assume that the longitudinal (L) wave generated by the MsS probe is propagated in the lengthwise direction of a finite size (a x d) plate. Since the probe is finite in length, the L wave beam spreads laterally as it propagates along the lengthwise direction of the plate. Some of the wave on the outskirts of the beam will eventually hit the lateral boundary of the plate at an angle θ_L. A portion of the L wave is then mode-converted to a shear-horizontal (SH) wave [5.1] and travels across the width of the plate at an angle θ_{SH} following Snell's law:

$$\sin \theta_{SH} / \sin \theta_L = V_{SH} / V_L \qquad (5.2)$$

where V_{SH} and V_L are the phase velocity of the SH and the L wave mode, respectively. When the SH wave arrives at the other side of the plate, a portion of it converts back to the L wave mode while the remaining portion of the wave is reflected back toward the other side of the plate. The portion of the beam that has gone through this mode-conversion process arrives at the probe later than the other portion of the beam that has traveled to the other end of

the plate and returned without going through the mode conversion. In the case of grazing incidence, where θ_L is approximately equal to 90°, the time separation Δt between the two is given approximately as [5.10],

$$\Delta t = d\sqrt{\left(\left(\frac{V_L}{V_{SH}}\right)^2 - 1\right)} \Big/ v_L \qquad (5.3)$$

where v_l is the group velocity of the L wave mode. For V_{SH} = 3.26 x 10^5 cm/sec, V_L = 5.43 x 10^5 cm/sec, and v_l = 5.42 x 10^5 cm/sec for the S0 wave at 60 kHz, and d = 1.23 m for the plate sample, Δt = 0.30 msec, which compares well with approximately 0.31 msec separation observed experimentally. A portion of the SH wave that is reflected back toward the other side of the plate is again mode-converted to the L wave and returns to the probe. Since this wave has traversed the plate width twice, its arrival time is delayed by another Δt. By repeating the process, a series of abnormal signals is thus produced.

Presently, little theoretical work is available in the literature on the beam pattern of a guided wave in a plate. However, it is not unreasonable to assume that the beam pattern of the guided wave would be very similar to that of an ultrasonic wave for which extensive work is available in the literature. Therefore, following the formula for the beam divergence of a rectangular sound radiator in a free field [5.11], the angle of beam divergence, γ, of a guided-wave probe of length D shown in Fig. 5.12 can be expressed as:

$$\sin \gamma_{-3} = 0.44\ \lambda/D \qquad (5.4)$$

$$\sin \gamma_{-10} = 0.74\ \lambda/D \qquad (5.5)$$

where γ_{-3} and γ_{-10} are the angle of divergence at -3 and -10 dB lines of the beam relative to the amplitude along the z-axis, respectively, and λ is the wavelength of the guided wave (here λ is equal to the phase velocity divided by the frequency). The calculated angles of beam divergence of the S0 and A0 mode waves for the 30-cm-long MsS probe used in this study are given in Table 5.2.

The beam divergence angles in Table 5.2 are those in the free field; that is, the sound field of the outgoing beam. In the pulse-echo technique, generation and detection of the wave are achieved using the probes placed at one location. In this case, the sound field of a reflector (which is called the echo field) is of interest because the divergence of the reflected beam influences the detected signal amplitude. The angles for γ_{-3} and γ_{-10} in the free field are equivalent to those for γ_{-6} and γ_{-20} in the echo field, respectively.

The plate sample used in this study was 1.23 meters wide and 6.11 meters long. When the beam of 60-kHz S0 mode wave generated by the MsS probe reaches the far end of the plate, the width of the beam at -3 and -10 dB lines becomes, respectively, 2 x 6.11 x tan 7.7° = 1.65 meters and 2 x 6.11 x tan 13.1° = 2.84 meters. The beam widths are larger than the width of the plate sample. This diverging beam leads to the phenomenon of secondary signal generation via mode conversion at the lateral boundaries of the sample. In the preceding discussion on the Δt, the calculated and experimental values showed a small discrepancy (0.30 msec versus 0.31 msec). This discrepancy is an error concerning the calculated values since it assumed grazing incident angle whereas the actual incident angle of the beam can be significantly smaller than 90°.

The generation of abnormal secondary signals occurs only for the S0 wave mode and not for the A0 mode. This is because the phase velocity of the A0 mode is smaller than that of the SH mode (e.g., 1.08 x 10^5 cm/sec at 20 kHz, 1.72 x 10^5 cm/sec at 60 kHz, and 2.07 x 10^5 cm/sec at 100 kHz as determined using the DISPERSE program); consequently, the conversion which must satisfy Snell's law, can not take place.

In summary, the data in Fig. 5.9 show that both the S0 and the A0 wave modes can be generated and detected using the MsS probe. Since the first A0 signal is larger in amplitude than the first S0 signal, the probe design used in this experiment appears to be more effective in generating the A0 wave mode than the S0 wave mode. The tendency of the probe to simultaneously produce both modes is not a significant concern because the

primary wave mode generated and detected can be controlled by applying a phased-array principle using multiple probes.

5.2.2.2 Defect Detection

Before inducing a notch in the plate sample, data were acquired from one end of the test article using the pulse-echo technique while controlling the MsS probes to generate and detect either the S0 or the A0 wave mode. Mode control was achieved using a total of three MsS probes (one for transmitting and two for differential receiving) whose relative positions from each other and from the probe end of the plate sample were adjusted to maximize the signal amplitudes of the desired wave mode. Figure 5.13 presents the resulting data for the S0 mode and the A0 mode waves. The data in Fig. 5.13(a) were obtained by exciting the transmitting MsS probe with a 5–cycle, 40-kHz sinusoidal pulse. The data in Fig. 5.13(b), on the other hand, were obtained by exciting the transmitting MsS probe with a 2-cycle, 20-kHz sinusoidal pulse. The S0 mode data in Fig. 5.13(a) show the secondary signals after each end-reflected signal. These secondary signals, produced by mode conversion at the lateral boundaries of the plate sample together with the unsuppressed A0 mode signals, make the signal pattern complicated. For long-range inspection of a large welded-plate structure (e.g., NPP concrete containment liner) using the S0 mode wave, secondary signals produced from the welds may interfere with defect detection. Because of the mode-converted secondary signals and the presence of unsuppressed A0 mode signals, the attenuation of the S0 mode wave in the plate material is difficult to determine from the data in Fig. 5.13(a). However, the apparent wave attenuation (which includes the loss due to beam divergence) may be determined by using the amplitudes of the first arriving signals of the end-reflected signals. The first arriving signals represent the waves that traveled along the straight path normal to the MsS probe. Secondary signals represent the waves that diverged from the straight path and, thus would be lost. Using the amplitudes of the first arriving signal of the first and second end-reflected signals, the apparent attenuation is determined to be approximately 0.33 dB/m.

The A0 mode data in Fig. 5.13(b), unlike the data in Fig. 5.13(a), show a relatively simple signal pattern. The data also exhibit low-amplitude S0 mode signals that were not completely suppressed. The unsuppressed S0 mode signals form most of the background noise signals. Due to the dispersion of the A0 mode, the pulse length of the A0 signals is elongated with time and it is interesting to observe that the second end-reflected signal is larger in amplitude than the first signal. The same behavior is also observed with the A0 mode signals in Fig. 5.13(a). The cause of this erratic behavior is presently uncertain. Using the first and the third end-reflected signals, the attenuation coefficient of the 20-kHz A0 wave was determined to be approximately 0.086 dB/m.

Operating the MsS probes to generate and detect one of the S0 and A0 mode waves, data were acquired after inducing a 10-cm-long notch at 4.06 meters from the probe end of the plate. This process was then repeated after increasing the notch length to 20 and then to 30 cm. Notch depth was kept at approximately 50 percent of the plate thickness. Results are shown in Figs. 5.14 and 5.15 for the 40-kHz S0 mode wave and the 20-kHz A0 mode wave, respectively. In both cases, the signals from all three notches were observable, indicating that long-range guided-wave inspection of plates using the MsS technique is feasible. Figure 5.16 presents plots of defect signal amplitude versus the notch length. As in the case of guided-wave inspection of piping [5.12], the amplitudes of the defect signals increase approximately linearly with notch length, also indicating the feasibility of determining the severity of a defect from the defect signal. The amplitude of a signal from a reflector, such as a notch or corrosion, is proportional to the cross-sectional area of the defect (in the plane normal to the guided wave beam propagation) relative to the total beam width of the interrogating guided wave. Therefore, the product of both length and depth of a defect influences the defect signal amplitude. Consequently, separate determination of both length and depth of a defect from a single data trace is not generally feasible. However, since the relative area of a given-size defect to the total beam width of the guided wave will vary with the mode and frequency of the guided wave employed for inspection, the signal amplitude from the same defect will also vary. The marked difference in the amplitude of the 30-cm-long notch relative to the end-reflected signal amplitude in Figs 5.14 and 5.15, for example, confirms the variation of the defect signal with the guided wave mode and frequency used for detection (in this case, 40-kHz S0 mode and 20-kHz A0 mode). Taking advantage of this variation, it appears feasible to separately determine both the depth and the length of a defect by combining two or more sets of data taken using different guided wave modes and frequency.

Assuming that the signal-to-noise ratio required for detection is 6 dB and that the defect signal amplitude is linearly proportional to the notch length, the minimum detectable length of a 50-percent wall notch can be estimated

using the data in Fig. 5.16 and a simple linear interpolation. For example, assume that the defect is located approximately 4 meters from the MsS probe, as in the test setup used in this investigation. In order for a defect to be detectable, its signal amplitude is required to be at least twice (i.e., 6 dB) that of the background noise level. Based on the background noise level and the notch signal amplitude plots in Fig. 5.16, the minimum detectable length of a 50 percent through-wall notch is estimated to be about 10 cm for the 40-kHz S0 wave and about 1.5 cm for the 20-kHz A0 wave. If the defect is located at a distance of 15 meters from the MsS probe, the defect signal amplitude would be further reduced by the wave attenuation over that distance, which is equal to 0.33 dB/m x 2 x 15 m = 10 dB for the 40-kHz S0 wave and 0.086 dB/m x 2 x 15 m = 2.58 dB for the 20-kHz A0 wave. The minimum detectable notch length at the 15-meter distance is then about 44 cm for the 40-kHz S0 wave and about 1.8 cm for the 20-kHz A0 wave. Although the data in Fig. 5.16 show that the A0 wave is much better than the S0 mode for defect detection, this may not be true since the background noise level can be reduced, particularly for the S0 mode, by improving the MsS probe. For the same cross-sectional area of defect, the signal amplitude from a corrosion pit is generally equal to or larger than the signal amplitude from a notch [5.12]. Therefore, the results obtained with the 20-kHz A0 wave suggest that a 50-percent through-wall 1.8-cm-diameter corrosion pit located within a 15-meter distance could be detectable using the MsS technique.

Referring to the 40-kHz S0 wave data in Fig. 5.14, there was also a secondary notch signal that was produced by mode conversion at the lateral boundaries of the plate sample. The presence of the notch did not seem to affect the end-reflected signal significantly; but it produced a noticeable reduction in the amplitude of the secondary end-reflected signals, indicating that the notch reflects a substantial portion of the mode-converted SH wave while the wave traverses the plate.

The effect of the notch on the end-reflected signal of the 20-kHz A0 wave data in Fig. 5.15 is dramatic as its peak-to-peak amplitude is reduced from approximately 0.27 volts with a 10-cm-long notch to 0.12 volts with a 30-cm-long notch. The influence of the notch on the end-reflected signal is understandable since the beam divergence angle of the A0 mode is relatively small. Therefore, when a notch becomes significantly long relative to the width of the outgoing beam, a significant portion of the outgoing beam is reflected from the notch, which substantially reduces the amount of beam reaching the far end of the plate.

5.2.2.3 Conclusions from Experimental Studies

Results indicate that (1) guided waves have potential for performing global, long-range inspections of plates and plate-like structures such as the metallic pressure boundary of NPP containments, and (2) guided waves are expected to work well for inspection of plates backed by concrete on either one or both sides. For a given MsS probe size, the beam-divergence angle is significantly smaller for the A0 mode wave than the S0 mode wave. Because of the smaller beam divergence and associated benefits such as a higher spatial resolution, a smaller energy loss through beam spreading and less probability of extraneous signal generation from interaction with welded boundaries, the A0 mode wave would be better for use in plate inspection than the S0 mode wave. One disadvantage of good beam collimation of the A0 mode is that a large defect can shadow the area behind it and, as a result, may create a blind spot.

5.3 MsS System and Time Requirements for Containment Inspection

Figure 5.17 presents a conceptual drawing of how a MsS system may be deployed for liner inspection. The MsS instrument, scanner-control box, and portable computer are set up on a cart. The scanner, which contains the MsS probes, is attached on the liner wall. The probe and scanner are connected to the instruments via a relatively long (15 to 30 meters) cable. At a given scan position, the wave is launched in one direction (e.g., upward in the figure) and the resulting data are acquired. The wave is then launched in the opposite direction (e.g., downward in the figure) and the data are acquired. This achieves inspection of both sides of the scanner up to the respective inspection range. The scanner is then moved to the next scan position and measurements repeated. The scan interval will be dependent on the size of the beam produced by the probe. In this manner, inspection of a large area of the liner, including areas backed on both sides by concrete (i.e., embedded), can be achieved cost-effectively.

The existing MsS system developed for pipe inspection consists of three main components: (1) MsS instrument containing transmitter and receiver electronics, (2) field-portable computer for data acquisition and analyses, and (3) MsS probes for pipe inspection including devices for providing a static bias magnetic field. In

order to implement the MsS technique for practical inspection of the containment metallic pressure boundary, the MsS system requires additional development in the following three areas: (1) MsS probes, (2) probe scanner, and (3) data acquisition and analysis system with custom software for examination control and data analysis. The present MsS instrument that contains transmitter and receiver electronics is suitable for plate inspection except for possible minor modifications.

The probe is the key to successful system performance. The preliminary probe design used in this feasibility study demonstrated the ability to launch and detect guided waves in a relatively thin (6.35-mm) steel plate. For practical implementation, additional work on the probe design is required in several areas:

- Applicability to a range of plate thickness since the containment pressure boundary thickness can range from about 6.35 mm (liner of reinforced concrete containment) to greater than 25.4 mm (steel containment vessel).

- Multiple probe design for control of wave directionality and wave mode. This is necessary to simplify signal pattern and subsequent data analyses.

- Device for providing static bias magnetic field necessary for MsS probe operation. A tradeoff study is required between the permanent magnet-based device and the electromagnet-based device considering the relative merits and demerits of each, such as handling ease, electric power requirement, weight, size, and cost.

Automated movement of the MsS probes along the containment wall surface will be needed for high examination productivity. A magnetically held wall crawler that can support the MsS probes and provide a static bias magnetic field required for MsS operation is envisioned. The magnetic wall crawler approach could conceivably serve the dual purpose of supporting the crawler on the wall as well as static magnetic field generation for the probes. An automated crawler will also increase inspection coverage due to its ability for remote guidance into small annuli between the wall and objects positioned near the wall, where manual repositioning of a probe carriage assembly would be precluded. Integrated control of the scanner can be accomplished by commercial single- or dual-axis motor control instrumentation in communication with the MsS system computer. In a typical examination, the scanner would be manually driven or positioned to a reference location. During data acquisition, it would step to each successive location along a linear path (horizontal or vertical), stopping at each step location to acquire data. Step increments of 30 cm are currently anticipated. Functional requirements of the scanner include the following:

- Ability to attach to and crawl on the vertical wall surface of containment wall while carrying the MsS probes and cables.

- Ability to progress in the forward or reverse direction along a single linear axis of motion as a minimum, with the ability to redirect to an orthogonal direction desirable.

- Ability to track its position relative to a reference point. The device should tolerate typical wall surface roughness or small step discontinuities without stalling.

- Ability to easily change MsS probes for increased productivity. The device, including attached cables and connectors, should also be designed for easy radioactive decontamination.

MsS data acquisition involves: (1) a pulsed excitation of the transmitting MsS probes to launch guided waves into the containment metallic pressure boundary; (2) detection of signals reflected from defects or geometric discontinuities such as welds and metallic attachments (e.g., studs, angles, or I-sections) in the receiving MsS probes; and (3) digitization of the detected signals, data processing and analysis, and data filing and storage. The existing MsS instrument developed for pipe inspection can perform steps (1) and (2) for plate inspection. Step (3) is performed in the rugged field-portable computer, and the majority of the system hardware and operating software is directly applicable for plate inspection. However, since plate inspection requires different inspection procedures and different manner of data presentation and analysis, some of the system software will need to be tailored to plate inspection. Additional developments needed in the system software for plate inspection include:

- The ability to control scanner motion both automatically and manually, retrieve scanner positional coordinates, and provide graphical displays of the data for analysis, as well as archival and hardcopy of all data and displays.

- Data analysis procedures for identification of anomalies and their locations as well as for differentiation of defects from geometric features such as welds and other attachments.

Since NPP containments vary in size and physical makeup, and numerous obstacles within the containment may prevent or delay access to the containment metallic pressure boundary when performing an inspection, it is difficult to determine inspection time accurately. Therefore, a more idealized estimate will be given based on the assumption of a horizontal linear scan. Additional assumptions include no obstacles in the scan path requiring avoidance or manual repositioning, and a maximum scan distance of 15 meters without instrumentation relocation. As indicated earlier, MsS data are acquired at each step increment along the scan axis. The step size is currently estimated at 30 cm. The coverage area for the guided waves will approximate a rectangular area extending above and below the scan axis up to a distance of at least 15 meters for a steel containment in a region that is not backed by concrete. The time to step to the next scan axis position and stop to acquire and average waveforms successively in both vertical directions is estimated at less than 4 minutes. This is based on the assumption that the pulse repetition rate is 10 and that 1000 waveforms are averaged for each of two directions plus position increment time. Therefore, actual scanning time for 15 meters of linear scan is 200 minutes (3.3 hours). Initial equipment setup time should be no more than 30 minutes, yielding a total time of less than 4 hours for a total coverage area of 450 m^2.

Previous information indicated that the concrete backing on the containment metallic pressure boundary would not increase wave attenuation significantly for the low-frequency A0 mode. This suggests that when a low-frequency A0 mode wave is used for inspection, the coverage area per unit time would not be significantly reduced, even if the portion of the containment metal pressure boundary backed on both sides by concrete is included in the inspection. For inspection of only the portion of the pressure boundary backed on both sides by concrete, data acquisition is needed in only one direction, thus reducing the scanning time by one-half. Opportunities to further decrease inspection time include being able to operate at higher pulse repetition rates and not requiring as much waveform averaging. Without actual experience of MsS inspection of a containment metallic pressure boundary backed by concrete, conservative estimates for these parameters were used. In each of these cases, the time required for data analysis was excluded since it is highly dependent on the average number of indications present and the quality of the data. There is currently no experience on which to base an estimate. Also, data analysis could be performed simultaneously with data acquisition, providing a second computer is available for running the analysis software. As data become available from a scan, they could easily be transferred via a communication linkage for real-time analysis to a separate location that does not need to be located in containment.

5.4 Conclusions and Recommendations

Several conclusions can be derived from this investigation:

- Although analytical and experimental studies were limited, guided waves appear to be capable of performing global, long-range inspections of plate-type structures, including areas that are difficult to access because of the presence of other equipment or attachments. Results of a limited experimental study confirm the capability of the MsS technique to generate and detect guided waves in plates and to detect a defect over a long range.

- Numerical modeling suggests that a low-frequency A0 mode wave (below approximately 0.5 MHz-mm, which corresponds to approximately 40 kHz in a 12.7-mm-thick plate or 20 kHz in a 25.4-mm-thick plate) is best suited for inspection of NPP metallic containment boundaries that are backed on either one or both sides by concrete. At other frequencies or modes, such as S0, the presence of concrete produces increased wave attenuation resulting in a significantly reduced inspection range.

- Since the MsS system has been developed to the point of commercial service for long-range inspection of piping in plants such as refineries, adaptation of the existing MsS system to NPP containment metallic pressure boundary inspection is expected to be straightforward.

The following work is recommended to systematically achieve the development and field implementation of a MsS system for inspection of NPP containment metallic pressure boundaries:

- Experimental validation of the capability to inspect plates backed on either one or both sides by concrete.
- Laboratory performance testing of the MsS probes and the existing MsS instrument to evaluate the capability of controlling wave direction and wave mode, operable plate thickness range, defect detectability, and inspection range.
- Develop a probe scanner, including scanner carriage and motion control.
- Develop MsS system software for data acquisition and analysis.
- Integration of the MsS system tailored for inspection of containment pressure boundaries through testing of a "mock-up" of a containment metallic pressure boundary.
- Field evaluation of the integrated MsS system.
- System refinement and commercialization.

5.5 References

5.1 C. Kittel, "Physical Theory of Ferromagnetic Domains," *Rev. Modern Phys* 21, 1949.

5.2 J. Krautkramer and H. Krautkramer, *Ultrasonic Testing of Materials*, Chapter 8, 4th Ed., Springer Verlag, New York, New York, 1990.

5.3 H. Kwun and K.A. Bartels, "Magnetostrictive Sensor Technology and Its Applications," *Ultrasonics* 36, pp. 171–178, 1998.

5.4 R.C. Williams, "Theory of Magnetostrictive Delay Lines for Pulse and Continuous Wave Transmission," *IEEE Trans. on Ultrasonics Engineering* UE-7, pp. 16–38, New York, New York, 1959.

5.5 H. Kwun, *Feasibility of Magnetostrictive Sensor Inspection of Containments*, NUREG/CR-5724 (ORNL/SUB/98-SZ272V), U. S. Nuclear Regulatory Commission, Washington, D. C., March 1999.

5.6 B. Pavlakovic, M. Lowe, D. Alleyne, and P. Cawley, "Disperse: A General-Purpose Program for Creating Dispersion Curves," *Review of Progress in Quantitative Nondestructive Evaluation*16, (Edited by D. O. Thompson and D. E. Chimenti), Plenum Press, New York, New York, pp. 185–192, 1997.

5.7 B. Pavlakovic and M. Lowe, *DISPERSE User's Manual*, Version 1.0, University of London, England,1997.

5.8 *Development of Magnetostrictive Sensor for Plate Inspection,* Southwest Research Institute Project 17-9077, Southwest Research Institute, San Antonio, Texas, 1999.

5.9 H. Kwun and K. A. Bartels, "Experimental Observation of Elastic-Wave Dispersion in Bounded Solids of Various Configurations," *J. Acoust. Soc. Am.* 99, pp. 962–96, 1996.

5.10 J. Krautkramer and H. Krautkramer, *Ultrasonic Testing of Materials*, Chapter 16, Section 2, 4th Ed., Springer Verlag, New York, New York, 1990.

5.11 J. Krautkramer and H. Krautkramer *Ultrasonic Testing of Materials*, Chapter 4, Section 5, 4th Ed., Springer Verlag, New York, New York, 1990.

5.12 H. Kwun and C. Dynes, "Long-Range Guided-Wave Inspection of Pipe Using the Magnetostrictive Sensor Technology—Feasibility of Defect Characterization," *Nondestructive Evaluation of Utilities and Pipelines II*, Edited by W. G. Reuter, SPIE Vol. 3398, pp. 28–34, Bellingham, WA, 1998.

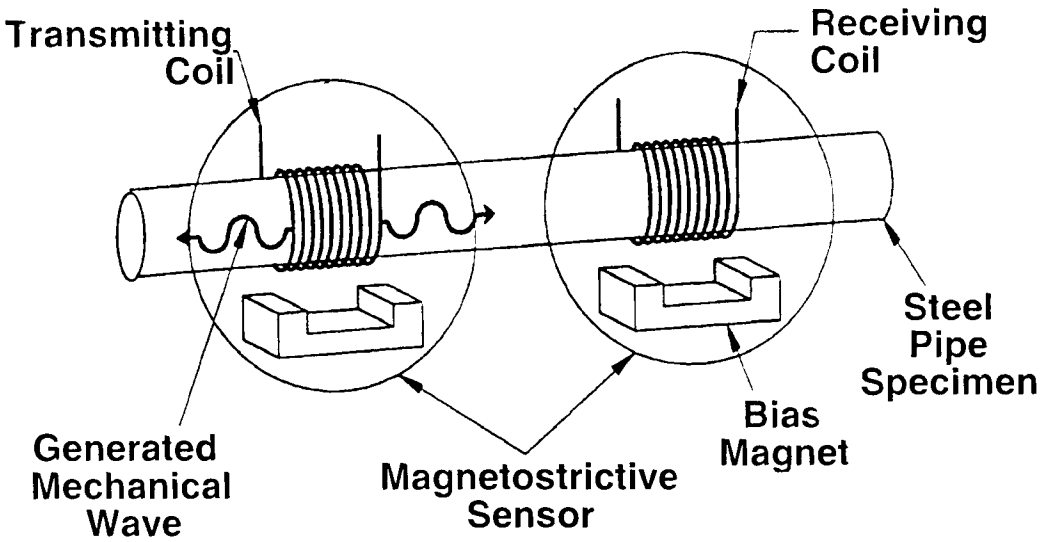

Fig. 5.1 Schematic of magnetostrictive sensor setup for generation and detection of guided waves in pipes.

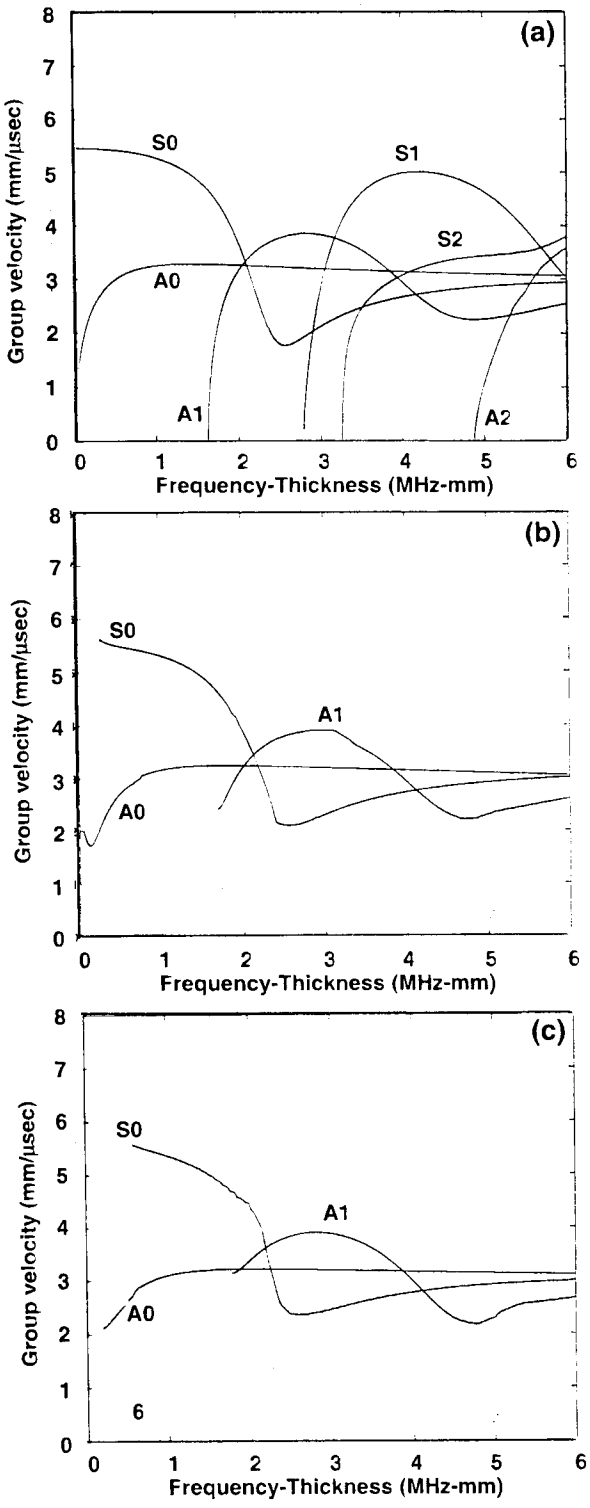

Fig. 5.2 Calculated dispersion curves for longitudinal guided waves in a plate for three conditions: (a) plate is free, (b) plate is backed by concrete on one side, (c) plate is backed by concrete on both sides.

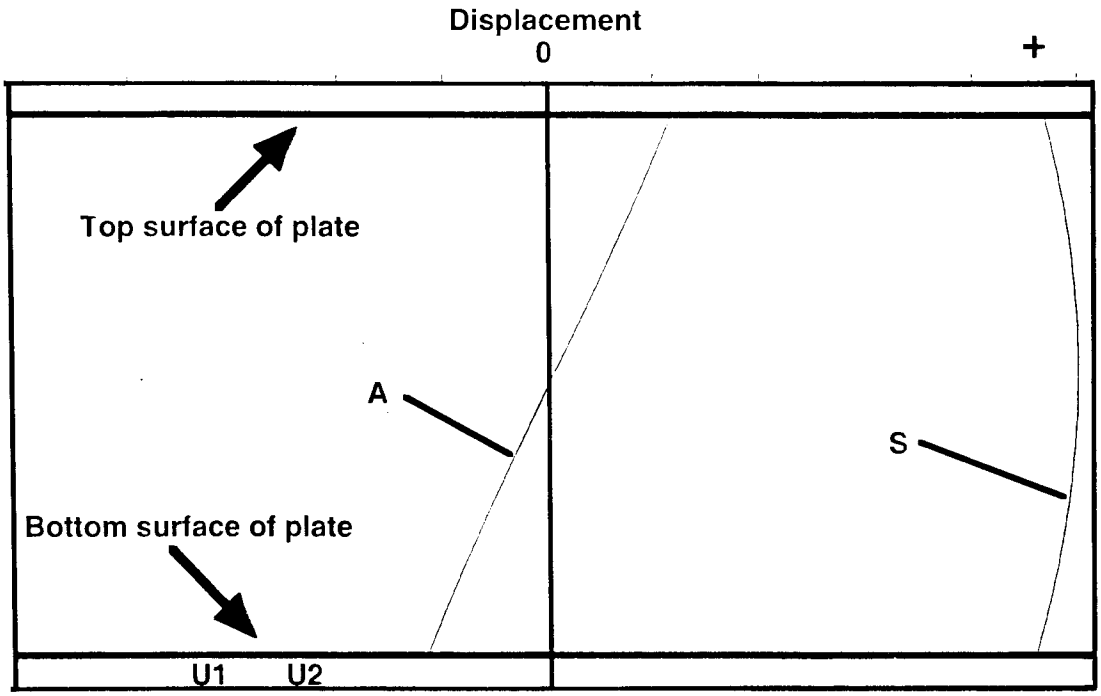

Fig. 5.3 Displacements of antisymmetric (A) and symmetric (S) wave modes across plate thickness.

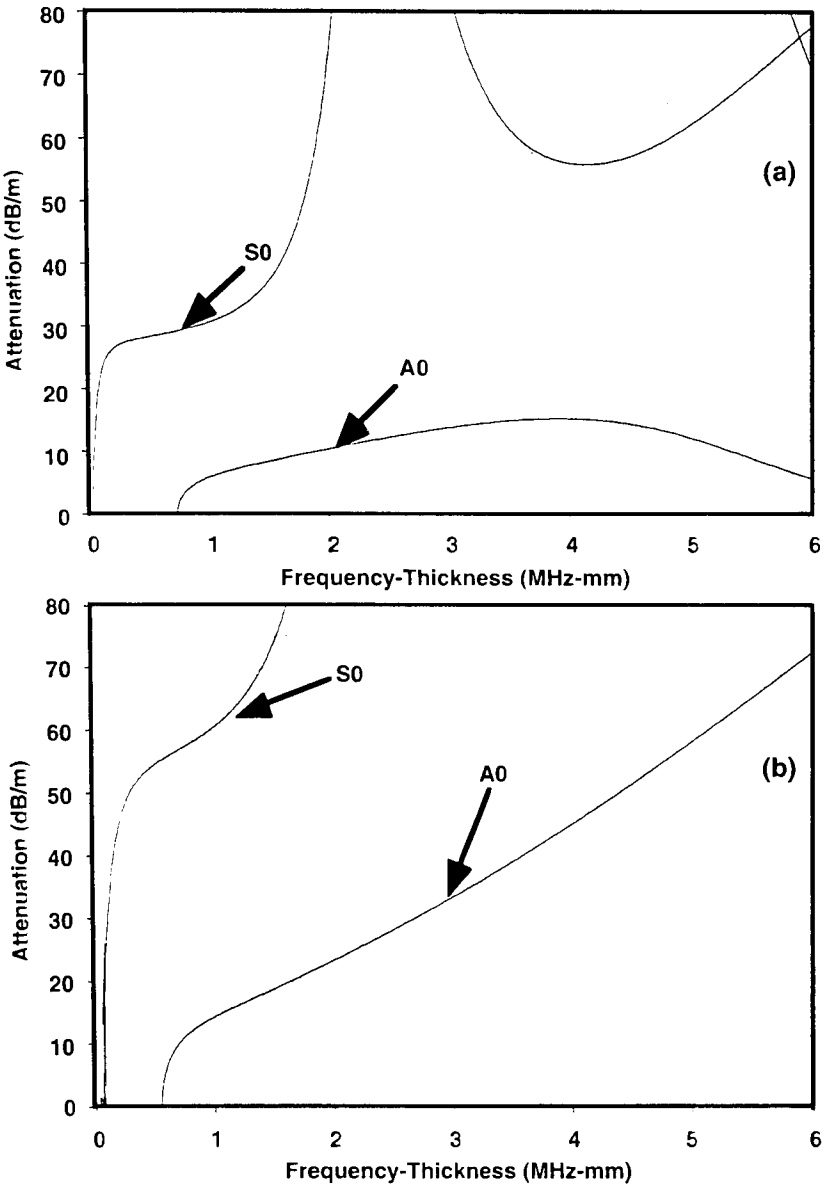

Fig. 5.4 Calculated wave attenuation for: (a) plate backed by concrete on one side and (b) plate backed by concrete on both sides.

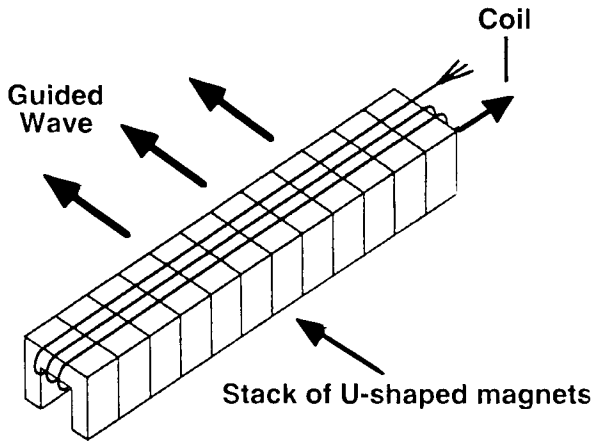

Fig. 5.5 Schematic of a coil wound around a stack of U-shaped magnets.

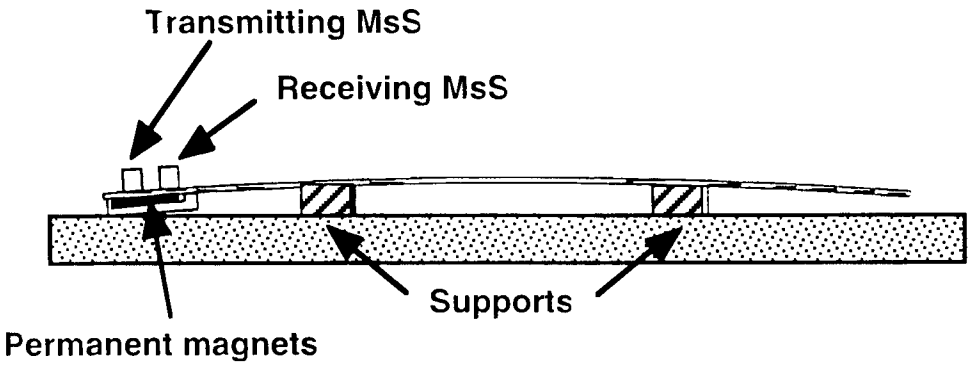

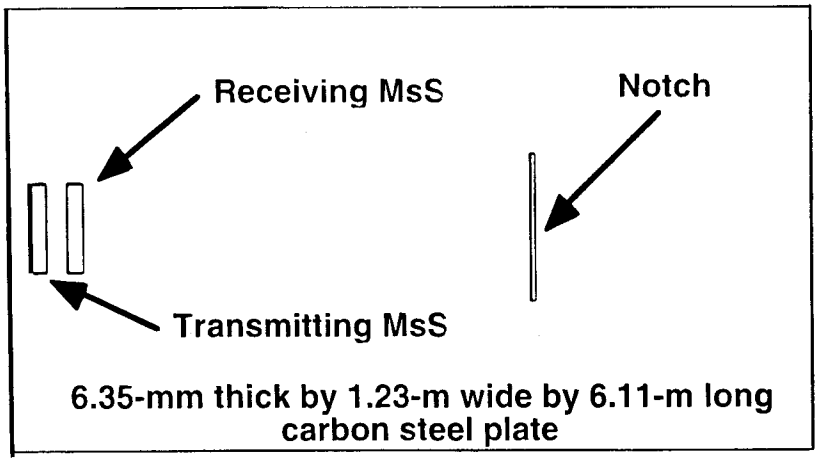

Fig. 5.6 Schematic of plate test article with setup for MsS probes.
(Permanent magnets are arranged on bottom of plate for convenience).

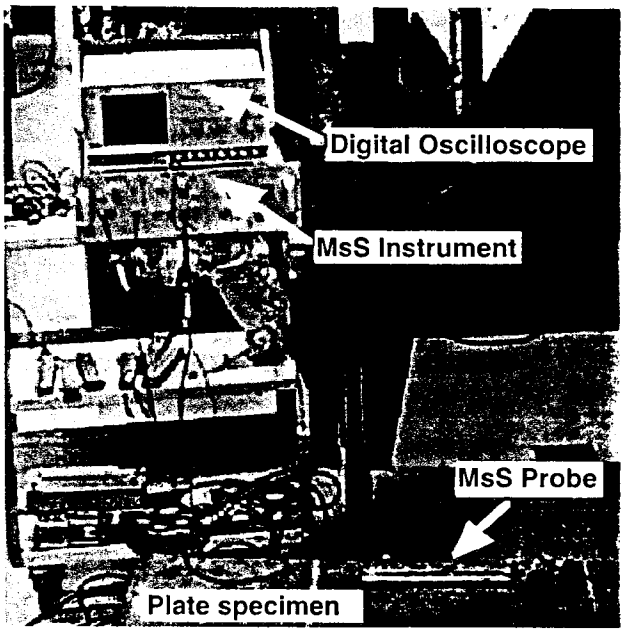

Fig. 5.7 Photograph of the overall experimental arrangement.

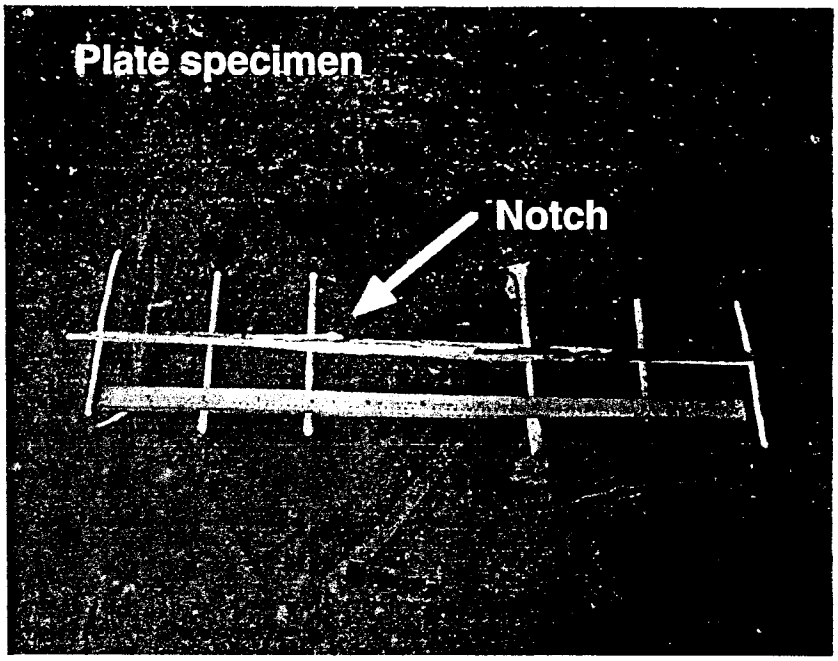

Fig. 5.8 Photograph of the 30-cm-long notch in plate specimen.

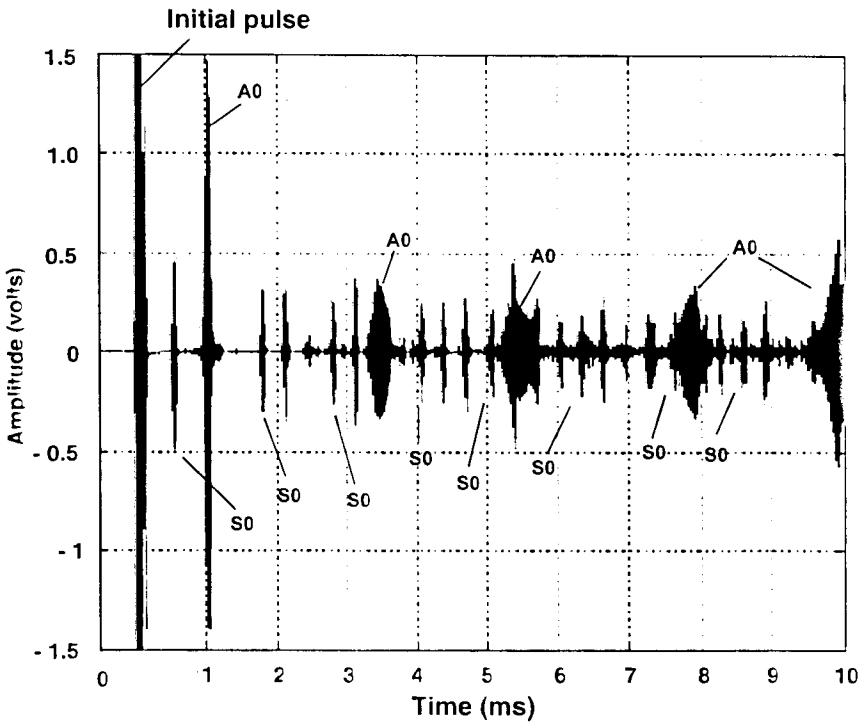

Fig. 5.9 MsS data from plate specimen using pitch-catch technique.

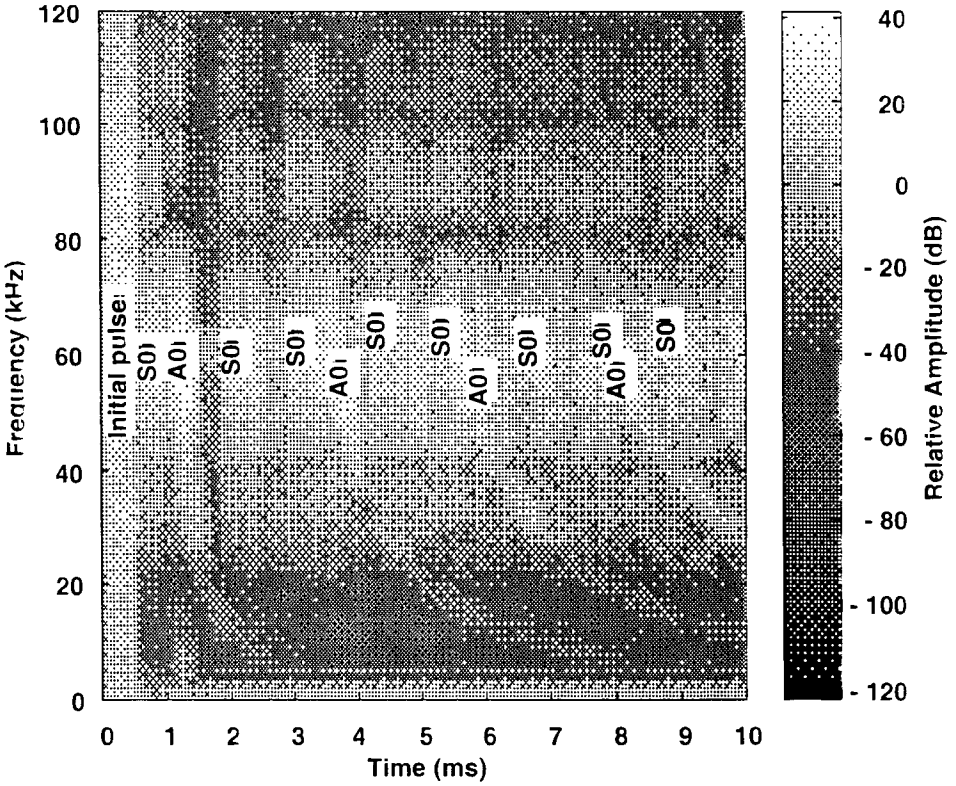

Fig. 5.10 Time-frequency representation of data in Fig. 5.9 obtained by using short-time fourier transform (STFT).

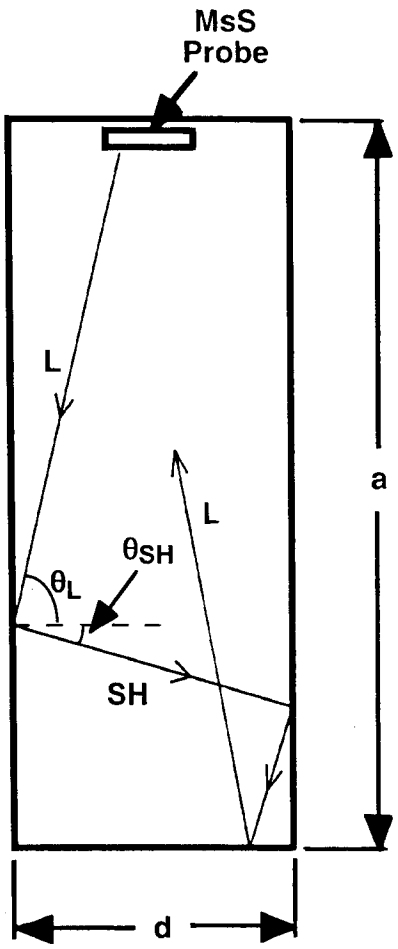

Fig. 5.11 Illustration of mode conversion at the lateral boundaries of a finite-sized plate.

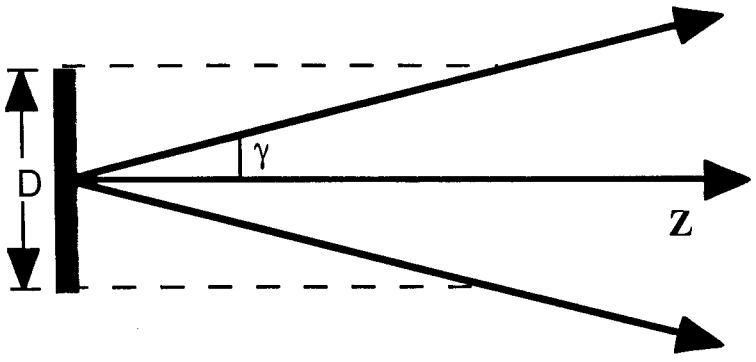

Fig. 5.12 Divergence of the beam from a guide-wave probe of length D.

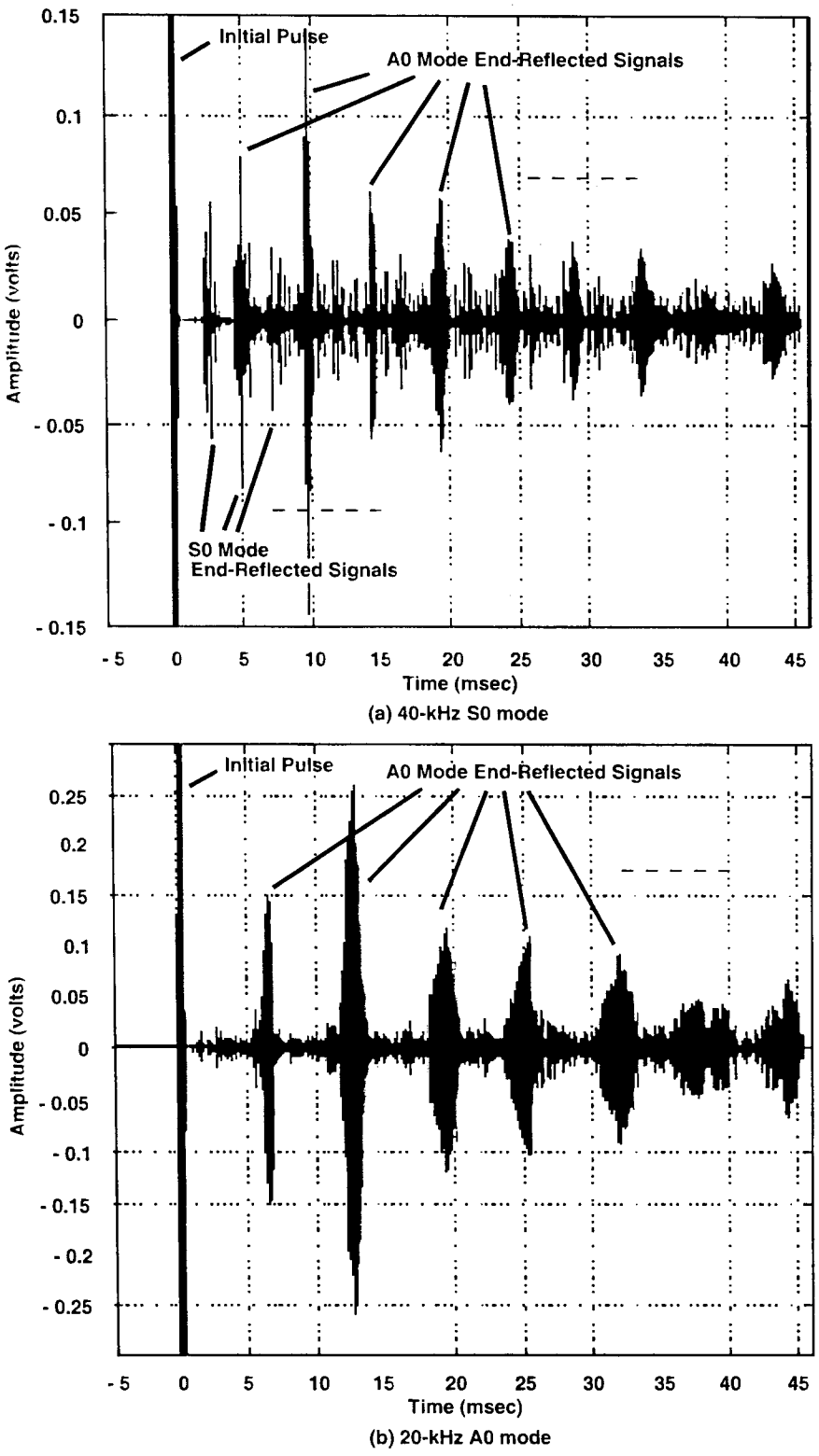

Fig. 5.13 MsS data using pulse-echo mode for steel plate prior to introducing a defect. Dotted lines indicate that signals continue to occur.

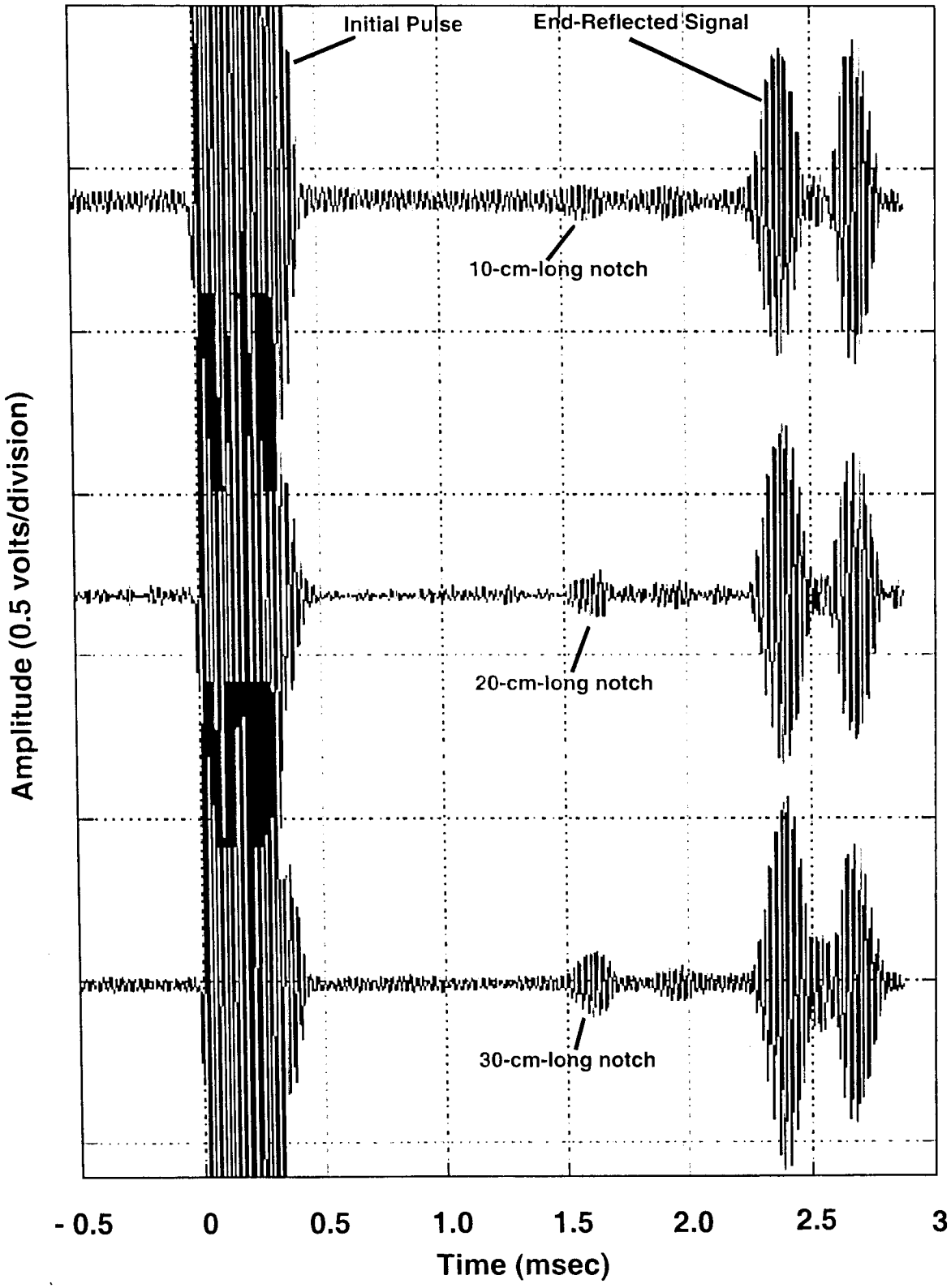

Fig. 5.14 Pulse-echo data for 40-kHz S0 mode obtained from plate containing different length notches.

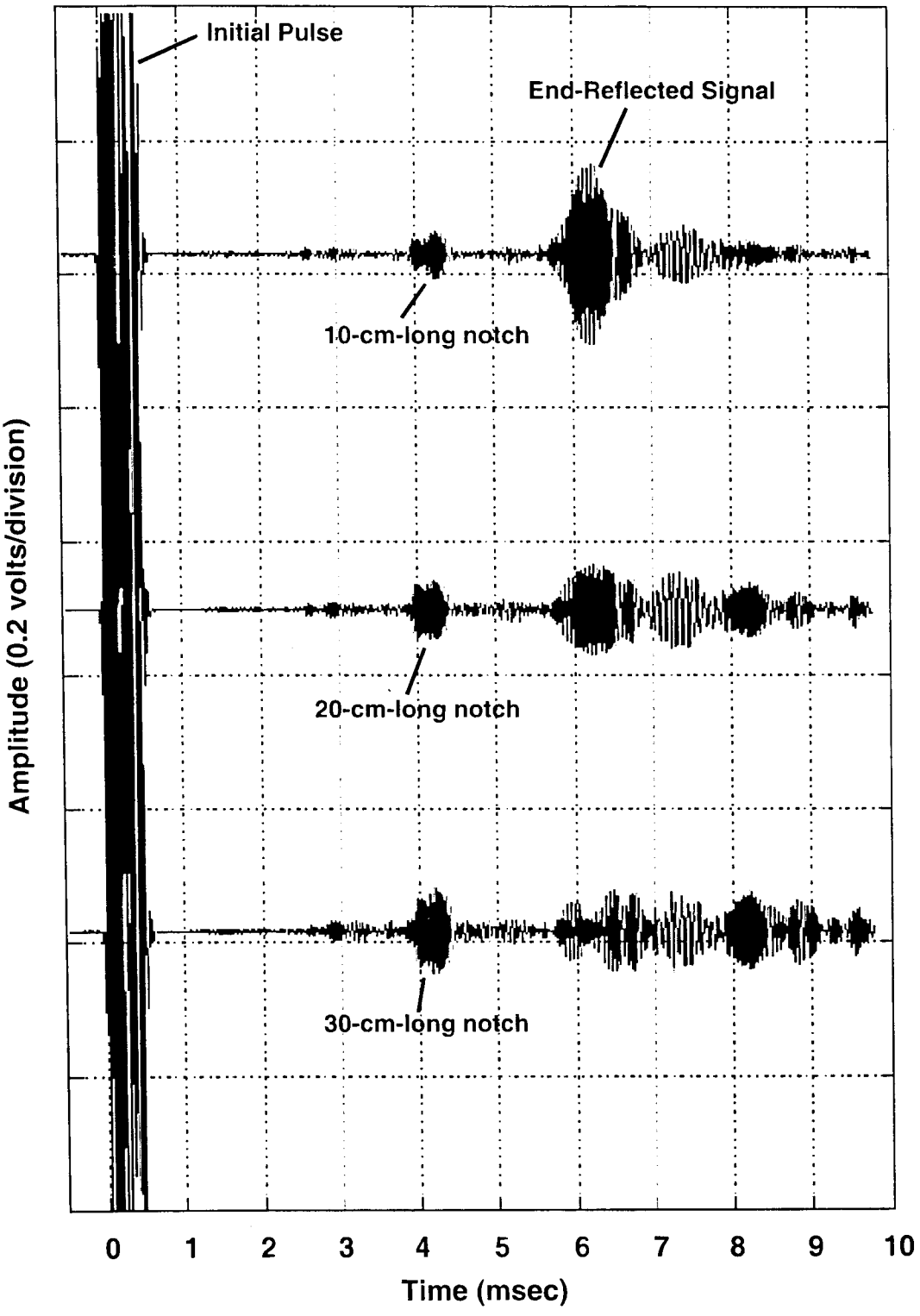

Fig. 5.15 Pulse-echo data for 20-kHz A0 mode obtained from plate containing different length notches.

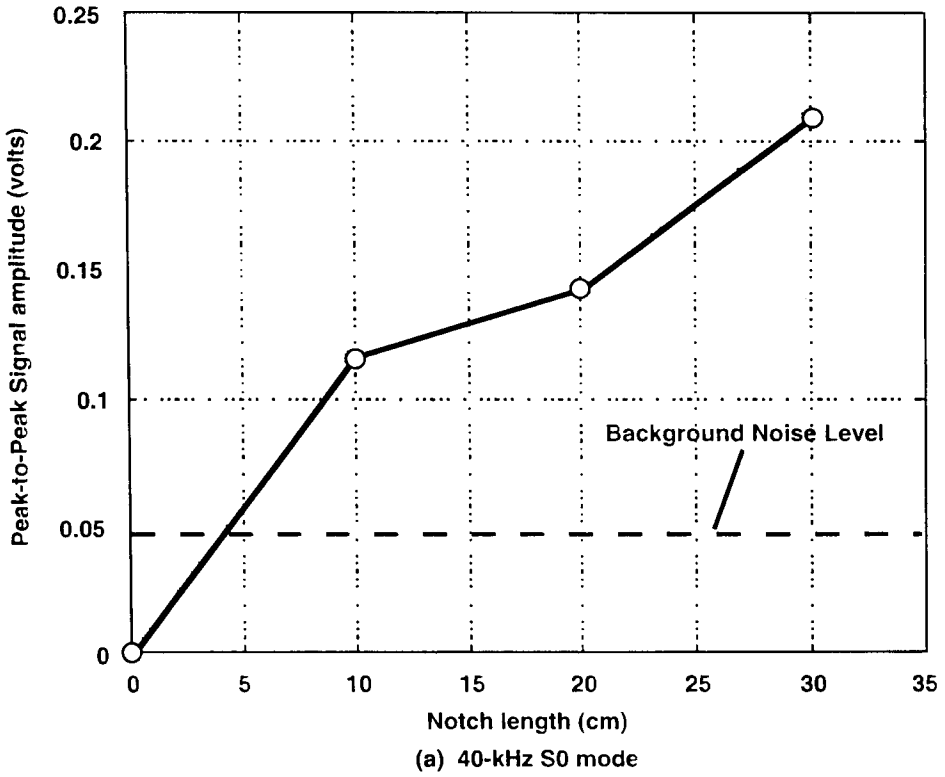

(a) 40-kHz S0 mode

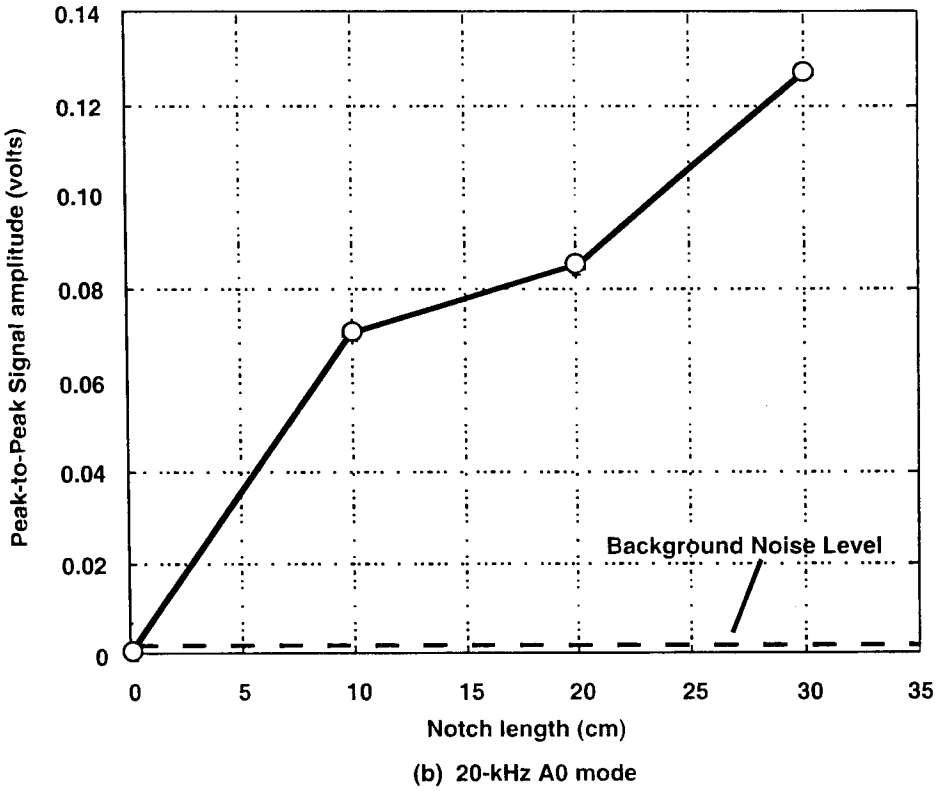

(b) 20-kHz A0 mode

Fig. 5.16 Plots of signal amplitude versus notch length.

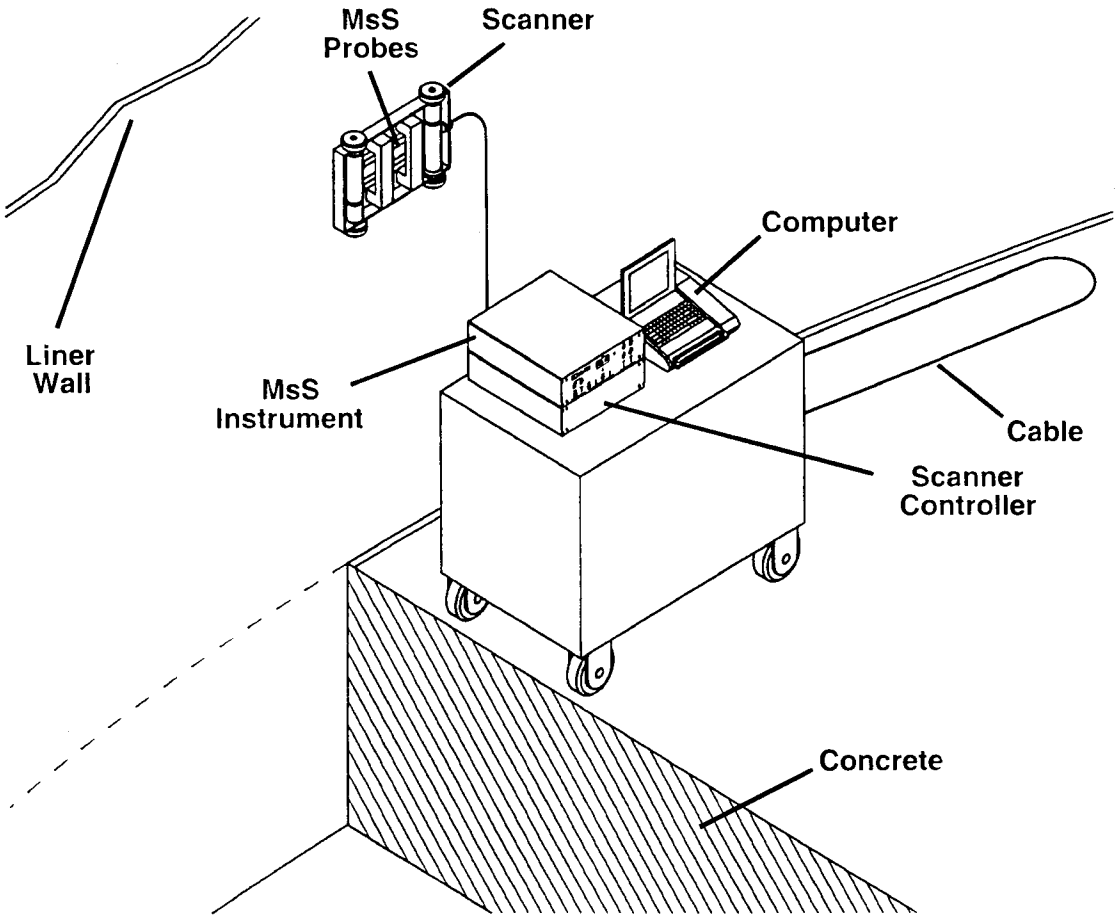

Fig. 5.17 Conceptual drawing of MsS system deployed for liner inspections.

Table 5.1
Material Property Values

Property	Material	
	Steel Plate	Concrete
Density, g/cm^3	7.93	2.2
Compressional wave speed, cm/sec	5.96×10^5	4.30×10^5
Shear wave velocity, cm/sec	3.26×10^5	2.30×10^5

Table 5.2
Calculated Beam Divergence Angles

Mode	Frequency (kHz)	λ (cm)	γ_{-3} (deg)	γ_{-10} (deg)
S0	20	27.2	23.5	42.2
	60	9.05	7.7	13.1
	100	5.42	4.6	7.7
A0	20	5.40	4.6	7.7
	60	2.87	2.4	4.1
	100	2.07	1.8	2.9

6. MULTIMODE GUIDED WAVE TECHNIQUES•

6.1 Introduction

Ultrasonic waves can be generated by either an oblique angle-beam or normal-beam technique. In the oblique angle-beam technique a longitudinal-wave transducer mounted on an acrylic angle-beam shoe generates guided waves in a pipe or plate structure. This approach is similar to that used for finding anomalies in a "V"-joint weld and has been investigated as a technique for inspection of inaccessible regions of NPP containment metallic pressure boundaries [6.3, 6.4]. The ultrasonic beam, having large side lobes, spreads out as it is reflected from the boundaries to somewhat limit the inspection resolution of this technique for the scenario of interest. This potential limitation however can be overcome through use of an array of sensors. Another potential limitation of this technique results from mode conversion, where both longitudinal and shear waves result after reflections from the boundary, regardless of the kind of incident wave being used. The multi-reflected waves influence the signal-to-noise ratio and make the echoes from an anomaly difficult to interpret. Use of bistatic acoustic imaging has been demonstrated to reduce the inner wedge reverberant field and to eliminate the through-thickness standing echoes. Thus, if a competing signal can be identified, it in all likelihood can be removed from the return signal during post-processing, increasing the probability of detecting the presence of an anomaly.

As an alternative, the guided wave technique exhibits promise since guided waves can propagate in embedded plates for a long distance. Much work has been reported recently on ultrasonic guided waves for inspection of free plates, pipes, and various structures [6.5-6.8]. Magnetostrictive sensors (MsS) have been employed to generate guided waves in plates [6.9]. As the MsS technique does not have mode control ability, all possible guided wave modes are generated. Based on a short-time Fourier transform (STFT), dispersion curves in a low frequency range were obtained for the A0 and S0 modes experimentally [6.9]. However, in a practical inspection, single-mode generation is desirable in order to simplify signal interpretation. A MsS array however can be used to implement mode control by suppressing the undesired modes. As the frequency associated with the currently used MsS technique is generally less than 200 kHz, anomaly detection sensitivity and resolution is reduced relative to higher frequency methods.

6.2 Multimode Guided Waves

The multimode guided wave technique is more sensitive than techniques which utilize shear waves (e.g., electromagnetic acoustic transducers), provides a global inspection technique for characterizing corrosion damage, follows the contour of the structure, can travel long distances (e.g., 100 m depending on frequency and mode characteristics), and can interrogate different regions or cross sections (i.e., depths) of the component inspected [6.5-6.9, 6.10, 6.11]. The guided plate waves can be excited at one point on the structure, propagate over considerable distances, and be received at a remote point on the structure. Table 6.1 presents a summary of advantages of guided wave techniques. Although this technique has been used with success to detect defects in piping materials, until recently its applicability to plate-type materials has not been demonstrated.

A countless number of guided wave modes at specific frequencies could be selected for a particular non-destructive evaluation problem, each point producing special sensitivities by way of wave structure across the thickness of the component being studied, and also specific penetration powers as a result of interface and surface displacement values and subsequent energy leakage into neighboring media [6.12]. The mode and frequency choice has a strong influence on non-destructive evaluation and flaw detection, classification, and sizing potential as well as the ability to propagate guided waves over long distances, despite the presence of coatings and other surrounding media. Phase velocity dispersion curves serve as the guide to controlling and selecting various guided wave modes [6.7]. From a guided wave mode generation point of view the phase velocity curve is necessary to determine an entry angle of the wave excitation since the phase velocity of a mode is related to the entry angle via Snell's law. Dispersion curves for a particular structure are generated numerically. Corresponding group velocity curves describe the velocity at which the mode propagates and allows for localization of a defect. With a variable angle shoe, modes can be generated along a horizontal line (i.e., constant velocity which depends on the angle of incidence

---

• Material presented in this chapter was developed from information provided in two reports [6.1, 6.2] prepared under a subcontract with Professor Joseph L. Rose of the Pennsylvania State University (University Park).

of the normal beam into the wedge) on the phase velocity dispersion curves. Varying the angle and frequency allows for the possible generation of modes with a phase velocity greater than the phase velocity in the shoe [6.7].

Controlling and selecting the guided wave mode/frequency combination is critical in obtaining optimal performance of the guided wave technique. First, a dominant single mode should be generated to simplify interpretation of echoes. Second, the sensitivity of a guided wave depends significantly on both the mode number and frequency at which it is excited. One mode/frequency combination may reflect strongly from a certain type of defect. Hence, the ability to generate guided wave modes at a variety of points on the dispersion curve is key to achieving optimal performance of the guided wave technique. The approach to mode and frequency selection is therefore crucial, which can ultimately be based on theoretical and/or experimental means. One aspect of a theoretical approach beyond dispersion curve analysis includes theory of elasticity computations of displacement distributions across a structure. The focus can be on achieving in-plane or out-of-plane optimal values on a surface or at a specific location inside a structure in an attempt at flaw analysis or improved penetration power. From an experimental point of view, an angle-beam transducer at a specific angle can be used to achieve a particular phase velocity value. Unfortunately, the presence of a phase velocity spectrum due to a transducer source influence, size and velocity pattern, as well as the frequency spectrum itself, often limits the ability to specifically achieve the particular mode and frequency of choice. Multiple modes can be obtained.

6.2.1 Theoretical Background

Figure 6.1 presents a coordinate system that could be used for SH wave propagation. For Lamb wave propagation, consider the particle velocity to be in the x_1-x_2 plane direction rather than in the x_3 direction shown. Phase velocity and group velocity dispersion curves can be generated for each [6.13]. A sample Lamb wave dispersion curve for a steel plate is shown in Fig. 6.2a and an example of a SH phase velocity dispersion curve is illustrated in Fig. 6.2b. Note that some SH modes are dispersive, but for n = 0 the mode is non-dispersive. Wave structure is identical along a particular SH mode but changes drastically along a Lamb wave mode. When using guided waves to penetrate a steel plate embedded in concrete, it becomes necessary to consider wave structure at the surfaces of the plate and subsequent energy leakage into the concrete. Rather than study this phenomenon theoretically, a variety of different Lamb wave modes and SH mode situations were studied. It is know that phase velocity and frequency tuning would be useful in this Lamb wave case in order to modify wave structure and, hence, energy leakage into the concrete. For the SH case, only the n = 0 mode was considered, but excellent results were obtained.

At a frequency of 565 kHz used for the Lamb wave experiments, there are several modes propagating in the 25.4 mm-thick steel plate. Two modes are studied with emphasis on pseudo-surface (combined A0 and S0 modes) waves and the A3 mode. The wave structures of both modes are shown in Fig. 6.3. Both Figs. 6.3a and 6.3b show the in-plane and out-of-plane displacements, each with a different distribution pattern. From Fig. 6.3a, it can be seen that the energy focuses close to the plate boundary area on the same side of the transducer. Therefore, it can detect anomalies on one side only. In order to find anomalies close to the other side using the pseudo-surface mode, the transducer needs to be moved to the other side. Although more tedious for experimentation, this wave mode can determine which side the anomalies are close to, and thus provide more information about anomalies. Compared with pseudo-surface waves, A3 modes have the energy distribution across the entire plate thickness and can detect anomalies on the both sides of the plate.

6.2.2 Experiment

A limited experimental investigation has been conducted to demonstrate the feasibility of using the guided wave technique for identification and location of thickness reductions in the metallic pressure boundary of NPP containments. The specimens studied are shown in Fig. 6.4, and include a free plate (no concrete) with two anomalies (plate 1), a plate embedded in concrete with one anomaly (plate 2), and a plate embedded in concrete but having no anomalies (plate 3). All three plates are 25.4-mm thick by 203-mm wide by 914-mm long. For practical purposes, the thickness of the concrete, when present, is large enough that it can be considered a "half space." The plate specimens provide a benchmark for studying various aspects of guided wave inspection, including sensitivity, transmission ability across anomalies, inspection reliability, and penetration ability.

6.2.2.1 SH Waves

SH guided waves have particle displacements in the shear horizontal direction, which is perpendicular to the propagation direction. SH waves are sensitive to the transverse boundary conditions. Therefore, a transducer couplant for SH waves should be a highly viscous material such as honey. Although coupling requirements once limited applications of SH waves, advancements of electromagnetic acoustic transducers (EMATs) have resulted in SH waves once again receiving a lot of attention because of the couplant-free advantage of EMATs. Figure 6.5a presents a schematic of a typical EMAT application system and Fig. 6.5b shows a picture of the EMAT's used in the experiments. The grid spacing of the EMAT's is 17.7 mm, which determines the corresponding frequency for generating the non-dispersive SH wave mode (i.e., 200-250 kHz). The non-dispersive SH wave mode has the same phase velocity as the SH bulk wave velocity (3200 m/s), and a uniform displacement distribution across the plate thickness.

The waveforms obtained from testing the three plate specimens are shown in Fig. 6.6. Figure 6.6a presents the reflected echoes for the free plate with two anomalies (plate 1) and shows that both anomalies can be detected by using the SH waves. Because the non-dispersive SH wave mode has a uniform particle displacement distribution, some energy can pass the first anomaly to be reflected by the second anomaly. The backwall echo (BWE) shows good penetration ability of the SH wave mode. Figures 6.6b and 6.6c present the anomaly echoes for the plate containing an anomaly embedded in concrete (plate 2). The echoes are obtained by putting the transducer at end A on the top and bottom surfaces of the plate, respectively. From Figs. 6.6b and 6.6c it can be seen that the SH guided waves have the same sensitivity to the anomaly whether the transducer is located on the top or bottom plate surface, even though the anomaly is just on the top surface. The signal for transducer placed at end B of plate 2 is shown in Fig. 6d. The signal for the plate specimen embedded in concrete but without an anomaly (plate 3) is shown in Fig. 6e and demonstrates insensitivity to the concrete edge and the plate-concrete interface. The strong backwall echo demonstrates the excellent penetration power of the SH guided waves across the steel-concrete interface.

6.2.2.2 Lamb Waves

Unlike SH waves, Lamb waves have particle displacement distribution in both parallel and perpendicular directions to the propagation direction. Lamb waves are sensitive to both transverse and normal boundary conditions. Common couplants can be used for generating Lamb waves. A transducer mounted on a wedge for Lamb wave generation is shown in Fig. 6.7. The frequency and wedge angle determines the generated Lamb wave mode. Two wedge angles were considered at the frequency of 565 kHz. When the wedge was set to 62 degrees, it generated the A0 and S0 modes simultaneously, both having the same phase velocity (3030m/s) at the working frequency, which degenerates into pseudo-surface waves. As the pseudo-surface wave has energy distribution close to the plate boundary, it is very sensitive to an anomaly close to the boundary. However, it is not sensitive to the anomalies on the other side of the plate. Figure 6.8a is the pulse-echo signal for the transducer placed at the opposite surface (bottom) to anomalies on the free plate (plate 1). It can be seen that both anomalies are ignored and only a backwall echo is received. If the transducer is placed on the same surface (top) as the anomalies, however, only the first anomaly echo can be received, as shown in Fig. 6.8b, which means that most energy close to the plate boundary is reflected back by the first anomaly. This is a different case than occurred for the SH waves due to the uniform energy distribution feature of the SH wave mode.

In order to obtain a fairly uniform energy distribution across the plate thickness for Lamb waves, the wedge angle was changed to 38 degrees. Once again, the tone burst frequency was 565 kHz. The phase velocity and group velocity of the generated Lamb waves were 4385 m/s and 2220 m/s, respectively. As a result, the A3 Lamb wave mode was generated (Fig. 6.3b). Figures 6.9a and 6.9b present the pulse-echo signals for the free plate (plate 1) with the transducer on the top and bottom surfaces, respectively. The signals shown in Figs. 6.9a and 6.9b indicate that by generating the A3 Lamb wave mode, the transducer can detect anomalies from either the top or bottom surfaces of the plate. The Lamb wave mode also shows a great sensitivity to anomalies. Figures 6.9c and 6.9d provide the signals for the plate containing an anomaly embedded in concrete (plate 2) when the transducers were placed at ends A and B, respectively. Compared with SH waves, Lamb waves show a higher signal to noise ratio in Figs. 6.9c and 6.d. Figure 6.9e is the pulse-echo signal for the plate embedded in concrete without an anomaly (plate 3). Multiple echoes were received from the plate-concrete interface before the backwall echo, indicating a disadvantage of the Lamb wave mode. This problem could be overcome by setting a threshold for an anomaly call. Most anomalies of

major concern would probably be more than 20% the plate thickness and reflect stronger echoes than those from the plate-concrete interface. Use of multi-mode Lamb wave signals can also be considered for an anomaly call.

6.3 Elements of Defect Sizing in a Wave Guide Using SH Guided Waves

The Boundary Element Method (BEM) is being developed to study the interaction of various guided wave packets of energy with various corrosion boundaries in a structure. This study is being carried out on elliptical-shaped scatterers with a variation in defect depth and length values as shown in Fig 6.10. This type of reflection could model items of interest such as corrosion boundaries and pitting. Corrosion and surface breaking defects, of course, will be more complex than the nice geometrical figures used in the BEM studies. The BEM program is being developed, though, to handle greater variations in the geometrical shaped reflectors compared to elliptical pitting. Frequency spectrums for the amplitudes of the scattered modes in both-pulse echo and through-transmission modes are discussed. Characterization of the defect depth and length is implemented for some special situations based on features of the BEM results. For initial experiments reported in this section, artificial corrosion and crack type defects were fabricated with different depths and lengths in 10-mm-thick steel plates. Theoretical and experimental data on the scattering of SH waves is obtained, demonstrating potential for solving this difficult classification problem. The goal of the modeling efforts is therefore to establish guidelines so that the best modes and frequencies could be considered for impingement to provide the best chance of success in determining the defect shape and size characteristics. An electromagnetic-acoustic transducer (EMAT) technique for SH waves excitation is used.

Ultrasonic guided waves are being used extensively for defect and materials characterization; some theoretical and experimental results using BEM are available [6.13-6.17]. The finite-element method (FEM) for the Lamb and SH wave scattering problem has been analyzed elsewhere [6.18-6.21]. The electromagnetic-acoustic transducer (EMAT) technique for SH wave excitation has also been described elsewhere [6.22].

6.3.1 Problem Statement and Solution

The boundary value problem for an elastic isotropic plate presented in Fig. 6.10 is considered. The incident time harmonic wave is propagating in the positive X_1 direction. The mode incident on the crack results in both reflected and transmitted waves of all orders of the propagation modes that could exist in the plate for a given frequency. The crack considered has an elliptical shape, with horizontal axis 2a and vertical axis b.

For any frequency, scattering from a crack generates a finite number of propagating and countable numbers of nonpropagating modes. For the SH modes the particle displacement vector has only an X_3 component. Displacement and stress for the friction-free boundary conditions can be presented in a form [6.13]:

Displacement

$$u_3^n(x_1,x_2,t) = U^n(x_1,x_2)e^{-i\omega t} = \begin{cases} B_n \cos(n\pi x_2/d)e^{i(k_n x_1-\omega t)} & (symmetric\ \mathrm{mod}es) \\ A_n \sin(n\pi x_2/d)e^{i(k_n x_1-\omega t)} & (antisymmetric\ \mathrm{mod}es) \end{cases} \tag{6.1}$$

Stress

$$\tau_{23}^n(x_1,x_2,t) = T_{23}^n(x_1,x_2)e^{-i\omega t} = \begin{cases} -B_n\mu q_n \sin(n\pi x_2/d)e^{i(k_n x_1-\omega t)} & (symmetric\ \mathrm{mod}es) \\ A_n\mu q_n \cos(n\pi x_2/d)e^{i(k_n x_1-\omega t)} & (antisymmetric\ \mathrm{mod}es) \end{cases} \tag{6.2}$$

$$\tau_{13}^n(x_1,x_2,t) = T_{13}^n(x_1,x_2)e^{-i\omega t} = \begin{cases} ik_n B_n\mu \cos(n\pi x_2/d)e^{i(k_n x_1-\omega t)} & (symmetric\ \mathrm{mod}es) \\ ik_n A_n\mu \sin(n\pi x_2/d)e^{i(k_n x_1-\omega t)} & (antisymmetric\ \mathrm{mod}es) \end{cases}$$

$$k_n^2 = (\frac{\omega}{c_T})^2 - (\frac{\pi n}{d})^2; \ldots q_n^2 = (\frac{\omega}{c_T})^2 - k_n^2 \ldots (n = 0,1,2,\ldots)$$

where A_n and B_n are unknown coefficients and $d=2h$. Note that the amplitudes of the SH modes (Eqn. 6.1) are independent of frequency and wave number. Hence wave structure of the SH mode does not vary along the entire dispersion curve. This is in contrast to Lamb wave behavior, where the wave field is a function of the position on the dispersion curve. The total displacement field is the superposition of the incident and scattered wave fields. The time dependent term $e^{-i\omega t}$ is omitted elsewhere.

$$U(x_1,x_2) = A_p^{IN}U^p(x_2)e^{ik_p x_1} + \sum_{n=0}^{\infty} A_n^{\pm}U^n(x_2)e^{\pm ik_n x_1} \tag{6.3}$$

where, A_p^{IN} is the known amplitude of the incident p_{th} mode, and $A_n^{\pm}$ denotes the unknown amplitudes of the scattered waves traveling in the positive and negative x_1 directions respectively. $U^n(x_2)$ denotes the known amplitude of the n_{th} mode for the traction free plate, and k_n represents wave numbers of SH waves. The summation in Eqn. (6.3) is over all propagating and evanescent modes that can exist in a plate for a particular frequency of interest.

Far away from a defect only the amplitudes of the propagating modes are significant. This is expressed by keeping only the real roots k_n, according to the phase velocity dispersion curves as shown in Fig. 6.11. The solution of the problem can be obtained by coupling the BEM solution for the rectangular area and a far-scattered field on the boundaries $\Gamma_{\pm}$ (Fig. 6.10a). This approach is effective for a rectangular area with a large enough length L. Therefore the far-field displacement and stress on the boundaries $\Gamma_{\pm}$ can be expressed only by using propagating modes.

The boundary-value problem for modeling the rectangular area leads to the following boundary integral equation [6.13, 6.14].

$$C(\xi)U(\xi) + \int_{\Gamma} \frac{\partial U^*(\xi,x)}{\partial n} U(x)d\Gamma(x) = \int_{\Gamma} U^*(\xi,x)\frac{\partial U(x)}{\partial n} d\Gamma(x) \tag{6.4}$$

where Γ is the total boundary of the modeling area, the value of $C(\xi)$ depends on the boundary smoothness and $\partial U/\partial n$ is the derivative of U with respect to the outward normal to the boundary Γ. The terms $U(x)$ and $\partial U(x)/\partial n$ are the boundary values of the displacements and tractions. $U^*(r)$ is the fundamental solutions in the frequency domain expressed through a Hankel function of the first kind [6.10].

$$U^*(r) = \frac{i}{4}H_0^1(\frac{\omega}{c_T}r) \tag{6.5}$$

The procedure to obtain a numerical solution of Eqn.(6.4) by using coupling conditions on the boundaries $\Gamma_{\pm}$ and finding the reflection and transmission coefficients is discussed elsewhere [6.13, 6.14].

The results presented here are used for a sizing study of elliptical defects with 2a equal to 0.3, 6.35, and 12.7 mm. Reflection and transmission coefficients versus frequency are shown in Fig. 6.12 for an n = 0 incident mode, n = 0 reflected and transmitted mode from the 0.3 mm notch defect. There is an excellent monotonic change in amplitude versus percent through wall depth for all frequencies. A sample result is shown in Fig. 6.13 for 0.5 MHz. Sample results are illustrated in Figs. 6.14 and 6.15 for grooves of 6.35 and 12.7 mm compared to the 0.3 mm elliptical defect. There is sometimes a monotonic change of amplitude with defect depth, but not at all frequencies.

Generally, many BEM computer runs could be conducted to seek a reflection characteristic such that there would be a monotonic increase with depth of a reflector. At this time, sizing is only possible if the reflector type is known. Therefore the focus will be on the 0.3-mm-wide notch-type defect. Theoretical results were shown in

Figs. 6.12 and 6.13 with a monotonic change of amplitude with through-wall size. Future work should focus on both defect detection and quantification. BEM tools are now available to assist in this study.

6.3.2 Experiment

Experiments were conducted on nine steel plates, each of which had either a groove or notch in one surface. The size of a defect was either 0.3, 6.35, or 12.7-mm wide with a depth equal to either 10%, 30% or 50% the through-plate thickness. Two electromagnetic SH wave transducers (SH EMATs) were used to generate and receive horizontal shear waves in the steel plate using a tone burst signal generator and oscilloscope system. Both through-transmission and pulse-echo modes were used. On each plate, a reference signal was obtained by separating the two EMATs 76.2 mm. The non-defect signal amplitude was then recorded. For through transmission, the two EMATs were 76.2 mm apart with each transducer 38.1 mm from the centerline of the defect (see Fig. 6.16a). A sample through-transmission signal is shown in Fig. 6.17. A sample pulse-echo waveform for the setup shown in Fig. 6.16b is shown in Fig. 6.18. The envelope peak-to-peak value of the signal was measured and the transmission coefficient calculated by dividing it by that of the reference signal. For the pulse-echo mode, the two EMATs were put side by side and on the same side of the defect to simulate the pulse-echo mode. They were located 38.1 mm away from the center of the defect. Similar calculations to above can provide the reflection coefficient. A through-transmission result is shown in Fig. 6.19. It can be seen that the trend of the curve for the theoretical and experimental results is consistent. Let's now focus on the 0.3-mm-wide-notch-type defect to see if a linear relationship with size can be obtained. Excellent results are shown for both the through-transmission mode in Fig. 6.20 and for the pulse-echo mode in Fig. 6.21.

6.4 Concluding Remarks

Both SH and Lamb wave modes can be used for the inspection of steel containment structures, both somewhat insensitive to the concrete boundary for specific velocity and frequency values. On the other hand, strong benefits of the SH wave mode via an EMAT transducer was demonstrated with overall improved signal-to-noise ratio with practically no interference from the concrete interface and the non-contact testing potential.

Preliminary results presented here show that defect quantification analysis can be carried out for SH guided wave impingement onto a defect in a wave guide. Both pulse-echo and through-transmission methods were considered. In particular, the possibility of a monotonic increase in amplitude change with size is noted. Potential advantages of shear-horizontal waves compared to "Lamb" type waves include less mode conversion, constant wave structure for a particular mode for all frequencies, and less sensitivity to boundary conditions because of the lateral particle velocity. Presented BEM results can be used to establish data acquisition and analysis guidelines for development of a test protocol and quantification algorithm development program. Besides modeling and BEM analysis, feature extraction possibilities could also be obtained from experimental or calibration standards using guidelines established in this study.

6.5 References

6.1 J. Li and J.L. Rose, "Guided Wave Inspection of Containment Structures," *Materials Evaluation* 59(6), pp. 783-787, June 2001.

6.2 J.L. Rose and X. Zhao, "Anomaly Throughwall Depth Measurement Potential with Shear Horizontal Guided Waves," *Materials Evaluation* 59(10), pp. 1234-1238, October 2001.

6.3 J.E. Bondaryk, C.N. Corrado and V. Godino, *Feasibility of High Frequency Acoustic Imaging for Inspection of Containments*, NUREG/CR-6614, U. S. Nuclear Regulatory Commission, Washington, D.C. (August 1998).

6.4 J. Rudzinsky, J. Bondaryk, and M. Conti, *Feasibility of High Frequency Acoustic Imaging for Inspection of Containments: Phase II*, ORNL/NRC/LTR-99/1, Lockheed Martin Energy Systems, Inc., Oak Ridge National Laboratory, Oak Ridge, Tennessee, July 1999.

6.5 Y. Cho and J.L. Rose, "Guided Waves in a Water Loaded Hollow Cylinder," *Nondestructive Testing & Evaluation* 12, pp. 323-339, 1996.

6.6 J.L. Rose, D. Jiao and J. Spanner, Jr., "Ultrasonic Guided Wave NDE for Piping," *Materials Evaluation* 54(11), pp. 1310-1313, November 1996.

6.7 M.J. Quarry and J.L. Rose, "Multimode Guided Wave Inspection of Piping Using Comb Transducers," *Materials Evaluation* 57(10), pp. 1089-1090, October 1999.

6.8 D.N. Alleyne and P. Cawley, "Long Range Propagation of Lamb Wave in Chemical Plant Pipework," *Materials Evaluation* 45(4), pp. 504-508, April 1997.

6.9 H. Kwun and K.A. Bartels, "Experimental Observation of Elastic-Wave Dispersion in Bounded Solids of Various Configurations," *J. Acoustical Society of America* 99(2), pp. 962-968, February 1996.

6.10 D.N. Alleyne and P. Cawley, "The Interaction of Lamb Waves With Defects," *IEEE Transactions on Ultrasonics, Ferro Electrics, and Frequency Control* 39(3), pp. 381-397, 1992.

6.11 D. N. Alleyne and P. Cawley, "The Long-Range Detection of Corrosion in Pipes Using Lamb Waves," *Review of Progress in Quantitative NDE*, Plenum Press, New York, NY, pp. 2075-2080, 1995.

6.12 J.L. Rose, S.P. Pelts and M.J. Quarry, "A Comb Transducer Model for Guided Wave NDE," *Ultrasonics* 36, Elsevier Publishers, New York, NY, pp. 163-169, 1998.

6.13 J.L. Rose, *Ultrasonic Waves in Solid Media*, Cambridge University Press, New York, NY,1999.

6.14 Y. Cho and J.L. Rose, *J. Acoustical Society of America* 99(4), pp. 2097-2109, 1996.

6.15 J.L. Rose, S.P. Pelts and Y. Cho, *Journal of Nondestructive Evaluation*, 19(2), pp. 55-66, 2000.

6.16 S.P. Pelts, J.P. Cysyk and J.L. Rose, *Review of Progress in Quantitative Nondestructive Evaluation* 16, pp. 137-143, 1996.

6.17 Y. Cho, D.D. Hongerholt and J.L. Rose, *IEEE Transactions on Ultrasonics, Ferro Electrics, and Frequency Control* 44(1), pp. 44-52, 1997.

6.18 A. Abduljabbar and S.K. Datta, *J. Applied Physics* 54(2), pp. 461—472, 1983.

6.19 S.K. Datta, Y. Al-Nassar and A.H. Shah, *Review of Progress in Quantitative Nondestructive Evaluation* 10, pp. 97-104, 1991.

6.20 M. Koshiba, S. Karakida and M. Suzuki, *IEEE Trans. Sonics Ultrasonics*, SU-31, pp. 18-25, 1984.

6.21 M. Koshiba, K. Hasegawa and M. Suzuki, *IEEE Trans. Ultrasonics, Ferro Electrics, and Frequency Control* 34(4), pp. 461-466, (1987).

6.22 C.M. Fortunko, R.B. King and M. Tan, *J. Applied Phys.*, 53, 3450-3458, 1982.

6.23 S. Kobayashi, "Chapter 4, Elastodynamics," *Boundary Element Methods in Mechanics*, North-Holland Publishers, Amsterdam, The Netherlands, pp.192-255, 1987.

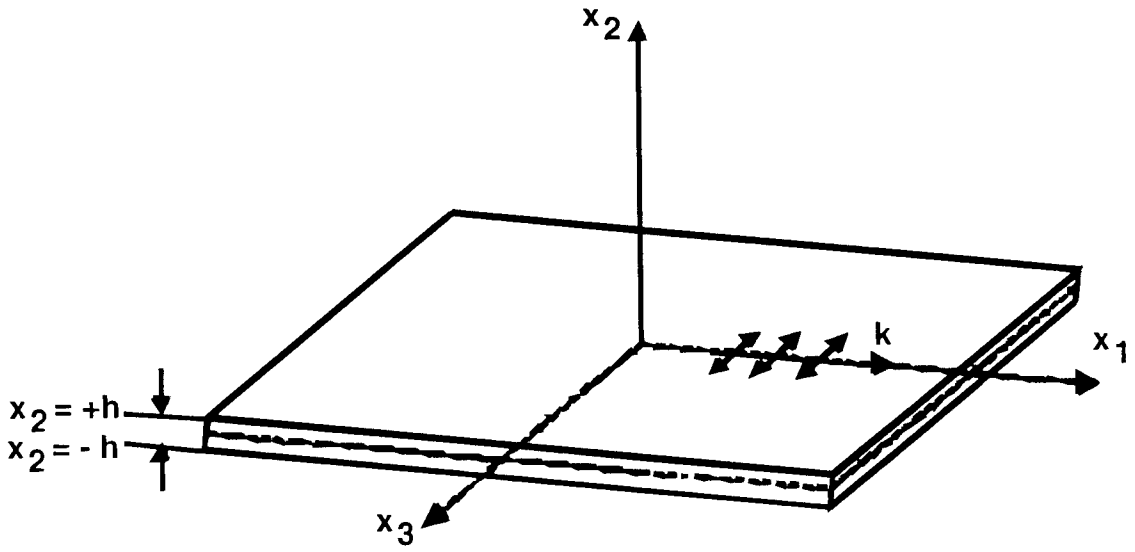

Fig. 6.1 SH wave propagation mode where propagation is along x_1 and particle displacements are along x_3.

(Particle displacements for Lamb wave propagation mode are in x_1-x_2 plane.)

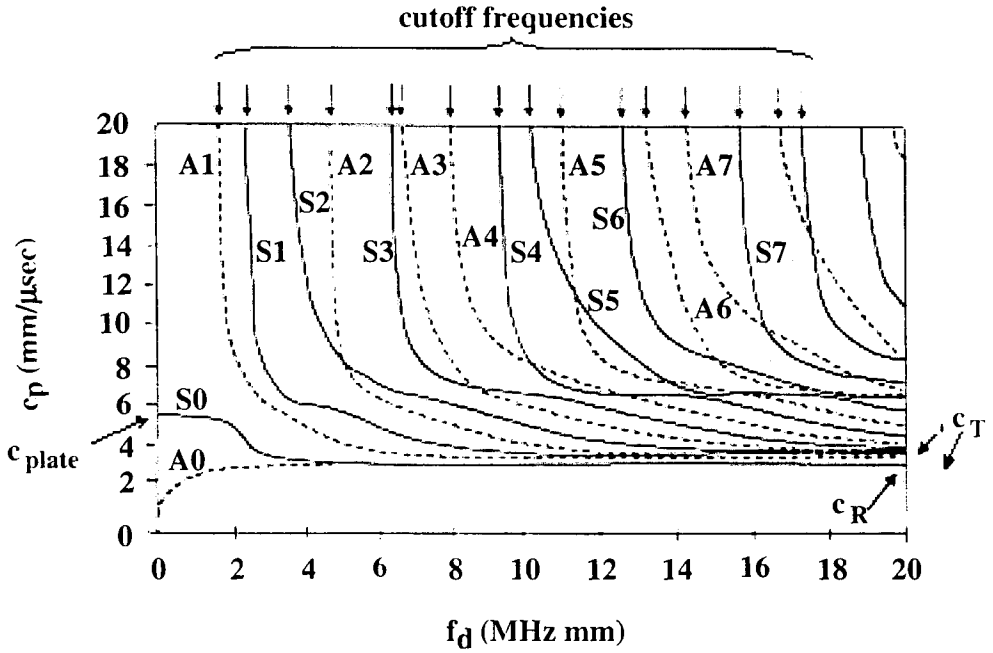

(a) Sample Lamb wave phase velocity dispersion curves

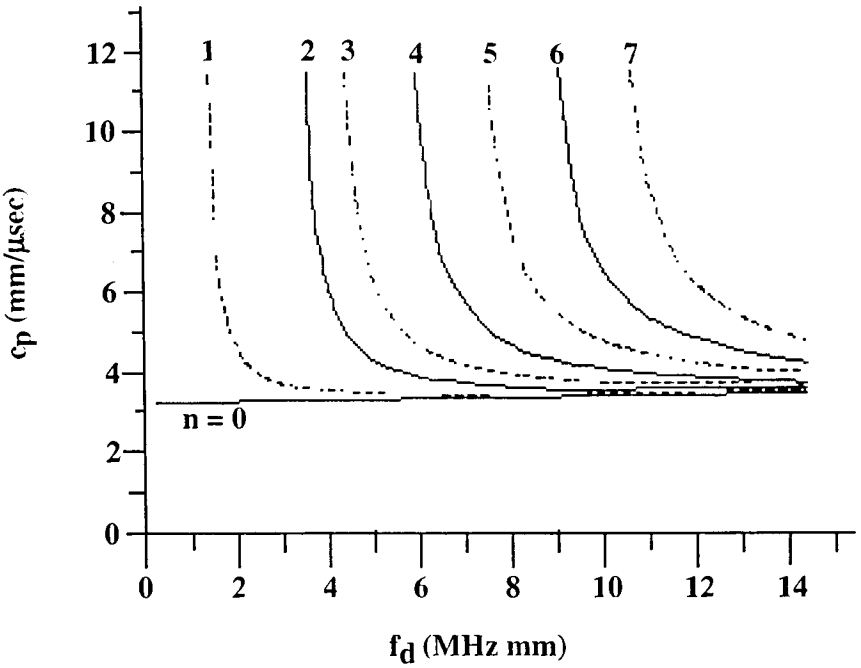

(b) Sample SH mode phase velocity dispersion curves: solid curves denote symmetric modes and dashed curves antisymmetric mode

Fig. 6.2 Sample dispersion curves for steel plate (c_T = 3.1 μm/msec).

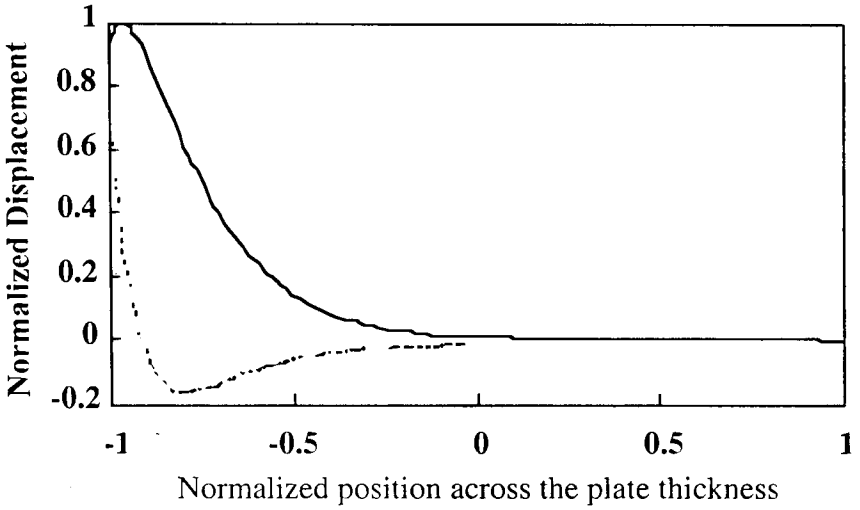

(a) Wave structure for the pseudo-surface wave mode

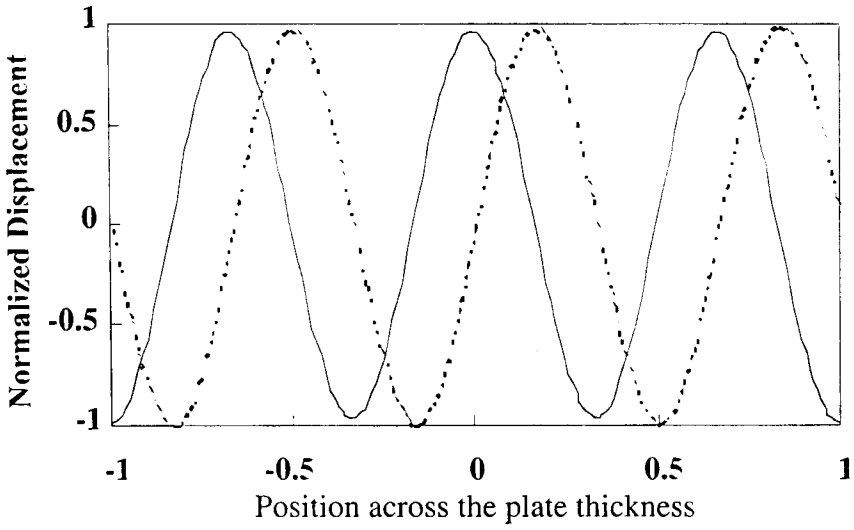

(b) Wave structure for theA3 mode

Fig. 6.3 Wave structures for the pseudo-surface mode and A3 mode at frequency of 565 kHz.

(The plate thickness is 25.4 mm. Solid line is out-of-plane displacement and dashed line is in-plane displacement.)

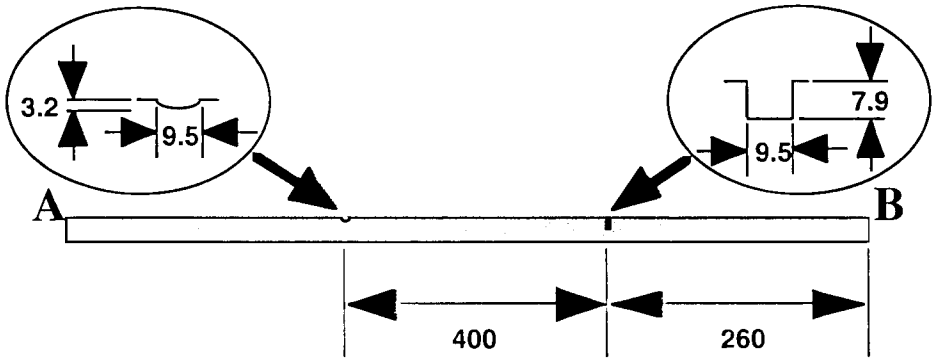

(a) Plate 1

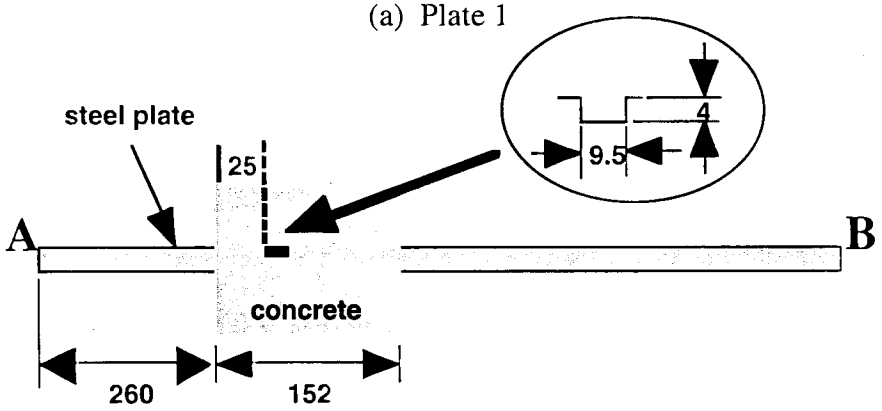

(b) Plate 2

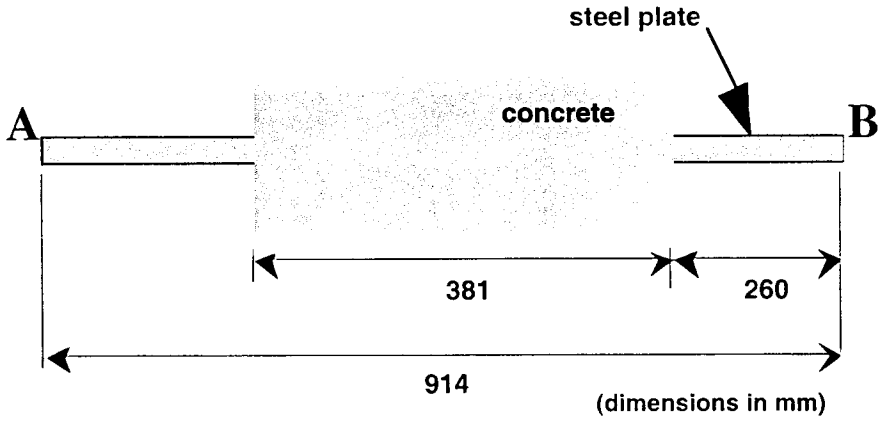

(c) Plate 3

Fig. 6.4 Schematics of plate specimens.

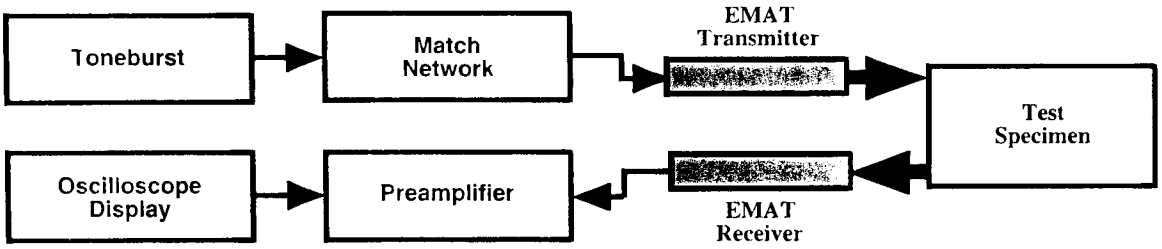

(a) Schematic of an EMAT application system.

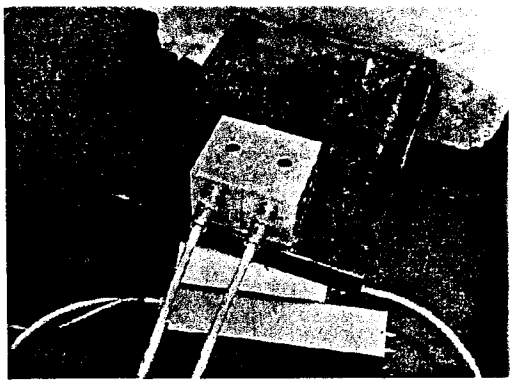

(b) An EMAT system for concrete inspection.

Fig. 6.5 Typical EMAT system and application.

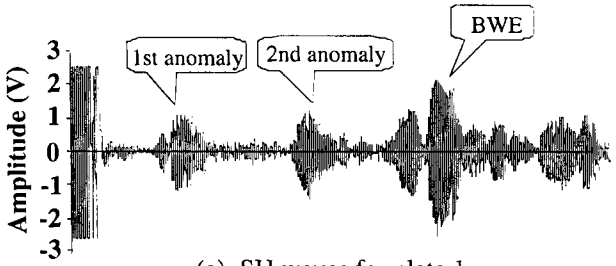

(a) SH waves for plate 1

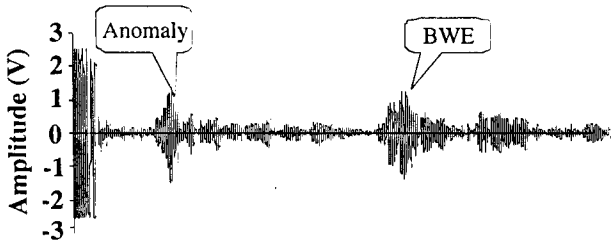

(b) SH waves for plate 2: transducer at position A top surface

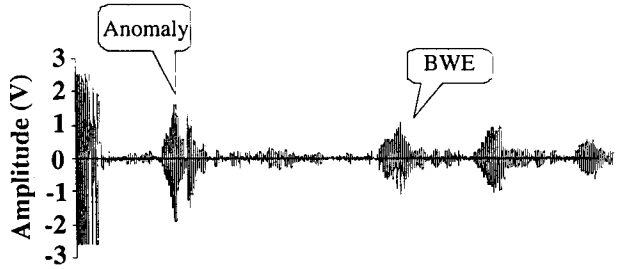

(c) SH waves for plate 2: transducer at position A bottom surface

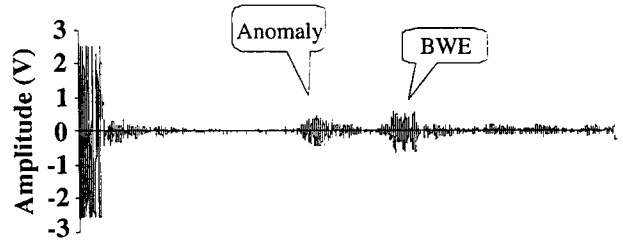

(d) SH waves for plate 2: transducer at position B top surface

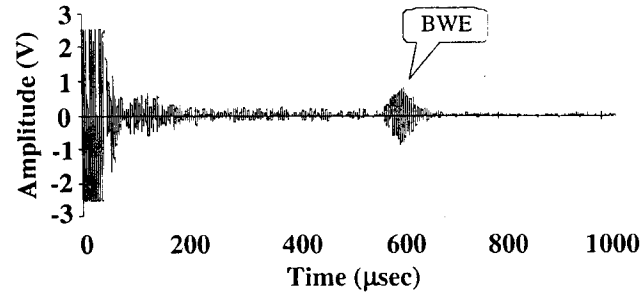

(e) SH waves for plate 3: transducer at position A top surface

Fig. 6.6 SH guided wave experimental results with EMAT SH system.

(Frequency = 240 kHz, nondispersive SH wave mode.)

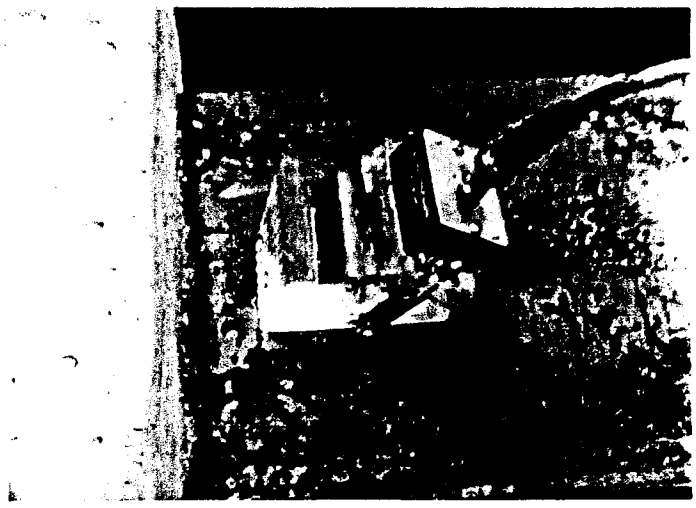

Fig. 6.7 Transducer mounted on wedge for Lamb wave excitation.

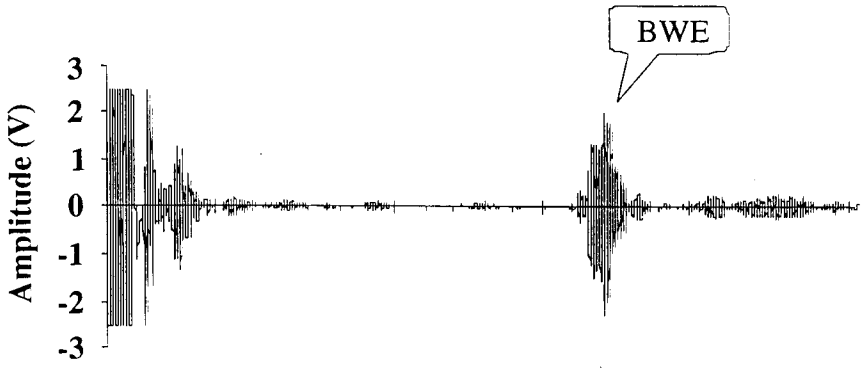

(a) Pulse echo signal plate 1: transducer at position A bottom surface

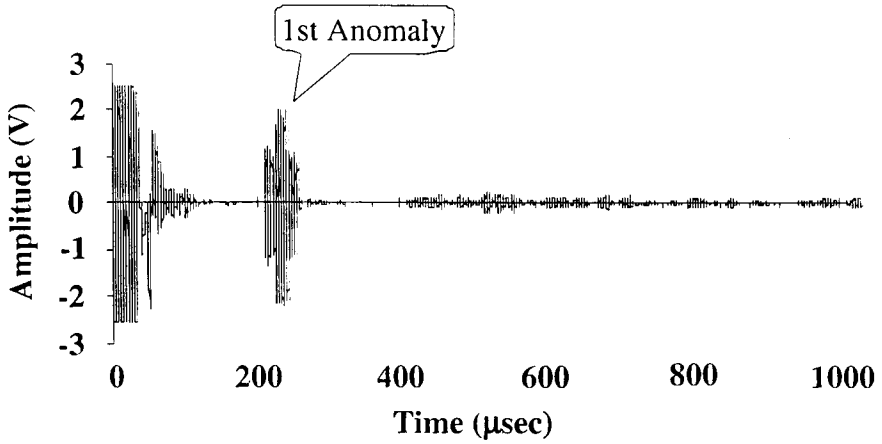

(b) Pulse echo signal plate 1: transducer at position A top surface

Fig. 6.8 Pseudo-surface Lamb wave mode for plate inspections.

(Frequency = 565 kHz; wedge angle = 62°)

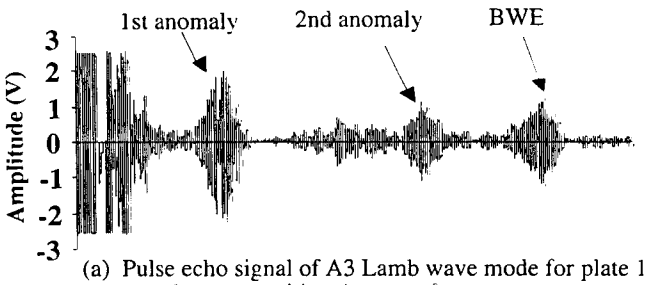

(a) Pulse echo signal of A3 Lamb wave mode for plate 1: transducer at position A top surface

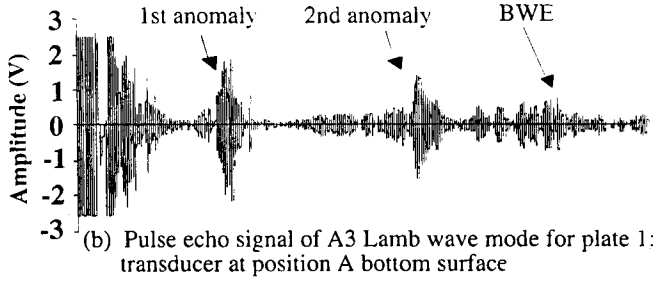

(b) Pulse echo signal of A3 Lamb wave mode for plate 1: transducer at position A bottom surface

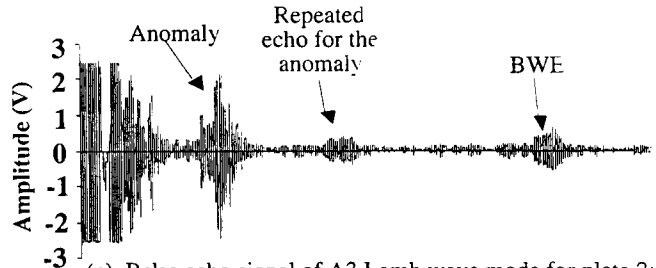

(c) Pulse echo signal of A3 Lamb wave mode for plate 2: transducer at position A top surface

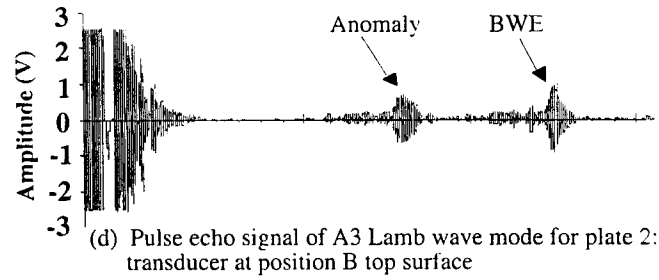

(d) Pulse echo signal of A3 Lamb wave mode for plate 2: transducer at position B top surface

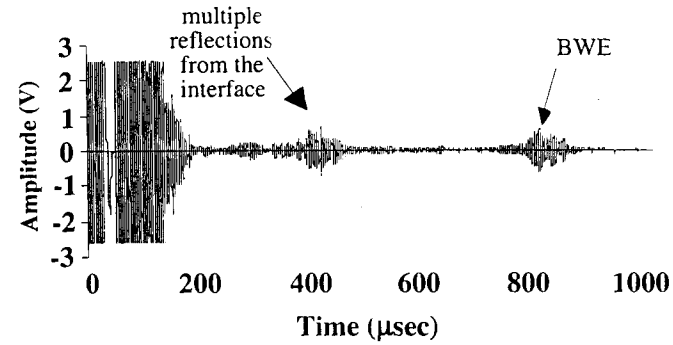

(e) Pulse echo signal of A3 Lamb wave mode for plate 3: transducer at position A top surface

Fig. 6.9 Pulse-echo signals for the A3 Lamb wave mode.

(Frequency = 565 kHz, wedge angle = 38°.)

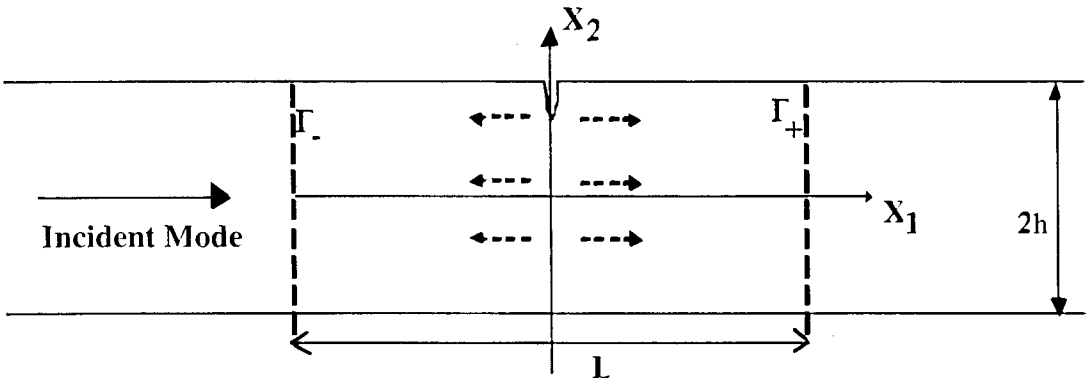

(a) Plate model, solid and dashed arrows show incident and scattering modes, respectively. (Area contained between Γ± lines is used for BEM modeling)

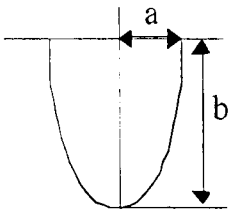

(b) Prameters for an elliptical-shaped flaw

Fig. 6.10 Boundary Element Method (BEM) wave scattering model.

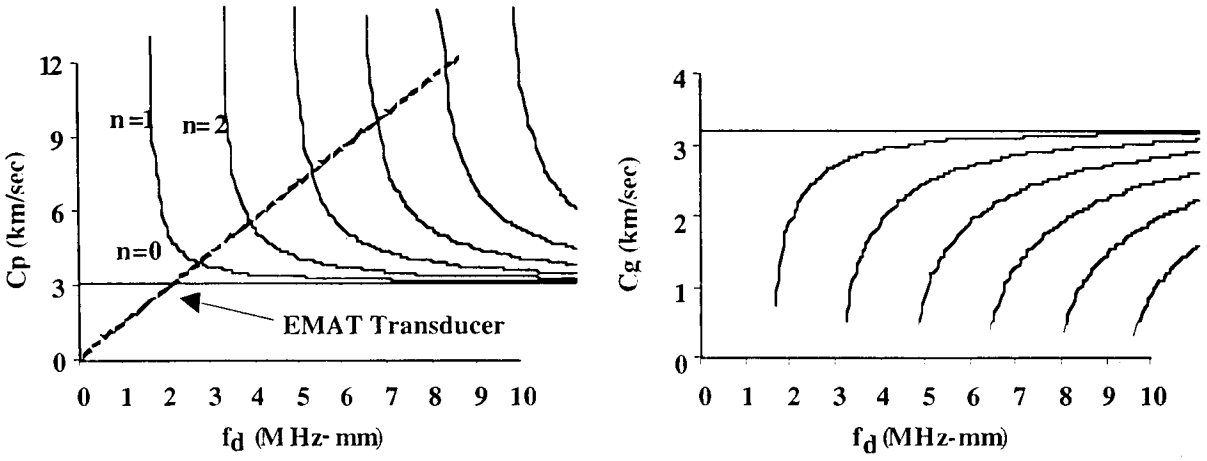

(a) Phase velocity dispersion curves **(b) Group velocity dispersion curves**

Fig. 6.11 SH phase and group velocity dispersion curves for 10-mm-thick steel plate.

(c_L = 5.9 km/sec, c_T = 3.2 km/sec)

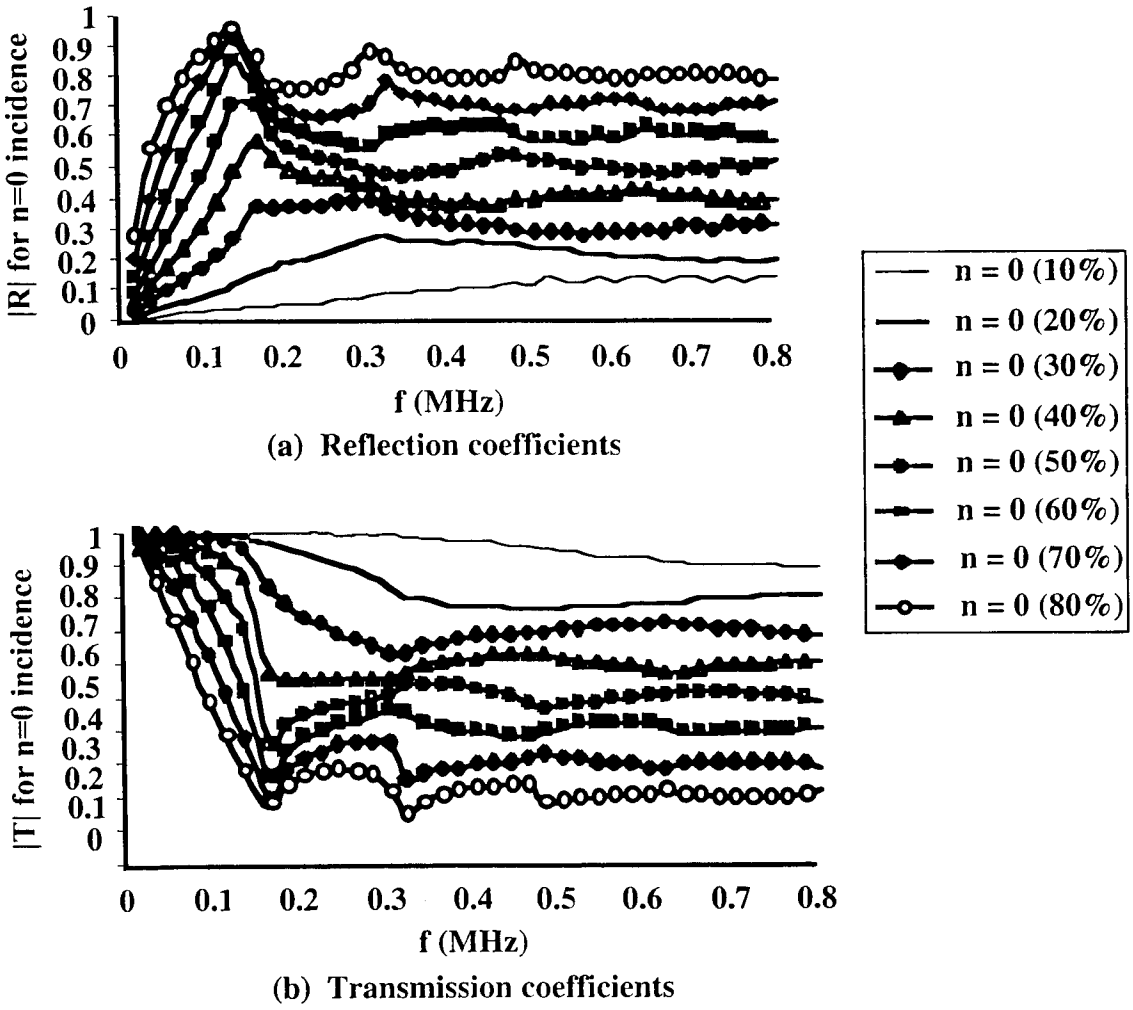

Fig. 6.12 Reflection and transmission coefficients.

(n = 0 mode under n = 0 incident mode for 0.3-mm elliptical notch width and 10 to 80 percent through-plate thickness depth)

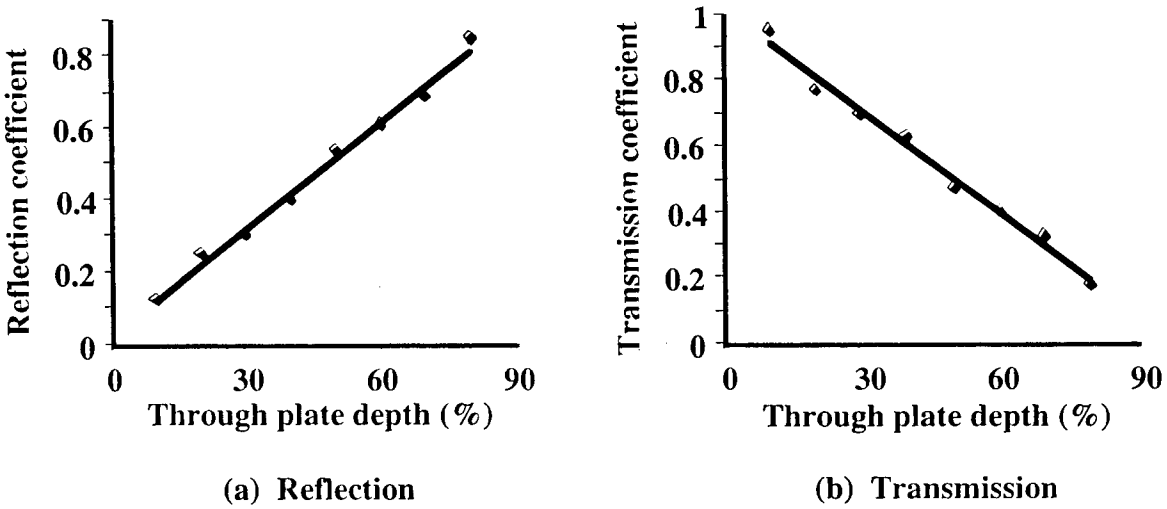

Fig. 6.13 Reflection and transmission coefficients showing linear increase in amplitude with percent through-wall depth.

(n = 0 mode under n = 0 incident mode at a frequency of 0.5 MHz)

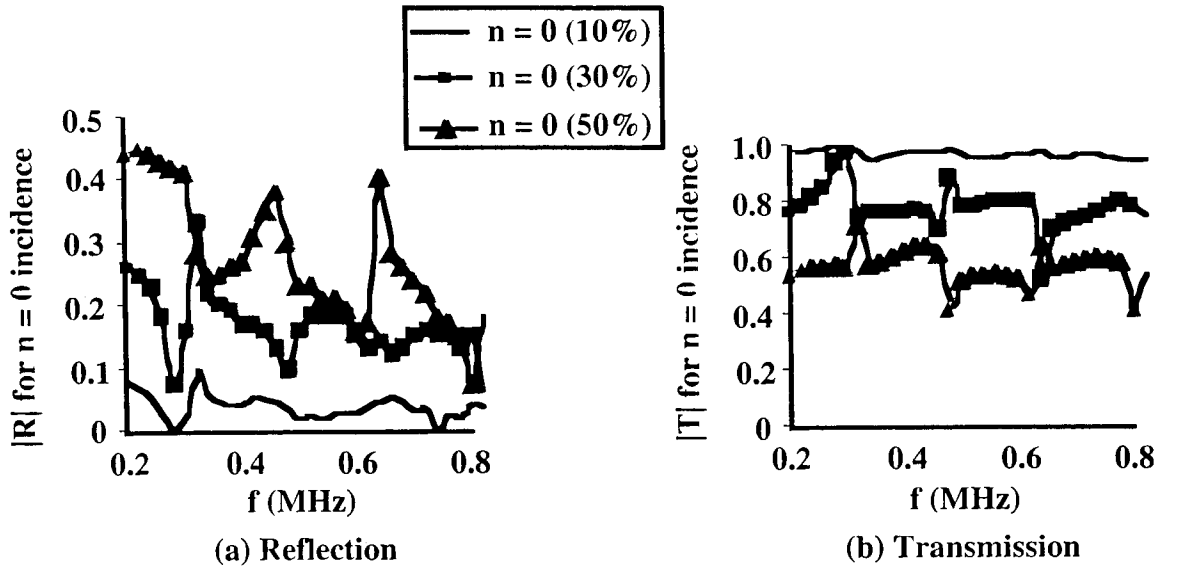

Fig. 6.14 Reflection and transmission coefficients for 6.35-mm elliptical defect width and either 10, 30 or 50 per cent through-plate thickness depth.

(n = 0 mode under n = 0 incident mode)

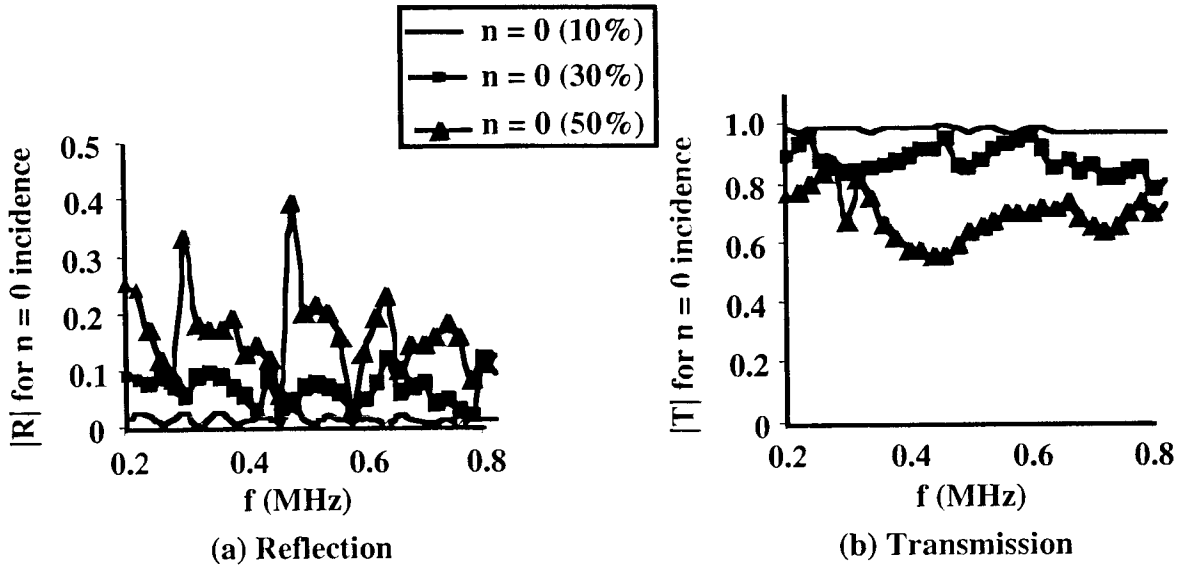

Fig. 6.15 Reflection and transmission coefficients for 12.7-mm elliptical defect width and either 10, 30 or 50 per cent through-plate thickness depth.

(n = 0 mode under n = 0 incident mode)

(a) Through transmission mode; EMATs are 3 in. away from each other and 1.5 in. from center groove.

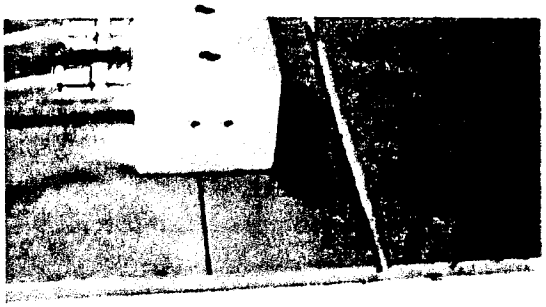

(b) Pulse-echo mode; EMATs are 1.5 in. away from center groove.

Fig. 6.16 Experimental setup.

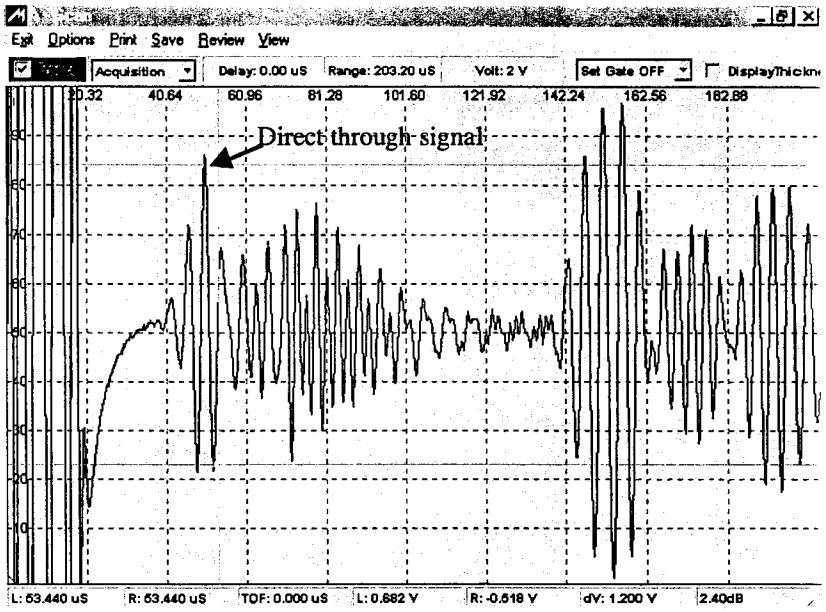

Fig. 6.17. Through-transmission signal from a 0.3-mm-wide notch 10 percent through depth of 10-mm-thick plate.

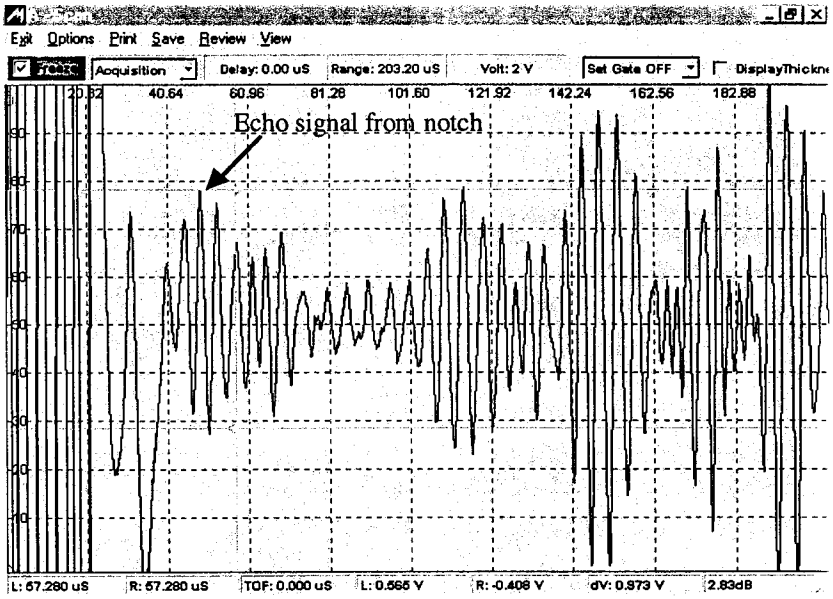

Fig. 6.18. Pulse-echo signal from a 0.3-mm-wide notch 30 percent through depth of 10-mm-thick plate.

(SH wave of mode 0)

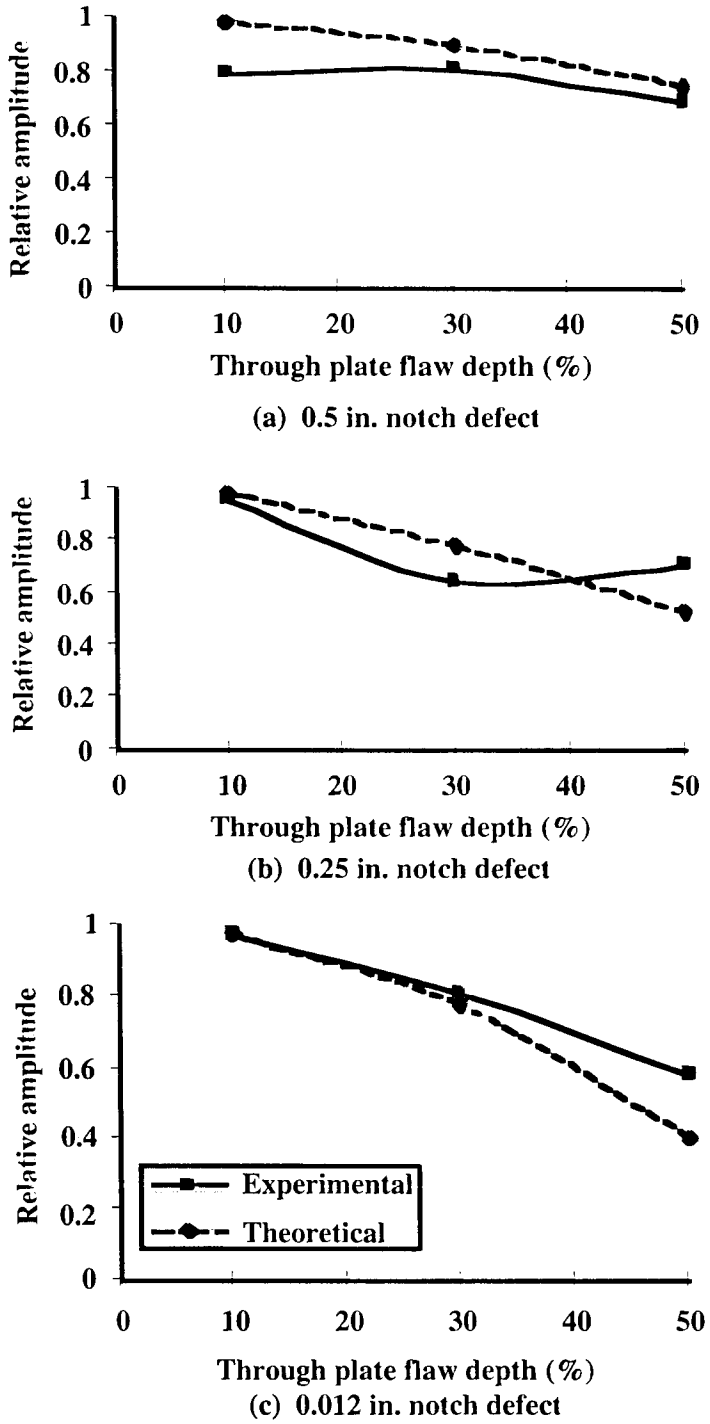

Fig. 6.19 Theoretical and experimental relative amplitude results for 12.7-mm, 6.35-mm, and 0.3-mm-wide notches of different depth in a 10-mm-thick plate.

(76.2-mm transducer separation, 205 kHz, n = 0 mode)

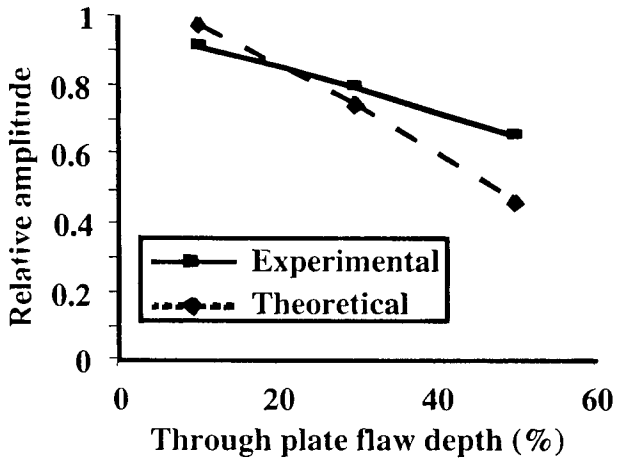

Fig. 6.20 Theoretical and experimental through-transmission signal amplitude versus through-plate flaw depth for 0.3-mm-wide notch.

(n = 0 mode at 205 kHz)

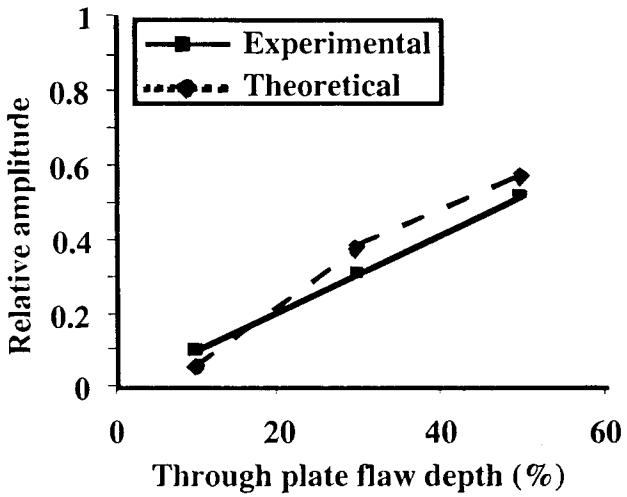

Fig. 6.21 Theoretical and experimental pulse-echo signal amplitude versus through-plate flaw depth for 0.3-mm-wide notch.

(n = 0 mode at 205 kHz)

Table 6.1

Benefits of Guided Waves

- The ability to inspect or screen a long length of a structure using only one probe position, thus greatly increasing the cost effectiveness of an inspection
- The ability to inspect, simultaneously, the entire cross-sectional area of a structure resulting in 100% coverage
- No need for complicated and expensive scanning/insertion/rotation devices since the probe can be stationary during the inspection
- An increased sensitivity to many defects in the structure because of mode and frequency selection options, hence wave structure choice
- The ability to inspect structures under water or insulation, if necessary, without loss of sensitivity
- The possibility of multimode/frequency examination for defect classification and sizing, hence improving overall probability of detection and inspection reliability

Source: Reference [6.12].

7. SUMMARY, CONCLUSIONS AND RECOMMENDATIONS

7.1 SUMMARY

The overall objective of this study was to provide a status report with respect to potential approaches for inspection of inaccessible portions of containment pressure boundaries. In meeting this objective, containment structures are described, current inspection and testing techniques and requirements are summarized, prior research is reviewed, and results obtained from three activities specifically addressing inspection of inaccessible regions of containment metallic pressure boundaries summarized.

Each boiling-water reactor (BWR) or pressurized-water reactor (PWR) unit in the U.S. is located within a much larger metal or concrete containment that also houses or supports the primary coolant system components. Prototypical metal and concrete containments are described, as well as design criteria. Service-related degradation factors that can potentially affect the ability of a nuclear power plant containment to perform satisfactorily in the unlikely event of a severe accident by reducing its structural capacity or jeopardizing its leak-tight integrity are noted. Interior and exterior containment surface areas that could experience accelerated degradation and aging are identified. Current testing and inspection requirements are reviewed, including a discussion of the maintenance and license renewal rules. Several instances of containment pressure boundary component degradation at commercial nuclear power plants in the United States are described.

Nondestructive examination is the primary method used to evaluate the presence and significance of indications of degradation of the containment pressure boundary. Selection of the appropriate method depends on the type and nature of the degradation, the component geometry, and the type and circumstances of inspection. Cost and availability are also factors. Nondestructive examination methods for metallic materials principally involve surface and volumetric inspections to detect the presence of degradation (i.e., loss of section due to corrosion or presence of cracking). The surface examination techniques primarily involve visual, liquid penetrant, and magnetic particle methods. Volumetric methods include ultrasonic, eddy current, and radiographic. Brief descriptions, primary applications, and dominant sources of variance for each of these techniques are provided. ASME rules for surface and volumetric examination of containment pressure boundary components and acceptance standards are noted.

Prior investigations conducted using conventional ultrasonics and electromagnetic acoustic transducers are summarized. In Germany, an extensive evaluation was conducted by Technical Inspection Service (Munich) to evaluate the feasibility of using ultrasonic methods to detect corrosion damage of the containments of PWRs or liners of BWRs in areas that are inaccessible (i.e., embedded bottom portion of containments of PWRs, areas of containments of PWRs adjoining platforms, penetrations through the containments of PWRs, and steel liners of BWRs inside pressure-suppression chamber). In order to establish suitable search units (favorable signal-to-noise ratio) for detection of metal containment corrosion, a calibration block with simulated corrosion was prepared (i.e., sharp-edged and a cambered shallow pit). Several angle beam search units were used to examine the calibration block (45°, 60°, 70°, and 90°). Results obtained showed that the sharp-edged pit was detectable (signal-to-noise ratio >12, input angles from 45° to 90°), but the rounded pit (input angles from 35° to 80°) could not be detected. Supplemental testing performed on a PWR containment and corroded calibration blocks indicate that it was possible to detect well-developed corrosion pits (pit depth of same order of magnitude as ultrasonic wave length) with 45° angle beam 2 MHz search units within a distance of up to 130 mm below the interface between the concrete and metal containment. The capability of adapting electromagnetic acoustic transducers (EMATs) to detect corrosion in Mark 1 containment vessels and correlating EMAT signals with corrosion damage to make quantitative evaluations were evaluated in the laboratory by Innovative Sciences, Inc. (San Leandro, California) for the Electric Power Research Institute. Pulse-echo and through transmission-modes were evaluated. Simulated corrosion-like defects (13-mm wide by 102-mm long by 11-mm deep) were milled into a 2.1-m-wide by 4.9-m-long by 25.4-mm-thick plate at a distance of 0.6 m from one end. Experimental results show that SH waves scattered from planar slots (also for planar cracks and similar boundaries) produce signals that are measurable at substantial distances (3 m or more) from a small (two wavelength) scatterer that extends halfway through the plate. In the pulse-echo geometry, a flaw at least half-way through the plate thickness and two wave lengths long (~127 mm) provided strong scattering signals that could be detected at distances to 4.6 m. Rounding of the flaw causes the signal to become weaker and spreads it more over a larger angle (i.e., scattered energy from planar slot is primarily SH_0 mode while semi-circular

slot scatters a great deal of energy into other modes). Results reported in the German and EPRI studies were sufficiently encouraging that limited studies have been funded to investigate high-frequency bistatic acoustic imaging, magnetostrictive sensors, and multimode Lamb and horizontal shear guided wave techniques.

Analytical and experimental simulations were conducted by Cambridge Acoustics/Engineering Technology Center (Cambridge, MA) to investigate the feasibility of applying high-frequency acoustic imaging techniques to the detection and localization of thickness reductions in the metallic pressure boundaries of NPP containments. The analytical study used an elastic layered-media code (OASES Code, Massachusetts Institute of Technology) to perform a series of numerical simulations to determine the fundamental two-dimensional propagation physics. The range-dependent version of the OASES Code successfully modeled the steel containment and steel-lined concrete containment scenarios using the discrete notch approach. For the steel containment scenario significant degradations (> 2 mm) located below the concrete/air interface give reasonable intrinsic backscatter levels (-15 dB) that are 10 – 15 dB above the expected noise level due to surface imperfections. Dependence of degradation depth is small, but measurable. Although the embedding concrete introduced large losses that limits the penetration ability, results indicate that acoustic imaging technology can be applied to this scenario. For the steel-lined reinforced concrete containment scenario, the thin steel liner in conjunction with the concrete produced unacceptably high signal losses to concrete (~100 dB). Application of acoustic imaging technology to this scenario seems unlikely. In an effort to not only provide a basis for improving the numerical models, but also to continue the feasibility study in a more practical forum, the analytical study was followed by a series of controlled laboratory experiments. The experiments attempted to limit conditions to two-dimensional scenarios where only degradation variations in the direction of the incident wave were considered, and flat plates could be used as propagating media. The testing equipment consisted of a pulser/receiver card, a high frequency analog-to-digital acquisition board, software, piezoelement contact transducers, coupling wedges, and industrial grade ultrasonic gel couplant. The system's input/output dynamic range was experimentally determined by measuring the maximum signal that the system could inject and the minimum signal that the system could read. Measurement repeatability was quantified and wave guide effects on signal propagation were addressed. The signal level returned from "artificial" degradations was evaluated using uniform cross-section slots, either rectangular, rounded, or "V" shaped, cut across the width of a 203-mm wide by 25-mm thick steel plate. The final series of tests to assess the individual components of signal loss involved measuring the effect that concrete had on waves travelling in an embedded plate and involved steel plates with and without flaws embedded in concrete. Results of the experimental studies indicate that the measurement system displayed an input/output dynamic range of 125 dB. Therefore, in the absence of competing signals, 105 dB of losses can be incurred while still maintaining a 20 dB signal-to-noise ratio. Results obtained from rectangular, rounded, and "V" shaped notches provide a preliminary basis for estimating reflected signal levels from a vast array of two-dimensional degradations. Results for the steel plates embedded in concrete indicate that an additional 1.6 dB and 1.4 dB of signal loss is incurred for each centimeter of two-way signal travel when using 45° and 70° coupling wedges, respectively. Thus, waves directed at shallow angles are least affected by the concrete, regardless of coupling condition, and may be of more value for the inspection scenario of interest. Results from the signal-loss component experiments provide a basis for estimating the total loss induced on an incident signal for many scenarios (e.g., in the absence of competing signals, a 4-mm-deep rounded degradation located 30 cm below the air/concrete interface for the steel containment scenario should be detectable using a 70° coupling wedge because 50 dB of signal-to-noise ratio remains after estimated losses of 73 dB). Competing signal environments (e.g., compressional wave field) may mask the signal return to make defect detection difficult; however, use of bistatic measurements and discrimination techniques can minimize or eliminate competing signals.

A preliminary study was conducted by Southwest Research Institute (San Antonio, TX) to investigate the feasibility of applying magnetostrictive sensor technology to inspection of plate-type materials and to evaluate its potential for detecting and locating thickness reductions in a NPP containment metallic pressure boundary resulting from corrosion. This study involved both modeling and experimental studies. Dispersion properties of Lamb waves, which refer to longitudinal guided waves in plates, were investigated theoretically using a general-purpose software package called DISPERSE (Imperial College, University of London). Using this software package, dispersion curves of Lamb waves were calculated for three different boundary conditions—free boundary, one side in contact with concrete, and both sides in contact with concrete. In the modeling studies the plate was assumed to be 12.7 mm thick, and the concrete was assumed to be infinitely thick and perfectly bonded to the plate. Comparing the A0 mode velocities for the free plate and plates backed by concrete, there was only a slight decrease (i.e., no more than 0.3 mm/μsec) in the low-frequency range (i.e., below 1 MHz-mm). Overall, the effect of concrete on the group velocity appeared to be relatively small. In addition to dispersion curves, the DISPERSE program calculated

wave attenuation. Results show a large increase in attenuation when concrete was placed on one side of a plate. As might be expected, the effect of concrete on attenuation increased by a factor of two or more when the concrete was placed on both sides of the plate. Attenuation was significantly less for the A0 mode than for the S0 mode and so the A0 mode would be better than the S0 mode for long-range inspection of plates backed by concrete on one or both sides. Analytical results thus indicate that it appears possible to achieve long-range inspection under this scenario using a low-frequency A0 wave mode. Experimental studies used a carbon steel plate (ASTM A-36), approximately 6.35-mm-thick by 1.23-m-wide by 6.11-m long placed on two wooden supports, as the test article. The transmitting and receiving MsS probes were approximately 30 cm long and 2.5 cm wide. Initial activities addressed the capability of the MsS to generate and detect guided waves. After investigating guided-wave generation and detection capability using the pitch-catch technique, the feasibility of detecting defects in the plate was investigated using the pulse-echo technique. For this purpose, a notch was machined into the plate at a position corresponding to approximately 2/3 the plate length. The notch was approximately 3-mm deep by 6-mm wide, with the length changed from 10 to 30 cm in 10–cm increments to evaluate the relationship between notch length and signal amplitude. Amplitudes of the defect signals were found to increase approximately linearly with notch length, indicating the feasibility of determining the severity of a defect from the defect signal. The amplitude of a signal from a reflector, such as a notch or corrosion, is proportional to the cross-sectional area of the defect (in the plane normal to the guided wave beam propagation) relative to the total beam width of the interrogating guided wave. Therefore, the product of both length and depth of a defect influences the defect signal amplitude. However, since the relative area of a given-size defect to the total beam width of the guided wave will vary with the mode and frequency of the guided wave employed for inspection, the signal amplitude from the same defect will also vary. Taking advantage of this variation, it appears feasible to separately determine both the depth and the length of a defect by combining two or more sets of data taken using different guided wave modes and frequency. For the 20 kHz A0 wave mode and using parameters established during the experimental investigation, it appears that a 50-percent through-wall 1.8-cm-diameter corrosion pit located within a 15-meter distance could be detectable using the MsS technique. No experiments were conducted using plates embedded in concrete.

A limited investigation addressing defect detection and sizing has been conducted by the Pennsylvania State University (University Park) using the guided wave technique. The specimens studied included a free plate (no concrete) with two anomalies, a plate embedded in concrete with one anomaly, and a plate embedded in concrete but having no anomalies. All three plates were 25.4-mm thick by 203-mm wide by 914-mm long. The plate specimens provided a benchmark for studying various aspects of guided wave inspection, including sensitivity, transmission ability across anomalies, inspection reliability, and penetration ability. Initially horizontal shear guided waves generated by electromagnetic acoustic transducers were used to interrogate the plate specimens. The waveforms obtained from testing the plate specimens with defects indicates that both defects located on the same side of the plate can be detected as well as a defect embedded in concrete. Insensitivity to the concrete edge and the plate-concrete interface was also demonstrated. The plates were also interrogated using Lamb waves generated by a transducer mounted on a wedge. The frequency and wedge angle determined the generated Lamb wave mode. Two wedge angles were considered at the frequency of 565 kHz – 62 and 38 degrees. For the 62 degree wedge, when the transducer was located on the same surface as the anomalies, the surface wave generated was very sensitive to the closest anomaly, but not to the second anomaly. When placed at the opposite surface (bottom) to the anomalies on the free plate both anomalies were ignored and only a backwall echo was received. In order to obtain a fairly uniform energy distribution across the plate thickness for Lamb waves, the wedge angle was changed to 38 degrees. By generating the A3 Lamb wave mode, the transducer could detect anomalies from either the top or bottom surfaces of the plate and the Lamb wave mode exhibited good sensitivity to anomalies. The anomaly embedded in concrete was also detectable. Compared with horizontal shear waves, Lamb waves show a higher signal-to-noise ratio, but received multiple echoes from the plate-concrete interface. This problem can be overcome by setting a threshold for an anomaly call. Most anomalies of major concern would probably penetrate more than 20% the plate thickness and reflect stronger echoes than those from the plate-concrete interface. Use of multi-mode Lamb wave signals therefore can also be considered for an anomaly call. In the second part of this investigation, the Boundary Element Method (BEM) was developed to study the interaction of various guided wave packets of energy with various corrosion boundaries in a structure. The goal of the modeling effort was to establish guidelines so that the best modes and frequencies could be considered for impingement to provide the best chance of success in determining the defect shape and size characteristics. This study was carried out on elliptical-shaped scatterers with a variation in defect depth and length values. This type of reflection was selected because it could model items of interest such as corrosion boundaries and pitting. An electromagnetic-acoustic transducer technique for horizontal shear wave excitation was used in the experimental part of the investigation. For initial experiments, artificial

corrosion and crack type defects were fabricated with different depths and widths in 10-mm-thick steel plates. An excellent monotonic change in amplitude versus percent through-wall depth was obtained for all frequencies investigated. Preliminary results show that defect quantification analysis can be carried out for horizontal shear guided wave impingement onto a defect in a wave guide. In particular, the possibility of a monotonic increase in amplitude change with size was noted. Potential advantages of shear horizontal waves compared to "Lamb" type waves include less mode conversion, constant wave structure for a particular mode for all frequencies, and less sensitivity to boundary conditions because of the lateral particle velocity. BEM results can be used to establish data acquisition and analysis guidelines for development of a test protocol and quantification algorithm development program. Besides modeling and BEM analysis, feature extraction possibilities could also be obtained from experimental or calibration standards using guidelines established in this study.

Table 7.1 presents a summary and characteristics of the techniques evaluated for inspection of inaccessible regions of NPP containment metallic pressure boundaries.

7.2 CONCLUSIONS

Inspection of inaccessible portions of metallic pressure boundary components of NPP containments (e.g., fully embedded or inaccessible containment shell or liner portions, the sand pocket region in Mark I and II drywells, and portions of the shell obscured by obstacles such as platforms or floors) requires special attention. Embedded metallic portions of the containment pressure boundary may be subjected to corrosion resulting from ground water permeation through the concrete; a breakdown of the sealant at the concrete-containment shell interface that permits entry of corrosive fluids from spills, leakage, or condensation; or corrosion may occur in areas adjacent to floors where the gap contains a filler material that can retain fluids. Corrosion, should it occur, may challenge the containment structural integrity and, if through-wall, can provide a leak path to the outside environment. At present nondestructive evaluation techniques for use in determining the condition of the containment pressure boundary are time-consuming and costly because they tend to examine only a small area at a time. A nondestructive technique is required that can be used remotely to examine inaccessible regions of the containment metallic pressure boundary. Such a technique ideally should also be capable of performing global inspections so that determination of the overall condition of the containment metallic pressure boundary can be achieved in a cost- and performance-effective manner. Identification and/or development of such technique(s) becomes increasingly important as the median age of the NPPs now exceeds 20 years, and in the not-too-distant future several of these plants will be nearing the end of their initial operating license period.

The performance of a commercially available fully-integrated angle-beam inspection system was evaluated through both numerical and experimental studies. The numerical studies indicated that for the embedded steel-lined concrete containment scenario, the thin steel liner with concrete backing combine to give unacceptably high signal loss to the concrete for small degradations close to the interface. However, for the embedded steel containment scenario, significant degradations (i.e., 2 mm) below the concrete-air interface give a reasonable intrinsic backscatter level that is sufficiently above the expected noise level to be detectable. Experimental results using 25-mm-thick steel plates show that notches contained in the plates were detectable using high-frequency acoustic-imaging technology. When the plates were embedded in concrete, the concrete caused additional signal loss, but defects such as a 4-mm-deep rounded degradation located up to 30 cm below the air-concrete interface should be detectable. The losses to the concrete were strongly dependent on the coupling conditions between the steel and concrete, and ultrasonic waves directed at shallow angles were least affected by the concrete, regardless of coupling condition.

Magnetostrictive sensor-generated guided waves that had been used for inspection of long lengths of piping and tubing has been successfully adapted for application to guided wave inspection of plate-type materials. Modeling studies suggest that a low frequency A0 mode wave (e.g., 20 kHz in a 25.4-mm-thick steel plate are best suited for inspection of containment boundaries backed on one or both sides by concrete. Experimental results demonstrated that the magnetostrictive sensor technique can generate and detect guided waves in plates and detect a defect over a long range, including defects contained in areas difficult to access because of equipment or attachments. The amplitude of signals reflected from notches machined in a steel plate was affected by the product of defect length and depth in the plate normal to the guided wave beam propagation. The effect of a defect embedded in concrete was not evaluated experimentally using magnetostrictive sensors.

Lower frequency methods appear to be best for inspection of plates bounded by concrete because of reduced attenuation, but sensitivity to defects and defect resolution are reduced relative to higher frequency methods. Horizontal shear and Lamb wave modes can be used for inspection of steel containment structures, both somewhat insensitive to the concrete boundary for specific velocity and frequency values. Strong benefits of the horizontal wave mode via an electromagnetic acoustic transducer were demonstrated with overall improved signal-to-noise ratio, practically no interference from the concrete interface, and the non-contact testing potential. Although preliminary, results show that defect quantification analysis can be carried out for horizontal shear guided wave impingement onto a defect in a wave guide. Both pulse-echo and through-transmission methods were considered. In particular, the possibility of a monotonic increase in amplitude change with size was noted. Potential advantages of horizontal shear waves compared to "Lamb" type waves includes less mode conversion, constant wave structure for a particular mode for all frequencies, and less sensitivity to boundary conditions because of the lateral particle velocity. The Boundary Element Method (BEM) can be used to establish data acquisition and analysis guidelines for development of a test protocol and quantification algorithm development program. Besides modeling and BEM analysis, feature extraction possibilities could also be obtained from experiment or calibration standards using guidelines established in this study.

7.3 RECOMMENDATIONS

Conventional ultrasonic inspection techniques generate ultrasonic beams that tend to spread out as the beam is reflected from the component boundaries to limit the technique's inspection resolution. Also, mode conversion occurs where both longitudinal and shear waves are present after reflections from component boundaries to potentially influence the signal-to-noise ratio and make the defect echoes difficult to interpret. Furthermore, multiple echoes can be received from the plate-concrete interface and, unless the correct combination of frequency and wedge-input angle is selected, only the first of a series of defects will be detected, or defects may not be detectable at all from the opposite surface of a plate containing a surface defect. Therefore, techniques utilizing guided waves that interrogate the specimen cross section (i.e., provide energy distribution across component cross section) should be investigated in more detail (e.g., electromagnetic acoustic transducers, magnetostrictive sensors, and multimode guided wave methods).

A series of laboratory experiments should be conducted to evaluate candidate systems under more prototypical conditions. Specimens should be fabricated and tested that would evaluate effects such as flaw geometry (e.g., notch, flat-bottom holes, and thinned areas), size (e.g., width, length, and depth), orientation, and location relative to the plate-concrete interface; three-dimensional effects (e.g., plate curvature); structural discontinuities (e.g., welds, anchor, or studs); and the presence of concrete as well as the quality of the bond between the concrete and steel. As a part of these investigations instrumentation systems should be optimized to control wave direction and mode, establish operable plate thicknesses, inspection range, and defect detectability data generated (e.g., probability of defect detection curves). Signal processing should be investigated as a method to discriminate between defects of potential significance and other scatterers (e.g., welds, concrete voids, and anchor studs). In addition to being able to detect defects, work needs to be done on sizing and classifying the severity of a particular defect. Development of the BEM approach should continue to establish guidelines so that the most effective wave modes and frequencies can be considered for impingement to provide the optimum probability for determining a defect shape and size characteristics. Work should also be conducted on developing a system that can perform global inspections through use of comb transducers or transducer arrays. Once these experiments have been completed, the most promising of the three potential candidate systems should be evaluated under representative field conditions and optimized.

Table 7.1
Summary of Techniques Evaluated for Inspection of Inaccessible Regions of NPP Metallic Pressure Boundaries

Method	Principle of Operation	Advantages	Limitations	Flaw Detection		
				Detect	Locate	Size
Ultrasonics	Uses sound waves of short wavelength and high frequency (e.g., 0.5 to 20 MHz) to detect surface and subsurface flaws; alternating current voltage applied across crystal faces of piezoelectric materials causes expansion and contraction that generates a compression wave in surrounding media; inclusions and imperfections detected by partial reflection or scattering of ultrasonic waves, time of transit of wave through test object, and features of spectral response for either a transmitted or reflected wave	Good penetration capability; high sensitivity to permit detection of small flaws; good accuracy relative to several other NDE methods; only one surface needs to be accessible	Rough surfaces present problems relative to signal scattering; coupling critical; significant attenuation of surface waves due to presence of concrete at interface; generally operates at high frequencies which limits inspection range and resolution; masking of surface flaws when located at same surface as transducer	Yes	Yes	No[a]

[a]Sizing not evaluated as part of limited study.

Table 7.1 (Cont.)
Summary of Techniques Evaluated for Inspection of Inaccessible Regions of NPP Metallic Pressure Boundaries

Method	Principle of Operation	Advantages	Limitations	Flaw Detection		
				Detect	Locate	Size
Magnetostrictive Sensor (MsS)	Magnetic force produced directly in structure by setting magnetic domains in material into a vibrational mode through application of alternating magnetic fields; magnetic force generates guided waves at sonic and ultrasonic frequencies; detection of guided waves is achieved by reverse process where guided waves cause magnetic domains to vibrate which causes magnetic induction of the material to change with time; changing magnetic induction induces electrical voltage in magnetostrictive coil; occurrence time of a defect signal and signal amplitude used to determine severity and location of a defect	Operating frequency from few Hz to several hundred kHz; sensor has broad frequency response; used at temperatures up to Currie temperature of material under inspection; noncontact; couplant free; requires minimum surface preparation; inspection range can exceed several hundred feet in pipe structures; inspects entire structure cross section; can be modified for application to nonferromagnetic materials	Operates at relatively low frequencies which limits defect detection sensitivity and resolution; does not have mode control capability which complicates signal interpretation; experiments not conducted in this study with concrete interface present (See footnote Pg. 81)	Yes	Yes	No[a]

[a]Sizing not evaluated as part of limited study.

Table 7.1 (Cont.)
Summary of Techniques Evaluated for Inspection of Inaccessible Regions of NPP Metallic Pressure Boundaries

Method	Principle of Operation	Advantages	Limitations	Flaw Detection		
				Detect	Locate	Size
Electromagnetic -acoustic Transducer (EMAT)	Transmitter coil excited by high-frequency current induces eddy current into surface of metal examined; eddy current interacts with magnetic field generated by transmitter coil to provide Lorentz force that interacts with alternating current applied by EMAT and an externally supplied magnetic flux to generate guided plate waves; reflected elastic waves detected by reverse process in which the wave in the presence of a static magnetic field gives rise to eddy currents in the metal that induces a voltage into EMAT coil	Couplant not needed; successfully used for long-range inspection of tubes and steel sheets; wave velocity independent of plate thickness; ultrasound can be generated through a surface coating up to 1.5-mm thick; complete cross section inspection; improved tolerance to non-uniform plate-concrete interface while maintaining sensitivity to anomalies	Efficiency is low and therefore signal-to-noise ratio may be poor; loses sensitivity when gap to surface of component inspected is increased; non-ferromagnetic materials require special preparation	Yes	Yes	Yes[a]

[a]Some preliminary sizing-related studies conducted as part of limited study.

Table 7.1 (Cont.)
Summary of Techniques Evaluated for Inspection of Inaccessible Regions of NPP Metallic Pressure Boundaries

Method	Principle of Operation	Advantages	Limitations	Flaw Detection		
				Detect	Locate	Size
Multimode Guided Waves	Plate impinged obliquely with a tone-burst from a relatively large transducer; refraction and reflection at interfaces produces many new signal packets; by adjusting angle of incidence or frequency the reflected and refracted energy within the plate will constructively interfere launching many plate wave modes with waves propagating parallel to surface; each of guided wave modes has a particular wave structure that determines the sensitivity of the particular mode to a particular flaw type; mode and frequency combinations chosen to maximize sensitivity and penetration power	Inspect long lengths of a structure from one location; inspects entire structure cross section; increased sensitivity to defects because of mode and frequency selection options; can inspect structures under water or beneath insulation; possibility of improved defect classification and sizing because of multimode/frequency examination	High transducer profile or wedge size may limit applications to larger structures; generates guided waves by Snell's law which may not enable guided waves to be produced in lower phase velocity materials; not applicable to high temperatures; difficult to generate pure wave mode because of phase variations as wave enters structure through wedge	Yes	Yes	No[a]

[a]Sizing not evaluated as part of limited study.

Internal Distribution

1. E. E. Bloom
2. J. M. Corum
3. E. Lara-Curzio
4. G. E. Michaels
5-10. D. J. Naus
11. A. E. Pasto
12. J. B. Roberto
13-14. J. J. Simpson
15. ORNL Patent Section
16. Central Research Library
17. Document Reference Section
18. Laboratory Records

External Distribution

19. S. Ali, NRC
20. H. G. Ashar, NRC
21. G. Bagchi. NRC
22. G. Barslivo, SKI
23. G. S. Bedi, NRC
24. Z. Bittnar, Czech Technical University
25. J. Carey, EPRI
26. T-Y. Chang, NRC
27. N. C. Chokshi, NRC
28. Commander and Director, USAE Waterways Experiment Station
29. J. F. Costello, NRC
30. K. Cozens, NEI
31. R. Danisch, Framatome
32. D. H. Dorman, NRC
33. B. R. Ellingwood, Georgia Tech
34. W. L. Gamble, University of Illinois
35-49. H. L. Graves, III, NRC
50. F. E. Gregor, LCM Engineering
51. W. Heep, NOK
52. G. Imbro, NRC
53. D. C. Jeng, NRC
54. P-T Kuo, NRC
55. H. Kwun, Southwest Research Institute
56. K. Manoly, NRC
57. H. W. Massie, DNFSB
58. M. E. Mayfield, NRC
59. T. McNulty, HSE
60. H. Müller, Universität Karlsruhe
61. A. J. Murphy, NRC
62. W. E. Norris, NRC
63. J. Philip, NRC
64. J. L. Rose, Pennsylvania State University
65. J. Rudzinsky, Cambridge Acoustical Associates
66. V. Schmitz, IzfP
67. S. P. Shah, Northwestern University
68. R. E. Shewmaker, NRC
69. H. Stephens, EPRI
70. D. Terao, NRC
71. J. P. Vora, NRC
72. H. Wiggenhauser, BAM
73. Office of Assistant Manager for Energy Research and Development, DOE-OR
74. Office of Scientific and Technical Information